Institute of Condensed Matter and Nanosciences
Molecular Chemistry, Materials and Catalysis division

Accessing Gas Adsorption Micro- and Macroscopically by in situ Powder Diffraction

---

Xiao Li

Supervisor: **Professor Yaroslav Filinchuk**

Thesis submitted in fulfilment of
the degree of Doctor in Sciences

Louvain-la-Neuve 2022

Institute of Condensed Matter and Nanosciences
Molecular Chemistry, Materials and Catalysis division

Accessing Gas Adsorption Micro- and Macroscopically by in situ Powder Diffraction

Xiao Li

Members of Jury:

Prof. Yaroslav Filinchuk (UCLouvain), supervisor
Prof. Eric Gaigneaux (UCLouvain), President
Prof. Gian-Marco Rignanese (UCLouvain)
Prof. Tom Leyssens (UCLouvain)
Dr. hab. Dmitry Chernyshov (ESRF, France)
Prof. Hai-Wen Li (HGMRI, China)

Thesis submitted in fulfilment of
the degree of Doctor in Sciences

Louvain-la-Neuve 2022

Abstract and Structure of the Thesis

Gas adsorption is a spontaneous interaction that occurs on the interface between the gas and a condensed phase. Porous materials, having large surface areas, reveal this phenomenon more pronouncedly. Porous materials are applied in many fields, such as gas storage, gas separation, sensoring, catalysis, drug delivery, etc. With the increase of demand, more functional porous frameworks, such as metal-organic frameworks, often with tunable porosities were developed in order to meet the applications in different fields. Traditionally, volumetric and gravimetric methods are widely applied to characterize surface area, pore volume and pore size distribution of a porous material, namely by analyzing the adsorption isotherms. However, there are some specific “adsorption-driven” phenomena that could not be explained from macroscopic data only. Therefore, as a complementary tool, an *in situ* diffraction is used, that can reveal and explain the structure evolution during gas adsorption.

In this project, we propose a new methodology based on *in situ* diffraction to obtain simultaneously micro- and macroscopic pictures of gas adsorption. As a porous material we use the first porous metal borohydride, γ-$Mg(BH_4)_2$. It contains a tubular-shaped microporous channel running through the volume diagonal of its cubic unit cell. The adsorption of a series of noble and fuel gasses is studied using *in situ* diffraction of X-rays and neutrons. The position and quantity of the guest molecules are followed using Rietveld refinement at constant pressure or temperature, producing experimental isobars and isotherms directly from diffraction data. These curves are fitted with relevant equations, allowing to extract the thermodynamic parameters of gas adsorption, such as isosteric heats of adsorption as a function of gas loading. We detect rearrangements of guests and correlate the changes with the adsorption properties and intermolecular interactions. Following the time evolution of the guest occupancies allow to access

the energy barriers related to gas adsorption and thus to shed light on the diffusion mechanisms. We used volumetric measurements as a supporting technique to characterize macroscopic properties at equilibrium and point out the pros and cons of the diffraction-based methodology.

In Chapter 1, we introduce the material we will work with throughout the thesis, the porous magnesium borohydride, γ-$Mg(BH_4)_2$. We are first discussing hydrides, mostly used for hydrogen storage, and then present porous materials in general. After that, synthesis and polymorphisms of $Mg(BH_4)_2$ are shortly described, with more focus on the porous γ-phase. This is followed by introduction into gas adsorption, from principles to methods, finishing with objectives of this thesis.

Chapter 2 is dealing with methodologies, those already known (bulk methods to characterize gas adsorption, diffraction methods in general) and those we are advancing or developing in this thesis (*in situ* diffraction methods to build adsorption isobars and isotherms and to study adsorption thermodynamics and kinetics). Chapter 2 gives a general overview, while methodologies being advanced are described more in detail in the chapters 3-7, containing results.

Chapter 3 describes the adsorption of Ar. Diffraction studies reveal a gradual rearrangement of guests within the pores, allowing twice higher Ar loading in the final state. Thermodynamic properties of adsorption were characterized by diffraction and volumetric methods. This is put in perspective of guest-guest and guest-host interactions.

In Chapter 4, the adsorption of H_2 and N_2 using neutron powder diffraction, volumetric gas adsorption and inelastic neutron scattering was studied. These gases show different adsorption sites and very different limiting capacities. H_2 packs extremely dense inside the pores, twice as dense as liquid hydrogen. Analysis of geometry of intermolecular interactions is providing ideas explaining this phenomenon.

In Chapter 5, we describe adsorption of very light He and Ne at sub-LN2 temperatures, using neutron and synchrotron X-ray diffraction. Guest rearrangements and guest-guest interactions are characterized and discussed. Theoretical DFT simulations reveal the stability of phases containing different amounts of adsorbed gas, and the related P-T phase diagrams.

In Chapter 6, an adsorption of light C1-C4 alkanes is described, using a combination of crystallographic techniques and volumetric methods. Particular attention is paid to finding thermodynamic parameters of gas adsorption from diffraction-based isotherms and isobars. γ-$Mg(BH_4)_2$ adsorbs exclusively smaller methane and ethane (showing a potential for separation through relatively narrow pore apertures) and shows high gravimetric adsorption capacities and heats of adsorption.

In Chapter 7 we address the adsorption kinetics by a novel *in situ* diffraction approach. Arrhenius analysis yields activation barriers, which are tentatively attributed to different diffusion mechanisms, governing the diffusion of Ar, Kr and Xe in γ-$Mg(BH_4)_2$.

Chapters 3-7, describing results, are also containing lengthy discussions. We shortly summarize them in essence in the following Chapter 8, where we also present our vision of perspectives.

A Statement on Contributions

The following five chapters will contain the results on my work, integrated in a form of manuscripts, along with contributions of other authors. Each chapter is actually a manuscript to be submitted in the near future or already submitted/published. Here is the description of my contribution to each chapter (article), along with a short description of the status of each publication.

Chapter 3 describes the adsorption of Ar in γ-$Mg(BH_4)_2$. This part of work will soon be submitted to *J. Am. Chem. Soc.* (before my private defense) when we collect the feedback from the co-authors. I am the first author and contributed to the synthesis of the samples, interpretation of diffraction data, volumetric data measurement and analysis, writing the manuscript and participating in discussions on all topics, including phenomenological modeling.

Chapter 4 describes H_2 (D_2) adsorption and its striking difference with the N_2 behavior. This work reveals an ultra-dense hydrogen in the pores, characterized by many independent techniques in a large collaboration: synchrotron diffraction, neutron powder diffraction, inelastic neutron scattering and volumetric measurements (at temperatures as low as 20 K, which is not easy to access in a laboratory). This chapter will be submitted to *Science* before my private defense. I contributed to the diffraction data analysis, synthesized the samples, participated in writing and discussions.

Chapter 5 describes the adsorption of He and Ne, the lightest gasses rarely considered for adsorption using the combination of diffraction methods and DFT simulation of adsorption energy of He, Ne and Ar. This work is the least complete in the sense of writing/editing and will be the last chapter to be submitted for publication, already after my public defense. I contributed to the sample synthesis, diffraction data analysis, writing the manuscript and will be the first author.

Chapter 6 describes the adsorption of two fuel gases, methane and ethane. I have contributed with volumetric measurements with writing the manuscript. This chapter will also be submitted before my private defense to one of the *ACS journals*.

Chapter 7 describes the adsorption kinetics of Kr, Xe, as well as Ar. This part has already been published in *Angew. Chem. Int. Ed.* in 2021 (doi: 10.1002/anie.202015019). I am the third author and contributed with the samples, measurement of diffraction data characterizing Ar kinetics, the related data analysis, discussion and writing the manuscript.

I am also a co-author of another work which will not be presented in this thesis but it shares a big part of my expertise described in other chapters. This is *in situ* diffraction experiments, yielding both structure and properties (such as isotherms) for the gas adsorbed in a porous framework, namely CO_2 in a flexible Zr-MOF of MIP-203 series. This work is the result of a collaboration with the group of Christian Serre, it has been published in *J. Am. Chem. Soc.* in 2019, doi: 10.1021/jacs.9b07816.

Acknowledgements

Time flies so fast and it has been more than four years since I first set foot in Belgium to study for a Ph.D. In retrospect, I spent one of the best periods of my life in Université Catholique de Louvain.

Firstly and most importantly, I would like to thank my supervisor, Prof. Yaroslav Filinchuk. Academically, he teaches me about crystallography and diffraction, providing me this very exploratory project. I always feel supported by him to try different ideas directly or indirectly related to my project. He encourages me to attend conferences and summer schools, working tirelessly to help me improve my posters or oral presentations. In life, he is acting like my friend to take care of me and introduce me a lot about European culture. There is an old saying from one of the four great classical novels in China, *Journey to the West*, that "a teacher for a day is equivalent to a father for a life". Yaroslav Filinchuk is more than a supervisor to me, more often he is like a friend and family.

Inside the university, I also want to thank Dr. Koen Robeyns, who is the principal of the diffraction lab. He is professional in crystallography and always makes himself available to answer questions and discuss the difficulties. I especially appreciate his contribution to correct the writing of my thesis. In the meanwhile, I want to thank my group colleagues and Prof. Tom Leyssens and his group members who all share the same floor. They have organized many interesting activities that makes my four-year PhD study alive. I would like also to thank all jury members for the time and competence devoted to the evaluation of this work. I am indebted to all the colleagues who have contributed to the results (described in the Chapters 3-7), their names are listed in the first page of each chapter.

I have been in ESRF to measure synchrotron radiation data many times. I could not make it a success without the support from persons there. So I would like to say thanks to Dr. Dmitry Chernyshov, Dr. Vadim Dyadkin, Dr. Iurii Dovgaliuk and all other staff from Swiss Norwegian Beam Lines at the ESRF. They provide me a fantastic working experience and a lot of technical supports. I will not forget the days and nights we spent together in front of the machines and monitors. We also thank BELSPO, the Belgian Science Policy Office providing the opportunity to use large facilities, like ESRF.

Prof. Hai-Wen Li has provided me chances to participate in international conferences in Japan with financial support. He also recommended me to Yaroslav Filinchuk from the beginning so that I had a pleasant four years here. Without his help, I may not even start my PhD study in Europe. He is like a lighthouse on the coast and always guides me in the right direction.

Personally I want to thank my girlfriend, Lu Bai, who is also finishing her Ph.D. in IMCN, UCLouvain. We met each other in this small city, Louvain-la-Neuve, and we share unanimous point of views of our life and future. You are the one that I want to share my whole life with. Hi, Lu Bai, will you marry me after our graduation?

I also appreciate some other friends who have studied, or are studying here. I could not list all your names here but it is my pleasure to make acquaintance with all of you.

Finally I would like to especially express my thanks to my father Zhi-Jie Li, and mother Guo-Xia Yao. It is not a simple way to be six thousands miles away from home to get further study. I have only gone home twice during this four years and thank you for your understanding and support. I miss you so much!

We thank FNRS, UCLouvain, and the Communauté Française de Belgique (ARC Grant). I appreciate the financial support from the China Scholarship Council (CSC). I love my motherland and I wish her to develop better and better.

Table of Contents

List of Abbreviations

MOF: Metal Organic Framework

DOE: Department of Energy of United States

PCT: Pressure-Composition-Temperature

IUPAC: International Union of Pure and Applied Chemistry

PCP: Porous Coordination Polymer

PCN: Porous Coordination Network

BDC: 1,4 - benzenedicarboxylic acid

CCDC: Cambridge Crystallographic Data Centre

ZIF: Zeolitic Imidazolate Framework

MIL: Matériaux de l'Institut Lavoisier

UiO: Universitetet i Oslo (University of Oslo)

IRMOF: Isoreticular Metal Organic Framework

IAST: Ideal Adsorbed Solution Theory

DFT: Density Functional Theory

THF: tetrahydrofuran

TMEDA: tetramethyl ethylenediamine

TMA: trimethylamine

TEA: triethylamine

XRD: X-Ray Diffraction

NMR: Nuclear Magnetic Resonance

NGA: Negative Gas Adsorption

PXRD: Powder X-Ray Diffraction

SNBL: the Swiss-Norwegian Beamlines at the ESRF

ESRF: European Synchrotron Radiation Facility in Grenoble

RT: Room Temperature

EBS: Extremely Brilliant Source

APS: the Advance Photo Source

Spring-8: Super Photon ring-8 in Japan

NPD: Neutron Powder Diffraction

NCNR: NIST (National Institute of Standards) Center for Neutron Research

HZB: Helmholte-Zentrum Berlin

SR-XPD: Synchrotron Radiation X-ray Powder Diffraction

DMS: Dimethyl sulfide

LDF: Linear Driving Force

DE: Double Exponential

PXRSD: Powder X-ray Synchrotron Diffraction

WAND^2:Wide Angle Neutron Diffractometer Squared

HFIR: High-Flux-Isotope Reactor

ORNL: Oak Ridge National Laboratory

INS: Inelastic Neutron Scattering

DoS: Density of States

SQRE: Simultaneous Quantum Rotational Excitation

BET: Brunauer–Emmett–Teller

SPV: Specific Pore Volume

LN2: Liquid Nitrogen

VASP: Vienna *ab−initio* Simulation Package

PAW: Projector Augmented Wave

CNG: Compressed natural gas

LNG: Liquefied natural gas

AB: Ammonia Borane

JMAK: Johnson-Mehl- Avrami-Kolmogorov

SEM: Scanning Electron Microscopy

List of Symbols

$\mathit{\Delta H}$: Enthalpy

wt%: weight percent

$H^{\delta+}$: cationic form of atomic hydrogen

$H^{\delta-}$: anionic form of atomic hydrogen

p_{eq}: equilibrium pressure

$\mathit{\Delta S}$: change in entropy

R: ideal universal gas constant

Å: angstrom

ρ: density, g/cm^3

$Z_{p,\,T}$: gas compressibility under a given pressure and temperature

K_{eq}: reaction equilibrium constant

d: crystal plane spacing

λ: wavelength, Å

I_e: scattering intensity of a single electron

I_a: scattering intensity of a single atom

f: scattering factor of an atom

$I_{(h\,k\,l)}$: diffraction intensity at the ($h\ k\ l$) direction

$F_{(h\,k\,l)}$: structure factor

K_α and K_β: characteristic X-ray radiation

$G_{h\,k\,l}$: peak shape function

R_p: profile factor

R_{wp}: weighted profile factor

R_{exp}: expected weighted profile factor

χ^2: reduced chi-square, statistical descriptor the quality of a fit

ΔH_{ads}: enthalpy of adsorption

k: reaction kinetic constant

E_a: activation energy

D_2: deuterium gas

pH_2: para-hydrogen

oH_2: ortho-hydrogen

nH_2: normal hydrogen, a mixture of ortho and para

Scientific Contributions

Publications

Wang S.J., Xhaferaj N., Wahiduzzaman M., Oyekan K., ***Li X.,*** et al. Engineering Structural Dynamics of Zirconium Metal Organic Frameworks Based on Natural C4 Linkers. *J. Am. Chem. Soc.* 2019, 141(43), 17207-17216).

Dovgaliuk I, Senkovska I, ***Li X***, et al. Kinetic Barriers and Microscopic Mechanisms of Noble Gas Adsorption by Nanoporous γ-$Mg(BH_4)_2$ Obtained by Means of Sub-Second X-Ray Diffraction. Angew. Chem. Int. Ed. 2021, 60, 5250-5256.

Li X, et al. Guests Rearrangement and Thermodynamics from Gas Adsorption Crystallography. Submitted.

Oh H, Tumanov N, Ban V, ***Li X,*** et al. Ultra-dense Hydrogen in Small Pore Hydridic Framework. Submitted.

Li X, et al. Helium and Neon Adsorption in Porous Magnesium Borohydride Studied by Neutron and X-Ray Powder Diffraction and DFT Simulation. To be submitted.

Conference participations

Poster, ***Energy Week 2018***, Fukuoka, Japan, 29/01/2018-02/02/2018;

Poster, ***Belgian Crystallography Symposium 10***, Brussels, Belgium, 17/10/2018;

Oral presentation, ***16th International Symposium on Metal Hydrogen Systems***, Guangzhou, China, 28/10/2018-02/11/2018;

Poster, Energy Week 2019, Fukuoka, Japan, 28/01/2019-01/02/2019;

Poster, ***1st International Gas Adsorption Summer School,*** Spetses, Greece. 09/09/2019-13/09/2019;

Oral presentation, ***Ph.D. Students' Day 2021,*** Louvain-la-Neuve, Belgium, 21/05/2021.

Chapter 1. Introduction

In this Chapter we will introduce the materials and phenomena we will deal with in this thesis. Namely, the porous materials, manifesting gas adsorption on their surface. More specifically, we will use a porous form of a light metal borohydride, known as γ-phase of $Mg(BH_4)_2$*. Therefore, we will first talk about hydrides, which are often considered in the context of hydrogen storage, and then present porous materials in general. After that, synthesis and polymorphisms of* $Mg(BH_4)_2$ *will be shortly described, with more focus on the porous γ-phase. This is followed by introduction into gas adsorption in solids, shortly describing principles and methods of characterization. We will formulate the objectives of the thesis at the end of this Chapter.*

1.1. From Metal Hydrides to Complex Hydrides

The substance that will be most investigated in this thesis is the compound very rich in hydrogen. Therefore we will cover shortly the two main classes of hydrogen-rich solids, typically used for hydrogen storage and thus discussed in this context. Metal hydrides are defined as the products of the chemical reaction between hydrogen and various metal systems (intermetallic compounds or alloys in a form of solid solutions)[1]. These functional materials are widely studied and applied in solid-state hydrogen storage field in the past decades, since they have a favorable thermodynamics and kinetics of hydrogen adsorption. Metal hydrides are usually evaluated by their gravimetric and volumetric capacity, cyclability and more generally reversibility of solid-state hydrogen storage, as well as by the commercial value of raw materials.

Metal hydrides were firstly found by Sieverts et al.[2] in 1912 while studying hydrogen adsorption of Pt-Au alloys[1]. With a systematic expansion of this family, the interstitial metal hydrides formed by the heavier *d*- and *f*-block metals have received significant attention due to their reversible hydrogen storage at near ambient conditions[3]. This type of intermetallic metal hydrides is usually expressed as $A_mB_nH_x$, A represents the metal element with a high affinity to hydrogen, and B represents the metal element that usually in a pure form has no interaction with or low affinity to hydrogen. Some typical and important families of intermetallic metal hydrides are listed in Table 1[4].

Even though the enthalpy of hydrogen uptake for an intermetallic metal hydride is moderate, typically $\Delta H \approx -30$ kJ/mol[5][6] (providing a fast hydrogen uptake and release), the gravimetric density of typically 1 to 2 wt% of hydrogen storage is low due to the high atomic mass of metals. To meet the target for on board hydrogen storage systems for vehicles, the Department of Energy of United States (DOE) has pointed out that the gravimetric and volumetric hydrogen storage density should reach

5.5 wt% and 40 g/L[7] respectively, in 2020; the targets were reviewed up and down afterwards. To meet this target, complex hydrides with light metal cations, such as Li, Na, K, Al, Mg, Ca and so on, have raised a great attention in recent years due to their high gravimetric density of hydrogen storage.

Table 1. The most important families of hydride forming intermetallic compounds including the prototype and the structure[4].

Intermetallic compound	**Prototype**	**Hydride**	**Structure**
AB_5	$LaNi_5$	$LaNiH_6$	Hexagonal
AB_2	ZrV_2, $ZrMn_2$, $TiMn_2$	$ZrV_2H_{5.5}$	Hexagonal or cubic
AB_3	$CeNi_3$, YFe_3	$CeNi_3H_4$	Hexagonal, $PuNi_3$ type
A_2B_7	Y_2Ni_7, Th_2Fe_7	$Y_2Ni_7H_3$	Hexagonal, Ce_2Ni_7 type
A_6B_{23}	Y_7Fe_{23}	$Ho_6Fe_{23}H_{12}$	Cubic, Th_6Mn_{23} type
AB	TiFe, ZeNi	$TiFeH_2$	Cubic, CsCl or CrB type
A_2B	Mg_2Ni, Ti_2Ni	$Mg_2Ni_2H_4$	Cubic, $MoSi_2$ or Ti_2Ni type

Light metal complex hydrides are compounds similar to inorganic salts. The hydrogen atoms form an anion by means of covalent bonds with a central atom, counterbalanced by a metal cation to form a complex metal hydride. This class is known for heavier transition metal hydrides, containing for example NiH_4 complexes[8][9], however in the context of light weight materials we can outline the following three group containing the anions[10]:

1) $[AlH_4]^-$, known as alanates. Since Bogdanovic and Schwichardi[11] have found in 1996 that Ti-doped $NaAlH_4$ can realize a reversible hydrogen uptake and release with about 4 wt% below 473 K, there has been an upsurge in research on complex hydride around the world. Typical alanates include $NaAlH_4$, $LiAlH_4$, $Mg(AlH_4)_2$, and Na_2LiAlH_6, the latter containing the hexacoordinated aluminum. Among them, the research on $NaAlH_4$ is the most extensive. The obstacle and key point for utilizing alanates is the poor kinetics of hydrogen uptake. Some researches investigated Ti-doped, Ce-doped, and Zr-doped catalysts which provide a good effect on alanates[12]–[16], however, there is still controversy on its catalytic modification mechanism. To improve the thermal stability, researchers further synthesized bimetallic alanates, Na_2LiAlH_6, which can absorb and release hydrogen reversibly at the temperature range from 463 to 753 K[17][18].

2) $[BH_4]^-$, known as borohydrides. Borohydride is a general name for the tetrahydroborate anion. The first metal borohydrides, $Al(BH_4)_3$ $Be(BH_4)_2$ and $LiBH_4$ were reported in 1940 by Schlesinger et al.[19]–[21] in the context of uranium enrichment program. Much later, due to the high hydrogen gravimetric density, borohydrides have attracted wide attention and had been developed into a big family with many derivatives[22]. However, the disadvantage of borohydrides is that their strong covalent bond B-H leads to a high thermal stability and increases the temperature of release of hydrogen. Simultaneously, the kinetics is poor as well, as well the H-reversibility is often absent. The current research work on borohydrides mainly focuses on improving their kinetic properties and re-absorbing hydrogen performance. For example, this can be reached by forming so called reactive hydride composites, as for instance $LiBH_4$-MgH_2 system[23]–[25]. This mixture gives products containing elements from each component, that are able to rehydrogenate under mild conditions, unlike the pure components. On the other hand, nano-sized borohydride hydrogen storage systems and the use of nano-size effects to improve kinetic and thermodynamic properties are also important research directions[26],[27]. In addition, the

thermodynamic stability of metal borohydrides is closely related to the electronegativity of the center metal cations, and generally decreases with the increase of electronegativity[28],[29]. Therefore, modifying the electronegativity of metal cation and developing new types of bimetallic borohydrides is another way to improve the re/dehydrogenation properties of metal borohydrides[30],[31].

3) $[NH_2]^-$, known as amides. The first case of reversible hydrogen storage by amides (Li-N-H system, in the form of reactive hydrogen composite) was reported by Chen et al.[32] in 2002. As $LiNH_2$ has the characteristics of a typical ionic compound, the kinetics and reversibility of re/dehydrogenation can be significantly improved by adding catalysts such as metals, metal salts or oxides[33]. Subsequently, based on the theory that a hydron ($H^{\delta+}$) can be easily combined with hydridic hydrogen ($H^{\delta-}$), new hydrogen storage systems consisting of metal amino compounds and metal hydrides or metal borohydrides were further developed, such as $LiNH_2$-LiH, $Mg(NH_2)_2$-MgH_2, $Ca(NH_2)_2$-CaH_2 and $LiNH_2$-$LiBH_4$[34]. These bi-anionic hydrogen storage systems have shown high hydrogen storage capacity and excellent hydrogen storage kinetics and thermodynamic properties, but the release of hydrogen is also accompanied by the production of impurity gases, such as ammonia, during the dehydrogenation, which limits their application in combination with fuel cells.

Some properties of several important complex hydrides are shown in Table 2[10]. Unfortunately, despite the effort of the past decades in development, none of the materials can have both mild re/dehydrogenation condition and high gravimetric hydrogen storage density at the same time.

One of the important characterization of metal hydrides is the Pressure-Composition-Temperature (PCT) diagram, as shown in Figure 1[35], left. The α-phase representing the host metal starts to dissolve some hydrogen as a solid solution, while the β-phase represents hydrides. While the two phases coexist, the isotherms show a flat plateau, the length of which determines the amount of hydrogen reversibly stored. According to van’t Hoff equation,

$$ln\left(\frac{p_{eq}}{p_{eq}^{0}}\right) = \frac{\Delta H}{RT} - \frac{\Delta S}{R}$$

Table 2[10]. Selected properties of some complex hydrides.

material	density (g/cm^3)	H-density (wt%)	H-density (kg/m^3)	T_m* (K)	ΔH_f (kJ/mol)
$LiAlH_4$	0.917	10.54		463^d	-119
$NaAlH_4$	1.28	7.41		451	-113
$KAlH_4$		5.71	53.2		
$Mg(AlH_4)_2$		9.27	72.3		
$Ca(AlH_4)_2$		7.84	70.4	>503^d	
$LiNH_2$	1.18	8.78	103.6	645-673	-179.6
$NaNH_2$	1.39	5.15	71.9	483	-123.8
KNH_2	1.62	3.66	59.3	611	-128.9
$Mg(NH_2)_2$	1.39	7.15	99.4	633	
$Ca(NH_2)_2$	1.74	5.59	97.3		-383.4
$LiBH_4$	0.66	18.36	122.5	541	-194
$NaBH_4$	1.07	10.57	113.1	778	-191
KBH_4	1.17	7.42	87.1	858	-229
$Mg(BH_4)_2$	0.989	14.82	146.5	593^d	
$Ca(BH_4)_2$		11.47		533^d	
$Al(BH_4)_3$	0.7866	16.78	132	208.5^d 317.5^b	

* d and b represent decomposition and boiling temperatures, respectively.

the enthalpy (*ΔH*) and entropy (*ΔS*) can be obtained, rationalizing the variation of the equilibrium pressure p_{eq} as a function of the reciprocal temperature, as shown in Figure 1, right.

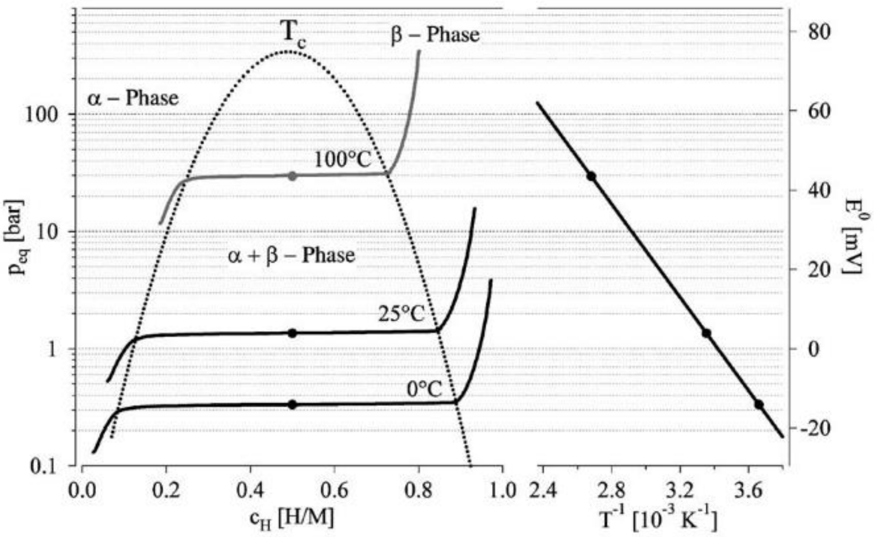

Figure 1[35]. PCT isotherms for a hypothetical metal hydride (left) and its van't Hoff plot (right).

1.2. Porous Solids

Porous materials are widely found among many types of materials in nature, including active carbon, zeolites, coordination polymers, and so on. Due to their high surface area and pore volume, porous materials have been applied in many domains, such as catalysis, adsorption, gas separation, ion exchange. According to a classification of the International Union of Pure and Applied Chemistry (IUPAC)[36], based on their pore size, porous materials are divided into micro- (< 2 nm), meso- (2 – 50 nm) and macro- (> 50 nm) porous materials.

In the past 25 years, a new type of porous materials, Metal Organic Frameworks (MOFs), has attracted great attention from researchers, and its related research has also shown rapid growth. MOFs, also known as Porous Coordination Polymers (PCPs) or Porous Coordination Networks (PCNs)[37], are reticular crystalline materials formed by metal ions or clusters as the center and organic ligands as the linker. The concept of MOFs was first proposed by Yaghi et al.[38] in 1995 and furthermore, in 1999, his team obtained one of the most famous MOFs, MOF-5 (see Figure 2), by reacting $Zn(NO_3)_2$ and 1,4 - Benzenedicarboxylic acid (BDC)[39], showing excellent thermal stability and gas storage performance. In the meanwhile, with the proposal of reticular synthesis and secondary building units[40], a large amount of new structures and compositions of MOFs emerge into the public. There are now more than 10000 MOF structures that can be access from the Cambridge Crystallographic Data Centre (CCDC)[41]. Based on different naming methods, some common and famous type of MOFs are Zeolitic Imidazolate Frameworks (e.g., ZIF-8)[42], Matériaux de l'Institut Lavoisier (e.g., MIL-53)[43], Universitetet i Oslo (e.g., UiO-66[44]), and so on.

Due to their tunable structure and the characteristics of both inorganic and organic materials, MOFs have potential applications in many aspects. So far, the researches on the properties and functions of MOFs reported in the literature mainly include catalysis, gas adsorption and separation, chemical sensors, luminescent function, drug delivery,

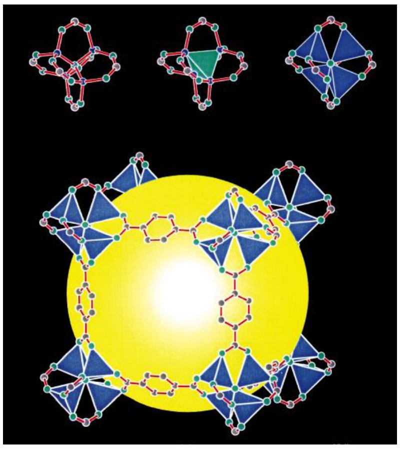

Figure 2[39]. Schematic illustration of the MOF-5 framework structure. The yellow sphere represents the void of MOF-5.

ion exchange[45]–[51], etc. Material chemists can synthesize a huge number of MOFs through design to adjust and optimize certain functional properties, and can also make MOFs have a variety of functional properties. Computations and simulations can also predict the performance of MOFs in terms of gas adsorption and separation, for various metal centres/cluster and linkers, which makes the family of MOFs have a great advantage in their design compared to other porous materials. In the following paragraphs, the application of MOFs in gas adsorption and separation will be introduced, as the main content of this thesis is about gas adsorption in a MOF-like hydride-based compound.

Studying the properties of gas adsorption of MOFs not only can greatly expand their application fields, but may also solve some key problems in separation of similar gases and related disciplines[52]. MOFs have a special microporous / mesoporous structures, and it usually has a large specific surface area, making it an excellent adsorption medium. Due to different pore sizes and shapes and chemical properties, different MOFs also exhibit different adsorption behaviors. Currently, MOF research on gas adsorption and separation mainly include fuel gases (H_2, CH_4), CO_2 capture, as well as light hydrocarbon separation (CH_4 / C_2H_6) and noble gases separation (Kr / Xe). Gas adsorption and separation are considered to be one of the areas where MOFs are most likely to achieve industrial applications[52]. Below we shortly cite some key points in these developments.

1. Gas storage

Hydrogen storage in MOFs was studied by Yaghi et al. and they found that MOF-5 has a high capacity of hydrogen sorption[53]. Furthermore, they studied the influence of synthesis routes of MOF-5 on its hydrogen storage capacity, and the adsorption binding sites of hydrogen by inelastic neutron diffraction[54][55]. These sites are not specific and show moderate adsorption enthalpy. However, molecular simulation reveals that hydrogen storage characterized by higher adsorption enthalpy can be attributed to the open metal sites, for example in Cu-BTC[56]. Subsequently, Zhou et al., Hupp et al., Schroder et al. and some other groups synthesized a series of Cu-MOFs with open metal site and high porosity and found that these types of MOFs showing a high hydrogen storage capacity[57]–[63]. Recently, Hischer et al.[64] have collected experimental data on hydrogen uptake at 77 K and 2.0-2.5 MPa of many different MOFs. They concluded that the volumetric absolute hydrogen uptake, obtained from the packing density of powder samples and from the single-crystal density, increases linearly with the volumetric surface.

Another major application of MOFs in the field of gas storage is methane (CH_4) storage. Kitagawa et al.[65] and Yaghi et al.[66] firstly applied MOFs in methane storage and they found that the capacity of CH_4 in the porous channel of IRMOF-6 can reach 155 cc/cm^3 at ambient environment. Snurr et al.[67] used molecular design to simulate and predict that the CH_4 adsorption capacity of IRMOF-993 can be as high as 188 cc/cm^3. Further studies showed that the ideal MOFs structure for the storage of CH_4 not only requires a larger specific surface area, but also a larger pore volume. The researchers virtually studied more than 130,000 MOF structures through computer simulations, and conducted a large-scale screening of the storage capacity of CH_4. The results showed that the CH_4 adsorption capacity of more than 300 kinds of MOFs exceeded the DOE standard (180 cc/cm^3). MOFs modified with methyl or ethyl groups usually show better CH_4 adsorption capacity.

2. Separation of gases

From the perspective of separation, the most extensive research of MOFs is carbon-capture related gas adsorption and separation, including natural gas purification (CO_2 / CH_4), synthesis gas separation (CO_2 / H_2) and noble gases separation (Kr / Xe). It is difficult to do directly use experimental measurements to determine the gas adsorption selectivity of porous materials. At present, people mainly use the single-component gas adsorption isotherm data of MOFs to estimate, using the Henry law selectivity and IAST (Ideal Adsorbed Solution Theory) prediction selectivity. With the rapid innovation of computational chemistry theory, such as molecular simulation and DFT (Density Functional Theory) calculations, it has been increasingly applied to the prediction of the adsorption and separation performance of gas mixtures in MOFs and to the study of microscopic mechanisms[67]–[70]. Most of the gas adsorption and separation for MOFs focuses on the influence of material’s structure on its properties, including pore size, functional group polarity, open metal sites, topological type, framework flexibility, guest molecule doping and so on.

MOFs with unsaturated (open) metal sites are not only excellent in gas storage, but also in multi-component gas separation[71]–[73]. And some large polar molecules or strong electrostatic guest molecules will cause a reversible transformation of the MOFs due to their flexible structures responding differently to different gas molecules. For example, in the classic MIL-53 series, there is a unique "step" phenomenon in the adsorption of CO_2 molecules, which has higher adsorption and separation performance[74]. More researches in this area were done by Suh et al., who developed a series of flexible structural MOFs called SNU and used them for gas adsorption and separation[75],[76]. Another way to improve the separation performance of MOFs is to modify the chemical environment of the surface of their pores, including directly using ligands with functional group or post-synthetic modification after the synthesis. For example, the amine-functionalized flexible MIL-53 shows higher CO_2 / CH_4 separation performance[77].

1.3. Porous Magnesium Borohydride

Magnesium borohydride, i.e., $Mg(BH_4)_2$, has intriguing features from both a fundamental and practical point of view. Among the borohydrides, it has the most complex crystal structures and the most polymorphs[78]. $Mg(BH_4)_2$ was firstly synthesized by Wiberg et al.[79] in 1950 and studied rapidly in the 21st century due to its high hydrogen content[80]–[82]. It has a high gravimetric hydrogen storage density of 14.9 wt%, and a lower thermal stability, which can allow the dehydrogenation happening around 523 K (compared to $LiBH_4$ with the gravimetric density of 18.5 wt%, with dehydrogenation according at nearly 673 K). At present, a lot of progress has been made in understanding $Mg(BH_4)_2$ as a material for hydrogen storage, in particular its thermodynamic and kinetic properties, its nanoconfinement, catalytical dehydrogenation and formation of reactive hydride composites. It also has the potential as an ionic electrolyte[83].

1.3.1 Strategies of $Mg(BH_4)_2$ Synthesis

The first attempt to synthesize $Mg(BH_4)_2$ is in 1950, by Wiberg et al.[79]. They found that the $Mg(C_4H_9)_2$ and diborane B_2H_6 will slowly react under room temperature according to the following reaction formula:

$$3Mg(C_4H_9)_2 + B_2H_6 \rightarrow 3MgH_2 + 2B(C_2H_5)_3$$

$$3MgH_2 + 3B_2H_6 \rightarrow 3Mg(BH_4)_2$$

However, due to the high toxicity and flammability of diborane and its derivatives, and to the fact that the actual product is a solvate of $Mg(BH_4)_2$, this method is not suitable for applications. Thus, subsequentially two synthesis strategies towards $Mg(BH_4)_2$ have been developed: solvent-based synthesis and solvent-free synthesis (solid phase synthesis).

1. Solvent-based synthesis

In 1954, Kollonitsch et al.[84] first proposed a new idea for preparing $Mg(BH_4)_2$: a mixture of $NaBH_4$ and $MgCl_2$ were reacted in cold ethanol to obtain an ethanol solution of $Mg(BH_4)_2$, and then the product was dried in vacuum. In 1955, Brown et al.[85] used solvent-based synthesis method to prepare $Mg(BH_4)_2$ with $MgCl_2$ and $NaBH_4$ as the reactants and diglyme as the solvent. In 1957, Koster et al.[86] added pre-milled

MgH_2 to triethylamine-borane under an argon atmosphere and heated it at 373 K. Then, the product was dissolved in n-hexane at room temperature, followed by filtration and washing, finally obtained the triethylamine adduct of magnesium borohydride. After the adduct is subjected to a vacuum treatment at 373-443 K, the low-temperature phase $Mg(BH_4)_2$ can be obtained with high yield. Plesek et al.[87] used ether as a solvent to react MgH_2 with diborane under high pressure, and finally heated the product to 423-453 K under vacuum to remove ether to obtain $Mg(BH_4)_2$ with a yield of 91%. In 1980, Konoplev et al.[88] used ether as a solvent to synthesize $Mg(BH_4)_2 \cdot 2Et_2O$ using a method similar to the one by Brown et al. The elemental analysis showed that the ratio of Mg and B in the composition was consistent with $Mg(BH_4)_2$, but the author did not analyze the remaining C content. The solvate released the solvent at temperatures exceeding the phase transition temperature for what we know now as α- to β-$Mg(BH_4)_2$ transition, therefore yielding the high temperature β-phase of $Mg(BH_4)_2$.

In 2007, an easy solvent-based synthesis strategy was proposed by Zanella et al.[89] as showed in the following:

$$3Mg(C_4H_9)_2 + 8BH_3 \cdot S(CH_3)_2 \\ \rightarrow 3Mg(BH_4)_2 \cdot 2S(CH_3)_2 + 2B(C_4H_9)_3 \cdot S(CH_3)_2$$

The authors use toluene as the solvent. Since $Mg(BH_4)_2$ is not soluble in toluene, after washing and drying steps, the product can be separated and pure $Mg(BH_4)_2$ can be obtained after removing the solvent. This synthesis method involves the insertion reaction of the BH_3 group on the dimethyl sulfide borane complex into the Mg-C bond in $Mg(C_4H_9)_2$. At the same time, the C_4H_9 group was completely replaced by the BH_4 group. In order to make the reaction complete, an excess of $BH_3 \cdot 2S(CH_3)_2$ is often used to avoid formation of the partial substitution product $Mg[BH_{4-n}(C_4H_9)_n]$. Since $S(CH_3)_2$ is a weak Lewis base, it does not need a high temperature to destroy the chemical bond between it and Mg. Therefore, in this study, the solvent can be removed already at 348 K for 13h.

Selection of solvents is a key point in solvent-based method to synthesize $Mg(BH_4)_2$[80]. Some solvents, such as tetrahydrofuran (THF) and tetramethyl ethylenediamine (TMEDA), have a strong bond to Mg, so it needs a high temperature to remove the adducts. Furthermore, high temperature could lead to the decomposition or transformation of $Mg(BH_4)_2$. While some other solvents, such as trimethylamine (TMA) and triethylamine (TEA), have a weak bond to Mg and leading to no stable adducts with $Mg(BH_4)_2$.

Industrially speaking, reactants should also be optimized and screened. Soloveichik et al.[90] pointed out that diborane is highly toxic, flammable, and unstable, so it is not suitable as a raw material for the preparation of $Mg(BH_4)_2$. From the perspective of safety and economy, the use of $NaBH_4$ and $MgCl_2$ as reactants, ether as the solvent, ion exchange as the method and the subsequent solvent removal, are currently more suitable synthetic methods. In 2012, Bateni et al.[91] replaced $MgCl_2$ with $MgBr_2$ and found that the later is easier to bind to $NaBH_4$ than $MgCl_2$, the reaction time is shorter, and excess $MgBr_2$ can be used as an additive to effectively reduce the dehydrogenation temperature of $Mg(BH_4)_2$.

2. Solvent-free synthesis

The solvent-free synthesis is environmental friendly, and shows high safety and economical perspective. Therefore, in addition to the above-mentioned solvent-based synthesis methods, some researchers have used solvent-free methods to directly synthesize $Mg(BH_4)_2$. The initial proposal is to synthesize $Mg(BH_4)_2$ from elements under a high hydrogen pressure. However, it requires high temperature and long reaction time, as well as the low yield. Zhang et al.[92] tried to prepare $Mg(BH_4)_2$ by hydrogenation using Mg powder and element B as precursors. They first mechanically ball-milled Mg and B under Ar atmosphere for 12 hours, and then hydrogenated them at 573 K. They found that only a small amount of Mg-B-H compounds were formed, and the product after hydrogenation was mainly MgH_2. The strong force of the B-B bond and the higher diffusion barrier of the B atom are the main reasons why it is difficult to transform the borane into $Mg(BH_4)_2$.

Another solvent-free synthesis strategy is to ball mill $MgCl_2$ with $LiBH_4$ or $NaBH_4$ under N_2 atmosphere[92]. The as-synthesized product is a mixture of amorphous $Mg(BH_4)_2$ with impurities such as LiCl or NaCl. Further steps of purification are needed to get pure $Mg(BH_4)_2$. In addition to ball milling, direct heat treatment of $LiBH_4$ and $MgCl_2$ at high temperature can also generate $Mg(BH_4)_2$ mixed with LiCl[92].

The preparing of $Mg(BH_4)_2$ by direct hydrogenation of MgB_2 (it is a dehydrogenation product of $Mg(BH_4)_2$) is the key to its future research on reversible hydrogen storage. In recent years, researchers have begun to try to directly react MgB_2 and H_2 to produce $Mg(BH_4)_2$, as shown in the following formula:

$$MgB_2 + 4H_2 \ \rightarrow Mg(BH_4)_2$$

For example, Severa et al.[92] heated up the pre-ball-milled MgB_2 under hydrogen pressure (400 bar) at 673 K, subsequently the pressure was increased up to 950 bar and kept the system for 108 hours to obtain $Mg(BH_4)_2$. More and more reports[93]–[96] have verified the feasibility of this method to produce $Mg(BH_4)_2$ and furthermore, with more moderate conditions and high yields. Currently, this method still require high pressure-temperature conditions, even in presence of catalysts. Moreover, the formation of stable amorphous intermediates, like $MgB_{12}H_{12}$, known as “boron sinks”, is an obstacle for the this synthetic route.

1.3.2 Polymorphism of $Mg(BH_4)_2$

Besides the potential attractiveness for hydrogen storage, another interesting property of $Mg(BH_4)_2$ is its polymorphism, which appears to be richer than that of any other Group I and II borohydrides. Solvent-based synthesis may produce hexagonal ($P6_122$) α-, cubic ($Id\text{-}3a$) γ-, orthorhombic ($Fddd$) β-, trigonal ($P3_112$) ζ-, and amorphous $Mg(BH_4)_2$ with high yields. Their crystallographic parameters are summarized in Table 3[78]. And the atomic coordinates can be found in the related references. Some phases can be directly synthesized by solvent-based methods while some phases can be observed after a phase transition. For example, the α-phase transforms to the β-phase upon heating[81],[84]. Therefore, α-$Mg(BH_4)_2$ is also referred as low-temperature phase while β-$Mg(BH_4)_2$ as high-temperature phase. γ- and α-$Mg(BH_4)_2$ can transform to δ phase, which gives a high volumetric hydrogen storage density as 147 g/L (ranking second among all the known hydrides), by compression[97][98] to pressures above 1.1-1.6 GPa. Remarkably, this phase remains stable at ambient conditions (when the pressure is relieved).

Table 3. Polymorphs of $Mg(BH_4)_2$ by experimentally observed.

Phase	Space group	cell parameters, Å	cell volume, $Å^3$	ρ, g/cm^3	Ref.
α-$Mg(BH_4)_2$	$P6_122$	a=b=10.33555 c=37.08910 α=β=90° γ=120°	3431.21	0.783	[99]
β-$Mg(BH_4)_2$	*Fddd*	a=37.04892 b=18.49186 c=10.85945 α=β=γ=90°	7439.82	0.76	[100]
γ-$Mg(BH_4)_2$	*Ia-3d*	a=b=c=15.7575 α=β=γ=90°	3912.57	0.55	[97]
δ-$Mg(BH_4)_2$	$P4_2nm$	a=b=5.4361 c=6.1468 α=β=γ=90°	181.65	0.987	[97]
ζ-$Mg(BH_4)_2$	$P3_112$	a=b=10.424 c=10.729 α=β=90° γ=120°	1009.7		[101]

The large number of $Mg(BH_4)_2$ polymorphs and their (meta)stability in a wide P-T range suggests that the structural reorganization is linked to breaking significant barriers related to Mg-BH_4 bonding. This interaction is not seen as entirely ionic, but more like a bonding between metal and ligand in the MOF family[97]. As a consequence, we can consider $Mg(BH_4)_2$ polymorphs as different topologies of linking nodes by linkers. Indeed, in all known $Mg(BH_4)_2$ structures, Mg atom has a tetrahedral coordination by 4 BH_4 groups, moreover often with only one specific MgH_8 coordination known as snub disphenoid, while the BH_4 group is always linearly coordinated by two Mg, via it opposite tetrahedral edges. With such a fixed local geometry of the constituents, only the topology of the framework varies. The next sub-chapter will illustrate the point of using the word “framework” clearly, for now we show below several crystal structures of $Mg(BH_4)_2$ polymorphs, presented as ionic structures assembled by packing cations and anions, see Figure 3[102].

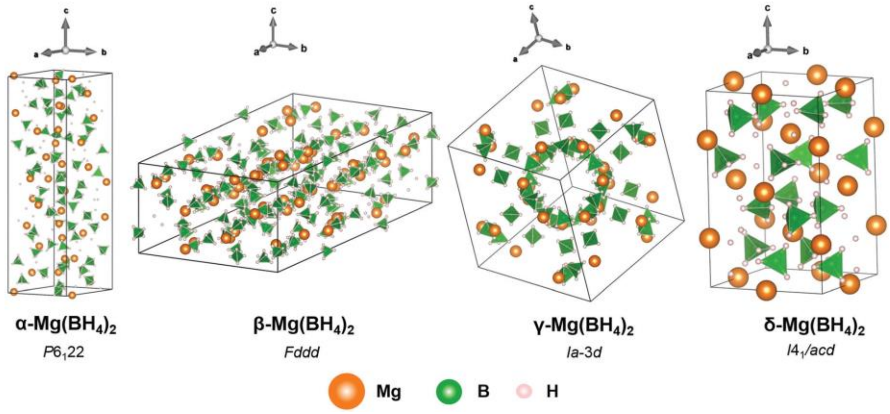

Figure 3. Reported crystal structures of different phases of $Mg(BH_4)_2$. Mg atoms are shown as orange spheres, BH_4 groups as green tetrahedra, and unit cells are defined by black lines[102].

1.3.3 The First Porous Borohydride: γ-$Mg(BH_4)_2$

γ-$Mg(BH_4)_2$ was reported as the first functional porous metal borohydride, and hydride in general[97]. The α-$Mg(BH_4)_2$ was pointed out to be porous in 2008[99], but was not shown to possess a functional porosity (i.e., guest uptake). The 3D framework structure is assembled already in the precursor, $Mg(BH_4)_2 \cdot 0.5S(CH_3)_2$, from which the solvent is subsequently removed under mild conditions, retaining the framework. In its crystal structure, each Mg ion is coordinated to four BH_4 groups in the form of a distorted tetrahedron, the resulting symmetry of the assembly is characterized by the space group *Ia-3d* (Figure 4). There are non-crossing porous channels in the structure, and the pore ratio is about 33%. The narrowest distance (aperture) within a pore is about 5.8 Å. This framework topology is similar to one of the predicted zeolitic SiO_2 and to the porous zinc imidazolate framework structure ZIF-72. In this kind of system, hydrogen will be stored in two ways, one in a form of the BH_4 group bound by covalent bonds, and the other in a form of hydrogen molecules physically adsorbed into nanopores. In terms of composition, it belongs to metal borohydride, while structurally speaking, it can be considered as a metal "inorganic" framework. This makes γ-$Mg(BH_4)_2$ a compound that has both the hydrogen storage properties of light metal hydrides and of metal organic frameworks.

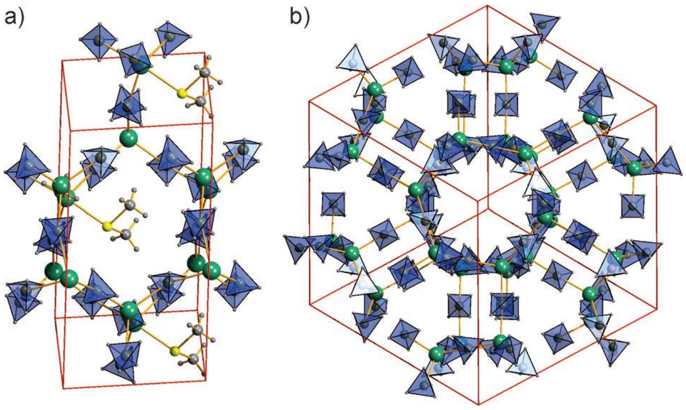

Figure 4. Crystal structures of nanoporous $Mg(BH_4)_2$ and its precursor. **a)** Monoclinic $Mg(BH_4)_2 \cdot 0.5S(CH_3)_2$ precursor. Unit cell parameters: a = 7.6325(4) Å, b = 13.8411(8) Å, c = 12.4290(8) Å, α=γ=90°, β = 103.833(3)°. Atomic coordinates can be found in ref. 97. **b)** Nanoporous cubic γ-$Mg(BH_4)_2$. Unit cell parameters can be seen in Table 3. Mg atoms are shown as green spheres, BH_4 groups as blue tetrahedra, S atoms in a) are shown as yellow spheres, and unit cells are defined by red lines[97].

In this project, we will mainly focus on the physisorption of different gases in γ-$Mg(BH_4)_2$ and study their adsorption behavior, including thermodynamics, kinetics, interaction and so on by *in situ* diffraction. Chemical hydrogen storage or the potential use as solid state electrolyte (which are thought as main application domains of magnesium borohydride), will not be further discussed in this section as it is not strongly related to this project.

1.4. Gas Adsorption by Solids

1.4.1 Introduction to Adsorption

Adsorption is the phenomenon of interaction of gas molecules with a solid surface. The reverse process of adsorption is named desorption, as shown in Figure 5. Under lower temperatures, higher pressures, or at high affinity to the solid, the adsorbed gas can almost entirely saturate the surface of the interface. Therefore, to increase the amount of the interacting gas, all industrial adsorbents have a large specific surface areas (usually well over 100 m^2/g), so they are highly porous or consist of very fine particles.

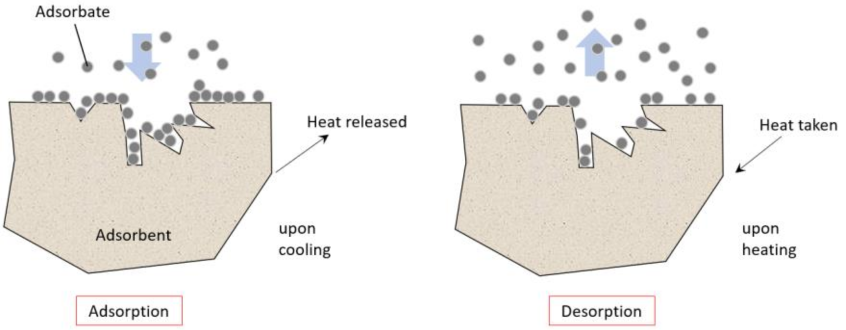

Figure 5. Schematic pictures of adsorption and desorption.

The difference between adsorption and absorption should be mentioned here because of their similarity of spelling they are often interchanged. However, there are substantial distinctions between them. Absorption is a physical or chemical phenomena or a process that occurs when atoms, molecules or ions enter the bulk phase, such as liquid or solid material. So it is a bulk phenomenon. In contrast, adsorption is a surface phenomenon. Generally speaking, sorption is a more general word that encompasses absorption, adsorption, and ion exchange. A cartoonist's version of the difference between adsorption and absorption is shown in Figure 6[103]. For porous materials, one can consider the gas is *adsorbed* on the surface of the pores. However, since for crystalline materials containing nanopores (of the size of the molecules), the gas sorption is occurring in the bulk, sometimes even altering the structure of the host matrix by relatively strong guest-host interactions. Indeed, this justifies the use of *absorption* as a proper term, however *adsorption* is still commonly used in this context.

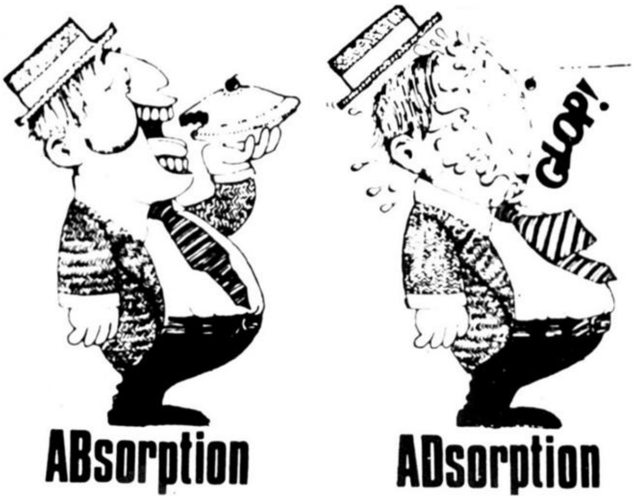

Figure 6. Cartoonist's illustration of the difference between absorption and adsorption[103].

The applications of adsorption can be traced back to ancient times as described by Weber et al.[104]: "It is good to keep water in copper vessels to expose it to sunlight and to filter it through charcoal". Contemporary, adsorption techniques become more and more important, as often stressed in the field of surface science[105]. Some adsorbents are used on large scale as desiccants, catalysts, and catalyst support, while some others are used for gas storage, gas separation, liquid purification, drug delivery and so on. With the development of diverse porous solids as functional adsorbents, adsorption phenomena are especially vital to nearly all the applications involving MOFs, as described in sub-Chapter 1.3.

1.4.2 Classification of Isotherms

An adsorption isotherm is a set of data points that shows the connection between the adsorbate's pressure and the quantity adsorbed at a certain temperature, usually expressed in terms of mass of adsorbent. When it comes to characterizing the adsorption capacity of MOFs, isotherms are the most often used data set.

According to Brunauer et al.[106], they observed and classified five different types of isotherms in 1940, and subsequentially, the results have been applied by IUPAC in 1985, with an update in 2015[107]. The classification of different types of physisorption isotherms concluded from IUPAC is shown in Figure 7.

Microporous materials, such as activated carbon, molecular sieve zeolite, some MOFs, with relatively small exterior surfaces produce reversible Type I isotherms. A Type I isotherm reveals a monolayer adsorption and the amount adsorbed approaches a limiting value as the uptake is governed by the reachable micropore volume instead of the internal surface area. Type I(a) isotherms have a sharper increase of uptake at low pressure compared to that of Type I(b) isotherms. This is because adsorbents, which show a Type I(b) isotherm, often have a large range of pore size distribution and the pore sizes are larger than the adsorbate gases, whereas Type I(a) isotherm are found with materials providing micropores that are near the dimensions of the adsorbate gases.

Reversible Type II and Type III isotherms are given by the adsorbents in which multilayer physisorption becomes dominant. Type

II exhibits a significant adsorption with a knee (labeled B) corresponding to monolayer creation, and the isotherm diverges when the saturation pressure is approached due to the infinite layers of stacking allowed. In opposite, Type III shows a convex with no discernable inflection point, demonstrating weak adsorption to the surface.

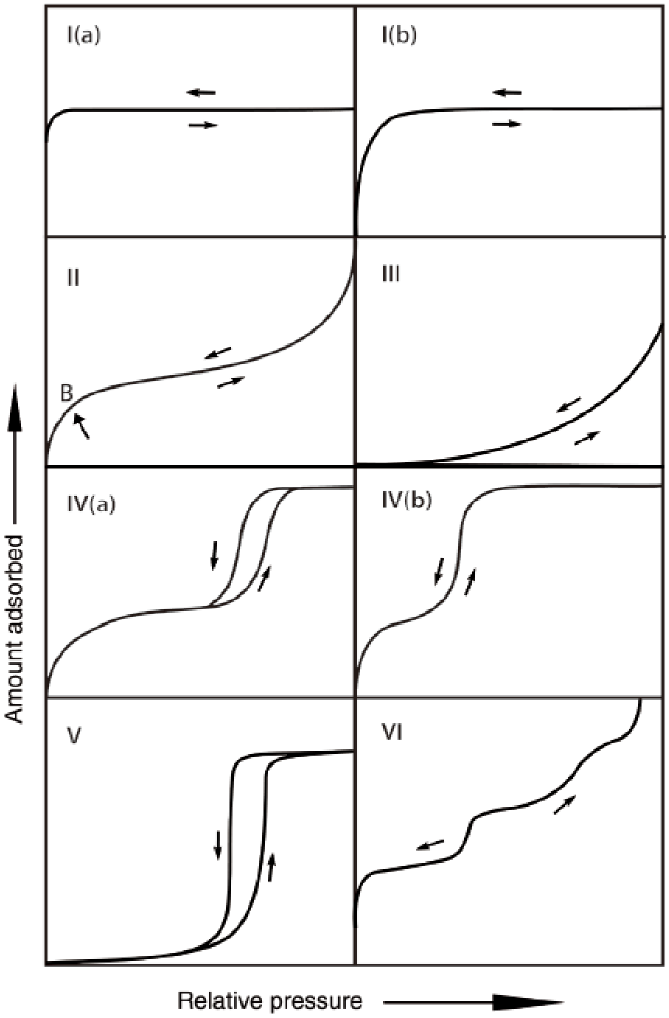

Figure 7. Classification of physisorption isotherms[107].

Type IV isotherms are usually produced by mesoporous adsorbents. The adsorption interactions, as well as the interactions between the molecules in the condensed form, control the adsorption behavior in mesopores. In this case, the initial adsorption behavior on the mesopore walls takes the same path as the corresponding part of a Type II isotherm. In the case of the Type IV(a) isotherm, hysteresis is associated with capillary condensation while it is not present in a Type IV(b) isotherm. This occurs when the pore width exceeds a certain critical width, which is dependent on the adsorption system and temperature. With adsorbents having mesopores of smaller width, completely reversible Type IV(b) isotherms are observed.

Type V isotherms can be described by the adsorbents which have a weak interaction between adsorbents and adsorbates. In the low p / p_0 range, the Type V isotherm shape is very similar to that of Type III, and at higher p / p_0, the interaction becomes significant and gives the isotherm shape in the figure. A similar hysteresis loop can be observed for systems showing slow kinetics of gas adsorption or most typically desorprtion, but the Figure above illustrates a truly equilibrium diagram.

The reversible stepwise Type VI isotherm is usually representative of layer-by-layer adsorption on a highly uniform nonporous surface.

1.4.3 Isobars

Likewise, plotting isobars where the equilibrium capacity is related to temperature at a constant pressure is also possible. However, isobars are not commonly used by researchers in the domain of physisorption. In general, the most common source of adsorption capacity data for MOFs are isotherms.

In this work, on the contrary, isobars data of gases adsorbed in γ-$Mg(BH_4)_2$ are widely measured by diffraction. Detailed information and methods will be introduced in the next chapter (Methodology).

1.4.4 XRD for Analysis of Adsorption

With the explosive growth of different kinds of porous solids, there are more and more "adsorption driven" phenomena, especially appearing in flexible MOFs. Flexible MOFs are also called soft porous crystals, which exhibit the structural transformability in the process of adsorption, responding to external stimulus, such as varied temperature, pressures, and types of adsorbates[108][109]. However, traditional adsorption measurements, such as volumetric and gravimetric measurements (these measurements will be introduced in chapter 2), cannot meet the demand to understand the guest-host systems microscopically for structural flexibility. To enable such investigations, a wide range of *in situ* characterizations were explored in recent years, including XRD and NMR. In this section, several examples of "adsorption driven" phenomena studied by *in situ* diffraction will be introduced.

1. Breathing behavior

Breathing behavior is the reversible transition of MOFs structure, including the change of unit cell and sometimes the space group. Serre et al.[110] have reported the first flexible nanoporous MOF, Cr-MIL-53 in 2002. They found this material exhibits a fully reversible transition

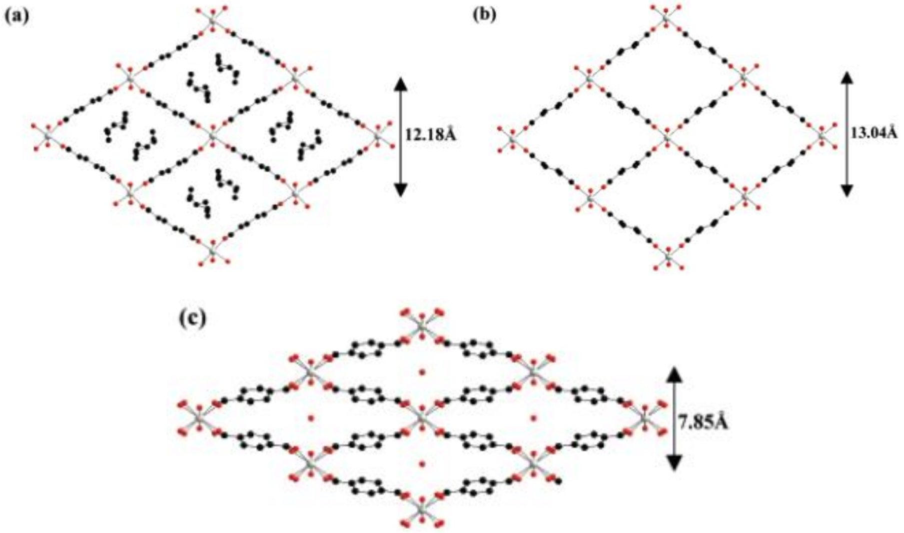

Figure 8. Crystal structures of pore systems of **a)** MIL-53as, **b)** MIL-53ht, **c)** MIL-53lt[110].

between its low-temperature form (MIL-53lt) and high-temperature form (MIL-53ht), followed by a large breathing effect of over 5 Å. The free acid can be removed from the as-synthesized form (MIL-53as) so that MIL-53ht can be obtained with a surface area over 1500 m^2/g. Their crystal structures are shown in Figure 8. Later in 2010, their group also investigated CO_2 and CH_4 adsorption in this flexible framework MIL-53(Al)[111]. The isotherms of both gases are shown in Figure 9, combined with the changes between a large-pore (lp) and narrow-pore (np) configuration as a function of pressure, temperature and the nature of gas.

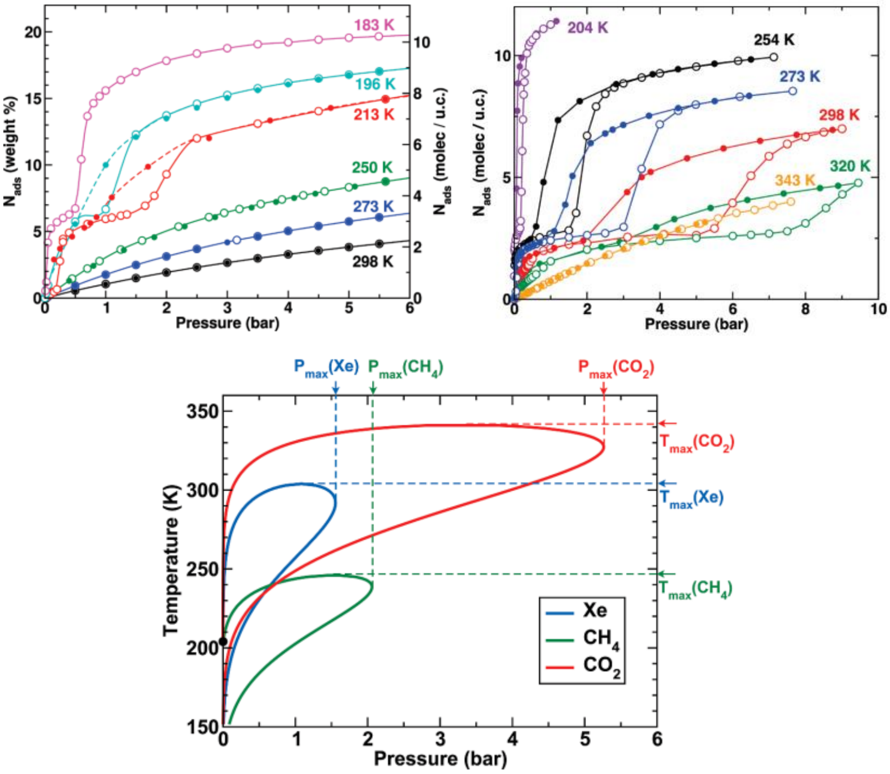

Figure 9. Adsorption isotherms of CH_4 and CO_2 in MIL-53(Al) and its pore transition configuration. **top left**, isotherms of adsorption and desorption of CH_4 from 0 – 6 bar at varies temperatures; **top right**, isotherms of adsorption and desorption of CO_2 from 0 – 10 bar at various temperatures, open symbols: adsorption; full symbols, desorption. **bottom middle**, schematic phase diagram showing different temperatures, pressures, and gases dependence on np and lp phases[111].

2. Negative gas adsorption

Negative gas adsorption (NGA) has been reported by Krause et al.[112] in 2016 as an adsorption transition in DUT-49. Commonly the amount of gases uptake increases with increasing pressure at constant temperature in an isothermal measurement. On contrast, in their research, they found a spontaneous desorption of gas (methane and n-butane) occurs during pressure increase in a defined temperature as shown in Figure 10. *In situ* PXRD (powder X-ray diffraction) data of methane adsorption at 111 K has been applied to demonstrate a structure transformation between open-pore structure DUT-49*op* and contracted-pore structure DUT-49*cp*, which leads to this NGA phenomena. Detailed crystalline structure parameters are shown in Figure 11. As a supplement, diffraction methods can investigate this unusual adsorption phenomenon from a microscopic point of view, inaccessible to standard isotherm measurements.

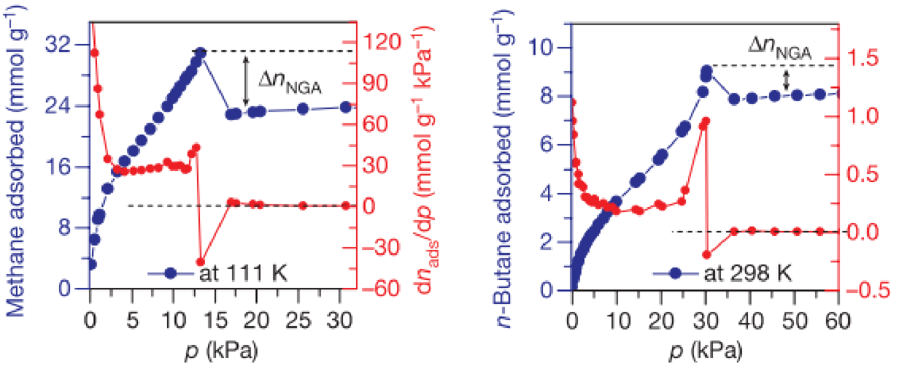

Figure 10. Adsorption isotherms of methane and *n*-butane in DUT-49 showing an NGA phenomena[112].

3. Linker rotation (gate-opening / closing)

Linker rotation usually happens in a flexible MOF giving rise to a structure transition from a close-pore system to an open-pore system, with the increase of specific surface area, namely in an open-pore form. Different from breathing behavior, linker rotation does not change the unit cell parameters of the crystals. Fairen-Jimenez et al.[113] has studied

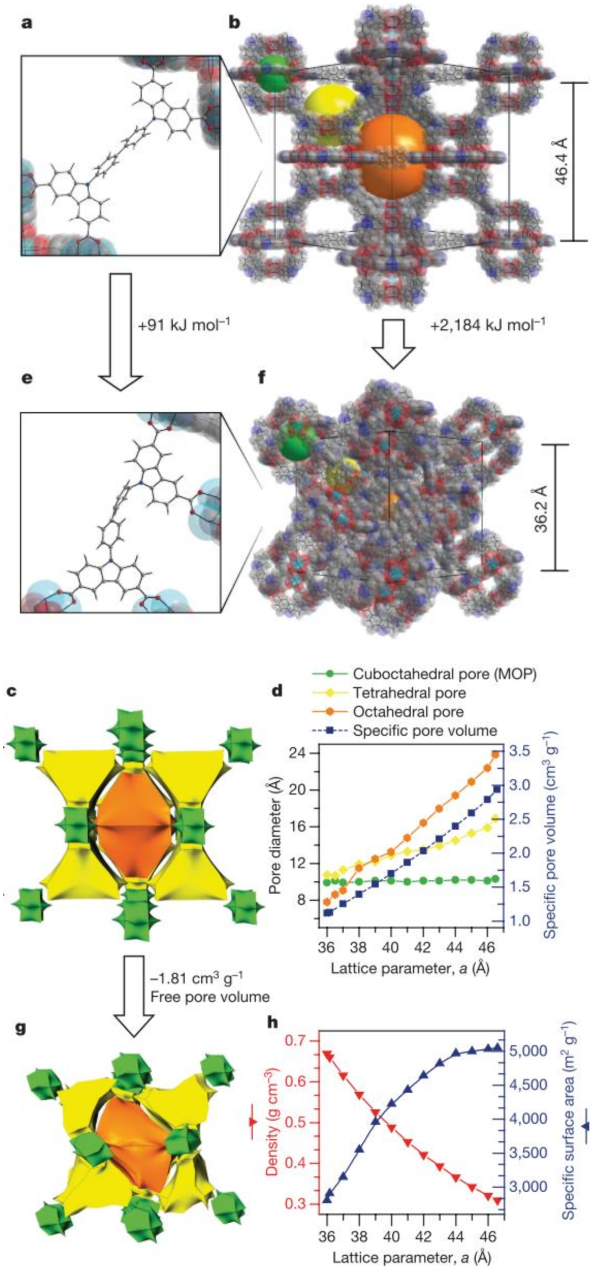

Figure 11. a) e), structure of DUT-49*op* and DUT-49*cp*, respectively; **b) f),** view of crystal structure along [110]. C is shown as dark grey, N as blue, O as red, Cu as cyan, and H as light grey; **c) g),** Representation of pore transformation from DUT-49*op* to DUT-49*cp*; **d),** Evolution of pore sizes and free pore volume during contraction from DUT- 49*op* to DUT-49*cp*; **h),** Evolution of density and accessible geometric surface area[112].

and simulated the existence of structural flexibility of ZIF-8 by adsorption of large molecules under high pressure. A new phase was observed at 14700 bar, ZIF-8HP, showing the same space-group symmetry (*I*4-3*m*) as ZIF-8, while a reorientation of the imidazolate linker, gives access to more porosity. J. W. Brown et al.[114] reported the ability to release a guest in a controllable manner from IRMOF-74-III in response to an external stimulus. IRMOF-74-III has an identical structure as MOF-74. However, each organic unit in azo-IRMOF-74-III is adorned with a photoswitchable azobenzene unit that can be switched between its *cis* and *trans* conformation using a 408 nm wavelength light (two conformations are shown in Figure 12).

As a short conclusion, XRD is a common technique to characterize crystalline porous MOFs, such as their stability, flexibility, and adsorption mechanisms. Furthermore, *in situ* XRD is also widely applied by researchers to understand the "adsorption-driven" phenomena. Commonly, diffraction is used to find a microscopic picture (explanation) of the unexplained phenomena (anomalies) found from macroscopic measurements, typically these are adsorption isotherms from volumetric and gravimetric techniques.

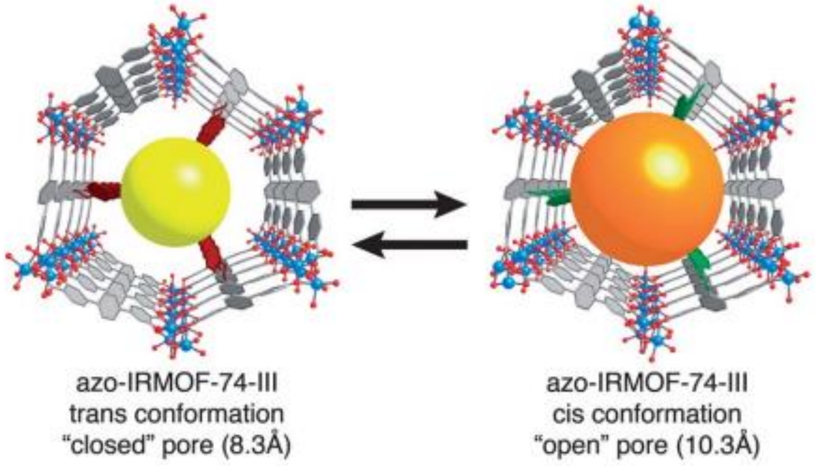

Figure 12. A view on two conformations of the ligand in IRMOF-74-III along the channel[114].

1.5. Objectives of this project

The first objective of this project is to study the adsorption properties of γ-$Mg(BH_4)_2$, the first hydride with functional porosity. The surface of its pores is made of hydrogen atoms bearing partially negative charge. It was shown in 2011[97] to adsorb small molecules like H_2, N_2 and dichloromethane, and in 2014[115] to show a very unusual reversible transition from the crystalline to the amorphous phase. Our laboratory has extensive experience working with this material. We decided to use a series of similar gases having different diameter, such as noble gases (He, Ne, Ar, Kr, Xe), fuel gases (C1 to C4 alkanes), as well as N_2 and H_2. The use of similar probes will allow us to understand the nature of the guest-host interactions, reveal and point out the role of guest-guest interaction, understand the size factors and so on. We are interested to find new or unusual adsorption properties of this materials that may lead to improved gas storage or separation. We want to understand if the nature of this framework gives added value, namely analyzing whether the unique hydridic character of its surface plays an important role or it is the size and geometry of its 1D channels defining adsorption properties; or we may have both effects.

The second objective is to develop a new methodology to study adsorption by diffraction methods. Indeed, diffraction yields not only information on the position of guests inside pores, but also their quantity, thus allowing to follow it as a function of pressure and temperature. As a result, both micro- and macroscopic pictures of interaction can be built, respectively from the point of view of structure and properties. Ideally, this should be done from the same experiment, coupling every point along the isobars or isotherms with the structural information. This should allow to detect and explain unusual phenomena, such as consecutive or competitive filling of several adsorption sites, evolution of interactions leading to transitions etc. The macroscopic properties studied at different P-T conditions yield information on adsorption thermodynamics, such as isosteric heats of adsorption, thus these data can also be potentially obtained from diffraction. It is also tempting to explore the time coordinate to study kinetics of gas adsorption. Ideally, this should allow to plot time-dependent occupancies yielding activation barriers, and put together with structure, to identify the underlying mechanisms of gas adsorption. Despite these aims are very ambitious, we will show them being achieved in the following chapters.

1.6. Strategy and Motivation

As described in the objectives, we want to determine the factors influencing the adsorption behavior of different gases. It is either the geometry of the porous framework, such as size and shape of its inner surface, or the chemical nature of the inner surface defining the guest-host interactions. We study adsorption of noble gases consisting of chemically neutral non-polarized molecules, having different size along the series from He to Xe, later moving to gasses capable for more specific interactions, such as methane/ethane or diatomic hydrogen and nitrogen. Each system is studied by *in situ* diffraction, to access both structure and thermodynamics of gas adsorption, advancing progressively this new approach.

First we start with the simple, neutral and “standard” gas, studying argon adsorption in γ-$Mg(BH_4)_2$ and surprisingly finding the guest rearrangement upon gas loading. The next chapter deals with more complex diatomic H_2 and N_2, having significantly different size and thus showing drastically different adsorption behavior. Then we study adsorption of small noble gasses, He and Ne, two rarely studied adsorbates due to their low adsorption energy, thus the experiments must be done at sub-LN2 temperatures. As a result, these systems reveal guest re-arrangements similar to both Ar and H_2, all defined by guest-guest repulsion within the pore pocket. Then we move to the largest molecules, the fuel gasses methane and ethane, probing the guest-host interactions, since only one large molecule can be hosted in each pore pocket. We end up with the chapter on physisorption of heavy noble gasses, with the focus on adsorption kinetics. All along these lines we use diffraction techniques, combined with more classical volumetric methods. We progressively discover the role of probe size and the specific guest-host interactions offered by the porous hydridic framework studied in this work.

Regarding motivation, we want to notice that with the emergence of new kinds of porous materials, such as different classes of metal-organic frameworks (MOFs), during the last twenty years, volumetric and gravimetric methods are not sufficient to reveal and explain the adsorption behavior. There are some unique “adsorption-driven” phenomena happening especially in flexible MOFs, such as breathing effect, negative gas adsorption and gate opening. In the rigid porous frameworks, one can have several sites occupied by a guest, consequently or in parallel, involving a guest rearrangement. Powder diffraction under specific pressure-temperature conditions is an efficient way to determine the structure of a crystalline material, and it has been applied to get understanding of adsorption in such complex systems. Thus, in each chapter of results in this thesis we are developing and validating methodologies offering a complete evaluation of gas adsorption (from structure to thermodynamic and kinetic properties of adsorption) based on diffraction methods. We use both Laboratory X-ray, synchrotron and neutron powder diffraction, from helium temperatures and up to above ambient T. Thus, this work is addressing the properties of the selected interesting system and the advancement of the new methodologies, as stated in the objectives above.

1.7. References

[1] Young K., *Metal Hydrides*. Reference Module in Chemistry, Molecular Sciences and Chemical Engineering. **2018**.

[2] Sieverts A., Jurisch E. Platin, Rhodium und Wassemtoff. Berichte der Dtsch. *Chem. Gesellschaft.* **1912**, 45(1):221-229.

[3] Ley M. B., Jepsen L. H., Lee Y. S., et al. Complex hydrides for hydrogen storage - new perspectives. *Materials Today*, **2014**, 17(3):122-128.

[4] Bianchini C., Barbaro P., *Catalysis for Sustainable Energy Production*. Wiley-Vch. **2009**.

[5] Hirscher M., Züttel A., Borgschulte A., Schlapbach L. Handbook of Hydrogen Storage. *Ceramic Transactions*. **2009**, 22.

[6] Züttel A., Remhof A., Borgschulte A., Friedrichs O. Hydrogen : the future energy carrier. *Philosophical Transactions of the Royal Society A: Mathematical, Physical and Engineering Sciences.* **2010**, 1923(368): 3329-3342.

[7] Technical Targets for Onboard Hydrogen Storage for Light-Duty Vehicles. https://www.energy.gov/eere/fuelcells/doe-technical-targets-onboard-hydrogen-storage-light-duty-vehicles.

[8] Yvon K., Renaudin G., Wei C. M., Chou M. Y. Hydrogenation-Induced insulating state in the intermetallic compound $LaMg_2Ni$. *Phys. Rev. Lett.* **2005**, 94(6): 66403.

[9] Chotard J. N., Filinchuk Y., Revaz B., Yvon K. Isolated $[Ni_2H_7]^{7-}$ and $[Ni_4H_{12}]^{12-}$ ions in $La_2MgNi_2H_8$. *Angew. Chem. Int. Ed.* **2006**, 45(46): 7770-7773.

[10] Orimo S., Nakamori Y., Eliseo J. R., Zu A., Jensen C. M. Complex Hydrides for Hydrogen Storage. *Chem. Rev.* **2007**, 107(10): 4111-4132.

[11] Bogdanović B., Schwickardi M. Ti-doped alkali metal aluminium hydrides as potential novel reversible hydrogen storage materials. *J. Alloys. Compd.* **1997**, 253:1-9.

[12] Zidan R. A., Takara S., Hee A. G., Jensen C. M. Hydrogen cycling behavior of zirconium and titanium-zirconium-doped sodium aluminum hydride. *J. Alloys Compd.* **1999**, 285(1-2): 119-122.

[13] Fan X., Xiao X., Chen L., Yu K., Wu Z., Li S. Active species of $CeAl_4$ in the $CeCl_3$-doped sodium aluminium hydride and its enhancement on reversible hydrogen storage performance. *Chem. comm.* **2009**, 44: 6857-6859.

[14] Wang P., Kang X., Cheng H. M. Exploration of the Nature of Active Ti Species in Metallic Ti-Doped $NaAlH_4$. *J. Phys. Chem. B.* **2005**, 109(43):

20131-20136.

[15] Liu Y., Liang C., Zhou H., Gao M., Pan H., Wang Q. A novel catalyst precursor K_2TiF_6 with remarkable synergetic effects of K, Ti and F together on reversible hydrogen storage of $NaAlH_4$. *Chem. comm.* **2011**, 47(6): 1740-1742.

[16] Xiao X., Fan X., Yu K., et al. Catalytic Mechanism of New TiC-Doped Sodium Alanate for Hydrogen Storage. *J. Phys. Chem. C.* **2009**, 113(48): 20745-20751.

[17] Wang F., Liu Y., Gao M., Luo K., Pan H., Wang Q. Formation Reactions and the Thermodynamics and Kinetics of Dehydrogenation Reaction of Mixed Alanate Na_2LiAlH_6. *J. Phys. Chem. C.* **2009**, 113(18): 7978-7984.

[18] Fan X., Xiao X., Chen L., et al. Direct synthesis and hydrogen storage behaviors of nanocrystalline Na_2LiAlH_6. *J. Mater. Sci.* **2011**, 46(10): 3314-3318.

[19] Schlesinger H. I., Sanderson R. T., Burg A. B. Metallo Borohydrides. I. Aluminum Borohydride. *J. Am. Chem. Soc.* **1940**, 62(12): 3421-3425.

[20] Burg A. B., Schlesinger H. I. Metallo Borohydrides. II. Beryllium Borohydride. *J. Am. Chem. Soc.* **1940**, 62(12): 3425-3429.

[21] Schlesinger H. I., Brown H. C. Metallo Borohydrides. III. Lithium Borohydride. *J. Am. Chem. Soc.* **1940**, 62(12): 3429-3435.

[22] Paskevicius M., Jepsen L. H., Schouwink P., et al. Metal borohydrides and derivatives-synthesis, structure and properties. *Chem. Soc. Rev.* **2017**, 46(5): 1565-1634.

[23] Kou H., Xiao X., Li J., et al. Effects of fluoride additives on dehydrogenation behaviors of $2LiBH_4 + MgH_2$ system. *Int. J. Hydrogen Energy*. **2011**, 37(1): 1021-1026.

[24] Kou H., Sang G., Zhou Y., et al. Enhanced hydrogen storage properties of $LiBH_4$ modified by NbF_5. *Int. J. Hydrogen Energy*. **2014**, 39(22): 11675-11682.

[25] Kou H., Sang G., Huang Z., et al. Comprehensive hydrogen storage properties and catalytic mechanism studies of $2LiBH_4$-MgH_2 system with NbF_5 in various addition amounts. *Int. J. Hydrogen Energy.* **2014**, 39(13): 7050-7059.

[26] Shao J., Xiao X., Fan X., et al. Low-Temperature Reversible Hydrogen Storage Properties of $LiBH_4$: A Synergetic effect of nanoconfinement and nanocatalysis. *J. Phys. Chem. C.* **2014**, 118(21): 11252-11260.

[27] Nielsen T. K., Bo U., Gosalawit R., et al. A Reversible Nanoconfined Chemical Reaction. *ACS Nano.* **2010**, 4(7): 3903-3908.

[28] Nakamori Y., Li H., Kikuchi K., et al. Thermodynamical stabilities of metal-borohydrides. *J. Alloys Compd.* **2007**, 446: 296-300.

[29] Nakamori Y., Miwa K., Ninomiya A., et al. Correlation between thermodynamical stabilities of metal borohydrides and cation

electronegativites : First-principles calculations and experiments. *Phys. Rev. B.* **2006**, 74(4): 045126.

[30] Fang Z. Z., Kang X., Wang P., Li H. W., Orimo S. I. Unexpected dehydrogenation behavior of $LiBH_4/Mg(BH_4)_2$ mixture associated with the in situ formation of dual-cation borohydride. *J. Alloys Compd.* **2010**, 491(1-2): L1-L4.

[31] Jiang K., Xiao X., Deng S., et al. A Novel Li-Ca-B-H Complex Borohydride : Its synthesis and hydrogen storage properties. *Phys. Chenistry C.* **2011**, 115(40): 19986-19993.

[32] Chen P., Xiong Z., Luo J., Lin J., Tan K. L. Interaction of hydrogen with metal nitrides and imides. *Nature.* **2002**, 420(6913): 302-304.

[33] Ichikawa T., Hanada N., Isobe S., Leng H. Y., Fujii H. Hydrogen storage properties in Ti catalyzed Li-N-H system. *J. Alloys Compd.* **2005**, 404: 435-438.

[34] Chen P., Xiong Z., Wu G., Liu Y. Metal-N-H systems for the hydrogen storage. *Scr. Mater.* **2007**, 56(10): 817-822.

[35] Wenger P., Rentsch S., Mauron P., Emmenegger C. $LiBH_4$ a new hydrogen storage material. *J. Power Sources.* **2003**, 118(1-2): 1-7.

[36] Sing K. S. Reporting physisorption data for gas/solid systems with special reference to the determination of surface area and porosity. *Pure Appl. Chem.* **1985**, 57(4):603-619.

[37] Sun Y., Zhou H. C. Recent progress in the synthesis of metal-organic frameworks. *Sci. Technol. Adv. Mater.* **2015**, 16(5): 54202-54212.

[38] Yaghi O. M., Li G., Li H. Selective binding and removal of guests in a microporous metal-organic framework. *Nature*. **1995**, 378(6558): 703-706.

[39] Li H., Eddaoudi M., O’Keeffe M., Yaghi O. M. Design and synthesis of an exceptionally stable and highly porous metal-organic framework. *Nature*. **1999**, 402(6759): 276-279.

[40] Yaghi O. M., O’Keeffe M., Ockwig N. W., Chae H. K., Eddaoudi M., Kim J. Reticular synthesis and the design of new materials. *Nature.* **2003**, 423(6941): 705-714.

[41] Li A., Perez R. B., Wiggin S., Ward S. C., Wood P. A., Fairen-Jimenez D. The launch of a freely accessible MOF CIF collection from the CSD. *Matter.* **2021**, 4(4): 1105-1106.

[42] Park K. S., Ni Z., Côté A. P., et al. Exceptional chemical and thermal stability of zeolitic imidazolate frameworks. *Proc. Natl. Acad. Sci.* **2006**, 103(27): 10186-10191.

[43] Millange F., Serre C., Férey G. Synthesis , structure determination and properties of MIL-53as and MIL-53ht : the first Cr^{III} hybrid inorganic-organic microporous solids : $Cr^{III}(OH)\cdot\{O_2C\text{-}C_6H_4\text{-}CO_2\}\cdot\{HO_2C\text{-}C_6H_4\text{-}CO_2H\}_x$. *Chem. comm.* **2002**, 8: 822-823.

[44] Cavka J. H., Jakobsen S., Olsbye U., et al. A New Zirconium inorganic building brick forming metal organic frameworks with exceptional stability. *J. Am. Chem. Soc.* **2008**, 130(42): 13850-13851.

[45] Li J. R., Kuppler R. J., Zhou H. C. Selective gas adsorption and separation in metal-organic frameworks. *Chem. Soc. Rev.* **2009**, 38(5): 1477-1504.

[46] Lee J., Farha O. K., Roberts J., Scheidt K. A., Nguyen S. T., Hupp J. T. Metal-organic framework materials as catalysts. *Chem. Soc. Rev.* **2009**, 38(5): 1450-1459.

[47] Furukawa H., Cordova K. E., O'Keeffe M., Yaghi O. M. The chemistry and applications of metal-organic frameworks. *Science.* **2013**, 341: 1230444.

[48] Zhao C., Dai X., Yao T., et al. Ionic exchange of metal-organic frameworks to access single nickel sites for efficient electroreduction of CO_2. *J. Am. Chem. Soc*. **2017**, 139(24): 8078-8081.

[49] Horcajada P., Gref R., Baati T., et al. Metal-organic frameworks in biomedicine. *Chem. Rev.* **2012**, 112(2): 1232-1268.

[50] Cui Y., Yue Y., Qian G., Chen B. Luminescent functional metal-organic frameworks. *Chem. Rev.* **2012**, 112(2): 1126-1162.

[51] Li J., Sculley J., Zhou H. Metal-organic frameworks for separations. *Chem. Rev.* **2012**, 112(2): 869-932.

[52] Mueller U., Schubert M., Teich F., Puetter H., Pastre J. Metal-organic frameworks - prospective industrial applications. *J. Mater. Chem.* **2006**, 16(7): 626-636.

[53] Rosi N. L., Eckert J., Eddaoudi M., et al. Hydrogen storage in microporous metal-organic frameworks. *Science*. **2003**, 300(5622): 1127-1129.

[54] Kaye S. S., Dailly A., Yaghi O. M., Long J. R. Impact of preparation and handling on the hydrogen storage properties of Zn_4O (1,4-benzenedicarboxylate)$_3$ (MOF-5). *J. Am. Chem. Soc.* **2007**, 129(46): 14176-14177.

[55] Rowsell J. L., Eckert J., Yaghi O. M. Characterization of H_2 binding sites in prototypical metal-organic frameworks by inelastic neutron scattering. *J. Am. Chem. Soc.* **2005**, 127(42): 14904-14910.

[56] Yang Q., Zhong C. Understanding hydrogen adsorption in metal-organic frameworks with open metal sites : a computational study. *J. Phys. Chem. B.* **2006**, 110(2): 655-658.

[57] Sun D., Ma S., Ke Y., Collins D. J., Zhou H. An interweaving MOF with high hydrogen uptake. *J. Am. Chem. Soc.* **2006**, 128(12): 3896-3897.

[58] Wang X., Ma S., Yuan D., et al. A large-surface-area boracite-network-topology porous MOF constructed from a conjugated ligand exhibiting a high hydrogen uptake capacity. *Inorg. Chem.* **2009**, 48(16): 7519-7521.

[59] Farha O. K., Yazaydın A. Ö., Eryazici I. et al. De novo synthesis of a metal-organic framework material featuring ultrahigh surface area and gas storage

capacities. *Nat. Chem.* **2010**, 2(11): 944-948.

[60] Yan Y., Yang S., Blake A. J., et al. A mesoporous metal-organic framework constructed from a nanosized C_3-symmetric linker and $[Cu_{24}(isophthalate)_{24}]$ cuboctahedra. *Chem. comm*. **2011**, 47(36): 9995-9997.

[61] Lin X., Telepeni I., Blake A. J., et al. High capacity hydrogen adsorption in Cu (II) tetracarboxylate framework materials: the role of oore size , ligand functionalization, and exposed metal sites. *J. Am. Chem. Soc.* **2009**, 131(6): 2159-2171.

[62] Yan Y., Blake A. J., Lewis W., et al. Modifying cage structures in metal-organic polyhedral frameworks for H_2 storage. *Chem. - A Eur. J.* **2011**, 17(40): 11162-11170.

[63] Zhou W., Wu H., Yildirim T. Enhanced H_2 adsorption in isostructural metal - organic frameworks with open metal sites: strong dependence of the binding strength on metal ions. *J. Am. Chem. Soc.* **2008**, 130(46): 15268-15269.

[64] Balderas-Xicohténcatl R., Schlichtenmayer M., Hirscher M. Volumetric Hydrogen Storage Capacity in Metal–Organic Frameworks. Energy Technol. 2018, 6(3):578-582.

[65] Kondo M., Yoshitomi T., Seki K., Matsuzaka H., Kitagawa S., Seki K. Three-dimensional framework with channeling cavities for small molecules: $\{[M_2(4,4'\text{-bpy})_3(NO_3)_4]\cdot xH2O\}_n$ (M = Co, Ni, Zn). *Angew. Chem. Int. Ed.* **1997**, 36(16): 1725-1727.

[66] Eddaoudi M., Kim J., Rosi N., et al. Systematic design of pore size and functionality in isoreticular MOFs and their application in methane storage. *Science.* **2002**, 295(5554): 469-472.

[67] Düren T., Bae Y. S., Snurr R. Q. Using molecular simulation to characterise metal-organic frameworks for adsorption applications. *Chem. Soc. Rev.* **2009**, 38(5): 1237-1247.

[68] Jiang J., Babarao R., Hu Z. Molecular simulations for energy, environmental and pharmaceutical applications of nanoporous materials: from zeolites, metal-organic frameworks to protein crystals. *Chem. Soc. Rev.* **2011**, 40(7): 3599-3612.

[69] Keskin S., Liu J., Rankin R. B., Johnson J. K., Sholl D. S. Progress, opportunities, and challenges for applying atomically detailed modeling to molecular adsorption and transport in metal-organic framework materials. *Ind. Eng. Chem. Res.* **2009**, 48(5): 2355-2371.

[70] Yang Q., Liu D., Zhong C., Li J. R. Development of computational methodologies for metal-organic frameworks and their application in gas separations. *Chem. Rev.* **2013**, 113(10): 8261-8323.

[71] Lee K., Isley W. C., Dzubak A. L., et al. Design of a metal-organic framework with enhanced back bonding for separation of N_2 and CH_4. *J. Am. Chem. Soc.* **2014**, 136(2): 698-704.

[72] Valenzano L., Civalleri B., Chavan S., Palomino G. T., Areán C. O., Bordiga

S. Computational and experimental studies on the adsorption of CO, N_2, and CO_2 on Mg-MOF-74. *J. Phys. Chem. C.* **2010**, 114(25): 11185-11191.

[73] Geier S. J., Mason J. A., Bloch E. D., et al. Selective adsorption of ethylene over ethane and propylene over propane in the metal-organic frameworks M_2(dobdc) (M = Mg, Mn, Fe, Co, Ni, Zn). *Chem. Sci.* **2013**, 4(5): 2054-2061.

[74] Llewellyn P. L., Bourrelly S., Serre C., Filinchuk Y., Férey G. How hydration drastically improves adsorption selectivity for CO_2 over CH_4 in the flexible chromium terephthalate MIL-53. *Angew. Chem. Int. Ed.* **2006**, 45(46): 7751-7754.

[75] Xie L. H., Suh M. P. Flexible metal-organic framework with hydrophobic pores. *Chem. Eur. J.* **2011**, 17(49):13653-13656.

[76] Hong D. H., Suh M. P. Selective CO_2 adsorption in a metal-organic framework constructed from an organic ligand with flexible joints. *Chem. Comm.* **2012**, 48(73): 9168-9170.

[77] Couck S., Denayer J. F., Baron G. V., Rémy T., Gascon J., Kapteijn F. An amine-functionalized MIL-53 metal-organic framework with large separation power for CO_2 and CH_4. *J. Am. Chem. Soc.* **2009**, 131(18): 6326-6327.

[78] Zavorotynska O., El-Kharbachi A., Deledda S., Hauback B. C. Recent progress in magnesium borohydride $Mg(BH_4)_2$: Fundamentals and applications for energy storage. *Int. J. Hydrogen Energy*. **2016**, 41(32): 14387-14403.

[79] Wiberg E., Bauer R. Zur Kenntnis eines Magnesium-bor-wasserstoffs $Mg(AlH_4)_2$. *Zeitschrift für Naturforsch. B.* **1950**, 5(7): 397-398.

[80] Chłopek K., Frommen C., Léon A., Zabara O., Fichtner M. Synthesis and properties of magnesium tetrahydroborate, $Mg(BH_4)_2$. *J. Mater. Chem.* **2007**, 17(33): 3496-3503.

[81] Riktor M. D., Sørby M. H., Chłopek K., et al. In situ synchrotron diffraction studies of phase transitions and thermal decomposition of $Mg(BH_4)_2$ and $Ca(BH_4)_2$. *J. Mater. Chem.* **2007**, 17(47): 4939-4942.

[82] Li H. W., Kikuchi K., Nakamori Y., Miwa K., Towata S., Orimo S. Effects of ball milling and additives on dehydriding behaviors of well-crystallized $Mg(BH_4)_2$. *Scr. Mater.* **2007**, 57(8): 679-682.

[83] Mohtadi R., Matsui M., Arthur T. S., Hwang S. J. Magnesium borohydride: from hydrogen storage to magnesium battery. *Angew. Chem.* **2012**, 124(39): 9918-9921.

[84] Kollonitsch J., Fuchs O., Gábor V. New and known complex borohydrides and some of their applications in organic syntheses. *Nature.* **1954**, 173(4394): 125-126.

[85] Brown H. C., Mead E. J., Subba Rao B. C. A Study of solvents for sodium borohydride and the effect of solvent and the metal ion on borohydride Reductions. *J. Am. Chem. Soc.* **1955**, 77(23): 6209-6213.

[86] Koster R. New methods for preparation of metal borohydrides. *Angew.*

Chem.. **1957**, 69: 94.

[87] Plešek J., Heřmánek S. Chemistry of boranes. IV. On preparation, properties, and behavior towards Lewis bases of magnesium borohydride. *Collect. Czechoslov. Chem. Commun.* **1966**, 31(10): 3845-3858.

[88] Konoplev V. N. Synthesis of magnesium borohydride. *Zhurnal Neorg. Khimii.* **1980**, 25(7): 1737-1740.

[89] Zanella P., Crociani L., Masciocchi N., Giunchi G. Facile high-yield synthesis of pure, crystalline $Mg(BH_4)_2$. *Inorg. Chem.* **2007**, 46(22): 9039-9041.

[90] Soloveichik G. L., Andrus M., Gao Y., Zhao J. C., Kniajanski S. Magnesium borohydride as a hydrogen storage material: Synthesis of unsolvated $Mg(BH_4)_2$. *Int. J. Hydrogen Energy.* **2009**, 34(5): 2144-2152.

[91] Bateni A., Scherpe S., Acar S., Somer M. Novel approach for synthesis of magnesium borohydride, $Mg(BH_4)_2$. *Energy. Procedia.* **2012**, 29: 26-33.

[92] Zhang Z. G., Zhang S. F., Wang H., Liu J. W., Zhu M. Feasibility study of the direct synthesis of $Mg(BH_4)_2$ complex hydrides by mechanical milling. *J. Alloys Compd.* **2010**, 505(2): 717-721.

[93] Li H. W., Matsunaga T., Yan Y., Maekawa H., Ishikiriyama M., Orimo S. Nanostructure-induced hydrogenation of layered compound MgB_2. *J. Alloys Compd.* **2010**, 505(2): 654-656.

[94] Pistidda C., Garroni S., Dolci F., et al. Synthesis of amorphous $Mg(BH_4)_2$ from MgB_2 and H_2 at room temperature. *J. Alloys Compd.* **2010**, 508(1): 212-215.

[95] Pitt M. P., Webb C. J., Paskevicius M., Sheptyakov D., Buckley C. E., Gray E. M. In situ neutron diffraction study of the deuteration of isotopic $Mg^{11}B_2$. *J. Phys. Chem. C.* **2011**, 115(45): 22669-22679.

[96] Gupta S., Hlova I. Z., Kobayashi T., et al. Facile synthesis and regeneration of $Mg(BH_4)_2$ by high energy reactive ball milling of MgB_2. *Chem. Comm.* **2013**, 49(8): 828-830.

[97] Filinchuk Y., Richter B., Jensen T. R., Dmitriev V., Chernyshov D., Hagemann H. Porous and dense magnesium borohydride frameworks: Synthesis, stability, and reversible absorption of guest species. *Angew. Chem. Int. Ed.* **2011**, 50(47): 11162-11166.

[98] George L., Drozd V., Saxena S. K., Bardaji E. G., Fichtner M. Structural phase transitions of $Mg(BH_4)_2$ under pressure. *J. Phys. Chem. C.* **2009**, 113(1): 486-492.

[99] Filinchuk Y., Černý R., Hagemann H. Insight into $Mg(BH_4)_2$ with synchrotron X-ray diffraction: Structure revision, crystal chemistry, and anomalous thermal expansion. *Chem. Mater.* **2009**, 21(5): 925-933.

[100] Her J. H., Stephens P. W., Gao Y., et al. Structure of unsolvated magnesium borohydride $Mg(BH_4)_2$. *Acta. Crystallogr. B Struct. Sci. Cryst. Eng. Mater.* **2007**, 63(4): 561-568.

[101] Richter B., Ravnsbæk D. B., Tumanov N., Filinchuk Y., Jensen T. R. Manganese borohydride; synthesis and characterization. *Dalt. Trans.* **2015**, 44(9): 3988-3996.

[102] Dimitrievska M., White J. L., Zhou W., Stavila V., Klebanoffc L. E., Udovicb T. J. Structure-dependent vibrational dynamics of $Mg(BH_4)_2$ polymorphs probed with neutron vibrational spectroscopy and first-principles calculations. *Phys. Chem. Chem. Phys.* **2016**, 18(36): 25546-25552.

[103] Tien C. *Introduction to Adsorption,Basics, Analysis, and Applications*. Elsevier, 2018.

[104] Weber W. J., Morris J. C. Kinetics of adsorption on carbon from solution. *J. Sanit. Eng. Div.* **1963**, 89(2): 31-59.

[105] Dabrowski A. Adsorption-from theory to practice. *Adv. Colloid Interface Sci.* **2001**, 93(1-3):135-224.

[106] Brunauer S., Deming L. S., Deming W. E., Teller E. On a theory of the Van der Waals adsorption of gases. *J. Am. Chem. Soc.* **1940**, 62(7): 1723-1732.

[107] Thommes M., Kaneko K., Neimark A. V, et al. Physisorption of gases, with special reference to the evaluation of surface area and pore size distribution (IUPAC Technical Report). *Pure Appl. Chem.* **2015**, 87(9-10): 1051-1069.

[108] Schneemann A., Bon V., Schwedler I., Senkovska I., Kaskel S., Fischer R.A. Flexible metal-organic frameworks. *Chem Soc Rev.* **2014**, 43(16): 6062-6096.

[109] Ghoufi A., Benhamed K., Boukli-Hacene L., Maurin G. Electrically induced breathing of the MIL-53(Cr) metal-organic framework. *ACS Cent. Sci.* **2017**, 3(5): 394-398.

[110] Serre C., Millange F., Thouvenot C., et al. Very large breathing effect in the First Nanoporous Chromium(III)-Based Solids: MIL-53 or $Cr^{III}(OH)\cdot\{O_2C\text{-}C_6H_4\text{-}CO_2\}\cdot\{HO_2C\text{-}C_6H_4\text{-}CO_2H\}_x\cdot H_2O_y$. *J. Am. Chem. Soc.* **2002**, 124(45): 13519-13526.

[111] Boutin A., Coudert F. X., Springuel-Huet M. A., Neimark A. V., Férey G., Fuchs A.H. The behavior of flexible MIL-53(Al) upon CH_4 and CO_2 adsorption. *J. Phys. Chem. C.* **2010**, 114(50): 22237-22244.

[112] Krause S., Bon V., Senkovska I., et al. A pressure-amplifying framework material with negative gas adsorption transitions. *Nature.* **2016**, 532(7599): 348-352.

[113] Fairen-Jimenez D., Moggach S. A., Wharmby M. T., Wright P. A., Parsons S., Düren T. Opening the gate: Framework flexibility in ZIF-8 explored by experiments and simulations. *J. Am. Chem. Soc.* **2011**, 133(23): 8900-8902.

[114] Brown J. W., Henderson B. L., Kiesz M. D., et al. Photophysical pore control in an azobenzene-containing metal-organic framework. *Chem. Sci.* **2013**, 4(7): 2858-2864.

[115] Ban V., Soloninin A. V., Skripov A. V., et al Pressure-collapsed amorphous $Mg(BH_4)_2$: An ultradense complex hydride showing a reversible transition to the porous framework. *J. Phys. Chem. C.* **2014**, 118(40): 23402-23408.

Chapter 2. Methodology

Abstract

The volumetric and gravimetric methods are the most common and well-developed techniques to characterize the gas adsorption properties and the porosity of porous materials. Diffraction methods are usually applied to determine the crystal structure or understand the structure evolution by in situ measurements, in order to give an explanation of properties. In this chapter, firstly the methodology of volumetric, gravimetric and diffraction methods will be presented in detail to understand the principles. Afterwards, we will introduce Rietveld refinement to process diffraction data collected upon gas adsorption, allowing to extract atom positions and occupancies of the guests, thus accessing adsorption phenomena both from micro- and macroscopic levels. Also, the synthesis of the material which we use in this work, γ*-*$Mg(BH_4)_2$*, will be presented.*

2.1. Gas Adsorption Measurements

Adsorption measurements are necessary to obtain the surface properties of porous materials. As described in the previous chapter, adsorption isotherms (isobars) are especially important results to investigate the adsorption-related phenomena and properties, such as surface area, porosity, pore volume, adsorbate capacity, adsorption entropy and enthalpy. To measure gas adsorption isotherms, there are usually two laboratory techniques: volumetric methods and gravimetric methods. These two methods have been developed and improved over many years, exhibiting the advantages of relatively uncomplex experiment, controllable errors and easy analysis of results.

2.1.1. Volumetric Methods

Volumetric methods can be easily implemented using a gas dosing-evacuating-system of known volume in which the temperature and pressure can be measured accurately. The theory on which the volumetric methods is based is the ideal / real gas law:

$$PV = (Z)nRT$$

where the P represents the pressure, V is the volume, n is the number of gas particles, R is universal gas constant, T is the temperature. Z represents the gas compressibility, of which $Z = 1$ when the gas is considered as ideal. However, in a real case, the gas compressibility is related to temperature and pressure conditions. So, to measure adsorption isotherms, the value of gas compressibility cannot be ignored. Usually, the tabulated compressibility or vey complex real equations of state are used for each gas, in a wide P-T range.

Volumetric methods can be performed in a numbers of way but both the varied and measured parameter that determines the amount of adsorbed gas is principally the pressure. Therefore, volumetric methods should be better termed as manometric methods[1]–[3]. In this work, all gas adsorption isotherms that are done by volumetric methods refer to manometric methods.

A schematic diagram of a basic manometric system is shown in Figure 1[4]. V_1 and V_2 (in this figure, V_2 represents the volume of the chamber excluding the sample volume) represent two known volumes, and valves A, B and C control the gas inlet and outlet. Samples are loaded in the volume V_2 and under the circumstance of an accurate temperature controlling system. First, the whole system is evacuated under vacuum. And subsequently valve A is open while the valves B and C are closed to let the gas fill volume V_1 with a certain pressure P_i. Afterwards, the valve A is closed and C is open to fill both volume V_1 and V_2. The loss in pressure (when the system reaches equilibrium, the final pressure is P_f) beyond which is caused by the volume change from V_1 to $(V_1 + V_2)$ will be assumed to be the result of gas uptake by samples in volume V_2.

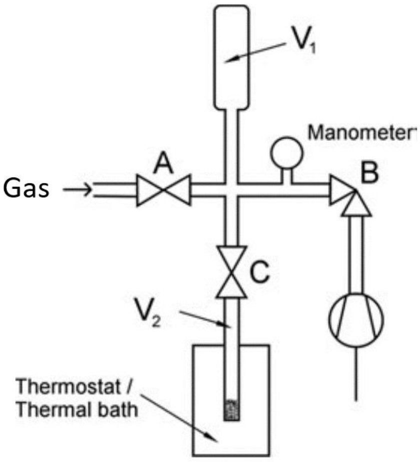

Figure 1. A schematic diagram of a basic manometric system of adsorption / desorption measurement[4].

So assuming all the system temperature, T is constant during the single-step measurement, the amount of gas adsorbed Δn can be express as the following:

$$\Delta n = \frac{P_i V_1}{Z_{i,T} RT} - \frac{P_f (V_1 + V_2)}{Z_{f,T} RT}$$

In this equation, $Z_{i,T}$ and $Z_{f,T}$ are the gas compressibilities at initial pressure and final pressure under temperature T, respectively. To continuously measure an adsorption isotherm, the subsequent step will use P_f and Δn as a starting point. As a conclusion, the total amount of gas uptake after m steps, n_m, is given by[4]:

$$n_m = \sum_{j=1}^{m} \left[\frac{P_{f,j-1,T} V_2}{Z_{f,j-1,T} RT} + \frac{P_{i,j,T} V_2}{Z_{i,j,T} RT} - \frac{P_{f,j,T} (V_1 + V_2)}{Z_{f,j,T} RT} \right]$$

Several steps are required in order to measure adsorption isotherms:

1) Sample pre-treatment

Some porous materials could possibly pre-adsorb H_2O or CO_2 from air at ambient condition and these molecules occupy the pore space, leading to inaccurate measurements of adsorption isotherms[5]. Therefore, an activation is necessary to “clean” the pore space. Usually the samples should be exposed to vacuum at a high temperature to desorb the molecules which are pre-adsorbed in the porous materials.

2) Determination of the sample volume

Since the volumes V_1 and V_2 are known in the system (shown in Figure 1), it is necessary to determine the sample volume by a pycnometry method. This method involves the measurement of the free volume of V_2 chamber, using a gas that is usually known to have no interaction with samples at given conditions, typically helium, to indirectly obtain the volume of the sample.

3) Adsorption isotherms measurements

After the steps 1) and 2), the isotherm measurements can be programmed based on the principle described above. At each pressure point, a time dependence of pressure is measured and fitted with a kinetic law in order to determine the (asymptotic) equilibrium pressure. The fitting is done regularly and automatically. Once the confidence level for the determination of the equilibrium pressure is attained, a point is fixed on the equilibrium pressure-composition diagram and the system injects a new portion of gas.

All the gas adsorption isotherms in this work that are done by manometric methods were performed on an IMI-HTP analyzer from Hiden Isochema (UK). It is designed to characterize hydrogen storage materials using manometric method up to pressures 200 bar, at a wide temperature range. Other gas physisorption, such as noble gases, N_2, CH_4 and C_2H_6 are also available to be measured on this analyzer.

Figure 2. Adsorption device, Hidden IMI-HTP analyzer that used in this work, picture taken from: https://hidenisochema.com/hiden-products/imi-htp/

2.1.2. Gravimetric Methods

In this thesis, the gravimetric method was not used, however, it is worth to mention this technique as it is another well-accepted method to measure gas adsorption isotherms. A gravimetric system is composed of a gas supply, a microbalance, vacuum pumps and adsorption vessel placed inside a thermostat, as shown in Figure 3[2]. Similarly to the manometric method, once the sample is pre-treated, the gas can be introduced at a certain pressure and the adsorption process can be monitored on the balance due to the adsorption of the gas, as well as the buoyancy of the sample in the environment of the surrounding gas. Stepwise increase of pressure can be carried out for the determination of isotherms.

Compared to the manometric method, the gravimetric one has larger errors when measuring light gases such as H_2. On the opposite, it is more sensitive and accurate on measuring gases or vapors with high molecular weight. Gravimetric method is less prone to errors of volume calibration, done by pycnometry for the volumetric techniques, and offers some complementarity given the very different nature of the measured parameter (weight compared to pressure for pycnometry). For example, gravimetry can use the difference between the mass of hydrogen and deuterium to make sure the weight gains are related as exactly double, to exclude the other sources of errors. On the other hand, gravimetric methods are prone to errors related to the strong interaction with impurities, for example residual water, becoming the main problem of this technique.

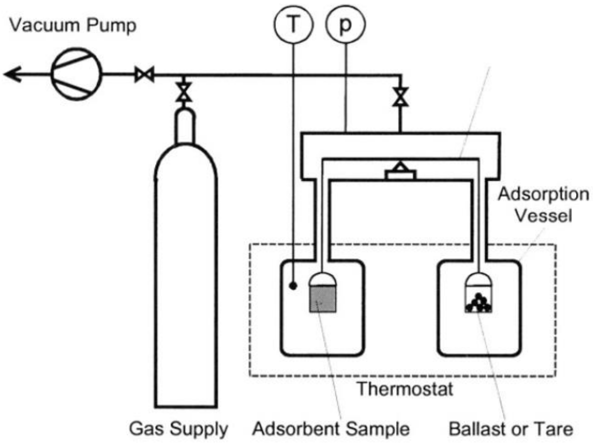

Figure 3. A schematic picture of a gravimetric system[2].

2.1.3. Modeling of Adsorption Isotherms

Adsorption isotherms are important characteristics of porous materials. They should be well understood and interpreted in order to optimize the overall adsorption mechanism and to develop an effective system[6]. Analytical approaches are numerous and well developed. For examples, Ayawei et al.[7] have applied linear and non-linear regression analysis for a number of adsorption isotherms, based on different numbers of parameters in one isotherm function. In our work, gas adsorption in γ-$Mg(BH_4)_2$ will be described with a simple Langmuir adsorption model.

Irving Langmuir presented his theory about adsorption onto a simple surface in 1918[8]. Due to his contribution to surface chemistry, he won the Nobel Prize in 1932. As described in his model, adsorption and desorption are reversible reactions:

$$A_{(gas)} + adsorbent \rightleftharpoons adsorbent \cdot \theta_A A$$

where A represents a gas, θ_A ($0 \leq \theta_A \leq 1$) is the proportion (occupancy) of the gas A in the adsorbent, i.e., the ratio of volume of gas adsorbed (V) to the volume of the surface of the adsorbent (V_m). Considering the equilibrium pressure of gas A is p_A, and the reaction equilibrium constant is K_{eq}, the Langmuir equation can be expressed:

$$\theta_A = \frac{V}{V_m} = \frac{K_{eq} p_A}{1 + K_{eq} p_A}$$

This formula is suitable to describe type I isotherms classified by IUPAC. When the pressure is very low, the gas uptake is proportional

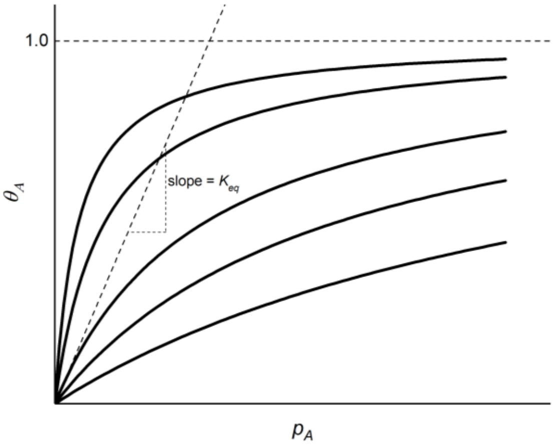

Figure 4. Graphical illustration of the Langmuir equation with different K_{eq}.

to the equilibrium pressure (Henry's law), $\theta_A = K_{eq}p_A$. While the pressure is very high ($\theta_A \approx 1$), the gas uptake is the single-layer adsorption capacity, which is independent of the pressure.

Experimentally, θ_A is also the ratio of gas uptake (y) to theoretical gas capacity, a, of an adsorbent. So the Langmuir equation can be transferred and applied in the following formula:

$$y = a \cdot \frac{K_{eq}p_A}{1 + K_{eq}p_A}$$

2.2. Diffraction Studies

2.2.1. Principles of X-ray Diffraction

Diffraction is one of physical phenomena occurring when an X-ray electromagnetic wave irradiates the crystal. The electrons around the atoms in the crystal are vibrated by the X-rays periodically changing electric field, so that each electron becomes a secondary wave source that emits spherical electromagnetic waves. The frequency of the emitted spherical wave is consistent with that of incident X-rays. Based on the periodicity of the crystal structure, the scattered waves of individual electrons in the crystal can interfere with each other and be superimposed, giving rise to discrete diffraction images.

1. Diffraction conditions (geometry)

The first expression historically developed is Bragg’s law, a simple mathematical formula that gives a relation between the crystal plane spacing d, the wavelength of X-rays λ, and the angle θ between X-ray and crystal lattice planes, as shown in the following equation and in Figure 5[9]:

$$2dsin\theta = n\lambda$$

where *n* is the diffraction order (*n* = 1, 2, 3…). It was first proposed in 1913 by Lawrence Bragg and his father William Henry Bragg[10] who were awarded Nobel Prize in 1915. This equation gives access to the interplanar distance, i.e., a microscopic information on the scale of atomic size. The three-dimensional version of the Bragg's equation is known as Laue's conditions, which have a graphical representation given by Ewald. The diffraction data are presented in so-called reciprocal space, and given the dimensionality of the space, requires the use of three indices (instead of only one, *n*, in Bragg's law), named *h*, *k* and *l*.

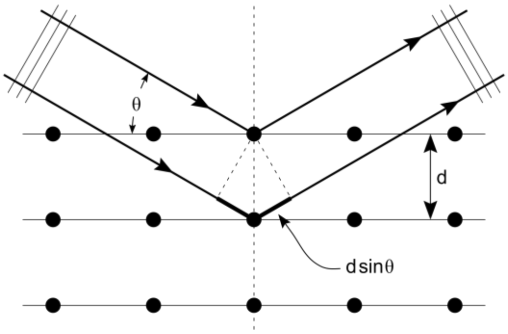

Figure 5. A schematic diagram of Bragg diffraction[9].

2. Diffraction intensity

The X-ray diffraction intensity of a crystal is determined by the type, number and arrangement of atoms in a unit cell of the crystal. To start, the electron at position A shown in Figure 6, scatters X-ray with the intensity at position P expressed as:

$$I_e = \frac{e^4 I_0}{2R^2 m^2 c^2}(1 + cos^2 2\theta)$$

where *e* and *m* are the charge and mass of an electron, respectively, *c* is the speed of light, I_0 is the incident X-ray intensity, 2θ is the diffraction angle, and *R* is the distance.

Assuming that all electrons in an atom (atomic number *Z*) are concentrated on one point, the scattering intensity of X-rays by such an

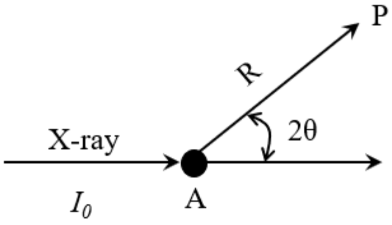

Figure 6. An electron is scattered under X-ray.

atom can be expressed as:

$$I'_a = Z^2 I_e$$

However, in actual situations, the scattering phase of each electron to X-ray is different, thus its intensity is reduced compared to that of all electrons concentrated at one point. Therefore, the scattering intensity of X-rays by actual atoms can be corrected by the scattering factor *f*, which decreases with increasing θ:

$$I_a = f^2 I_e$$

For a unit cell composed of *x* atoms, the diffraction intensity ($I_{(h\,k\,l)}$) produced in the ($h\ k\ l$) diffraction direction is not equal to the simple sum of the intensities produced by the *x* atoms.

$$I_{(h\,k\,l)} \neq \sum I_e f_j^2 = I_e |F(h\,k\,l)|^2$$

The structure factor, a complex number (or a vector) F($h\ k\ l$), is related to the distribution of atoms in the unit cell, namely the crystal structure, via a Fourier transformation. The intensity of the reflection can be expressed as a square of the structure factor and is related to the atomic coordinates as:

$$|F(h\,k\,l)|^2 = [\sum f_j cos2\pi\big(hx_j + ky_j + lz_j\big)]^2 + [\sum f_j sin2\pi\big(hx_j + ky_j + lz_j\big)]^2$$

where (x_j, y_j, z_j) are the fractional coordinates of atoms present within the unit cell. This equation reveals the connection between diffraction intensity and the atomic positions. Thus, the measurement of intensities of diffraction, allows to access the information about the distribution of atoms in the unit cell.

The inverse transformation is much more complex, though, since the intensities do not reveal the orientation (phase) of the F(*h k l*) vector, but only its magnitude. This prohibits a direct use of the inverse Fourier transformation, and thus a direct experimental access to the atomic coordinates (structure). This is known as a phase problem in crystallography, which has no exact solution. However, today there is a number of efficient methods allowing to either find the missing phase information (such as direct methods, but also Patterson method, isomorphous substitution, resonant methods etc.) and do the inverse Fourier transformation to visualize the structure; or to solve the structure by global optimization in direct space (Monte Carlo methods) or by charge flipping. The latter methods are computationally consuming but allow to focus directly on structure solution in direct space, drawing help from empirical information about molecular structure that is commonly available to the chemist.

In our work, the step that can be considered as structure solution was limited only to the location of a guest inside the pores of the crystalline material, having already a known crystal structure. This was done using program FOX[11], implementing global optimization in direct space.

2.2.2. X-ray Powder Diffraction

Crystalline powders can be considered as an ensemble of many fine single crystals in various orientations. Therefore, instead of obtaining diffraction spots, the powder diffraction yields rings which can be observed on the area detector, and each ring corresponds to a certain diffraction angle. A schematic diagram[12] and an example of an experimental results are shown in Figure 7.

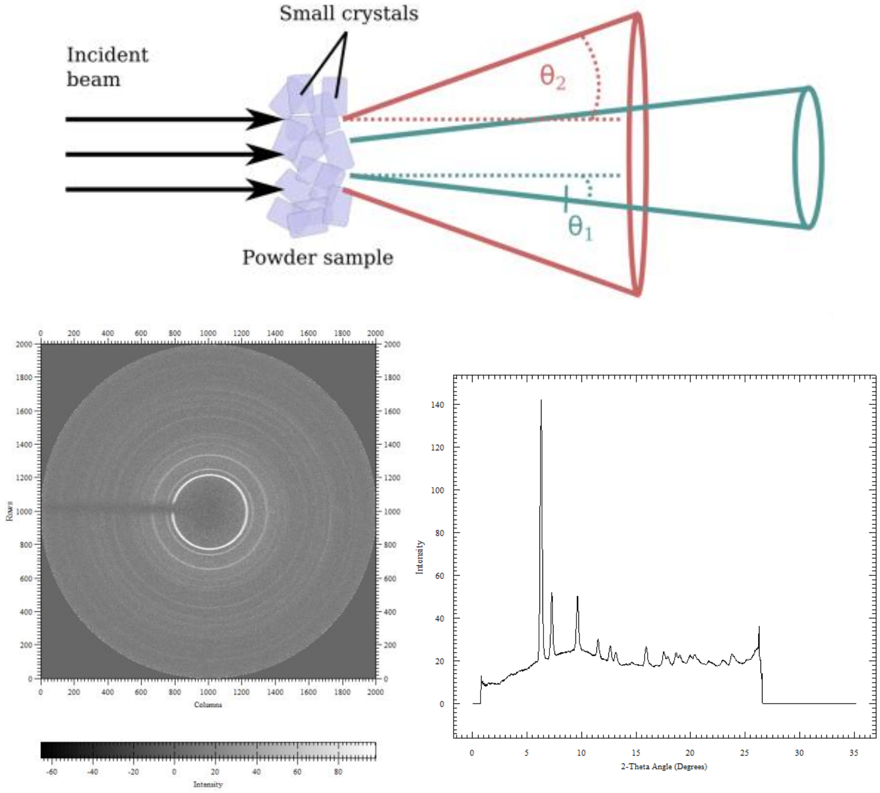

Figure 7. A schematic picture of powder diffraction[12] (**up**) with cones in red and green representing diffraction peaks having different *h k l* indices; and an example of powder diffraction rings for γ-$Mg(BH_4)_2$ and its integrated intensities observed in our lab, Data reduction was done using software FIT2D[13] (**bottom**).

2.2.3. X-ray Sources

X-rays were firstly discovered by Röntgen in 1895 while investigating the effects of high voltage electrical discharges in evacuated glass tubes[14]. In this work, we used two sources of X-rays: X-ray tubes (lab technique) and synchrotron radiation (done at the Swiss-Norwegian Beamlines, SNBL at the European Synchrotron Radiation Facility, ESRF).

1. X-ray tubes

In X-ray tubes, X-rays are generated by high-speed cathode electrons continuously bombarding the anode target materials, which is usually metallic Cu, Mo, W, or, Cr and so on. After the electron is accelerated in the electric field (usually ≥ 30 kV) and has enough energy, when it collides with the anode material, the electronic configuration of atoms will be excited and the de-excitation will produce characteristic radiation, among which are high-energy lines known as K_α and K_β. We use K_α band, that is separated using a focusing mirror, serving also as a monochromator. In addition, at high resolution, the K_α line can be seen to be a doublet, containing $K_{\alpha 1}$ and $K_{\alpha 2}$. They have very similar wavelength and can not be separated using a filter or a mirror. The mixed wavelength complicates the visual examination of data and of the refinement process, but can easily be taken account of in the structure refinement. The Table 1 shows the characteristic radiation wavelength of common target materials.

Table 1. the characteristic radiation wavelength of common anode materials.

Anode materials	Mo	Cu	Cr	Fe	Ag	Co	W
λ (K_α), Å	0.71	1.54	2.29	1.94	0.56	1.79	0.21

The basic X-ray diffraction data in this work were measured with our lab X-ray diffractometers consisting of two Incoatec X-ray generators (mixed Mo K_α radiation, weighted average $\lambda = 0.71073$ Å) with MAR345 image plate detectors. A microfocus beam setup consisting of an Incoatec source is used to measure single crystals. A high-brilliance Incoatec source with a larger beam is used to measure powder samples in capillaries (transmission mode). In the earlier stage of this work, we used rotating anode generator, with two exists equipped with focusing optics, producing similar beams to the ones from the Incoatec sources. The old setup required though expensive maintenance and regular repair. An Oxford Cryosystem is available for low temperature measurements (80 - 400 K) as well as a heat blower for high temperature conditions (RT - 800 K).

2. Synchrotron radiation

Compared to X-ray tubes, synchrotron radiation has several advantages for high resolution diffraction measurements, such as much more intense, highly collimated beam, tunable wavelengths and so on. It is the electromagnetic radiation emitted by electrons or positrons moving close to the speed of light when they change the direction of movement. This radiation was found on circular accelerators in 1947[15], which later were evolved specifically to the accelerators dedicated to X-ray production, named synchrotron sources.

Currently, the most widely used synchrotron radiation is its third generation. After the major upgrade (EBS), the ESRF is now the forth generation source. A schematic diagram of the installation is shown in Figure 8. The electron is accelerated first in linear accelerator, than in a booster ring and emitted into the storage ring. Undulators and wigglers allow to oscillate relativistic electrons to produce a strong X-ray beam. Subsequently, the radiation is modified by optical elements, hitting the sample to get the scattering registered. Several famous high-energy third generation synchrotron radiation facilities are ESRF in Europe (6 GeV), APS in the USA (7 GeV), and Spring-8 in Japan (8 GeV).

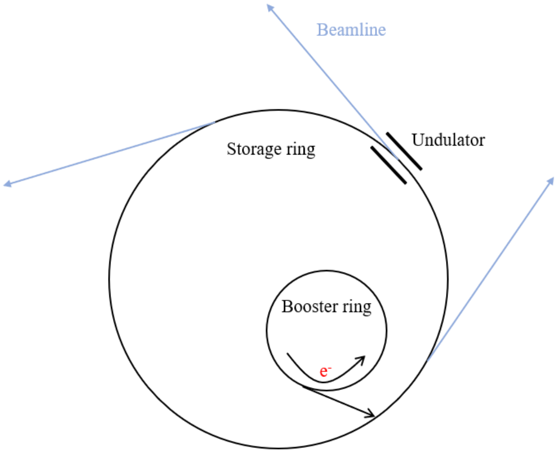

Figure 8. A schematic representation of a synchrotron (counter clockwise direction corresponds to the Spring-8 synchrotron, using positrons).

In this work, all the diffraction data collected upon gas adsorption were measured by X-ray diffraction at the SNBL beamline (BM01) at the ESRF, Grenoble (France). It is equipped with a pixel detector PILATUS2M detector (from Dectris, Switzerland), combing the advantages of pixel detector technology (low noise, fast readout, no correlation between pixels) with flexible goniometry and easy re-positioning of the detector and of the goniometer in vertical and horizontal directions.

2.2.4. Neutron Diffraction

Neutron diffraction is complementary to X-ray diffraction. It relies on the sample principles, namely the diffraction and interferences of waves (thanks to the particle – wave dualism) with the periodical materials such as crystals. Neutrons particularly interact with nuclei, which makes it very useful to determine the localization of light elements, or distinguish elements with similar number of protons, as each nucleus have a specific scattering length[16]. Due to the different states of spin of some nuclei, there is a very large incoherent scattering cross section, leading to a very high background noise in the measured neutron diffraction pattern. This is especially problematic for hydrogen atom (^1H). Therefore, deuterated materials are often used in neutron diffraction measurements.

In our case, we used γ-$Mg(^{11}BD_4)_2$ with double isotopic substitution, when the neutron powder diffraction (NPD) was performed both on the high resolution powder diffractometer BT1 at the NIST Center for Neutron Research (NCNR), and on the high resolution powder diffractometer E9 at the BER-II research reactor at the Helmholtz-Zentrum Berlin (HZB).

2.2.5. *In situ* Diffraction Measurements

In situ can be simply understood as “during the reaction procedure” in the chemistry field. Therefore, an *in situ* diffraction measurement contains a third parameter besides intensities and 2θ positions of peaks. The results show the evolution of diffraction patterns along this third parameter, such as temperature (T) or pressure (P) but can also be a function of time (t) at given P-T conditions.

Figure 9 is the schematic diagram of experimental setup of an *in-situ* synchrotron radiation X-ray powder diffraction (*in-situ* SR-XPD) of the experiment when we measured adsorption properties of γ-$Mg(BH_4)_2$ at the ESRF. A temperature control is usually a blower to heat up, as well as cold N_2 stream (sometimes cold He to reach extremely low temperature such as ~10 K) to get to low temperatures. A gas dosing system is connected to the sample in a capillary to easily dose different gases or apply vacuum on the sample. *In situ* T-dependent or P-dependent diffraction measurements can be performed to produce diffraction data, what in turn can reveal to the structure of the material at each P-T condition, as well as the amount of the adsorbed gas. The latter can be plotted as adsorption isobars or isotherms respectively, which in turn give access to adsorption thermodynamics.

An *in situ* t-dependent diffraction can be used to characterize the adsorption kinetics. This is a new methodology proposed in a collaboration between our group and the team at the SNBL/ESRF[17]. A sample is loaded in the capillary and pressurized with the adsorbate gas, which is not adsorbed by the sample at room temperature. The capillary is first staying out of the beam, while the blower is fixed on the desired temperature. At time zero, the capillary is quickly moved into the set position (exposed to the X-ray beam) which also provides a temperature necessary for an adsorption experiment. At the same time, the diffractometer starts to record approximately 10 000 diffraction powder patterns every 0.2 to 0.5 seconds. This amount of data allows to reach dynamic range necessary for detecting faster and slower processes, characterized by different activation energies. Thus data have to be collected both at short time scales (with high time resolution) and long time scales. Detailed analysis of thermodynamics and kinetics using the *in situ* data will be introduced in sub-Chapter 2.4.

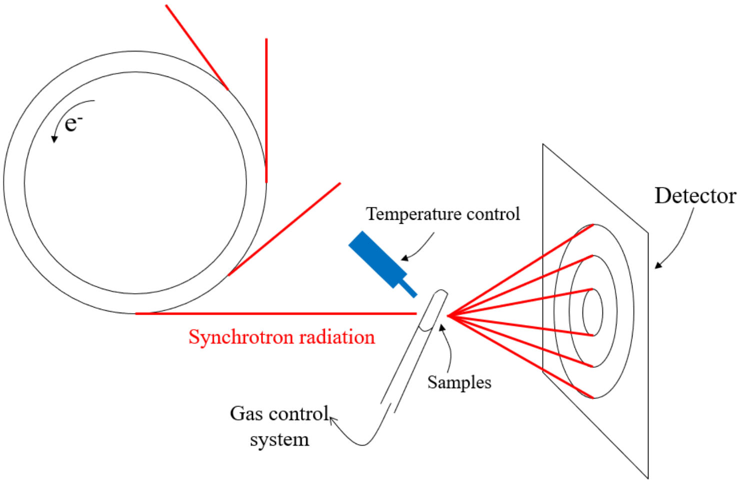

Figure 9. Schematic diagram of experimental setup of *in situ* diffraction measurements in ESRF. The temperature, data acquisition and the goniometer position are controlled automatically as a part of the experimental protocol.

2.3. Rietveld Refinement

Rietveld refinement can be considered as a very complex curve fitting, since a diffraction pattern can be thought of as a set of peaks having their positions and intensities. These are linked to a number of variables characterizing the structure (such as atomic positions, cell parameters) and the experimental profile (such as profile and background information). This refinement method was first proposed the group later joined by H. M. Rietveld who implemented this method in his code for structure refinement applied to NPD data[18]. The Rietveld refinement is based on the assumption of the crystal structure model expressed via structural parameters, combined with a certain peak shape function to calculate the diffraction pattern, and subsequently adjust the structural parameters and peak shape parameters to make the calculated diffraction pattern coincide with the experimental diffraction pattern. The method is a modification of the least square method used for single crystal diffraction, taking care of the peak overlap in the powder diffraction. It is aiming to determine to the best possible, using the experimental data and the approximate model, all the structural information, i.e., unit cell parameters, atomic positions and occupancies, temperature factors and so on. In this work, we refine and extract mostly the occupancies of gas molecules in pores, using diffraction powder patterns measured under variable P or T to subsequently obtain adsorption isotherms or isobars, as well as to get adsorption kinetics curves, from time dependences. Also, we are analyzing the changes of the guest positions, revealing in some cases quite unexpected reorganizations.

To evaluate the quality of the refinement results, the least squares method is usually used, i.e. a minimization of M, a difference between calculated powder profile intensity, Y_c and observed powder pattern intensity, Y_o, given by the following equation:

$$M = \sum w_i (Y_o - Y_c)^2$$

where w_i is the specific weight. And Y_c is the result of convolution of various factors that affect peak intensity. At any 2θ, Y_c can be simply expressed as:

$$Y_c = Y_b + \sum_{h\,k\,l} G_{h\,k\,l} * I_{h\,k\,l}$$

where Y_b is the intensity of background, $G_{k\,h\,l}$ is the peak shape function, for example, Gauss, Lorentz, Viogt, Pearson-VII, or Pseudo-Voigt, $I_{h\,k\,l}$ is integrated intensity of diffraction peak from ($h\ k\ l$).

Several factors can be used to evaluate the refinement results:

1. Profile Factor:

$$R_p = \frac{\sum |Y_o - Y_c|}{\sum Y_o}$$

2. Weighted Profile Factor:

$$R_{wp} = [\frac{\sum w_i(Y_o - Y_c)^2}{\sum w_i Y_o^2}]^{1/2}$$

3. Expected Weighted Profile Factor:

$$R_{exp} = [\frac{N - P}{\sum w_i Y_o^2}]^{1/2}$$

4. Reduced chi-square:

$$\chi^2 = \frac{\sum w_i(Y_o - Y_c)^2}{N - P} = (\frac{R_{wp}}{R_{exp}})^2$$

$(N - P)$ is the number of degrees of freedom. The value of R_{wp} and R_p should be as low as possible (acceptable when < 15 %), and the value of χ^2 should be close to 1.

To obtain accurate refinement results, high quality diffraction data is required. For example, NPD can help to precisely localize the position and synchrotron radiation can provide a high signal-to-noise ratio. And measuring diffraction information at high angles can also help to improve the precision of refinement.

In this work, all Rietveld refinements were performed by the Fullprof Suite[19], which is developed for Rietveld analysis of neutron and X-ray powder diffraction data. It is formed by a set of various crystallographic programs, including WinPLOTR, Fullprof, EdPCR, etc. It also allows a sequential refinement to run automatic refinement against a batch of *in situ* diffraction data and to plot the results.

2.4. Thermodynamics and Kinetics of Gas Adsorption

2.4.1. Thermodynamic Properties

In the adsorption field, thermodynamic properties mainly refer to the enthalpy of adsorption (or an isosteric heat of adsorption), $\varDelta H_{ads}$. It is a parameter to indicate the strength of interaction between adsorbates and adsorbents, but indirectly taking into account the other interactions, like guest-guest repulsion. The value of the adsorption enthalpy is equal to the heat released during the adsorption. There is a number of ways to determine the enthalpy of adsorption, while the most common way, which is called isosteric method, is to calculate the enthalpy by two adsorption isotherms (isobars) at two different temperatures (pressures), using a Clausius - Clapeyron equation:

$$\frac{d(lnP)}{d(1/T)} = \frac{\Delta H_{ads}}{R}$$

where R is the ideal universal gas constant. Using the conditions for the equal loading with a gas, (T_1 and P_1) and (T_2 and P_2), this equation can be practically transformed into:

$$\Delta H_{ads} = \frac{RT_1T_2}{T_2 - T_1}\ln\left(\frac{P_2}{P_1}\right)$$

This expression applies for a given loading, equal in two experiments, done either along two isotherms or two isobars. For each loading the heat should be determined, finally plotting the $\varDelta H$ as a function of composition (loading).

Another way is using van’t Hoff equation to calculate enthalpy of adsorption when a series of different-temperature isotherms is measured:

$$ln\, K_{eq} = -\frac{\varDelta H_{ads}}{RT} + \frac{\varDelta S}{R}$$

where K_{eq} is the reaction equilibrium constant. Drawing the linear curve of lnK_{eq} versus $1/T$, and $-\varDelta H_{ads}/R$ is expressed as the slope.

For isobars we use Logistic function to fit the loading as a function of temperature:

$$y = A_2 + \frac{A_1 - A_2}{1 + (\frac{T}{x_0})^p}$$

The physically meaning of logistic function for an isobar, A_1 is the final value of the maximum uptake. A_2 is an initial value for correction where $y(\infty)$ should be 0. x_0 represents the half-filled temperature.

The obtained analytical expression allows to interpolate the data points smoothly, calculating for each small loading step the T conditions that for two experimental isobars. This interpolation is fed into the Clausius-Clapeyron equation, providing ΔH_{ads} versus loading, you can see the example in the two Chapters describing Ar and CH_4/C_2H_6 adsorption respectively. The numerical interpolation provides similar values but is affected by noise, the latter is smoothened when using the analytical function.

Another approach to obtain thermodynamics of adsorption from diffraction method has been reported by Dovgaliuk et al in 2017[20]. They studied N_2 and C_2H_6 adsorption isobars by γ-$Mg(BH_4)_2$ and water uptake by MIL-91(Ti), and derived a thermodynamic description, based on Gorsky-Bragg-Williams approach for the lattice-gas Ising model, allowing to determine the thermodynamic parameters such as enthalpy, entropy and adsorption cooperativity from only one isobar. The expression used is following:

$$T = \frac{\Delta H_i - \Gamma_i(1 - 2\gamma_i)}{\Delta S_i - Rln(\frac{1 - \gamma_i}{\gamma_i})}$$

The subscript i is associated with guest adsorption by the site I, Γ is cooperativity, γ is a fraction of the adsorbed guest molecules. By fitting one single isobar with this expression, one can obtain ΔH, ΔS and Γ. In particular, the temperature of a half-filled (when γ_i =0.5) states gives an estimate of the ratio of enthalpy to entropy:

$$T_{1/2} = \frac{\Delta H_i}{\Delta S_i}$$

In another publication by Dovgaliuk et al[21], quasi-equilibrium and non-equilibrium Kr adsorption isobars by γ-$Mg(BH_4)_2$ were studied by diffraction method. The equilibrium isobars yielded thermodynamics parameters rationalized with the noncooperative lattice gas model,

$$\ln\left(\frac{\gamma}{1-\gamma}\right) = -\frac{\Delta H}{RT} + \frac{\Delta S}{R}$$

while the non-equilibrium isobars were used to estimate kinetics parameters (such as activation energy) analyzing the kinetic hysteresis, using a modified mean-field model adopted for the Arrhenius kinetics:

$$\alpha(T) = \gamma_{eq}(T) - \left(\gamma_{eq}(T) - \gamma_0\right)\exp\left(-\frac{A}{\beta} I(T, T_0, E_a)\right)$$

where β is temperature ramp rate, in K/min, the integral function in the exponent is:

$$I(T, T_0, E_a) = \int_{T_0}^{T} e^{-E_a/Rx} dx$$

This work exhibits a transition from the study of thermodynamics using equilibrium isotherms and isobars, to understanding that kinetics may influence these data to the point the kinetic hysteresis appears. This opens a door to estimate the activation barriers, but it should be more considered as a preliminary step. The dedicated study of kinetics must be done and fixed P-T conditions, but following the time coordinate. This is described in detail in the next sub-Chapter.

2.4.2. Kinetic Properties

The kinetic properties determine the rate of adsorption. From *in situ* *t*-dependent diffraction measurements (detailed measurements can be seen in Chapter 2.2.5), we can clearly observe different times of adsorption to the saturation for different *P*-*T* conditions. Measurement of kinetic data at different temperatures allow to attempt applying the Arrhenius equation, giving access to the activation energies[17]. This requires fitting the time resolved diffraction data with one or several exponents to describe the asymptotic behavior of the saturation. One has to take into account a possible diffraction damage, which is also affecting the capacity at saturation, showing time dependence (proportional to the exposure dose).

One way to approach the data analysis of t-dependent gas occupancies is the use a modified Kolmagorov-Avrami model[22],[23], which can be used to describe the kinetics of different chemical reactions[24]:

$$q(t) = q_{max}\left(1 - e^{(-kt)^n}\right)$$

where q_{max} is the saturated occupancy under given (P, T) condition, k in this expression represents the reaction kinetic constant, n is the order of the reaction. The value of k and n can be obtained by curve fitting.

To acquire the activation energy, the linear transformed Arrhenius equation is applied:

$$ln\, k = \frac{-E_a}{RT} + ln\, A$$

According to several kinetics measurements at different temperatures, the activation energy E_a can be calculated from the slope of the linear Arrhenius expression.

The key point to get correct activation energy is to find the best mathematical model $q(t)$ that represents the dynamics adsorption data. Landaverde-Alvarado et al[25] studied the kinetics of CO_2 sorption in a Zn-MOF that can be well described by linear driving force model (LDF), which considers the differences in concentration between empty and gas-loaded phases are the driving force for adsorption:

$$\frac{\partial q}{\partial t} = k_t(q^* - q)$$

q^* is the equilibrium concentration. They also fit the kinetic data to a micropore diffusion model ($k_t = 15D_s/R_p^2$) to confirm that diffusion inside the pores is the rate limiting step for adsorption.

Sometimes a multiple exponents model is needed to fit the kinetic data because there may be more than one diffusion barrier. Fletcher et al[26] studied adsorption kinetics by a Ni-MOF templated with methanol and ethanol (denoted as **M** and **E** respectively) and they found that neither methanol nor ethanol kinetic data on **M** followed the LDF model. So they proposed a double exponential (DE) model for **M**, assuming that there are two diffusion barriers which are thought to be through the pore window and along the pore cavities. The DE model is given below and the difference of LDF model and DE model is given in Figure 10.

$$q(t) = q_{max}\left[A_1\left(1 - exp(-k_1 t)\right) + A_2\left(1 - exp(-k_2 t)\right)\right]$$

A_1 and A_2 are related contributions for two diffusion barriers, with $A_1 + A_2 = 1$.

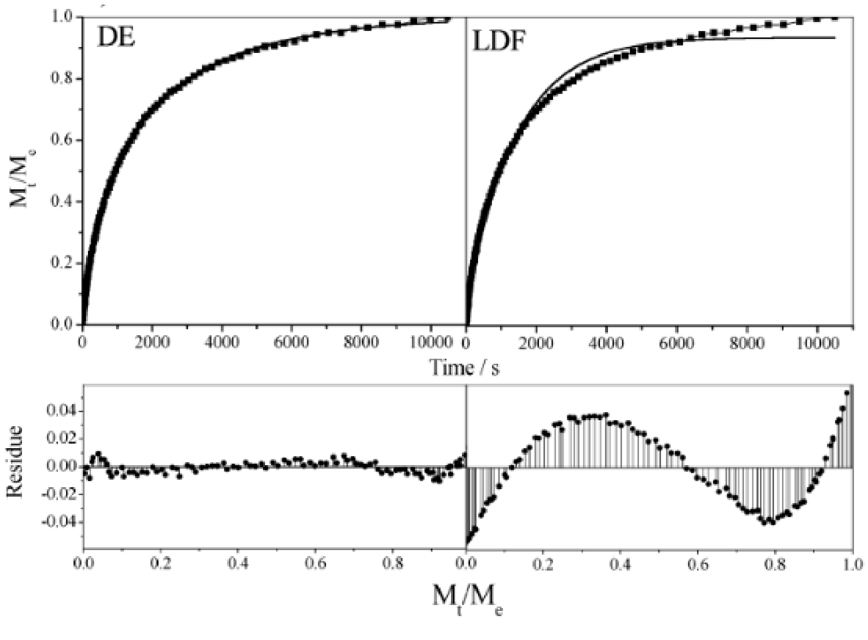

Figure 10. A comparison of adsorption kinetics fitting for adsorption of ethanol on porous structure **M** with two different models, double exponential model and linear driving force model[26].

2.5. Synthesis of γ-$Mg(BH_4)_2$

In this work, the main material we use is γ-$Mg(BH_4)_2$. As introduced in Chapter 1.4, magnesium borohydride has more rich polymorphism than any other metal hydrides, however, only its gamma phase shows a porous structure. The synthesis of *γ*-$Mg(BH_4)_2$ was performed using a modified procedure from reference[27]. The dimethyl sulfide complex of borane ($BH_3 \cdot DMS$) and di-*n*-butyl-magnesium (1M in heptane, 10 ml, 10 mmol) were taken from Sigma-Aldrich without further purification. Excess of $BH_3 \cdot DMS$ (3 ml, 31 mmol) was loaded in a modified 150 ml Schlenk flask (with a filter allowing easy vacuum filtration under inert atmosphere) equipped with a magnetic stirrer and dissolved in 15 ml toluene. The flask was filled with argon by several short vacuum/argon cycles before the $BH_3 \cdot DMS$ is added to the flask. Stoichiometric amounts of di-*n*-butyl-magnesium (1M in heptane, 10 ml, 10 mmol) was added dropwise to the solution. The reaction was stirred for two hours before filtrating the white precipitate and rinsing away the solvent with toluene 3×8 ml. The precipitate was dried under vacuum in the Schlenk line for 16 hours to get $Mg(BH_4)_2 \cdot \frac{1}{2}DMS$. Then the flask was placed in a silicon oil bath and heated to 343 K for drying under vacuum by a turbomolecular pump reaching residual pressures down to 10^{-5} mbar for over 60 hours to get γ-$Mg(BH_4)_2$. The quality check by diffraction of $Mg(BH_4)_2 \cdot \frac{1}{2}DMS$ and γ-$Mg(BH_4)_2$ is shown in Figure 11 up and bottom, respectively. The isotopic enriched γ-$Mg(^{11}BD_4)_2$ for NPD measurements was synthesized in the same strategy by using a $^{11}BD_3 \cdot DMS$ complex. The usual yield of each batch of γ-$Mg(BH_4)_2$ is about 50% to 60%, all samples are diffraction-pure.

It is worth mentioning that for every batch of γ-$Mg(BH_4)_2$, there is a proportion of non-porous amorphous phase of $Mg(BH_4)_2$ existing. This phase is invisible under diffraction and has no contribution to gas adsorption. A N_2 adsorption isotherm will be performed by manometric method to calibrate the proportion of gamma phase, as the capacity of N_2 adsorbed in γ-$Mg(BH_4)_2$ is known as γ-$Mg(BH_4)_2 \cdot \frac{2}{3}N_2$[27], namely every mole of γ-$Mg(BH_4)_2$ could maximumly adsorbs 2/3 mole of N_2.

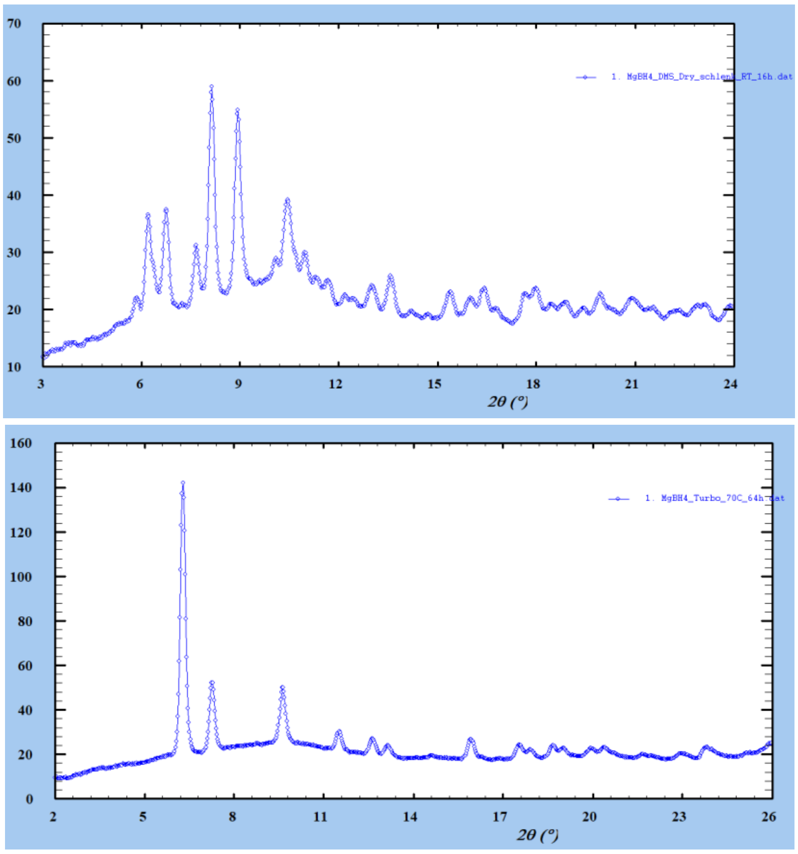

Figure 11. Diffraction powder patterns of $Mg(BH_4)_2$·½DMS (**up**) and γ-$Mg(BH_4)_2$ (**bottom**), data collected by MAR345 with a wavelength λ = 0.71073 Å and shown in WinPLOTR[28].

2.6. References

[1] Rouquerol J., Rouquerol F., Llewellyn P., Maurin G., Sing K. S. *Adsorption by powders and porous solids: Principles, methodology and applications*. Academic press. 2013.

[2] Keller J. U., Staudt R. *Gas adsorption equilibria: experimental methods and adsorptive isotherms*. Springer Science & Business Media. 2005.

[3] Blach T. P., Gray E. M. Sieverts apparatus and methodology for accurate determination of hydrogen uptake by light-atom hosts. *J. Alloys Compd.* **2007**, 446: 692-697.

[4] Broom D. P. *Hydrogen Storage Materials: The Characterisation of Their Storage Properties*. Springer Science & Business Media. 2011.

[5] Broom D. P., Hirscher M. Irreproducibility in hydrogen storage material research. *Energy Environ. Sci.* **2016**, 9(11): 3368-3380.

[6] El-Khaiary M. I. Least-squares regression of adsorption equilibrium data: comparing the options. *J. Hazard. Mater.* **2008**, 158(1): 73-87.

[7] Ayawei N., Ebelegi A. N., Wankasi D. Modelling and Interpretation of Adsorption Isotherms. *J. Chem.* **2017**, 1-11.

[8] Langmuir I. The adsorption of gases on plane surfaces of glass, mica and platinum. *J. Am. Chem. Soc.* **1918**, 40(9):1361-1403.

[9] Bragg W. H. IX. Bakerian Lecture. X-rays and crystal structure. *Philos. Trans. R. Soc. London. Ser. A, Contain. Pap. a Math. or Phys. Character.* **1915**, 215(523-537): 253-274.

[10] Bragg W. H., Bragg W. L. The reflection of X-rays by crystals. *Proc. R. Soc. London. Ser. A, Contain. Pap. a Math. Phys. Character.* **1913**, 88(605): 428-438.

[11] Favre-Nicolin V., Černý R. FOX ‘free objects for crystallography’: a modular approach to ab initio structure determination from powder diffraction. *J. Appl. Crystallogr.* **2002**, 35(6): 734-743.

[12] Mabey P. *A study on dense plasmas using molecular dynamics and X-ray scattering techniques.* Doctoral dissertation, University of Oxford. **2016**.

[13] Hammersley A. P. FIT2D: a multi-purpose data reduction, analysis and visualization program. *J. Appl. Crystallogr.* **2016**, 49(2): 646-652.

[14] Röntgen W. C. Uber eine neue Art von Strahlen. Sitzungsber. *Phys. Med. Ges. Wurtzb.* 1895, 9: 132-141.

[15] Elder F. R., Gurewitsch A. M., Langmuir R. V, Pollock H. C. Radiation from electrons in a synchrotron. *Phys. Rev.* **1947**, 71(11): 829.

[16] Willis B. T., Carlile C. J. *Experimental neutron scattering*. Oxford University Press. 2017.

[17] Dovgaliuk I., Senkovska I., Li X., Dyadkin V., Filinchuk Y., Chernyshov D. Kinetic barriers and microscopic mechanisms of noble gas adsorption by nanoporous γ-$Mg(BH_4)_2$ obtained by means of sub-second X-ray diffraction. *Angew. Chem. Int. Ed.* **2021**, 60(10): 5250-5256.

[18] Rietveld H. M. Line profiles of neutron powder-diffraction peaks for structure refinement. *Acta Crystallogr.* **1967**, 22(1): 151-152.

[19] Rodríguez-Carvajal J. Recent advances in magnetic structure determination by neutron powder diffraction. *Phys. B Condens. Matter.* **1993**, 192(1): 55-69.

[20] Dovgaliuk I., Nouar F., Serre C., Filinchuk Y., Chernyshov D. Cooperative adsorption by porous frameworks: diffraction experiment and phenomenological theory. *Chem. - A Eur. J.* **2017**, 23(70): 17714-17720.

[21] Dovgaliuk I., Dyadkin V., Donckt M. V., Filinchuk Y., Chernyshov D. Non-isothermal kinetics of Kr adsorption by nanoporous γ-$Mg(BH_4)_2$ from in situ synchrotron powder diffraction. *ACS Appl. Mater. Interfaces.* **2020**, 12(6):7710-7716.

[22] Avrami M. Close kinetics of phase change. *J. Chem. Phys.* **1939**, 7: 1103-1112.

[23] Kolmogorov A. N. On the statistical theory of the crystallization of metals. *Bull. Acad. Sci. USSR, Math. Ser.* **1937**, 1(3): 355-359.

[24] Serna-Guerrero R., Sayari A. Modeling adsorption of CO_2 on amine-functionalized mesoporous silica. 2: Kinetics and breakthrough curves. *Chem. Eng. J.* **2010**, 161(1): 182-190.

[25] Landaverde-Alvarado C., Morris A.J., Martin S.M. Gas sorption and kinetics of CO_2 sorption and transport in a polymorphic microporous MOF with open Zn (II) coordination sites. *J. CO2 Util.* **2017**, 19: 40-48.

[26] Fletcher A.J., Cussen E. J., Bradshaw D., Rosseinsky M. J., Thomas K. M. Adsorption of gases and vapors on nanoporous Ni_2(4,4′-Bipyridine)$_3(NO_3)_4$ metal-organic framework materials templated with methanol and ethanol: Structural effects in adsorption kinetics. *J. Am. Chem. Soc.* **2004**, 126(31): 9750-9759.

[27] Filinchuk Y., Richter B., Jensen T.R., Dmitriev V., Chernyshov D., Hagemann H. Porous and dense magnesium borohydride frameworks: Synthesis, stability, and reversible absorption of guest species. *Angew. Chem. Int. Ed.* **2011**, 50(47): 11162-11166.

[28] Rodriguez-Carvajal J., Roisnel T. WinPLOTR: a Windows tool for powder diffraction patterns analysis. *Mater. Sci. Forum.* 2001, 378(381): 118-123.

Chapter 3. Guests Rearrangement and Thermodynamics from Gas Adsorption Crystallography

Xiao Li[1]*, Mathieu Vander Donckt*[1]*, Iurii Dovgaliuk*[2,3]*, Dmitry Chernyshov*[2]*, Michael Heere*[4]*, Matthias Frontzek,*[5] *Simon Kimber,*[5] *Hai-Wen Li*[6] *and Yaroslav Filinchuk*[1*]

[1]Institute of Condensed Matter and Nanosciences, Université Catholique de Louvain, place L. Pasteur 1, B-1348 Louvain-la-Neuve, Belgium

[2]Swiss-Norwegian Beamlines at the European Synchrotron Radiation Facility, 71 avenue des Martyrs, Grenoble, 38000, France

[3]Institut des Matériaux Poreux de Paris, UMR 8004 CNRS, Ecole Normale Supérieure, Ecole Supérieure de Physique et de Chimie Industrielles de Paris, PSL Université, Paris, 75005, France

[4]Institute for Applied Materials – Energy Storage Systems (IAM–ESS), Karlsruhe Institute of Technology (KIT), Hermann–von–Helmholtz–Platz 1, 76344 Eggenstein–Leopoldshafen, Germany

[5]Neutron Scattering Division, Oak Ridge National Laboratory, 1 Bethel Valley Rd., Oak Ridge, Tennessee 37831, USA

[6]Hefei General Machinery Research Institute, 888 West Changjiang Road, Hefei 230031 Anhui Province, China

Abstract

The rational design of porous framework materials is of high demand for potential applications in storage, separation and delivery of guest molecules. The progress often depends on finding relationships between the crystal structure and the energetics of guest interactions within the pores. Here we show that argon adsorption in a porous γ-$Mg(BH_4)_2$ *demonstrates an isobar suggesting a consecutive occupation of two sites, while synchrotron X-ray and neutron powder diffraction reveal a gradual rearrangement of guests within the pores. At low loadings, the Ar atoms take the center of the pocket, while at higher loadings they move to the aperture, allowing 2 Ar atoms per pocket. This behavior is governed by short guest-guest contacts forming within the quasi-1D porous channel; a phenomenological description based on Ising-like lattice gas approach is given, reproducing well the Ar site redistribution. Adsorption isobars and isotherms are obtained directly from in situ diffraction, via refinement of guest occupancies. They are fitted analytically, yielding various thermodynamic parameters of adsorption. Thus, we obtain both micro- and macroscopic pictures of gas-solid interaction in a complex system from the same crystallographic experiments.*

3.1. Introduction

Material science of porous coordination polymers became state-of-the-art research field in the structural chemistry during the last three decades[1][2]. Particularly, metal organic frameworks (MOFs) and other porous frameworks attract much attention for potential applications in storage, separation and delivery of the guest molecules of interest[3][4]. The rationalization of the relationships between their crystal structure and guest uptake is critical for the design of such porous materials[5]. In this respect, the most essential characterization of their properties relies on gas adsorption isotherms studies[6]. This classical method gives an overall picture of the framework properties, which can be problematic for interpretation without complementary structural investigation upon guest uptake[7]. In particular, this can be the case when adsorption is accompanied by large framework flexibility[8][9] or negative gas adsorption[10]. The recent development of X-ray and neutron diffraction methods allows to probe the porous materials during gas adsorption at fixed temperature and pressure by taking snapshots of the crystal structure at certain points of an isotherm with monitoring the phase transitions during gas adsorption[11]. Such crystallographic studies have another important advantage to characterize the behavior of the guest uptake within the individual pores of the crystal structure[12][13], while the isotherm studies by bulk methods (volumetric or gravimetric) give access to a total gas uptake. Our recent investigations also show the possibility to estimate the thermodynamics parameters of such individual adsorption sites from variable temperature in situ powder X-ray synchrotron diffraction (PXRSD) combining it with appropriate phenomenological models[14]. Also, diffraction is specific to a particular crystalline phase, while data from bulk methods have to be corrected for a difficult-to-estimate amorphous phase fraction[15].

In this work we illustrate the application of variable-temperature PXRSD and neutron powder diffraction (NPD) to describe both structure and properties of a system where a complex (gradual) rearrangement of guest molecules occurs, with a focus on thermodynamics and guest-guest interactions. This was done for Ar adsorption in γ-$Mg(BH_4)_2$[16], a porous hydridic framework possessing quasi-1D channels. Due to the comparable atomic scattering powers of the guest molecules (Ar with $Z = 18$) and the host framework (Mg with $Z = 12$), X-ray diffraction yields very reliable data on the guest uptake, but most importantly, simultaneously providing the position of guests along the adsorption isobars and isotherms. This reveals guest-guest repulsion driven phenomena, which we characterized thermodynamically, and also using a phenomenological theory based on Ising-like approach. Complementary volumetric experiments were also done to validate the diffraction-based methodology and to point out the advantages.

3.2. Experimental Details

Synthesis of γ-$Mg(BH_4)_2$. The synthesis of γ-$Mg(BH_4)_2$ was performed using a modified procedure from the Reference[16]. Dimethyl sulfide complex of borane ($BH_3{\cdot}DMS$) and di-*n*-butyl-magnesium (1M in heptane, 10 ml, 10 mmol) were used from Sigma-Aldrich without further purification. Excess of $BH_3{\cdot}DMS$ (3 ml, 31 mmol) was loaded in a 150 ml Schlenk flask (modified with a filter allowing easy vacuum filtration under inert atmosphere) equipped with a magnetic stirrer and dissolved in 15 ml toluene. The flask was filled with argon by several short vacuum/argon cycles before the $BH_3{\cdot}DMS$ is added to the flask. Stoichiometric amounts of di-*n*-butyl-magnesium (1M in heptane, 10 ml, 10 mmol) was added dropwise to the solution. The reaction mixture was stirred for two hours before filtrating the white precipitate and rinsing away the solvent with toluene, 3×8 ml. The precipitate was dried under vacuum on a Schlenk line for 16 hours to get $Mg(BH_4)_2{\cdot}\frac{1}{2}DMS$. Then the flask was placed in a silicon oil bath and heated to 343 K. Solvent removal was done by using a turbomolecular pump reaching residual pressures down to 10^{-5} mbar for 60 hours, yielding crystalline

γ-Mg(BH$_4$)$_2$ containing some amorphous fraction.

A sample with double isotopic substitution, γ-Mg(^{11}BD$_4$)$_2$, containing ^{11}B and deuterium, was prepared for NPD experiments, starting from ^{11}BD$_3$·DMS.

***In situ* powder X-ray synchrotron diffraction (PXRSD) studies.** All the synchrotron powder diffraction data were collected with PILATUS@SNBL diffractometer[17] located at BM01 station from the Swiss-Norwegian Beamlines (SNBL) in the European Synchrotron Radiation Facility (ESRF, France). The 2D images were azimuthally integrated using PILATUS@SNBL software, calibrated with pyFAI on LaB$_6$ standard[18]. The capillaries with the samples were fixed to a gas dosing system, equipped with an electronic manometer (0.01 bar accuracy). For structural and thermodynamic characterization the series of isobar and isotherm experiments have been performed. The isobar experiments at p(Ar) = 1 and 10.5 bar were done using synchrotron radiation with λ = 0.74580 Å from 90 to 300 K and from 130 to 350 K, respectively. The temperature was linearly increased at the 5 K/min rate (heating and/or cooling) using Oxford Cryostream 700+.

The isotherm experiments were done at T = 150 K and 200 K, using synchrotron radiation with λ = 0.68660 Å. Several pressures of working gas, p(Ar), were stepwise applied to the sample in the capillary. At each pressure point, the adsorption/desorption diffraction data were measured every five minutes until equilibrium was reached (no changes of diffraction intensities observed).

Neutron Powder Diffraction (NPD) studies. NPD data were collected at the instrument HB-2C Wide Angle Neutron Diffractometer Squared (WAND^2), which is a neutron diffractometer with a position sensitive detector and oscillating collimator at the High-Flux-Isotope Reactor (HFIR) at Oak Ridge National Laboratory (ORNL), Oak Ridge, TN, USA[19]. The take-off angle is fixed at 51.5° and in combination with the Ge-monochromator (113) reflection a wavelength of λ = 1.482 Å was used. The use of sample with double isotopic substitution, γ-Mg(^{11}BD$_4$)$_2$, allowed to avoid difficulties related to adsorption and incoherent scattering. The sample holder was a cylindrically shaped Al sample holder (Al Bragg peaks were omitted in the refinements). A custom-made high-pressure rig was employed for Ar pressure fixed at 1 bar. The sample holder was inserted in a standard orange cryostat and the exposure time was fixed at 30 min at each of the 24 discrete temperatures between 292 K and 88.9 K. All (sequential) Rietveld refinement were made with the Fullprof software[20]. Further neutron powder diffraction measurements are planned with other small gas molecules within the frame of the "Energy research with Neutrons (ErwiN)" instrument at the MLZ, Germany[21].

Crystal structure determination and refinement. To localize Ar atoms inside the pores of γ-$Mg(BH_4)_2$, the atomic positions of the empty framework have been placed and fixed. The PXRSD data characterizing the state of the highest loading (1 bar and 90 K) was used to determine two positions of Ar atoms, see Figure. S1 and Tab. S1. The variable occupancies of guests were retained during the global optimization in FOX[22]. The calculations consistently resulted in two independent Ar atoms, located at the crystallographic positions *32e* with (*x x x*) coordinates, one is close to the center of the pore pocket, the other – closer to the aperture. The sequential variable-temperature refinement of the Ar atoms occupancies was performed using Fullprof[23], with the refinement of overall isotropic atomic displacement parameters and occupancies of Ar atoms. The same models were used for the isobaric and isothermal diffraction experiments, as well as for NPD data.

Volumetric physisorption measurements. The isotherms adsorption of nitrogen and argon were carried out with IMI-HTP analyzer from Hiden Isochema (UK), which ensures a high thermal stability and accurate pressure measurement. 1.92 mmol of γ-$Mg(BH_4)_2$ sample was loaded in the sample holder and 190 K adsorption isotherm of nitrogen was carried out to calibrate the proportion of the crystalline phase which contributes to adsorption in the sample of γ-$Mg(BH_4)_2$. We used the maximal adsorption capacity of N_2 (⅔ mol per mol of crystalline γ-$Mg(BH_4)_2$) from the previous diffraction studies[16] as a reference in order to calibrate the fraction of crystalline γ-$Mg(BH_4)_2$ in the sample. This calibration is necessary because the volumetric and gravimetric gas uptake by γ-$Mg(BH_4)_2$ in a bulk sample is affected by an inherent presence of a dense amorphous phase, its weight fraction varies from one batch to other[24]. As shown in Figure. S2 the saturation amount of N_2 was obtained determined to be 892.7 μmol, by means of fitting with the Langmuir equation. The fraction of the porous crystalline phase is defined as the ratio between experimental total amount of adsorption (n_{exp}) and theoretical total amount of adsorption (n_{the}), which is calculated from the following equation:

$$\sigma = \frac{n_{exp}}{n_{the}} = \frac{892.7}{1920\times{}^{2}/_{3}} = 0.7 \qquad (1)$$

Subsequently 200 K sorption isotherm of argon was performed without changing the sample. In order to compare directly the results with those from diffraction data (characterizing only the crystalline phase), the amount of argon atoms per unit cell was re-calculated from 200 K the volumetric isotherm as following:

$$N_{Ar} = \frac{n_{uptake}}{\sigma \cdot n_{\gamma}} \times Occ_{Mg} \qquad (2)$$

where N_{Ar} is the Ar atoms adsorbed per unit cell, n_{uptake} (mol) is the uptake of argon measured volumetrically, σ is the fraction of the crystalline phase, n_{γ} (mol) is the amount of γ-$Mg(BH_4)_2$ loaded, Occ_{Mg} (=24) is the occupancy of Mg atoms per unit cell.

3.3. Results and Discussion

Variable-temperature and pressure *in situ* powder X-ray synchrotron diffraction (PXRSD). Powder diffraction studies of γ-$Mg(BH_4)_2$ have been performed at constant Ar pressures of 1 and 10.5 bar upon cooling from 300 to 90 K and from 350 to 130 K, respectively. Within these temperature ranges, Ar uptake by γ-$Mg(BH_4)_2$ does not induce any phase transition, while a significant continuous change of the relative intensities is taking place, see Figure. 1. Similar behavior was observed for Ar isotherms measured at 150 and 200 K, see Figure. S3. The continuous evolution of the diffraction patterns allows us to perform the refinement of a single model of Ar-loaded *γ*-$Mg(BH_4)_2$, which is described below.

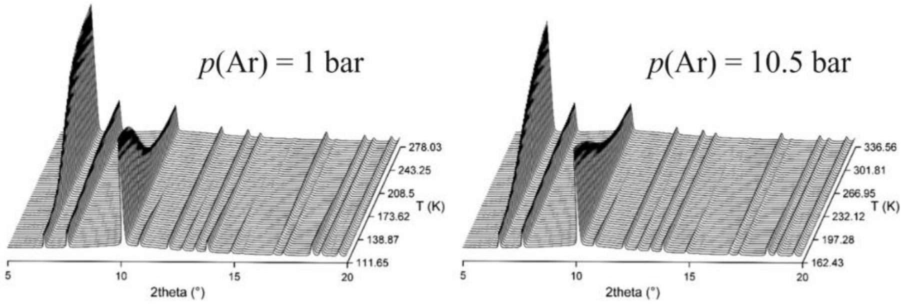

Figure 1. Variable-temperature powder X-ray diffraction patterns (λ = 0.74580 Å) of γ-$Mg(BH_4)_2$ loaded with Ar at 1 and 10.5 bar, upon cooling from 300 to 90 K and from 350 to 130 K, respectively.

Crystal structure of Ar-loaded *γ*-$Mg(BH_4)_2$. The pristine *γ*-$Mg(BH_4)_2$ (space group *Id*-3*a*) contains a 3D network of non-crossing 1D tubular channels, see Figure. 2[16]. The latter are built of BH_4^- units coordinated to Mg atoms. The narrowest part of the channel (aperture) is defined by a 5.8 Å distance between hydrogen atoms, while the size of the pocket between those apertures (i.e., the widest part) is about 7 Å. A pore pocket of these dimensions accommodate one N_2 or C_2H_6 molecule (16 per unit cell)[14], while for Ar atoms this space can be occupied by one of the two distinct adsorption sites. These two 32*e* crystallographic sites are located along the body diagonal [1 1 1] of the cubic structure, see Figure. 2a, b. At lower loadings, the adsorption site near the center of the pocket is filled. This site is denoted Ar(2) and is located close to the 16*b* crystallographic site 1/8 1/8/ 1/8 right in the center of the pocket. The other site, Ar(1), becomes dominant at higher loadings, while Ar(2) site gradually depopulates, see Figure. 2c (data points of occupancy versus temperature are listed in Table S2). Analysis of distances indicates that the Ar(2) site allows only one argon atom per pocket, forming mutually exclusive contacts with Ar(1) within the same pore. On the contrary, the depopulation of the Ar(2) site and the simultaneous filling of Ar(1) allows to host two Ar atoms per pore (as seen at lower temperatures at 1 bar), showing inter- and intrapore distances close to the sum of the Van der Waals radii of Ar (1.94 Å)[25], see Figure. 2a.

Interestingly, the total Ar uptake, obtained as a sum of Ar(1) and Ar(2) occupancies (Figure 2c, right), looks like a consequent filling of the first site and then the other at lower temperatures. The partial occupancies though clearly show a continuous structural change (redistribution) behind this macroscopic property.

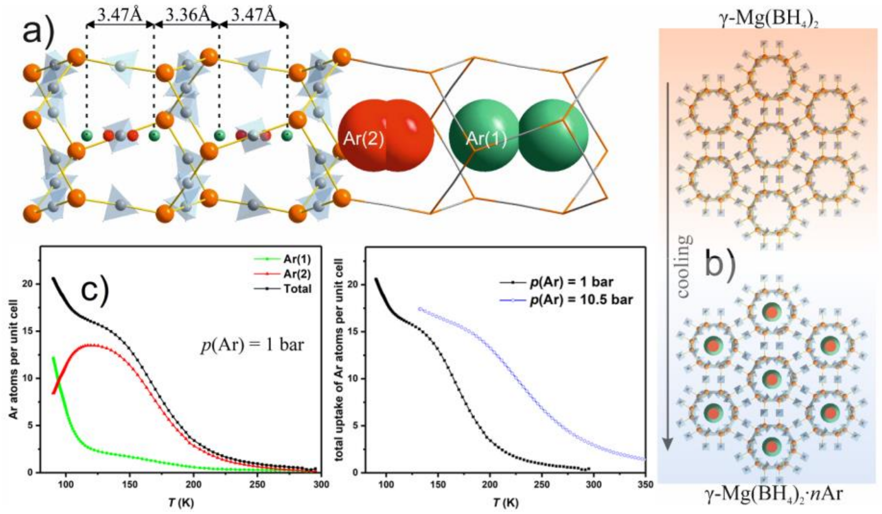

Figure 2. a) The representation of γ-Mg$(BH_4)_2$ framework's 1D channel filled with Ar atoms in two crystallographic positions; **b)** filling of the 1D channels upon cooling shown along [1 1 1] direction and **c)** variation of Ar occupancies indicating a redistribution of Ar between the two crystallographic sites. The right-hand side shows the total Ar uptake obtained as a sum of Ar(1) and Ar(2). Mg atoms shown as orange sphere, BH_4^- groups shown as light blue tetrahedral, Ar atoms in the pore center shown as red sphere and in the aperture shown as green sphere.

The same phenomenon was observed by neutron powder diffraction, see the comparison of Ar(2)/Ar(1) occupancy ratio from synchrotron and NPD data in Figure 3a. Due to the limited amount of NPD data, the Ar positions were fixed in the sequential refinement, while the occupancies were refined. To further reduce uncertainties, the isotropic displacement factors were also kept constant during the refinement at the values obtained from 90 K / 1 bar synchrotron data. The occupancy ratio Ar(2)/Ar(1) clearly shows a maximum at around 150 K, both from PXRSD and NPD data, with the Rietveld refinements at the lowest temperatures of the corresponding experiments given in Figure 3b.

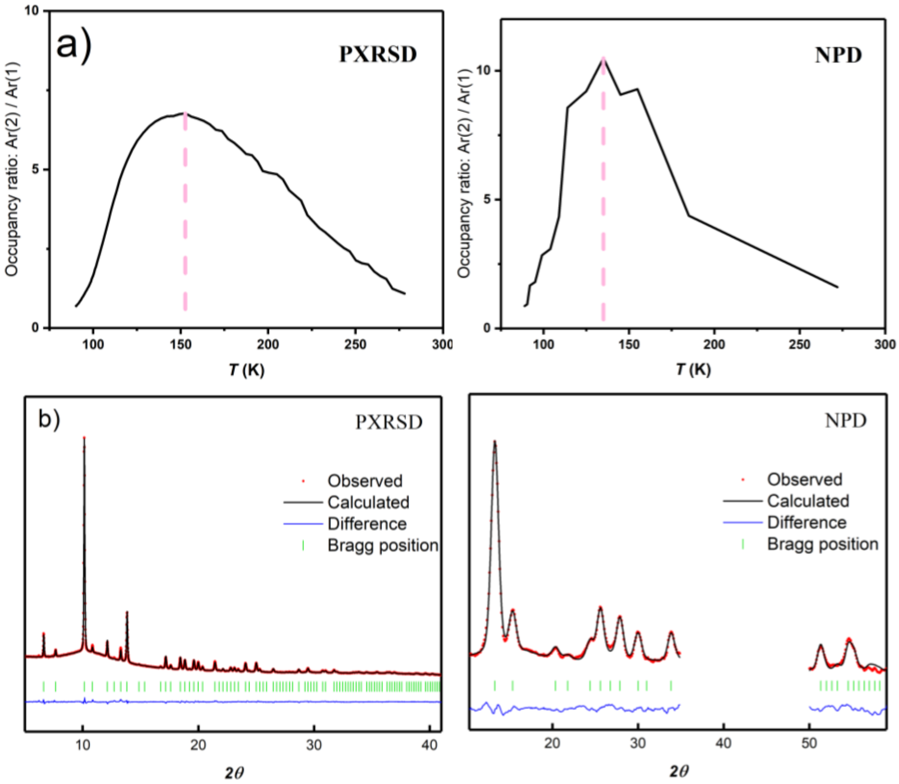

Figure 3. a) Occupancy ratio Ar(2)/Ar(1) obtained from sequential refinement to PXRSD (left) and NPD (right) data. **b)** Rietveld refinement of Ar-loaded γ-Mg(BH$_4$)$_2$ (left, λ = 0.74580 Å, *p* (Ar) = 1 bar, *T* = 90 K; *a* = 15.7824(2) Å; R$_{\mathrm{Bragg}}$ = 4.35 %; R$_F$ = 7.82 %) and Ar-loaded γ-Mg(^{11}BD$_4$)$_2$ (right, λ = 1.48700 Å, *p* (Ar) = 1 bar, *T* = 88.9 K, *a* = 15.7341(46) Å; R$_{\mathrm{Bragg}}$ = 3.88 %; R$_F$ = 8.14 %). The angular ranges containing contributions from the Al sample holder (from *2θ* = 35° to 50°) were excluded from the refinement on NPD data.

Adsorption isotherms from diffraction data: fitting to Langmuir equation and finding thermodynamic parameters. We took two synchrotron diffraction based isotherms at 150 and 200 K for calculation of the enthalpy of adsorption. At these temperatures, Ar(1) occupancy is not becoming significant, therefore the total over Ar(1) and Ar(2) sites does not exceed 1 atom per pocket or 16 atoms per unit cell. The isotherms are of perfect type I (see Figure 4a), with the excellent reversibility (no hysteresis see Figure S4) at both temperatures. To our great satisfaction, diffraction-derived isotherms at 200 K are very similar to those obtained by the volumetric method (amounts are corrected for the amorphous fraction, see above), Figure 4b.

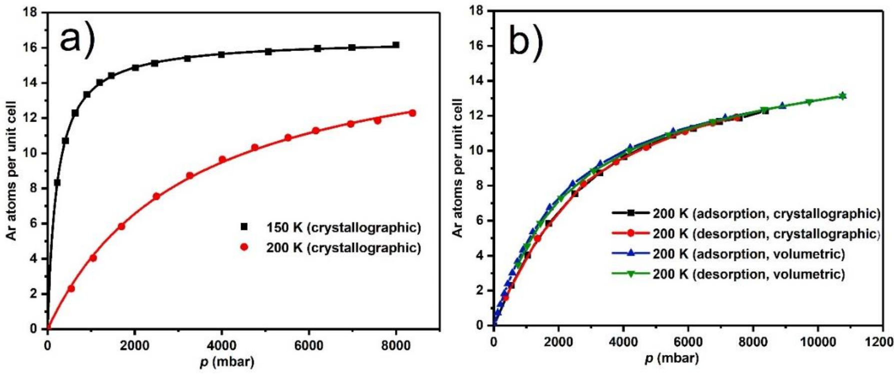

Figure 4. a) Langmuir fitting to the crystallographic isotherms measured upon adsorption at 150 K ($q_{\max}$ = 16.49(2), K_{eq} = 4.59(5)×10^{-3}) and 200 K ($q_{\max}$ = 17.13(23), K_{eq} = 3.10(11)×10^{-4}); b) The comparison of crystallographic and volumetric Ar adsorption and desorption isotherms at 200 K.

The adsorption isotherms were fitted using a Langmuir adsorption model, Figure 4a. This model is defined by the following expression:

$$q = \frac{q_{max} K_{eq} p}{1 + K_{eq} p} \tag{3}$$

where q is the uptake at different pressures, $q_{\max}$ is the saturation uptake, K_{eq} is the reaction equilibrium constant, and p is the gas pressure. The resulting fit enables to access the thermodynamic parameters characterizing gas adsorption, using the van't Hoff equation:

$$ln\, K_{eq} = -\frac{\Delta H}{RT} + \frac{\Delta S}{R} \tag{4}$$

The reaction equilibrium constant K_{eq} in equation (3) can be expressed with ΔH and ΔS as a function of $1/T$. As a result, both enthalpy and entropy of adsorption can be extracted from two isotherms. The results are shown in Table 1. Since only one volumetric isotherm is available, only the Gibbs energy can be calculated from K_{eq} using the equation (4), it compares very well with the value obtained from diffraction.

Table 1. Thermodynamics of Ar adsorption obtained from Langmuir equations fitted to diffraction-based and volumetric isotherms.

Method	**ΔG (kJ/mol)**	**ΔH (kJ/mol)**	**ΔS (J/(K·mol))**
crystallographic 150 K	6.7	-13.4	-134.4
crystallographic 200 K	13.4		
volumetric 200 K	13.0	-	-

Isosteric heats of adsorption derived from adsorption isotherms and isobars via Clausius-Clapeyron equation. The Clausius-Clapeyron equation is another classical relation, which can be used for the determination of the heat of gas adsorption. It assumes the adsorption as a phase transition, where the specific volume of the gas phase exceeds that of the condensed phase at the temperatures much lower than the critical temperature of the adsorbate. This assumption describes the adsorbate gas by the ideal gas law, giving the following equation:

$$ln\frac{P_1}{P_2} = -\frac{Q_{st}}{R}\left(\frac{1}{T_1} - \frac{1}{T_2}\right) \qquad (5)$$

where p_i are equilibrium gas pressures, T_i – the temperatures at which the amount of adsorbed gas at p_i is equal and Q_{st} – the isosteric heat of absorption. It should be pointed out, that this model neglects the variations in the heat of vaporization versus temperature and pressure and keeps them dependent on the guest loading only. Knowing that the isotherms and isobars are in equilibrium conditions (we examined the isobars especially at low temperatures, allowing more time to equilibrate), the isosteric heats of absorption as a function of loading can be obtained, as shown Figure 5. We used Logistic function to fit the isobars (see Figure S5). One can see that the resulting isosteric heats obtained from two crystallographic isotherms are close to the enthalpy of adsorption derived from the eq. (4), at least within the range of 2–14 Ar atoms per unit cell where the accuracy on the occupancies are high for both temperatures. The isosteric heats derived from the crystallographic isobars are slightly lower. Such difference can be related to a wide temperature range covered by isobars (300 K to 90 K at 1 bar and 350 K to 130 K at 10.5 bar) compared to the isotherms (150 and 200 K), keeping in mind the temperature and pressure variations of the adsorption enthalpy[26].

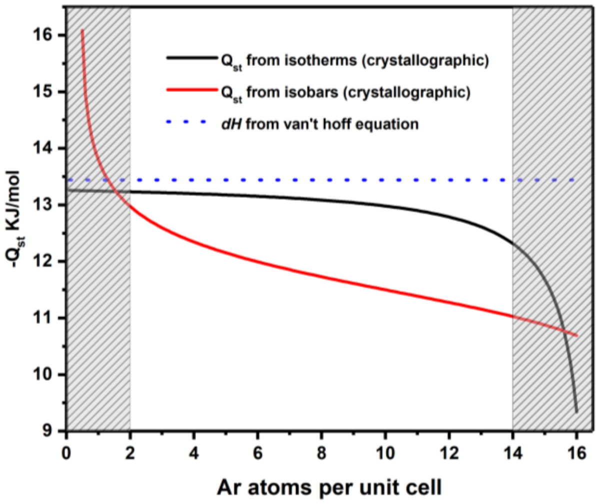

Figure 5. The comparison of the isosteric heats of adsorption and the enthalpy of adsorption obtained from the Clausius-Clapeyron and van’t Hoff equations (5) and (4). The confidence limits are fixed to 2-14 Ar per cell, as defined by the accuracy of Ar occupancies at both low and high temperatures.

The estimates of enthalpy from van’t Hoff equation (using Langmuir-fitted isotherms) are done neglecting interactions between the guest molecules. Such interactions, direct of mediated by the host structure, do manifest themselves in the shape of isobars, but are visible to a smaller extent in isotherms. The slope of the Q_{st} in Figure 5 reflects the repulsive interactions developing upon gas loading, well in agreement with the microscopic picture seen by diffraction.

Microscopic Ising-like lattice gas model. Considering the crystal structure containing short inter- and intrapore distances between Ar atoms we propose a model based on Ising-like lattice gas approach and present a mean-field solution that is able to catch the most essential feature of the uptake process documented in the experiment: the re-distribution of Ar atoms over the two sites inside the pore.

We consider a crystal that can exchange guest molecules with a reservoir; the system is governed by thermodynamics for a grand canonical ensemble. A site available for the guest molecule in a pore can be empty or occupied, for every such site we assign an occupation number σ that is set to –1 for the empty site and +1 if the site is occupied. Guest uptake locally corresponds to a transition from σ = –1 to σ = +1 at a given site. Every site can be seen as a two-level system with energies:

$$E_1(-1) = -\frac{\Delta}{2}, E_2(+1) = \frac{\Delta}{2}$$

$$\Delta = u - Tlnr = u - Ts \qquad (6)$$

where *u* stands for the energy difference and *r* indicates a degeneracy of the gas occupied site, or, more generally, accounts for the entropy associated with a single event of one guest uptake.

The above consideration assumes that a porous crystal stays in thermodynamic equilibrium with a surrounding bath implying that at given *P*, *T* a chemical potential in the crystal is homogeneous. This, in turn, assumes that we consider adsorption by the surface, diffusion from the surface to the bulk, and establishing equilibrium as “fast”; in other words, we assume that any relaxation processes are much faster than a change of external conditions. Whether these conditions are fulfilled with experiment has to be checked with a time-dependent measurement[27][28], for the data presented here we know that the equilibrium is reached at each point, producing full reversibility of gas loading.

Here we focus on the static properties for such a model system in equilibrium. Moreover, we restrict ourselves to the mean field approach thus neglecting correlation and fluctuation effects. For two sites A and B in a pore, the following mean-field Hamiltonian can be constructed:

$$H = -J\sum\sum\sigma_i\sigma_j + \frac{\Delta}{2}\sum\sigma_i \tag{7}$$

where we keep only nearest-neighbor interactions and assign an occupation number σ = –1 for the empty site and +1 if the site is occupied. The guest-guest interactions are expected to be stronger for closely spaced guest molecules and can therefore, at least approximately, be taken into account with effective nearest-neighbor interactions.

Here we account for both, intra-pore (J_{AB}) and inter-pore (J_1, J_2) interactions. Every pore with two sites is considered as a four-level system with the following energy levels:

$$E_1(-1,-1) = -\frac{\Delta_A}{2} - \frac{\Delta_B}{2} - J_{AB} + J_1\langle\sigma_B\rangle + J_2\langle\sigma_A\rangle$$

$$E_2(-1,+1) = -\frac{\Delta_A}{2} + \frac{\Delta_B}{2} + J_{AB} + J_1\langle\sigma_B\rangle - J_2\langle\sigma_A\rangle$$

$$E_3(+1,-1) = \frac{\Delta_A}{2} - \frac{\Delta_B}{2} + J_{AB} - J_1\langle\sigma_B\rangle + J_2\langle\sigma_A\rangle$$

$$E_4(+1,+1) = \frac{\Delta_A}{2} + \frac{\Delta_B}{2} - J_{AB} - J_1\langle\sigma_B\rangle - J_2\langle\sigma_A\rangle \tag{8}$$

A mean-field expectation value of the occupation number reads:

$$\sigma^{A}=\frac{\sum_{k=1}^{k=4}\sigma_{k}^{A}e^{-E_{k}/T}}{\sum_{k=1}^{k=4}e^{-E_{k}/T}}$$

$$\sigma^{B}=\frac{\sum_{k=1}^{k=4}\sigma_{k}^{B}e^{-E_{k}/T}}{\sum_{k=1}^{k=4}e^{-E_{k}/T}} \qquad (9)$$

The above equations may reproduce many different adsorption scenarios. An important feature of the model is that it allows for different uptake by sites A and B. Among those scenarios, there is a generic solution for two sites with small difference in the heat of adsorption, and negative intrapore interaction J_{AB} ("repulsion"), corresponding model isobars are shown in Figure 6.

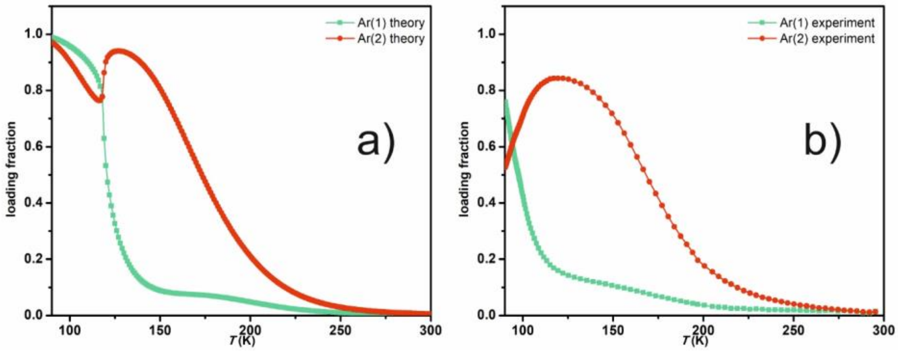

Figure 6. The simulated a) and experimental b) occupancies of two Ar adsorption sites in γ-Mg$(BH_4)_2$.

Here one can see that the adsorption starts at one site and this process suppresses or slows down the uptake at the second site. At certain temperature the second site is filling while the first one even loose part of the occupying guests – they migrate to the neighboring site, thanks to the interaction terms in the Hamiltonian. Experimental diffraction isobars show very similar behavior; however, the agreement is rather qualitative due to an oversimplified model and mean-field approximation. Further cooling should result in the filling of the remaining space at both positions, this scenario has not been observed in the experiment, and is actually impossible due to the too short Ar(1)-Ar(2) distance. However, this may be possible for smaller guests and/or larger pores. A somewhat similar behavior has been observed for CO_2 three site uptake by the porous Metal–Organic Frameworks CPO-27-M[29]; a variety of possible new scenarios reflecting guest-host, guest-guest intrapore and interpore interactions is still to be discovered. Isobars probed by diffraction together with Ising-like phenomenological models might serve as a powerful tool to uncover new collective phenomena associated with guest uptake and release by porous media.

3.4. Conclusions

Modern *in situ* X-ray and neutron diffraction analysis stands not only on the monitoring of adsorbate's crystal structure response upon guest uptake, but becomes a new tool for the evaluation of the thermodynamic parameters of such processes. Remarkably, an example of the guests redistribution upon Ar uptake in γ-$Mg(BH_4)_2$ demonstrates two extra strong points of this method: capability to characterize exclusively the crystalline part of the porous solid and to describe the guest-guest interactions within their pores. Another great advantage of the gas adsorption crystallography is the access to adsorption isobars, which are hardly obtainable by volumetric methods, as the non-isothermal calibration is overwhelmingly complicated. Adsorption isobars are more informative, as they cover wider range of chemical potential and thus are better suited to visualize directly specific features of guest-host and guest-guest interactions.

Further development of the experimental setup and application of the appropriate phenomenological models opens much room for characterization of either thermodynamics and/or kinetics[27] of guest uptake for individual adsorption sites. We believe that this approach is useful to a large variety of porous materials with various pore’s types, such as MOFs, zeolites and mesoporous silica, with hierarchically arranged pores. The capability to elucidate thermodynamics of gas adsorption at the individual pore level is of great interest for computation and modelling as well as for the rational design of porous materials.

.

3.5. References

[1] Li H., Eddaoudi M., O'Keeffe M., Yaghi O. M. Design and synthesis of an exceptionally stable and highly porous metal-organic framework. *Nature.* **1999**, 402(6759): 276-279.

[2] Férey G. Hybrid porous solids: Past, present, future. *Chem. Soc. Rev.* **2008**, 37(1): 191-214.

[3] Furukawa H., Cordova K. E., O'Keeffe M., Yaghi O. M. The chemistry and applications of metal-organic frameworks. *Science.* **2013**, 341(6149).

[4] Adil K., Belmabkhout Y., Pillai R. S., et al. Gas/vapour separation using ultra-microporous metal-organic frameworks: Insights into the structure/separation relationship. *Chem. Soc. Rev.* **2017**, 46(11): 3402-3430.

[5] He Y., Li B., O'Keeffe M., Chen B. Multifunctional metal-organic frameworks constructed from meta-benzenedicarboxylate units. *Chem. Soc. Rev.* **2014**, 43(16): 5618-5656.

[6] Kerry F. G. *Industrial Gas Handbook Gas Separation. Gas Separation and Purification.* CRS press. **2007**.

[7] Zhang J. P., Liao P. Q., Zhou H. L., Lin R. B., Chen X. M. Single-crystal X-ray diffraction studies on structural transformations of porous coordination polymers. *Chem Soc Rev.* **2014**, 43(16): 5789-5814.

[8] Sarkisov L., Martin R. L., Haranczyk M., Smit B. On the Flexibility of Metal − Organic Frameworks. *J. Am. Chem. Soc.* **2014**, 136(6): 2228-2231.

[9] Férey G. Structural flexibility in crystallized matter: From history to applications. *Dalt. Trans.* **2016**, 45(10): 4073-4089.

[10] Krause S., Bon V., Senkovska I., et al. A pressure-amplifying framework material with negative gas adsorption transitions. *Nature.* 2016, 532(7599): 348-352.

[11] Carrington E. J., Vitórica-Yrezábal I. J., Brammer L. Crystallographic studies of gas sorption in metal-organic frameworks. *Acta Crystallogr. Sect. B Struct. Sci. Cryst. Eng. Mater.* **2014**, 70(3): 404-422.

[12] Cho H.S., Yang J., Gong X., et al. Isotherms of individual pores by gas adsorption crystallography. *Nat. Chem.* **2019**, 11(6): 562-570.

[13] Gładysiak A., Deeg K. S., Dovgaliuk I., et al. Biporous metal-organic framework with tunable CO_2/CH_4 separation performance facilitated by intrinsic flexibility. *ACS Appl. Mater. Interfaces.* **2018**, 10(42): 36144-36156.

[14] Dovgaliuk I., Nouar F., Serre C., Filinchuk Y., Chernyshov D. Cooperative adsorption by porous frameworks: Diffraction experiment and phenomenological theory. *Chem. - A Eur. J.* **2017**, 23(70):17714-17720.

[15] Heere M., Hansen A. L., Payandeh S., et al. Dynamics of porous and

amorphous magnesium borohydride to understand solid state Mg-ion-conductors. *Sci. Rep.* **2020**, 10, 9080.

[16] Filinchuk Y., Richter B., Jensen T. R., Dmitriev V., Chernyshov D., Hagemann H. Porous and dense magnesium borohydride frameworks: Synthesis, stability, and reversible absorption of guest species. *Angew. Chem. Int. Ed.* **2011**, 50(47): 11162-11166.

[17] Dyadkin V., Pattison P., Dmitriev V., Chernyshov D. A new multipurpose diffractometer PILATUS@SNBL. *J. Synchrotron Radiat.* **2016**, 23(3): 825-829.

[18] Ashiotis G., Deschildre A., Nawaz Z., et al. The fast azimuthal integration Python library: PyFAI. *J. Appl. Crystallogr.* **2015**, 48(2):510-519.

[19] Frontzek M. D., Whitfield R., Andrews K. M., et al. WAND^2 - A versatile wide angle neutron powder/single crystal diffractometer. *Rev. Sci. Instrum.* **2018**, 89(9): 092801.

[20] Rodriguez-Carvajal J. FULLPROF: a program for Rietveld refinement and pattern matching analysis. In: *Satellite Meeting on Powder Diffraction of the XV Congress of the IUCr*. **1990**, 127.

[21] Heere M., Mühlbauer M. J., Schökel A. Knapp M., Ehrenberg H., Senyshyn A. Energy research with neutrons (ErwiN) and installation of a fast neutron powder diffraction option at the MLZ, Germany. *J. appl. crystallogr.* **2018**, 51(3): 591-595.

[22] Favre-Nicolin V., Černý R. FOX, “free objects for crystallography”: A modular approach to ab initio structure determination from powder diffraction. *J. Appl. Crystallogr.* **2002**, 35(6): 734-743.

[23] Rodríguez-Carvajal J. Recent advances in magnetic structure determination by neutron powder diffraction. *Phys. B Phys. Condens. Matter.* **1993**, 192(1):55-69.

[24] Stadie N. P., Callini E., Mauron P., Borgschulte A., Züttel A. Supercritical nitrogen processing for the purification of reactive porous materials. *J. Vis. Exp.* **2015**, (99): 52817.

[25] Vogt J., Alvarez S. Van der Waals Radii of noble gases. *Inorg. Chem.* **2014**, 53(17): 9260-9266.

[26] Koutsoyiannis D. Clausius-Clapeyron equation and saturation vapour pressure: Simple theory reconciled with practice. *Eur. J. Phys.* **2012**, 33(2): 295-305.

[27] Dovgaliuk I., Senkovska I., Li X., Dyadkin V., Filinchuk Y., Chernyshov D. Kinetic barriers and microscopic mechanisms of noble gas adsorption by nanoporous γ-$Mg(BH_4)_2$ obtained by means of sub-second X-ray diffraction. *Angew. Chem. Int. Ed.* **2010**, *60*(10), 5250-5256.

[28] Dovgaliuk I., Dyadkin V., Donckt M. V., Filinchuk Y., Chernyshov, D. Non-Isothermal kinetics of Kr adsorption by nanoporous γ-$Mg(BH_4)_2$ from in situ synchrotron powder diffraction. *ACS Appl. Mater. Interfaces.* **2020**, 12(6), 7710-7716.

[29] Pato-Doldán B., Rosnes M. H., Dietzel P. D. An In-depth structural study of the carbon dioxide adsorption process in the porous metal–organic frameworks CPO-27-M. *ChemSusChem.* **2017**, 10(8), 1710-1719.

Chapter 4. Ultra-dense Hydrogen in Small Pore Hydridic Framework

Hyunchul Oh[1,10], Nikolay Tumanov[2], Voraksmy Ban[2], Xiao Li[2], Bo Richter[3], Matthew R. Hudson[4], Craig M. Brown[4], Gail N. Iles[5,6], Dirk Wallacher[5], Scott W. Jorgensen[7], Luke Daemen[8], Rafael Balderas-Xicohténcatl[8], Yongqian Cheng[8], Anibal J. Ramirez-Cuesta[8], Michael Heere[9], Michael Hirscher[1], Torben R. Jensen[3]*, Yaroslav Filinchuk[2]**

[1]Max Planck Institute for Intelligent Systems; Heisenbergstrasse 3, D-70569 Stuttgart, Germany.

[2]Institute of Condensed Matter and Nanosciences, Université Catolique de Louvain; Place L. Pasteur 1, 1348 Louvain-la-Neuve, Belgium.

[3]Department of Chemistry and Interdisciplinary Nanoscience Center, Aarhus University, Langelandsgade 140, 8000 Aarhus C, Denmark.

[4]Center for Neutron Research, National Institute of Standards and Technology; Gaithersburg, MD 20899, USA.

[5]Department of Crystallography, Helmholtz-Zentrum Berlin; 14109 Berlin, Germany.

[6]School of Science, RMIT University; Melbourne, VIC 3000, Australia.

[7]Chemical and Environmental Sciences Lab General Motors R&D Center; 30500 Mount Rd, Warren, MI 48090, USA.

[8]Spallation Neutron Source, Oak Ridge National Laboratory; Oak Ridge, Tennessee 37831, United States.

[9]Institute for Applied Materials (IAM), Karlsruhe Institute of Technology (KIT); 76344 Eggenstein-Leopoldshafen and Heinz Maier-Leibnitz Zentrum (MLZ), Technische Universität München; Lichtenbergstr. 1, 85748 Garching, Germany.

[10]Department of Energy Engineering, Gyeongsang National University; Jinju, Gyeongnam, 52849 Republic of Korea.

Abstract

Nanoporous materials have attracted attention for extreme diversity of chemical composition, structures, and properties. A porous magnesium borohydride host framework with small pores and a unique partially negatively-charged non-flat interior has been investigated to identify exact host-guest interactions with H_2 *and* N_2 *using neutron powder diffraction, volumetric gas adsorption, and inelastic neutron scattering. Hydrogen and nitrogen have distinct and different adsorption sites within the structure with very different limiting capacities: 2.33* H_2 *and 0.66* N_2 *per* $Mg(BH_4)_2$*. Inside the pore, molecular hydrogen is packing extremely dense on two distinct sites. Independently, all three experimental methods yield twice the density of liquid hydrogen (144-132 g* H_2*/L of pore volume). This study reveals that densely packed hydrogen can be stabilized in small-pore materials at ambient pressures.*

4.1. Introduction

The widespread use of hydrogen as a fuel in personal and public transport vehicles is limited by the significant challenge of hydrogen storage. Current technology mainly focuses on molecular hydrogen storage in either gaseous (*e.g.*, $p(H_2)$ = 700 bar) or liquid forms, at cryogenic temperatures[1][2]. Unfortunately, there are limits to the volumetric and gravimetric storage density that current engineering technologies can provide. Hydrogen, as a molecule, can physically adsorb in a porous material by weak Van der Waals interactions (London dispersion forces) in a process that is called physisorption[3-5]. For practical applications of physisorbed hydrogen, enhancing the interaction energy between the molecule and the solid surface is necessary.

A nanoporous cubic magnesium borohydride, $\gamma\text{–}Mg(BH_4)_2$ (ρ = 0.550 g/cm^3, space group *Id*-3*a*) has a net of linear channels, with 33 % free pore volume[6]. The pore diameter is ≈ 9 Å, and the smallest aperture is ≈ 5.8 Å, enabling this compound to adsorb small molecules, such as dichloromethane, nitrogen, or hydrogen. This porous hydride has a unique non-flat, partially negatively-charged inner surface, where the hydridic $H^{\delta-}$ atoms are exposed into the pores. Using synchrotron radiation X-ray powder diffraction (SR-XRPD), nitrogen molecules were found to be located close to the centre of the pore, corresponding to one molecule per pore and thus reaching a limiting composition $\gamma\text{–}Mg(BH_4)_2\cdot 2/3N_2$. Hydrogen molecule positions could not be determined independently in the previous investigations due to H's small X-ray scattering length and were assumed to occupy the same position as N_2[6].

4.2. Experimental details

Experimental details can be seen in Appendix II.

4.3. Results and discussion

Using neutron powder diffraction (NPD), we have now accurately determined the location of the hydrogen atoms and molecules in the framework structure. Using isotopically enriched $\gamma\text{–Mg}(^{11}BD_4)_2$ samples and deuterium (D_2) gas the large neutron coherent cross-section of deuterium makes NPD the ideal diffraction technique to locate H atoms. High-resolution, high-flux neutron powder diffractometers are ideal for fast, *in situ* studies involving rapidly changing gas-solid systems, particularly when one of the gases is deuterium[7]. For the data analysis we first performed a Rietveld refinement of NPD data to confirm the 'empty' framework structure of $\gamma\text{–Mg}(BD_4)_2$ (see Figure S1 and Table S1) and the SR-XRPD based structural model $\gamma\text{–Mg}(BH_4)_2{\cdot}2/3N_2$ which corresponds to the full occupation of the pore with one nitrogen molecule, positionally disordered around the pore's centre (see Figure 1a and Table S2).

Remarkably, we discovered that the Rietveld refinement of the deuterium loaded sample indicates that the D_2 does not lie in the centre position of the pore as N_2 (comparison of the Rietveld refinement profiles for the two localization models is shown in Figure 1b left, and c). Instead, D_2 molecules are located close to the aperture of the pore and that the two D_2 molecules in the pore are symmetry equivalent and described with a single crystallographic site, denoted D11 (Figure 1b, middle and right).

The limiting composition of this structure corresponds to 4/3 D_2 per $Mg(BD_4)_2$, i.e., $Mg(BD_4)_2{\cdot}1.33D_2$, and is easily saturated at $p(D_2) = 27$ mbar at low temperature, $T = 25$ K. For the model description of the deuterium, it is represented by a quantum rotator often referred to as a 'super atom'[8] with a centroid of a sphere of nuclear density around the centre of mass of the D_2 molecule. It is described with a single

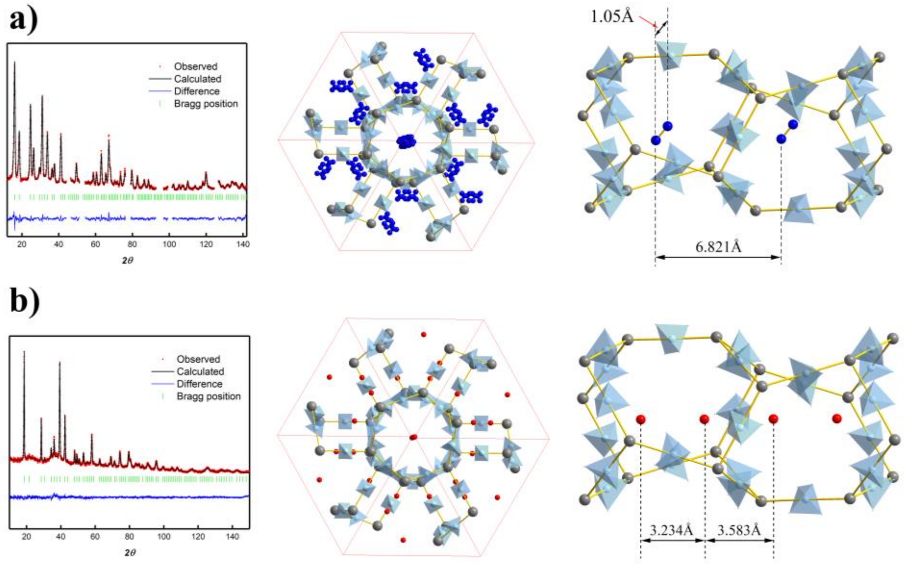

Figure 1. Neutron powder diffraction profiles for nitrogen and deuterium-loaded γ-$Mg(^{11}BD_4)_2$ along with projections of the crystal structures. **a)** Nitrogen-loaded γ-$Mg(^{11}BD_4)_2$ sample at 100 K and 3 bar (HZB data, $\lambda = 1.7982$ Å). **left picture** shows the Rietveld refinement profile. The angular ranges containing contributions from the Al can were excluded from the refinement. **middle picture** shows the superposition of nitrogen adsorption sites in the crystal structure of nanoporous γ-$Mg(BH_4)_2$, viewed along [111] direction. Mg atoms are shown as grey spheres, BH_4 groups as blue tetrahedra, disordered N_2 molecules shown as blue spheres, and the unit cell is defined by red lines. **right picture** is the porous channel running along the cubic diagonal displaying an N_2 molecule in the centre of the pore. The distance of two neighbouring N_2 molecules is at 6.82 Å. **b)** Deuterium-loaded γ-$Mg(^{11}BD_4)_2$ sample at 10 K (NIST data, $\lambda = 2.079$ Å). **left picture** shows the Rietveld refinement profile, using the new structural model that allows for the double hydrogen capacity, γ-$Mg(^{11}BD_4)_2 \cdot 1.33D_2$. **middle picture** shows the superposition of deuterium adsorption sites viewed along [111] direction, D_2-centroids shown as red spheres. **right picture** is the porous channel running along the cubic diagonal displaying two D_2 per pore taking positions close to the apertures. The distances of intra- / inter-pore D_2 are 3.234 Å and 3.583 Å, respectively.

positional parameter, one occupancy factor (that accounts for 2 atoms in a molecule, i.e., an occupancy of 2 indicates 1 molecule), and one atomic displacement parameter. The D11 site is located on the 3-fold axis, forming a one-dimensional chain along the [111] direction of the cubic unit cell (Figure 1b middle). The guest-guest contacts between deuterium molecules within the same pore and between different pores are 3.234(5) and 3.583(5) Å, respectively, see Figure 1b right. These distances are significantly shorter than the distances between H_2 centroids in solid hydrogen (~3.8 Å)[9], allowing a pore in γ–Mg(^{11}BD$_4$)$_2$ to accommodate two D_2 molecules closer to the apertures, while only one larger N_2 occupies the centre of the pore. Notice, that the kinetic diameter of D_2 and H_2 are similar, $d(H_2) = 2.89$ Å, whereas that of nitrogen is larger, $d(N_2) = 3.64$ Å (see Figure 1a right).

The host-guest interaction is defined by the contacts involving the framework's deuterium atoms, i.e., partially negatively charged hydrogen 'corners' of the borohydride groups, at 2.992(6) Å away from the D_2 centroid. This kind of host-guest interaction makes γ–Mg(BH$_4$)$_2$ a unique porous material exhibiting strong $H^{\delta-}\ldots H_2$ adsorption at ambient pressure. Metal-organic frameworks (MOFs) and hydrogen hydrates[10] do not contain hydridic hydrogen, so they do not exhibit similar molecular arrangements. The other example, metal hydride clathrates, do not contain original hydrogen molecules due to the transfer of electrons from metal atoms to H-atoms, and are stable only at high pressures[11]. The affinity of H_2 to $H^{\delta-}$ is also illustrated by the fact that deuterium molecules remain close to the aperture and not to the centre of the pore at low and intermediate hydrogen loadings. This is illustrated by γ–Mg(BD$_4$)$_2$·0.35D$_2$ and γ–Mg(BD$_4$)$_2$·1.05D$_2$, respectively, at $p(D_2) = 0.21$ and 0.43 mbar and $T = 25$ K (see Table S4 and Figure S4 summarizing the results of the neutron diffraction study). Thus, the D_2 molecule does not move to the centre of the pore, where more space is available, even at low loadings. We can conclude that the specific $H^{\delta-}\cdots H_2$ interaction leads to well-defined H_2 adsorption at the D11 site, both at low and high loadings.

Re-evaluating the previously published H_2 adsorption isobars extracted from SR-XRPD data using the N_2 model[6] with this γ–Mg(BH$_4$)$_2$ and D11 site as the model, provide an improved fit to the observed diffraction data collected at hydrogen pressures of 3.34 bar, 33.7 bar, and 105 bar and temperatures down to 80 K. The extracted isobars have more regular shapes and also give the maximum capacity of 4/3 H_2 per formula unit, in good agreement with neutron diffraction data. Chapter S2 in the supporting information provides more details and comparisons.

Structure revision using NPD and SR-XRPD data firmly shows that physisorbed hydrogen density in γ-$Mg(BH_4)_2{\cdot}1.33H_2$ reaches ~5.0 mass fraction (wt%). Considering the 0.60 cm^3/g total pore volume in γ-$Mg(BH_4)_2$, the observed density of hydrogen molecules in the pores of 0.082 g/cm^3 is higher than the density of liquid hydrogen at 21 K and 1 bar (71 g H_2/L) and close to solid hydrogen (86 g H_2/L).

Remarkably, at higher deuterium pressure at 25 K, we observed a second step of gas uptake. Analysis of NPD data reveals that a second D_2 site, denoted D22, starts to fill (Figure 2b), reaching saturation at $p(D_2)$ = 205 mbar and T = 25 K. D22 is not positioned on the 3-fold axis, running through the centre of the channel, therefore creating a short (self-excluding) D22...D22 distance of 1.94 Å between the two bypassing channels. As a consequence, the limiting occupancy of the D22 site is 50 %. Careful re-analysis of the diffraction data measured at $p(D_2)$ = 27 mbar, T = 25 K indicates that the D22 site is 14% filled at this pressure, while at 203 mbar it becomes fully occupied (50 %), reaching the limiting composition of $\gamma-Mg(BD_4)_2{\cdot}2.33D_2$. Rietveld refinement profiles are provided in Figure 2a and crystallographic data in Table S6. Extra weak diffraction peaks appear in the NPD patterns of $\gamma-Mg(BD_4)_2{\cdot}2.33D_2$, showing that the body-centred structure becomes primitive, most likely due to an order of D22 site in a lower symmetry space group (possibly *Pa*-3).

Thus, crystallographic data reveal the composition γ-$Mg(BH_4)_2{\cdot}2.33H_2$ at saturation, corresponding to 8.0 mass fraction (wt%) physisorbed hydrogen, and taking into account the hydrogen of the framework, this translates to a total gravimetric and volumetric H-content of 21.7 mass fraction (wt%) and 129 g/L respectively. Remarkably, the physisorbed hydrogen (2.33 H_2) is packed extremely

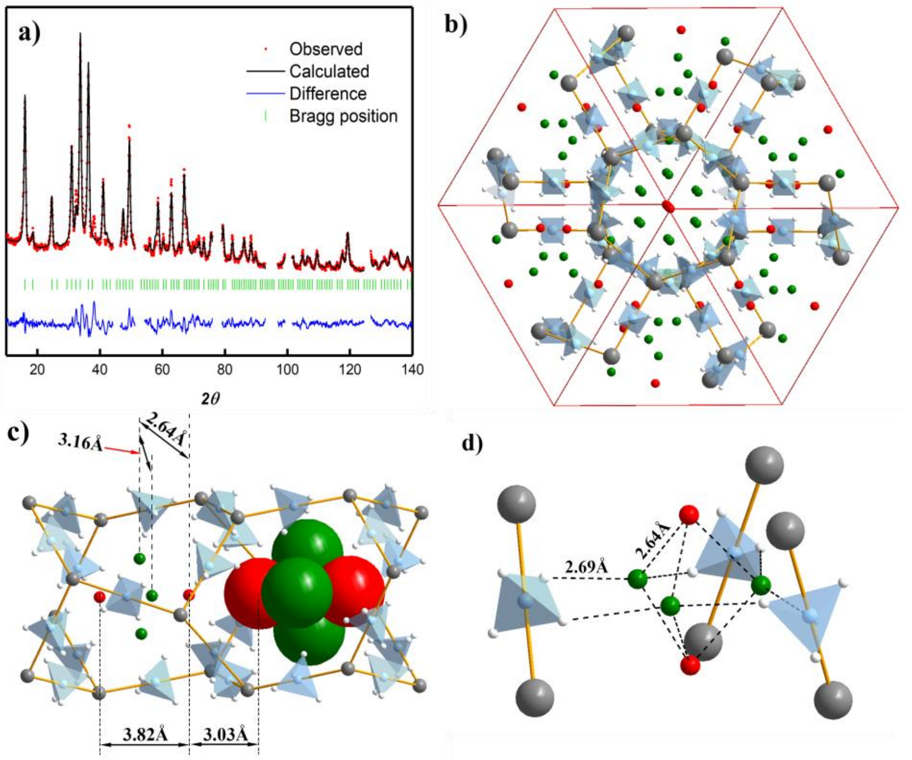

Figure 2. Deuterium-loaded γ-Mg($^{11}BD_4$)$_2$ at 25 K and 203 mbar. **a)** the Rietveld refinement NPD profile, $\lambda = 1.799$ Å. The angular ranges containing contributions from the Al can were excluded. **b)** Crystal structure containing two D_2 sites with the limiting composition of γ-$Mg(BH_4)_2 \cdot 2.33D_2$. Mg atoms are shown as grey spheres, BH_4 groups as blue tetrahedra, and the unit cell is defined by red lines, the D11 position of the D_2 centroids is shown as red spheres, the D22 position of the D_2 centroids as green spheres. **c)** The porous channel running along the cubic diagonal displays the two D_2 sites. The spheres in the right pore are shown with the van der Waals radius of hydrogen molecule in solid state at ambient pressure (1.52 Å)[12]. **d)** Environment of 5 H_2 molecules occupying the same pore, highlighting short B-$H^{\delta-}\ldots H_2$ and $H_2\ldots H_2$ contacts.

densely in the pores, with an estimated 144 g H_2 per litre of pore volume, which is twice the density of liquid hydrogen. This high density stems from the short contact distances between the H-atoms of the BH_4 group and the centres of the H_2 molecules (the shortest is D1...D22 of 2.69(1) Å) and within the trigonal bipyramidal cluster composed of five H_2 molecules shown in Figure 2c) (the shortest is D11...D22 of 2.64(1)

Å). The latter compares well with the 2.66 Å $H_2 \ldots H_2$ distance in phase I of solid H_2 at 5.4 GPa[13].

Spectroscopic characterization was performed using inelastic neutron scattering (INS) measurements on γ-$Mg(BD_4)_2$ with and without H_2 dosed[14]. INS is a technique that is particularly useful to identify the rotational features of the hydrogen molecule (H_2)[15][16].

Figure 3 shows the spectrum of para-hydrogen (pH_2) adsorbed on $Mg(BD_4)_2$ corresponding to $Mg(BD_4)_2 \cdot 1.46H_2$. With a correction for the ~30% amorphous non-porous magnesium borohydride, the effective loading of the crystalline porous fraction is $2.06H_2$ per Mg atom, indicating almost full loading of the two adsorption sites. The spectrum contains two rotational peaks at 13.9 meV and 14.6 meV. The higher energy transition is consistent with a free hydrogen rotor, red hashed area (see Figure 3) similar to solid hydrogen and hydrogen under confinement[17]; therefore, it can be assigned to the D11 site. The second rotational peak with lower intensity is consistent with a perturbed rotor, blue hashed area[15][18][19], and can be attributed to D22. Experimentally, at the maximum loading, the ratio between the areas of D22:D11 is 1:2.7 for INS and 1:1.33 for fully loaded state in NPD, see SI.

The total spectrum can be constructed using the contributions from the density of states (DoS) of the rattling modes of the hydrogen molecule, obtained from the spectra of normal hydrogen (nH_2, mixture of ortho and para), as presented in[20][21]. The convolution of the rotational transitions with the DoS yields the total spectrum (see SI section 5.5). As seen in Figure 3, trace II, the reconstructed spectrum lacks intensity at 27.8 meV. This peak at 27.8 meV has an energy that matches twice the transition $J_{0\to1}$ of the rotational peak (blue hashed area).However, there is no rotational transition of pH_2 that can account for this intensity (see Table S8). A similar effect can be seen when measuring hydrogen under high pressure (see SI section 5.5. and Figure S21). The small peak present in solid hydrogen at 29.1 meV at 100 bar increases manifold at 2500 bar. This peak is a consequence of a simultaneous quantum rotational excitation (SQRE) of two distinct pH_2

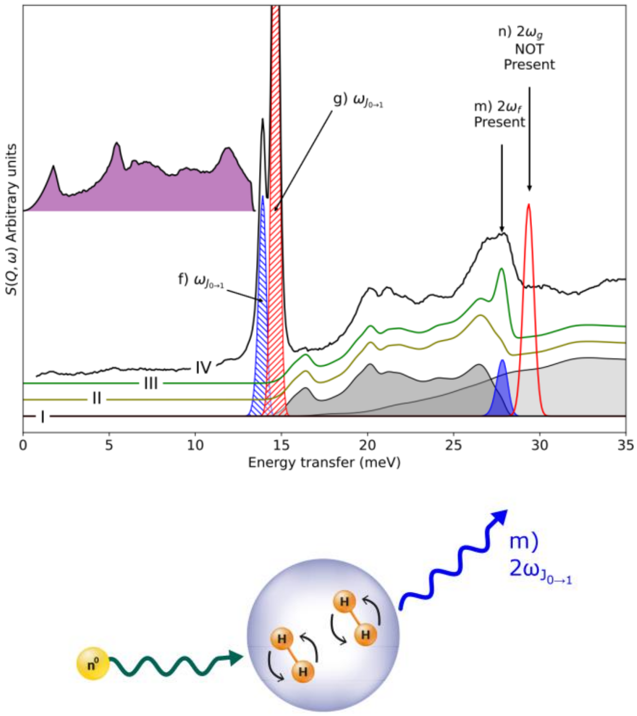

Figure 3. Inelastic neutron scattering spectra for deuterium-loaded $\gamma\text{-Mg(BD}_4)_2$. **Top,** INS spectra of $\text{Mg(BD}_4)_2$ loaded with 4 mmol of pH_2 (black). The vibrational DoS (purple upper area) is convoluted with the rotor transitions red and blue hashed areas, peaks f) and g) (see SI for peak full peak assignment). The resulting convolution is shown in the greyed-out areas in trace I to obtain the overtones and combinations. The sum of the overtones is shown in the trace labeled II. Trace III includes the contribution of the concurrent excitation of the $J_{0\rightarrow1}$ on two neighboring hydrogen molecules. **Bottom,** Scheme of simultaneous quantum rotational excitation (SQRE), a single neutron interacts simultaneously with two neighboring H_2 molecules. The resulting neutron transfers the energy required for two rotational transitions $2\omega_{J_{0\rightarrow1}}$(27.8 meV). Only the SQRE of the rotational transition at 13.9 meV shows in the spectrum. (All INS spectra presented in this paper have been measured at 5 K)

molecules. The pressure makes these molecules interact with each other and therefore, a single neutron scattering interaction with one of the molecules induces a simultaneous transition in the other molecule as well (see SI section 5.3). The neutron transfers the energy required for both excitations, $\omega_{eff} = 2\omega_{J_{0\rightarrow1}}$. Only the low energy rotational transition (Figure 3 peak f) exhibits this behavior. The peak at 14.6 meV does not show the equivalent transition at 29.2 meV, therefore these transitions correspond to two different adsorbed species.

By looking at the effect of pressure on highly enriched pH_2 and nH_2 (see SI section 5.5.) on the phonon spectrum of hydrogen, we can calibrate a “representative density” required for the effect of pressure to be observable. The corresponding pressure of 2915 bar is consistent with a hydrogen density of 132 g/L and an estimated average H_2-H_2 intermolecular distance of 3.29 Å (see SI section 5.6).

Furthermore, Figure S18 shows the effect of temperature on the INS spectra at the composition $Mg(BD_4)_2 \cdot 1.46H_2$. Observing the evolution of the peaks with temperature, we see a different behavior corresponding to two different sites for hydrogen molecules. The peaks at 13.9 meV and 27.8 meV, assigned to D22, disappear simultaneously when the temperature reaches 95 K. The peak at 14.7 meV, attributed to D11, is still observed up to 185 K. Thus, INS enable an independent determination of the high H_2 density inside the pore, and the rotational spectrum confirms the existence of two distinct sites for the hydrogen molecules, fully in agreement with neutron diffraction data.

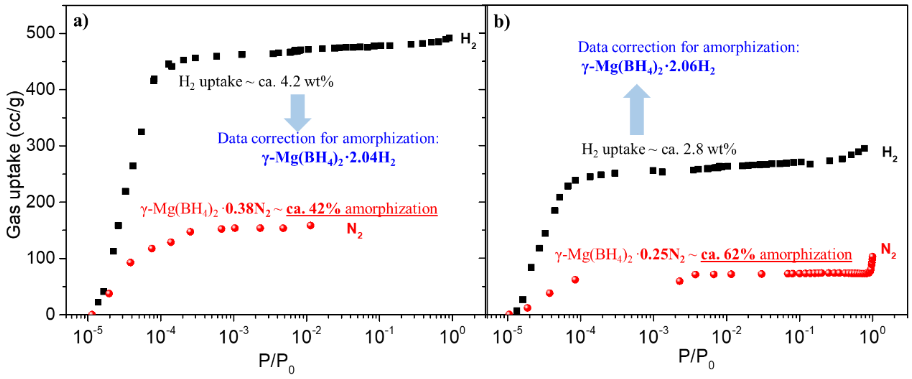

Figure 4. Adsorption isotherm of N_2 at 77 K and H_2 at 20 K, respectively. a) the first batch sample with short-term storage, exhibiting 42 % amorphization. Data correction for the amount of the amorphous phase results in γ-$Mg(BH_4)_2 \cdot 2.04H_2$. **b)** the second batch sample with long-term storage, exhibiting 62 % amorphization. Data correction for the amount of the amorphous phase results in γ-$Mg(BH_4)_2 \cdot 2.06H_2$.

To further verify the presence of two hydrogen adsorption sites and to characterize their thermodynamics with a macroscopic measurement, we used a volumetric Sieverts' apparatus, based on the measurement of the pressure variation with time for well calibrated volumes of gas equilibrated with the sample. Unlike diffraction methods, high-resolution adsorption measurements are not probing only the crystalline phase γ-$Mg(BH_4)_2$, and an amorphous fraction in all samples needs to be considered. We quantified the crystalline fraction of γ-$Mg(BH_4)_2$ by attributing the amount of the adsorbed nitrogen, as determined from a volumetric isotherm, to the adsorption in the crystalline phase only (see Chapter S4 for details and Figure 4 with two examples). Notably, the volumetric H_2 uptake corrected for the presence of the amorphous fraction consistently exhibits γ-$Mg(BH_4)_2{\cdot}2.04{\sim}2.06\ H_2$, very close to the limiting composition obtained from the crystallographic data ($\gamma-Mg(BH_4)_2{\cdot}2.33H_2$).

We observe about three times larger adsorption of H_2 as compared to N_2 for each sample. This is possibly a very rare example of two similar probe molecules, H_2 and N_2, with very different interactions with the topology of the surface, as pointed out previously[22]. Similar to the gas uptake in Figure 4, the Brunauer–Emmett–Teller (BET) surface area of γ–$Mg(BH_4)_2$ determined from N_2 isotherm at 77 K is only $S_{BET}(N_2) = 610\ m^2/g$, while the BET area calculated from the H_2 isotherm at 20 K is $S_{BET}(H_2) = 1787\ m^2/g$ or $1577\ m^2/g$, using a cross-sectional area of the hydrogen molecule based on the liquid or solid density, respectively (see Figure 4a). Furthermore, the total specific pore volume (*SPV*, max. uptake per sample mass / liquid gas density) of γ–$Mg(BH_4)_2$ determined from N_2 isotherm at 77 K is only 0.12 mL/g, while the *SPV* calculated from H_2 isotherm at 20 K is 0.51 mL/g. The crystallographic investigation reveals that the pore size and pore aperture in γ–$Mg(BH_4)_2$ allows both H_2 and N_2 to enter and reach the saturation. Thus, this study reveals unambiguous evidence for the strong correlation between the measured specific surface area and the probe molecule owing to different interactions with non-flat surface topology[22] rather than restricted access to the porous area of the structure mediated by pore aperture size. Please note that even though total uptake is reduced by aging due to sample amorphization (Figure 4b), the probe molecule effect consistently exhibits similar tendency (for the second batch, $S_{BET}(N_2) = 310$ m^2/g, $S_{BET}(H_2) = 1110$ m^2/g or 975 m^2/g, cross sectional area based on liquid or solid, respectively, and $SPV(N_2) = 0.08$ mL/g, $SPV(H_2) = 0.41$ mL/g, Figure 4b). Importantly, the ratios of total uptakes of H_2 and N_2, as well as of the respective BET areas and *SPV*s are very close to the ratio of H_2 and N_2 limiting uptakes seen by diffraction, namely 2.33/0.66 = 3.5 times. Moreover, diffraction studies show that the guest-host and the guest-guest interactions are responsible for the discrepancy in the surface area analysis, rather than the pores being too small for a particular particle as would be the case in size-exclusion.

Temperature-dependent gas adsorption experiments also provide access to the isosteric heats of adsorption, which characterize the strength of host-guest and guest-guest interaction. The isosteric heat of hydrogen adsorption as a function of the surface coverage is given in Figure 5a for γ–$Mg(BH_4)_2$ and copper benzene-1,3,5-tricarboxylate (CuBTC) MOF possessing similar pore diameter and H_2 uptake. The hydrogen adsorption enthalpy is almost constant at 6.1 kJ/mol up to ~50 % surface coverage and then decreases to 4.5 kJ/mol, while that of similar MOFs, e.g., CuBTC, typically decreases with coverage[23]. The decrease of the isosteric heat of adsorption at loading above 1.33H_2 per Mg can be explained by the host-guest and guest-guest repulsion involving atoms in the D22 site, which also coincides with the unit cell volume expansion by 0.67 % (while no expansion is observed upon filling the D11 site). Further evidence is also observed in the high-resolution low-pressure H_2 adsorption isotherm as shown in Figure 5b. In the logarithmic pressure scale, the isotherm exhibits clearly a two-step behavior which indicates adsorption at two sites with different adsorption enthalpies. Assuming monolayer adsorption in these sites, the maximum hydrogen content expected in the first adsorption site (D11) is ca. 57 % of the total uptake. Thus, the remaining ca. 43 % is assigned to be second site (D22), which also fits very well the NPD results.

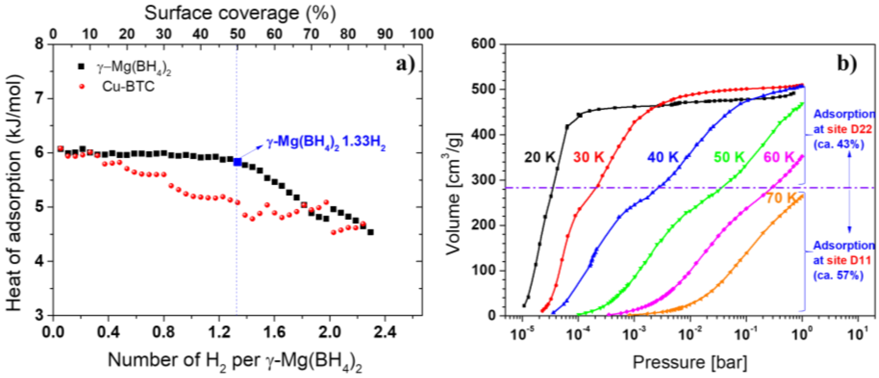

Figure 5. Characterization of hydrogen adsorption in γ-Mg(BH_4)$_2$ by volumetric methods. a) The comparison of the isosteric heat of hydrogen adsorption for γ-Mg(BH_4)$_2$ over MOFs (e.g. Cu-BTC possessing similar pore diameter and H_2 uptake) as a function of the surface coverage, recalculated to the H_2 loading per formula unit. Black square indicates γ-Mg(BH_4)$_2$ and red circle indicates Cu-BTC. **b)** High-resolution low-pressure H_2 adsorption isotherms for γ-Mg(BH_4)$_2$ at various temperatures between 20 and 70 K. With increasing temperature, two clear steps in the adsorption isotherms become visible.

4.4. Conclusions

γ-Mg(BH_4)$_2$ appears to be a unique hydridic framework with partially negatively charged H-atoms forming the pore's inner surface. Its small pores remarkably well distinguish N_2 and H_2 molecules, the latter having their own sites close to the H-atoms of the BH_4 groups. This work highlights an opportunity for development of hydridic porous frameworks for high-density hydrogen storage or as future materials potentially having high-T superconductivity and stability approaching ambient conditions. The high H_2 density in the pores may be due to the anisotropic shape of H_2 molecules normally seen at near ambient pressures as close-packed spheroids. In addition, at very high pressures, hydrogen molecules may show even more complex ordered patterns[24]. Association of H_2 molecules into so-called hydrogen clusters[25], where intermolecular distances of H_2 are in fact lengthened, has been reported. However, here we see a formation of smaller molecular units, di-hydrogen bonded tri-hydrogen, $B–H^{\delta-}\cdots H_2$, closer to what was previously defined theoretically as trihydrogen bonds involving a hydridic hydrogen or charge-inverted hydrogen bonds[26][27].

4.5. References

1. U. Eberle, M. Felderhoff, F. Schüth, Chemical and physical solutions for hydrogen storage. *Angew. Chemie - Int. Ed.* **48**, 6608–6630 (2009).

2. M. Hirscher, V. A. Yartys, M. Baricco, J. B. von Colbe, D. Blanchard, R. C. Bowman Jr., D. P. Broom, C. E. Buckley, F. Changn, P. Chen, Y. W. Cho, J.-C. Crivello, F. Cuevas, W. I. F. David, P. E. de Jongh, R. V. Denys, M. Dornheim, M. Felderhoff, Y. Filinchuk, G. E. Froudakis, David M. Grants, E. MacA. Gray, B. C. Hauback, T. He, T. D. Humphries, T. R. Jensen, S. Kim, Y. Kojima, M. Latroche, H.-W. Li, M. V. Lototskyy, J. W. Makepeace, K. T. Møller, L. Naheed, P. Ngene, D. Noréus, M. Nygård, S.-i. Orimo, M. Paskevicius, L. Pasquini, D. B. Ravnsbæk, M. V. Sofianos, T. J. Udovic, T. Vegge, G. S. Walkers, C. J. Webb, C. Weidenthaler, C. Zlotea, Materials for hydrogen-based energy storage – past, recent progress and future outlook. *J. Alloys and Compd.* **827**, 153548 (2020).

3. M. Hirscher, Hydrogen storage by cryoadsorption in ultrahigh-porosity metal-organic frameworks. *Angew. Chemie - Int. Ed.* **50**, 581-582 (2011).

4. L. J. Murray, M. Dinc, J. R. Long, Hydrogen storage in metal-organic frameworks. *Chem. Soc. Rev.* **38**, 1294-1314 (2009).

5. W. Grochala, P. P. Edwards, Thermal decomposition of the non-interstitial hydrides for the storage and production of hydrogen. *Chem. Rev.* **104**, 1283-1315 (2004).

6. Y. Filinchuk, B. Richter, T. R. Jensen, V. Dmitriev, D. Chernyshov, H. Hagemann, Porous and dense magnesium borohydride frameworks: Synthesis, stability, and reversible absorption of guest species. *Angew. Chemie - Int. Ed.* **50**, 11162-11166 (2011).

7. G. N. Iles, F. Devred, P. F. Henry, G. Reinhart, T. C. Hansen, Neutron diffraction studies for realtime leaching of catalytic Ni. *J. Chem. Phys.* **141**, 034201 (2014).

8. C. M. Brown, Y. Liu, T. Yildirim, V. K. Peterson, C. J. Kepert, Hydrogen adsorption in HKUST-1: a combined inelastic neutron scattering and first-principles study. *Nanotechnology* **20**, 204025 (2009).

9. I. F. Silvera, The solid molecular hydrogens in the condensed phase: Fundamentals and static properties. *Reviews of Modern Physics* **52**, 393-452 (1980).

10. A. Davoodabadi, A. Mahoudi, H. Ghasemi, The potential of hydrogen hydrate as a future hydrogen storage medium. *iScience* **24**, 101907 (2021).

11. H. Liu, I. I. Naumov, R. Hoffmann, N. W. Ashcroft, R. J. Hemley, Potential high-Tc superconducting lanthanum and yttrium hydrides at high pressure. *PNAS* **114**, 6990-6995 (2017).

12. S. S. Batsanov, Van der Waals Rradii of hydrogen in gas-phase and condensed molecules. *Struct. Chem.* **10**, 395-400 (1999).

13. R. M. Hazen, H. K. Mao, L. W. Finger, R. J. Hemley, Single-crystal x-ray diffraction of n-H_2 at high pressure. *Phys. Rev. B* **36**, 3944-3947 (1987).

14. A. J. Ramirez-Cuesta, Y. Q. Cheng, Studying materials and processes with VISION, VirtuES and ICEMAN. Modeling INS data with DFT methods. *Hamon.* **30**, 154-159 (2020).

15. I. F. Silvera, The solid molecular hydrogens in the condensed phase: Fundamentals and static properties. *Rev. Mod. Phys.* **52**, 393-452 (1980).

16. P. C. H. Mitchell, S. F. Parker, A. J. Ramirez-Cuesta, J. Tomkinson, Eds., *Vibrational Spectroscopy with Neutrons With Applications in Chemistry, Biology, Materials Science and Catalysis* (World Scientific Publishing, Singapore, 2005).

17. J. Bahadur, C. I. Contescu, A. J. Ramirez-Cuesta, E. Mamontov, N. C. Gallego, Y. Q. Cheng, L. L. Daemen, Y. B. Melnichenko, Properties of immobile hydrogen confined in microporous carbon. *Carbon* **117**, 383-392 (2017).

18. J. A. Young, J. U. Koppel, Slow neutron scattering by molecular hydrogen and deuterium. *Phys. Rev.* **135**, A603-A611 (1964).

19. J. Z. Larese, T. Arnold, L. Frazier, R. J. Hinde, A. J. Ramirez-Cuesta, Direct observation of H_2 binding to a metal oxide surface. *Phys. Rev. Lett.* **101**, 165302 (2008).

20. L. Ulivi, M. Celli, A. Giannasi, A. J. Ramirez-Cuesta, D. J. Bull, M. Zoppi, Quantum rattling of molecular hydrogen in clathrate hydrate nanocavities. *Phys. Rev. B* **76**, 161401(R) (2007).

21. T. A. Strobel, A. J. Ramirez-Cuesta, L. L. Daemen, V. S. Bhadram, T. A. Jenkins, C. M. Brown, Y. Q. Cheng, Quantum dynamics of H_2 trapped within organic clathrate cages. *Phys. Rev. Lett.* **120**, 120402 (2018).

22. T. Düren, F. Millange, G. Férey, K. S. Walton, R. Q. Snurr, Calculating geometric surface areas as a characterization tool for metal - organic frameworks. *J. Phys. Chem. C.* **111**, 15350-15356 (2007).

23. M. Hirscher, B. Panella, B. Schmitz, Metal-organic frameworks for hydrogen storage. *Microporous Mesoporous Mater*. **129**, 335-339 (2010).

24. C. J. Pickard, R. J. Needs, Structure of phase III of solid hydrogen. *Nat. Phys.* **3**, 473-476. (2007).

25. W. L. Mao, J. Mao, A. F. Goncharov, V. V. Struzhkin, Q. Guo, J. Hu, J. Shu, R. J. Hemley, M. Somayazulu, Y. Zhao, Hydrogen clusters in clathrate hydrate. *Science* **297**, 2247-2249 (2002).

26. C. F. Matta, L. Huang, L. Massa, Characterization of a trihydrogen bond on the basis of the topology of the electron density. *J. Phys. Chem. A* **115**, 12451-12458 (2011).

27. M. Jabłoński, Charge-inverted hydrogen bond vs. other interactions possessing a hydridic hydrogen atom. *Chem. Phys.* **433**, 76-84 (2014).

Chapter 5. Helium and Neon Adsorption in Porous Magnesium Borohydride Studied by Neutron and X-Ray Powder Diffraction and DFT Simulation

Xiao Li[1], *Iurii Dovgaliuk*[2,3], *Dmitry Chernyshov*[2], *Sergio Posada Pérez*[1], *Geoffroy Hautier*[1], *Michael Heere*[4], *Matthias Frontzek,*[5] *Simon Kimber*[5] *and Yaroslav Filinchuk*[1*]

[1]Institute of Condensed Matter and Nanosciences, Universite Catholique de Louvain, place L. Pasteur 1, B-1348 Louvain-la-Neuve, Belgium

[2]Swiss-Norwegian Beamlines at the European Synchrotron Radiation Facility, 71 avenue des Martyrs, Grenoble, 38000, France

[3]Institut des Matériaux Poreux de Paris, UMR 8004 CNRS, Ecole Normale Supérieure, Ecole Supérieure de Physique et de Chimie Industrielles de Paris, PSL Université, Paris, 75005, France

[4]Institute for Applied Materials – Energy Storage Systems (IAM–ESS), Karlsruhe Institute of Technology (KIT), Hermann–von–Helmholtz–Platz 1, 76344 Eggenstein–Leopoldshafen, Germany

[5]Neutron Scattering Division, Oak Ridge National Laboratory, 1 Bethel Valley Rd., Oak Ridge, Tennessee 37831, USA

Abstract

Helium and neon are light noble gases applied in biomedicine, cryogenics, lighting etc. We studied their adsorption in a crystalline porous framework, γ-$Mg(BH_4)_2$*, using in situ diffraction and density functional calculations (DFT). Adsorption isobars of He and Ne were plotted from sequential Rietveld refinement based on synchrotron X-ray powder diffraction data made a sub-LN2 temperatures. These unique experiments were validated by neutron powder diffraction using isotopically substituted γ-*$Mg(^{11}BD_4)_2$*. At lower temperatures we observed a second adsorption site for Ne, however, not for He, which is usually considered to be smaller than Ne. By means of DFT simulations, we calculated the adsorption energy for light noble gasses (He, Ne and Ar), shedding light on guest-guest interactions, and built P-T phase diagrams.*

5.1. Introduction

Helium (He) and Neon (Ne) are light noble gases with small atomic size and low polarizability. Helium is utilized in biomedicine as healing gas and cooling agent for superconducting magnets. In the meantime, it is an essential substance used in material manufacturing industry, nuclear reactors, leak monitoring, and automobile gasbags due to its inertness and small size[1]-[4]. Neon is generally known for its application in advertising lighting. It is also applied in medical lasers[5] for treatment of neck and head cancer. Due to its low liquefaction temperature, and in particular, its liquid-gas equilibrium curve covering around 40 K temperature range where no other liquids occur, neon is a very attractive gas for cryogenic applications[6][7]. Currently helium and neon are extracted from natural gas or liquid air by fractional distillation. Since this is an energy-costly process, these are expensive products thus the development of storage and transportation of He and Ne is of importance.

Physisorption is a potential answer to the need of storage, separation and transportation of gases. In recent years, crystalline porous frameworks, such as metal organic frameworks (MOFs), porous coordination polymers (PCPs), have raised a great interest among researchers due to their high surface area, functionalized pore surface and tunable structure over other porous materials[8][9]. These materials can not only be applied for gas storage and separation, but also for catalysis, sensing and so on[10]-[12]. There are known examples of He and Ne adsorption in silicalite (porous SiO_2)[13], zeolites[14]–[18], active carbon[19], carbon nanotubes[20][21] and nanohorns[22]. However, these are limited reports on He and Ne adsorption, and even less is known for adsorption in crystalline porous frameworks. Peter A. Wood et al[23] first reported experimental Ne adsorption within a metal-organic framework using PCN-200 and NiMOF-74 in the temperature range 100-295 K and pressures up to 100 bar. Hulvey et al[24] studied Ne adsorption both experimentally and computationally on HKUST-1 at

40-60 K, up to 0.8 bar. Barreto et al[25] also reported Ne adsorption on HKUST-1 and UiO-66 over a wide pressure and temperature ranges, firstly building a database of Ne adsorption on these two well known MOFs. Ribeiro et al[7] investigated Ne adsorption in MOF $Co_3(ndc)_3(dabco)$ from 77 K to 320 K and up to 100 bar; its behavior is similar to Ne adsorption in HKUST-1.

Low adsorption enthalpies of He and Ne require low temperature conditions, below the temperatures of liquid nitrogen (LN2), making these experiments less accurate with respect of the determination of microscopic properties[21]. Therefore, molecular simulation by DFT theory becomes a good tool for understanding and predicting the adsorption behavior of small noble gases in microporous frameworks. Ideally, simulations should be coupled with experimental structural studies. In this work, we investigated He and Ne adsorption in γ-$Mg(BH_4)_2$, the first complex hydride with porous structure[26]. This framework contains a 1D porous channel with 7 Å diameter in the wider part, allowing small molecules to be adsorbed and showing interesting host-guest interactions owing hydridic nature of the pore surface. X-ray synchrotron and neutron powder diffraction was performed below and above LN2 temperatures, allowing to locate guests and obtain the microscopic picture of atomic interactions. This serves as experimental basis for DFT calculations giving detailed insight into guest-host and guest-guest interactions, estimates of the heats of adsorption and predict the P-T phase diagrams.

5.2. Methods

***In situ* synchrotron radiation X-ray powder diffraction (SR-XRD) studies.** All the synchrotron powder diffraction data were collected at BM01 (Swiss-Norwegian Beam Lines, SNBL) at the European Synchrotron Radiation Facility (ESRF, France). The sample was loaded in a glass capillary connected with a gas dosing system, equipped with an electronic transducer (0.01 bar accuracy). The series of isobar experiments of neon (Ne) and helium (He) have been performed using synchrotron radiation with λ = 0.78487 Å. The isobar experiments were collected at p(Ne) = 10 bar from 35.7 K to 100 K and at p(He) = 7.19 bar from 18.8 K to 114 K, respectively. (See Figure 1). An Oxford Cryostream 600+ was operated at temperatures above 80 K, while open helium blower Helijet from Agilent was used below 80 K. *In situ* gas adsorption crystallography below LN2 temperatures is new to SNBL and to the ESRF experience in general, therefore we had to learn the behavior of the system and operational parameters allowing a gradual temperature change, control over icing of air on the surface of the capillary etc.

Neutron Powder Diffraction (NPD) studies. NPD data were collected at the instrument HB-2C Wide Angle Neutron Diffractometer Squared (WAND2), which is a neutron diffractometer with a position sensitive detector and oscillating collimator at the High-Flux-Isotope Reactor (HFIR) at Oak Ridge National Laboratory (ORNL), Oak Ridge, TN, USA[27]. The take-off angle was fixed at 51.5° and used in combination with the Ge-monochromator (113) reflection at a wavelength of λ = 1.482 Å. The sample was prepared with ^{11}B instead of natural B and deuterium (D=^{2}H) was used instead of ^{1}H, thus avoiding high absorption of the neutron beam and the incoherent scattering rising rise to a high background. The sample holder was a cylindrically-shaped Al sample holder, it contributed to the patterns with strong Al Bragg peaks, which we had to exclude from the refinements. A custom-made high-pressure rig was employed for various high gas pressures. The sample holder connected to the gas rig was inserted into a helium closed cycle refrigerator. The series of isobar experiments was done at p(Ne) = 8.5 bar from 33 K to 83 K and p(He) = 45 bar from 6.3 K to 121 K, respectively.

Computational Details. The periodic DFT based calculations described in the present work have been carried out using the Vienna *ab−initio* simulation package (VASP)[28]. The core electrons effect on the valence region was described by the projector augmented wave (PAW) method by Blöchl[29] as implemented by Kresse and Joubert[30]. The kinetic energy cut−off for the plane−wave basis set was truncated at 500 eV. The threshold for the convergence of the electronic optimization was 10^{-5} eV while the relaxation of the atomic positions was allowed until the forces acting on all the atoms were smaller than 0.01 eV $Å^{-1}$. For each of our simulations, we have optimized the geometries and evaluated the energies using the Perdew-Burke-Ernzerhof (PBE) exchange-correlation functional[31] and taking spin polarization into account. The long−range dispersion interactions were added to the PBE functional via the zero damping D3 (zero) semi empirical methods proposed by Grimme[32]. Γ-centered Monkhorst-Pack[33] grid of 5×5×5 **k**−points in the reciprocal space were used for the simulation of $Mg(BH_4)_2$ material.

The γ-$Mg(BH_4)_2$ structure has the space group $Ia\bar{3}d$ where Mg atoms occupy 24d Wyckoff positions are 8-fold coordinated to BH_4 tetrahedra. Boron atoms are placed on 48g Wyckoff positions. Due to the computational cost, we have employed the primitive cell of γ-$Mg(BH_4)_2$ available in Materials Project Database[34] (mp-1200811), that contains 12 Mg, 24 B, and 96 H atoms. The He, Ne, and Ar atoms have been placed initially on the 32e and 48g positions following the experimental evidence. Two different ways to fill the available sites for γ-$Mg(BH_4)_2$ with these noble gases (NG) have been considered in order to investigate the preferred adsorption site; the first model fills first 32e sites, with a maximum NG/Mg ratio of 1.33. Then, the adsorption on 48g site is carried out until a maximum NG/Mg ratio of 3.33. The second model mixes the adsorption on both sites randomly, without preference.

The adsorption energy has been calculated according to the following formula:

$$E_{ads} = E_{NG/\,\gamma-\mathrm{Mg(BH4)2}} - (E_{\gamma-\mathrm{Mg(BH4)2}} + E_{NG}) \qquad \text{(Eq. 1)}$$

where $E_{NG/\,\gamma-\mathrm{Mg(BH4)2}}$ is the energy of the noble gas atoms adsorbed on γ-$Mg(BH_4)_2$ structure, $E_{\gamma-\mathrm{Mg(BH4)2}}$ is the energy of the clean porous material, and E_{NG} is the energy of the isolated noble gas (mp-23158, mp-111, and mp-23155 for He, Ne, and Ar respectively, available in Materials Project Database).

The simulations were performed at 0 K and the effect of temperature and pressure were considered by means of the grand canonical approach. The thermodynamic potential of each phase can be written as the Legendre transform of the Gibbs free energy as follows:

$$\gamma = G - n_{NG} \times \mu_{NG} \qquad \text{(Eq. 2)}$$

where G is the free energy approximated by the DFT energy for a particular concentration of He, Ne, and Ar. The n_{NG} term represents the number of noble gas atoms adsorbed on γ-$Mg(BH_4)_2$ and μ_{NG} is the chemical potentials of noble gas as a function of T and P. One can express the μ_{NG} according to Eq.2

$$\mu_{NG}\,(T,p) = E_{DFT/NG} + \Delta\mu_{NG}\,(T,p) \qquad \text{(Eq. 3)}$$

where $E_{DFT/NG}$ is the DFT energy of the noble gas and $\Delta\mu_{NG}\,(T,p)$ defines how the chemical potential changes with T and P. For the noble gases in the material, the variation of μ_{NG} is related to the variation of translational partition function:

$$q_t = \left(\frac{2\pi m k_b T}{h^2}\right)^{3/2} V$$

$$\mu(T,p) = -RTln(q_t) + RTln(\frac{P}{P_0}) \qquad \text{(Eq. 4)}$$

where, V is the volume of the porous material, h is the Planck constant, m is the mass of the noble gas, k_B is the Boltzmann constant, T is the temperature in K, and P is the pressure in bar expressed relative to standard state (1 bar).

5.3. Results and Discussion

Crystal structure determination and refinement. For the structural determination of gas-loaded in γ-Mg(BH$_4$)$_2$, the atomic positions of the framework atoms have been fixed. The variable occupancies of Ne / He atoms have been implemented for the global optimization in FOX[35]. The data from the lowest temperatures (high gas loading) were used first in order to localize Ne / He atoms. From SR-XRD measurements, we found that He only takes place in the 32*e* crystallographic position, while Ne occupies 32*e* and 48*g* crystallographic positions at full loading, the same as H$_2$, described in the previous chapter. The sequential variable-temperature refinement of the Ne / He atoms uptakes was performed using Fullprof[36], with the refinement of overall isotropic atomic displacement parameters for the framework and guests and occupancies of Ne / He atoms. (See Figure 2). Ne in the 32e site was refined with anisotropic displacement parameters.

Figure 1 shows the evolution of powder patterns of: **a)** Ne and **b)** He adsorbed by γ-Mg(BH$_4$)$_2$, investigated by SR-XRD. The unit cell of γ-Mg(BH$_4$)$_2$ stays practically unchanged with loading because the peaks' positions do not change significantly. On the other hand, the integral intensities of peaks at $2\theta = 6.95°$ and $2\theta = 10.66°$ shows a dramatic change upon Ne uptake. This phenomenon allows us to perform refinement a γ-Mg(BH$_4$)$_2$·xNe with high accuracy. The

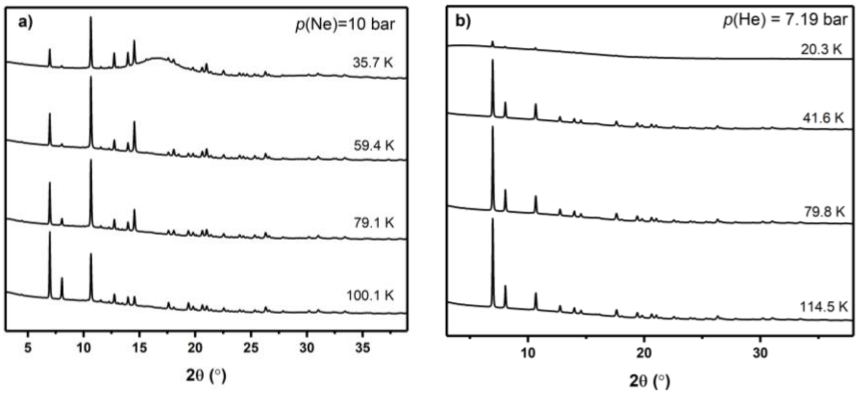

Figure 1. SR-XRD powder pattern of **a)** Ne adsorbed by γ-Mg(BH$_4$)$_2$ at 10 bar and **b)** He adsorbed by γ-Mg(BH$_4$)$_2$ at 7.19 bar, at four representative temperatures.

behavior was also observed for He adsorbed in γ-Mg(BH$_4$)$_2$, despite the change of relative intensities was less significant.

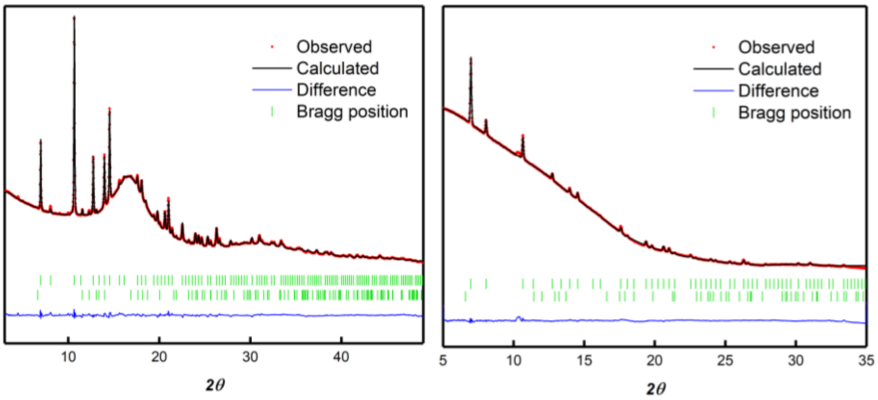

Figure 2. **Left,** Rietveld refinement of Ne in γ-Mg(BH$_4$)$_2$·1.67Ne (p (Ne) = 10 bar, T = 35.7 K; a = 15.8092 (2) Å; R$_{Bragg}$ = 8.69 %; RF = 13.00 %. **Right,** Rietveld refinement of He in γ-Mg(BH$_4$)$_2$·1.32He (p (He) = 7.19 bar, T = 18.8 K; a = 15.8057 (5) Å; R$_{Bragg}$ = 23.6 %; RF = 27.1 %. The second line of Bragg peaks is from ice condensed on outer walls of capillaries during this sub-LN2 experiments.

The Reitveld refinements of Ne and He loaded framwork is shown (Figure 2) for the highest loadings, correponding to the lowest temperatures (T$_{(Ne)}$ = 35.7 K, T$_{(He)}$ = 18.8 K) of the isobaric measurements by SR-XRD. Firstly, the guest atoms, Ne and He were localized by using FOX. At the condition of p = 10 bar, T = 35.7 K, Ne shows two adsorbed sites in γ-Mg(BH$_4$)$_2$, which are *32e* crystallographic positions, denoted as Ne1 site, and *48g* crystallographic position, denoted as Ne2 site (see Figure 3b). Ne1 site is situated along the porous channel of γ-Mg(BH$_4$)$_2$, running along the diagonal of the cubic unit cell, thus the atomic coordinates are constrained to be identical (x x x). The maximum uptake of Ne1 site is 32 atoms per unit cell, leading to a limiting composition of the structure γ-Mg(BH$_4$)$_2$·1.33Ne, considering there are 24 Mg atoms per unit cell. Ne2 is not located on the 3-fold axis, instead, it is of-centred from the channel axis. Due to a short distance of 1.94 Å of Ne2 … Ne2 between the two bypassing porous channels (this distance excludes their simultaneous occupation), the limiting value for Ne2 site occupancy is

50%. This leads to an extra one Ne atom per formula unit at the maximum loading, with the total limiting composition accounting for the two Ne sites, γ-$Mg(BH_4)_2 \cdot 2.33Ne$. Helium, usually considered to be smaller than neon, can be expected to show the same loading or higher, however, it only appears in the *32e* site (denoted as He1, identical to Ne1) down to the lowest temperatures (18.8 K) of the SR-XRD experiment.

Interestingly, both systems reveal a rearrangement of the guest, which is located near the center of the pore at low loadings, but predominantly fills a position near the aperture of the pore at higher loadings. The first site is denoted as Ne11 and He11 respectively for the two systems (this position is close to the center of the pore with coordinates *1/8 1/8 1/8*), while the second is denoted as Ne12 and He12, respectively. This behavior is similar to Ar, described in the Chapter 3.

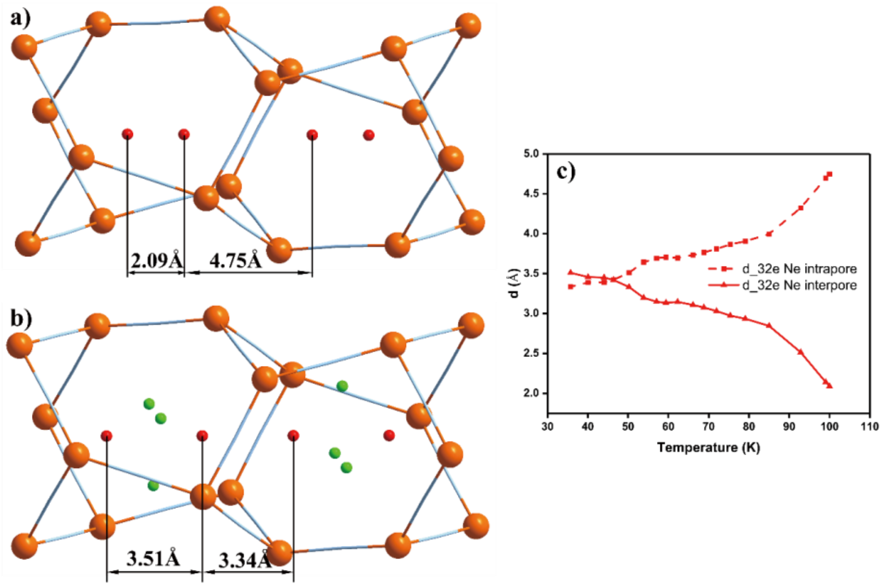

Figure 3. Two crystallographic positions of Ne adsorbed inside the channel of γ-$Mg(BH_4)_2$ are presented as red (Ne1) and green (Ne2) spheres. **a)** The 32*e* Ne1 position is located closer to the center of the pore at p(Ne) = 10 bar, T = 100 K. **b)** p(Ne) = 10 bar, T = 35.7 K the maximum loading is observed, on one hand owing to filling the of the second position, Ne2, on the other – due to the relocation of the Ne1 towards the aperture, allowing two Ne1 atoms per pore, illustrated by **c)** the variation of intrapore and interpore Ne1…Ne1 distances with temperatures.

This redistribution, modelled with two sites can be simulated with only one site having a variable position (denoted as Ne1). Taking Ne adsorption as an example, at *p*(Ne) = 10 bar, T = 100 K (Figure 3a), the distance between two Ne atoms of interpore is 2.09 Å while the intrapore is 4.75 Å. Due to the fact that the interpore distance of 2.09 Å is too short to allow two Ne atoms to occupy the position at the same time, it leads to the limiting capacity to 0.66 Ne atoms per γ-$Mg(BH_4)_2$, namely γ-$Mg(BH_4)_2\cdot0.66Ne$. As the temperature decreases, the Ne1 atom will move to the aperture of the pore and becoming evenly distributed along the channel at a nearly equal distances, with interpore distance of 3.51 Å and intrapore of 3.34 Å (Figure 3b, *p*(Ne) = 10 bar, T = 35.7 K). This rearrangement allows for two Ne per pore, resulting a double limiting capacity of Ne adsorbed by γ-$Mg(BH_4)_2$, i.e., γ-$Mg(BH_4)_2\cdot1.33Ne$. In addition, the longer distance of interpore opens the space and allows for the appearance of the Ne2 site (shown as the green spheres in Figure 3b) at even lower temperature, and further increases the limiting Ne capacity in γ-$Mg(BH_4)_2$ to γ-$Mg(BH_4)_2\cdot2.33Ne$.

He adsorption exhibits similar redistribution behavior for the He1 site, as shown in Figure 4. The initial distances of interpore and intrapore at *p*(He) = 7.19 bar, T = 114 K, are 1.2 Å and 5.63 Å, respectively (figure 4a). In this case, only one He atom can be allowed to occupy one pore (γ-$Mg(BH_4)_2\cdot0.66He$). While the temperature decreases to 18.8 K, the interpore distance becomes 2.81 Å, allowing a chance for two He atoms per pore (γ-$Mg(BH_4)_2\cdot1.33He$) as the van der Waals radius of He is 1.43 Å [ref. https://www.webelements.com/-helium/atom_sizes.html]. Compared to Ne1, He1 atoms are closer to the centre of the pore at higher temperatures, and couldn't open large enough space for extra He atoms to take place in 48g crystallographic positions at lower temperatures.

The sequential refinement of Ne and He atoms uptakes VS temperatures was performed using Fullprof subsequently and the results were extracted as shown in Figure 5. As described above, Ne atoms firstly occupy *32e* crystallographic positions along the porous channel, shown as the green curve in figure 5 left. At the temperature below 60 K, the second site, Ne2, starts to be occupied (red curve in figure 5 left) while the first site Ne1 still not fully reaches its capacity at 1.33 Ne atoms per Mg. With gradually the Ne2 site loading, the interpore distance between Ne1 site shows a visible faster increment from 60 K to 45 K (see figure 3c, below 60 K), where the Ne2 site uptake from 0 to 0.4 Ne atoms per Mg. The total uptake isobar curve reveals a double-adsorption-step, of which the adsorption behavior could be hardly explained by volumetric or gravimetric method in a macroscopic view. He uptake isobar is simpler than Ne. Its limiting capacity finally reaches1.33 atoms per Mg, however, we found that the error of He uptake is relatively larger, showing as the data points "fluctuating up

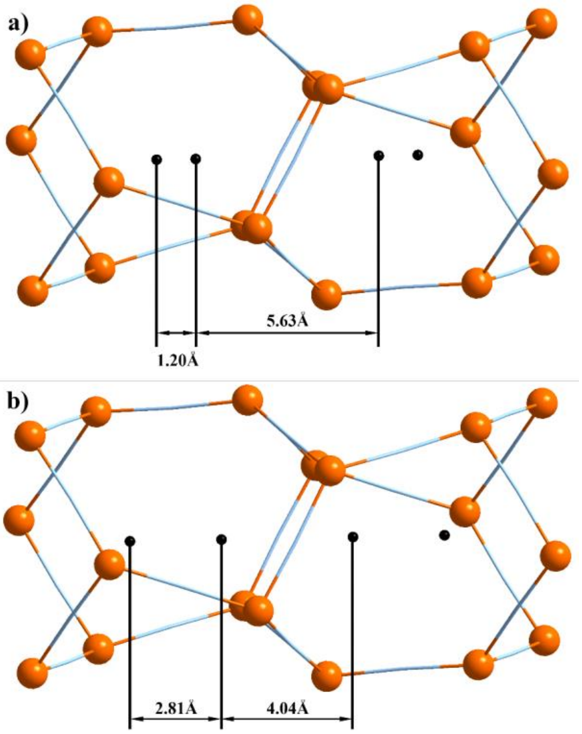

Figure 4. *32e* crystallographic positions of He adsorbed in the porous channel of γ-$Mg(BH_4)_2$ and the redistribution behavior. **a)** *p*(He) = 7.19 bar, T = 114 K, **b)** *p*(He) = 7.19 bar, T = 18.8 K. Mg atoms shown as orange spheres, tetrahedral BH_4 groups shown as blue sticks, He1 atoms shown as black spheres.

and down” in the Figure 5 right. Since He atom has a low electron density, it is not sensitive to X-ray and cannot be accurately located either. In order to correct and verify He adsorption behavior, we use neutron powder diffraction to accurately determine the location and occupancy of He in γ-$Mg(BH_4)_2$ as He atom has a large neutron scattering length.

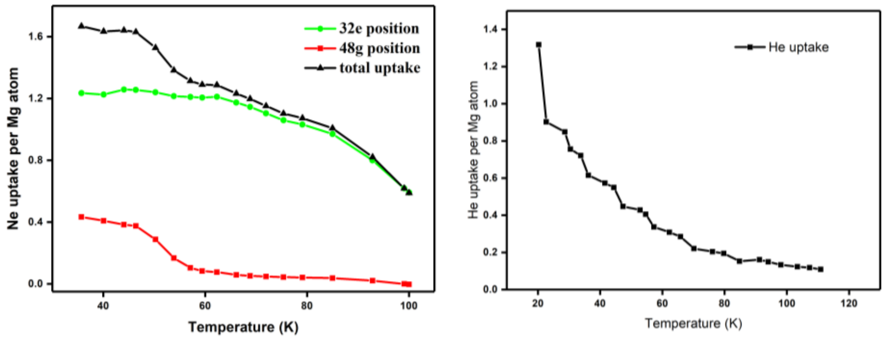

Figure 5. Isobar uptakes of Ne (left) and He (right) VS temperatures at p(Ne) = 10 bar and p(He) = 7.19 bar.

Detailed NPD data collection was mentioned above in the experimental section. Ne and He adsorption by isotopically enriched ^{11}B and ^{2}H of γ-$Mg(BH_4)_2$, namely γ-$Mg(^{11}BD_4)_2$, were carried out at p(Ne) = 8.5 bar from 33 K to 83 K and p(He) = 45 bar from 6.3 K to 121 K, respectively. The same steps of extracting Ne and He uptake and atomic distances were utilized to obtain their adsorption behaviors. First of all, the He adsorption behavior by γ-$Mg(^{11}BD_4)_2$ stays identical as that observed by SR-XRD (see Figure 6). Only *32e* position was occupied even in the cryogenic condition of T = 6.3 K at p(He) = 45 bar. An atomic redistribution of He at *32e* position was observed as well, that the movement direction of the atoms is from the center of the pore to the apertures, as the temperature decreases. At 121 K, the interpore distance of He atoms is 1.41 Å and intrapore distance is 5.37 Å, while at 6.3 K the values of interpore and intrapore distance change to 2.61 Å and 4.18 Å, respectively. Secondly, the isobar uptake of He stays a high consistency with that extracted from SR-XRD results and showing a more smoother curve due to the smaller errors.

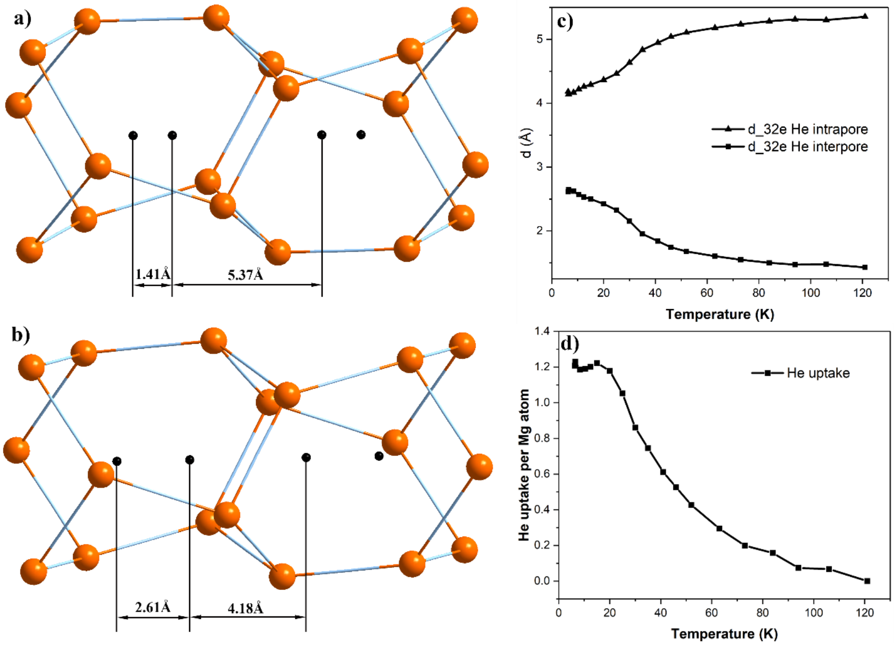

Figure 6. He adsorption behavior in γ-Mg($^{11}BD_4$)$_2$ detected by NPD analysis. **a)** *32e* crystallographic positions of He adsorbed in the porous channel of γ-Mg($^{11}BD_4$)$_2$ at *p*(He) = 45 bar, T = 121 K. **b)** *p*(He) = 45 bar, T = 6.3 K, **c)** the variable distance of inter / intrapore of He VS temperatures. **d)** isobar of He uptake VS temperatures. Errors are manually corrected based on the initial uptake of He at 121 K should be zero. Mg atoms shown as orange spheres, tetrahedral $^{11}BD_4$ groups shown as blue sticks, He1 atoms shown as black spheres.

The adsorption behavior of Ne analyzed by NPD (See Figure. 7) is consistent with that analyzed by SR-XRD. Two sites occupancy and *32e* site atomic redistribution were also observed.

To further understand the interaction of guest-guest and guest-host systems, and to better explain the different adsorption sites showing in two similar noble gases, we use DFT calculation to simulate He, Ne, as well as Ar (Chapter 3), since we understand very well the Ar adsorption behavior in γ-Mg(BH_4)$_2$. As a larger size gas atom compared to He and Ne, Ar atoms only occupy *32e* crystallographic position close to the centre of the pore at lower loadings and redistribute to the pore apertures when the loading increases. For Ar, there is no second site appearing at lower T or higher P.

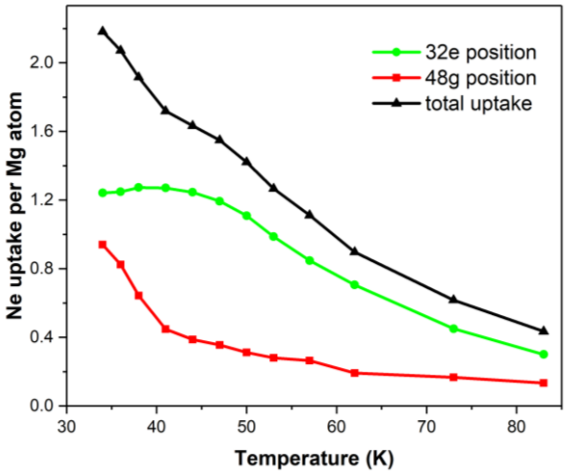

Figure 7. Adsorption isobar of Ne at 8.5 bar pressure obtained from NPD, along with contributions of the two sites (32*e* for Ne1 and 48*g* for Ne2).

Results of the computational study. DFT calculations suggest that He, Ne, and Ar prefer to be adsorbed on 32e sites. When the noble gases (NG) occupancy has values below to 1.33 NG/Mg ratio (full occupancy of 32e sites), to fill the 32e sites is lower in energy with respect to configurations that contain NG adsorbed on both 32e and 48 g sites. When the 32e site is totally filled, the NG atoms are placed on 48g. Therefore, DFT simulations are in agreement with experimental observations (Figures 3, 4, and 6) where it is evidenced that the 32e site is filled first. However, the computed adsorption enthalpy illustrated in Figure 8 shows remarkable differences between the He, Ne and Ar. First of all, the binding energy is stronger (more negative) as higher is the size of NG. Thus, lower adsorption energies are predicted for He atoms in comparison to the adsorption of Ne and Ar. Nevertheless, the amount of Ne and Ar is limited on γ-$Mg(BH_4)_2$ material.

The experiments have shown the He deposition until loading the 32e sites, although simulations suggest that it can fill both 32e and 48g sites of γ-$Mg(BH_4)_2$. As is plotted in Figure 8a, the adsorption energy *per* He atom is very weak -around 2.5 kJ/mol- and remains constant during the adsorption on 48g sites (from 1.33 He/Mg ratio forward). Despite of the guest-guest interaction energy is not repulsive, the adsorption enthalpy is very weak in comparison to other noble gases and very low temperatures are required to investigate the gas adsorption. The He adsorption in the center of the pore is slightly favorable than in the aperture, in agreement with NPD experiments. However, the weak binding energy predicted by DFT simulations may imply the difficulty to reach higher loadings from the experimental point of view.

With respect to Ne adsorption, the DFT results suggest that the Ne atoms can occupy half of the 48g sites after filling the 32e. DFT simulations at 0 K agree with the experimental results at 35 K and 10 bar (Figures 3 and 5 left) where the 48g site is partially filled with an adsorption enthalpy around 5 kJ/mol. Figure 8a illustrates that the adsorption energy becomes weaker at ratios greater than 2.33 Ne/Mg. This is because the Ne-Ne interaction is repulsive due to the close distance between 48g sites. Regarding Ar adsorption, our simulations predict a strong Ar-host interaction (>15 kJ/mol) when Ar atoms are adsorbed on 32e sites. Nevertheless, the results show an energy loss and large guest-guest repulsion when Ar is deposited on 48g sites after filling the 32e (from 1.33 Ar/Mg ratio forward). Figure 8a clearly show that the interaction energy decreases, although it is important to remark that the Ar-host interaction is more favorable than the Ne-host and He-host at ratios between 1.33-2.00 NG/Mg. We have observed a slight distortion of the γ-$Mg(BH_4)_2$ material due to the large Ar-Ar interaction, that displace Ar atoms from 48g sites to avoid the repulsion. At ratios greater than 2.33 Ar/Mg, the interaction energy between Ar and the host is repulsive (positive values), as is observed in Figure 8a.

DFT simulations overestimate the adsorption enthalpy of Ar (20~ kJ/mol) in comparison to the experimental evidence reported in Figure 8b. Nevertheless, these large values are obtained when Ar atoms are in the center of the pore (16b sites). In contrast to He and Ne, where the difference in energy between the center of the pore and the slightly displaced site (32e) is not significant, Ar clearly prefers to fill first the center of the pore. When the center is filled (0.66 Ar/Mg ratio), then Ar can be slightly displaced to 32e sites to accommodate one more Ar per pore, although it implies an energy cost as is reported in Figure 8a.

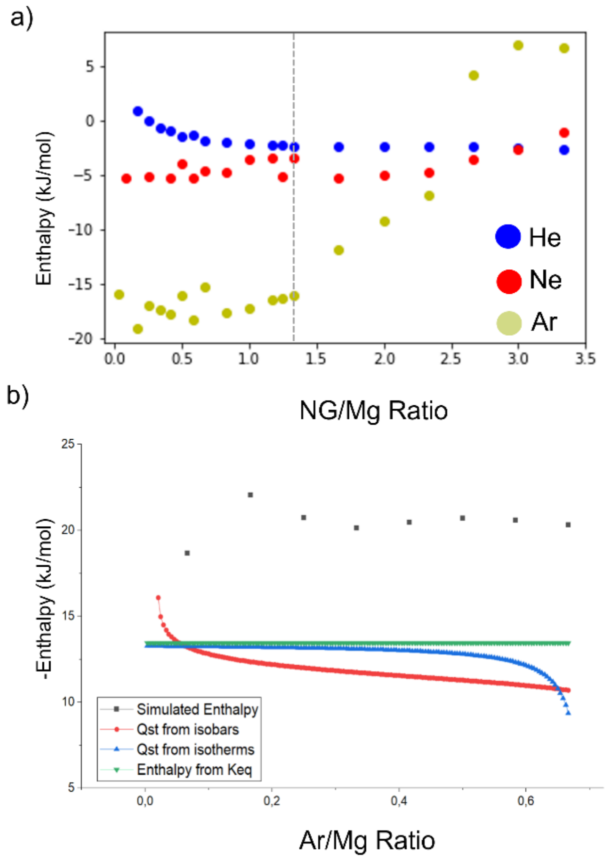

Figure 8. a) Interaction energy *per* He, Ne, and Ar atom on γ-$Mg(BH_4)_2$. Grey dashed line indicate the ratio (1.33 NG/Mg) where 32e site is totally filled. **b)** Comparison of Ar adsorption enthalpy plotted by experimental results and DFT simulations.

The grand potential phase diagrams (Figure 9) have been computed as a function of the temperature and pressure. With respect to He/γ-$Mg(BH_4)_2$ systems, a biphasic phase diagram is predicted (Figure 9a). At very low temperatures, one can observe that the full He-filled material is the most stable phase, whereas increasing the temperature implies the total desorption of He atoms. It can be explained by the weak interaction energy between He and γ-$Mg(BH_4)_2$. Despite our simulations at 0 K predict the favorable accommodation of He on both

32e and 48g sites, the adsorption energy is less than 2.5 kJ/mol which hinder the detection of high He loadings. Regarding Ne atoms, a few stable phases with different concentrations of Ne have been found (Figure 9b). The grand potential phase diagram shows the full loading of 32e sites between 40-80 K (1.33Ne/Mg ratio) and the partial adsorption of Ne on 48g sites at low temperatures (2.33 Ne/Mg ratio), in perfect agreement with the adsorption isobar plotted in Figure 7. Finally, the grand potential phase diagram of Ar@-γ-$Mg(BH_4)_2$ system (Figure 9c) discards the adsorption of Ar on 48g sites. Ar takes up the center of the pore (0.66 Ar/Mg ratio) at temperatures around 100-150 K and at low temperature is observed the distribution of Ar to the aperture sites (1.33 Ar/Mg ratio). According to our simulations, lower temperatures are required to slightly displace Ar atoms from centre to 32e sites, due to the predicted guest-guest repulsion. Note that higher temperatures are needed to desorb the Ar atoms, due to the large interaction with the porous material.

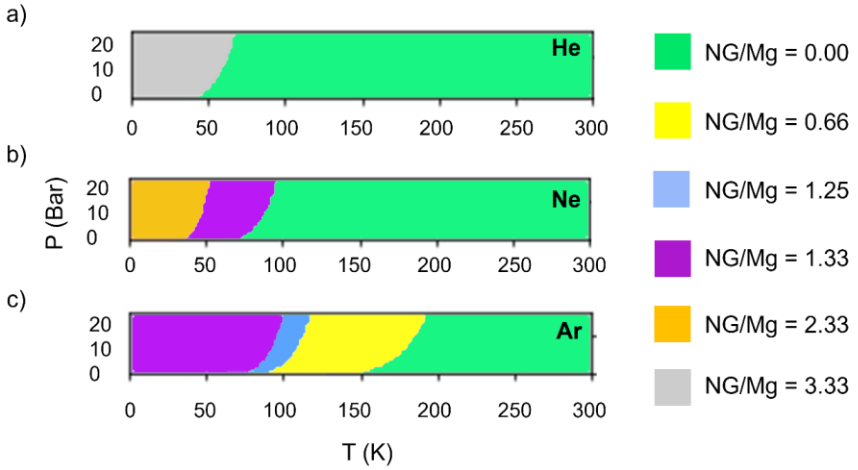

Figure 9. Grand potential phase diagram of He/γ-$Mg(BH_4)_2$ (a), Ne/γ-$Mg(BH_4)_2$ (b), and Ar/γ-$Mg(BH_4)_2$ (c) as function of temperature (K) and pressure (bar).

In summary, DFT simulations reveal that the adsorption energy of He, Ne, and Ar on γ-$Mg(BH_4)_2$ material is correlated with the size of the gas atoms. The larger the size, the more favorable the adsorption energy. However, large adsorption energy does not imply large concentrations of noble gas on γ-$Mg(BH_4)_2$. DFT calculations suggest that Ar is adsorbed on the centre of the pore and that decreasing the temperature can promote their displacement towards 32e sites, which duplicates the amount of Ar in γ-$Mg(BH_4)_2$. Ne can occupy the 32e and half of the 48g sites, in agreement with experimental predictions. However, DFT simulations show that He can fill both sites with a very low adsorption enthalpy, whereas the NPD experiments only detects the full loading of 32e sites. We have shown an excellent agreement between experiments and calculations to describe the Ar and Ne adsorption, although a slightly overestimation of binding energies is observed. Probably, the weak binding energy of He obtained by DFT is even superior than the experimental binding energy, which difficult the experimental detection of high loadings.

Table S1: Guest-Guest interaction energy (kJ/mol). Negative values implies attraction and positive values implies repulsion.

NG/Mg ratio (I)	NG/Mg ratio (F)	$E_{He\text{-}He}$ (kJ/mol)	$E_{Ne\text{-}Ne}$ (kJ/mol)	$E_{Ar\text{-}Ar}$ (kJ/mol)
0.166	0.333	-2.41	-5.02	-25.56
0.333	0.500	-2.89	-5.60	-9.55
0.500	0.666	-2.89	-6.46	-8.68
0.666	0.833	-2.51	-4.54	-17.75
0.833	1.000	-2.70	-6.37	-16.02
1.000	1.333	-3.08	-9.75	-8.30
1.333	1.666	-2.22	-2.61	8.87
1.666	2.000	-2.51	-2.80	8.59
2.000	2.333	-2.51	-3.28	11.48
2.333	2.666	-2.32	5.31	85.68
2.666	3.000	-3.66	9.75	32.71
3.000	3.333	-3.57	7.14	18.91

5.4. References

[1] Kantrowitz A., Tjønneland S., Freed P. S., Phillips S. J., Butner A. N., Sherman J. L. Initial clinical experience with intraaortic balloon pumping in cardiogenic shock. *J. Am. Med. Assoc.* **1968**, 203(2): 113-118.

[2] Declan B. Nuclear power’s new dawn. *Nature.* **2004**, 429(6989): 238-240.

[3] Berganza C. J., Zhang J. H. The role of helium gas in medicine. *Med. Gas Res.* **2013**, 3(1): 1-7.

[4] Munir M., Yar M., Ahsan F., Ayub K. Unprecedented saturation limit achieved by inorganic polycationic cluster $(Sb_7Te_8)^{5+}$ for light noble gases (He & Ne). *J. Mol. Graph. Model.* **2021**, 106: 107910.

[5] Cowen D., Tardieu C., Schubert M., et al. Low energy Helium-Neon laser in the prevention of oral mucositis in patients undergoing bone marrow transplant: results of a double blind randomized trial. *Int. J. Radiat. Oncol. Biol. Phys.* **1997**, 38(4):697-703.

[6] Martins D., De Sousa P. B., Catarino I., Bonfait G. 40 K liquid neon energy storage unit. *Phys. Procedia.* **2015**, 67: 1193-1198.

[7] Ribeiro R. P., Barreto J., Grosso Xavier M. D. G., et al. Cryogenic neon adsorption on $Co_3(ndc)_3(dabco)$ metal-organic framework. *Microporous Mesoporous Mater.* **2020**, 298: 110055.

[8] Férey G. Hybrid porous solids: Past, present, future. *Chem. Soc. Rev.* **2008**, 37(1): 191-214.

[9] Li J. R., Kuppler R. J., Zhou H. C. Selective gas adsorption and separation in metal-organic frameworks. *Chem. Soc. Rev.* **2009**, 38(5): 1477-1504.

[10] Meek S. T., Greathouse J. A., Allendorf M. D. Metal-organic frameworks: A rapidly growing class of versatile nanoporous materials. *Adv. Mater.* **2011**, 23(2): 249-267.

[11] Férey G. Yes, We Can! *Eur. J. Inorg. Chem.* **2016**: 4275-4277.

[12] Furukawa H., Cordova K. E., O’Keeffe M., Yaghi O. M. The chemistry and applications of metal-organic frameworks. *Science.* **2013**, 341(6149).

[13] Tomar D. S., Singla M., Gumma S. Potential parameters for helium adsorption in silicalite. *Microporous Mesoporous Mater.* **2011**, 142(1): 116-121.

[14] Vashchenko L. A., Katal V. V. Adsorption of helium on zeolite NaA. *Russ.*

Chem. Bull. **1996**, 45(5): 1230-1231.

[15] Arami-niya A., Ru T. E., Dresp G., Al Ghafri S., Jiao F., May E. F. Separation and purification technology measurements of helium adsorption on natural clinoptilolite at temperatures from (123.15 to 423.15) K and pressures up to 35 MPa. *Sep. Purif. Technol.* **2019**, 223: 1-9.

[16] Arami-niya A., Rufford T. E., Birkett G., Zhu Z. Gravimetric adsorption measurements of helium on natural clinoptilolite and synthetic molecular sieves at pressures up to 3500 kPa. *Microporous Mesoporous Mater.* **2017**, 244: 218-225.

[17] Yamk R., Yamk U., Heiden C., Danut J. G. Adsorption isotherms and heats of adsorption of neon and hydrogen on zeolite and charcoal Between 20 and 90 K. *J. Low Temp. Phys.* **1981**, 45(5): 443-455.

[18] Vashchenko L. A., Katal'nikova V. V., Serpinskii V. V. Adsorption of neon on zeolite NaA at low temperatures. *Bulletin of the Academy of Sciences of the USSR, Division of chemical science*, **1990**, 39(9): 1947-1949.

[19] Lozano-Castelló D., Jordá-Beneyto M., Cazorla-Amorós D., et al. Characteristics of an activated carbon monolith for a helium adsorption compressor. *Carbon*, **2010**, 48(1), 123-131.

[20] Majidi R., Taghiyari H. R., Ekhlasi M. Adsorption patterns of helium on carbon and cellulose nanotubes: Molecular dynamics simulations. *Nano* **2017**, 12(3):1750036.

[21] Foroutan M., Nasrabadi A. T. Molecular dynamics simulation study of neon adsorption on single-walled carbon nanotubes. *Phys. E Low-Dimensional Syst. Nanostructures.* **2010**, 43(1): 261-265.

[22] Krungleviciute V., Migone A. D., Pepka M. Characterization of single-walled carbon nanohorns using neon adsorption isotherms. *Carbon* **2008**, 47(3): 769-774.

[23] Wood P. A., Sarjeant A. A., Yakovenko A. A., Ward S. C., Groom, C. R. Capturing neon–the first experimental structure of neon trapped within a metal–organic environment. *Chem. Comm.* **2016**, 52(65): 10048-10051.

[24] Hulvey Z., Lawler K. V, Qiao Z., et al. Noble gas adsorption in copper trimesate, HKUST-1: An experimental and computational Study. *J. Phys. Chem. C.* **2013**, 117(39), 20116-20126.

[25] Barreto J., Xavier M. D., Ribeiro R. P., et al. Neon adsorption on HKUST-1 and UiO-66 Metal-organic frameworks over wide pressure and temperature ranges. *J. Chem. Eng. Data.* **2019**, 64(12): 5407-5414.

[26] Filinchuk Y., Richter B., Jensen T. R., Dmitriev V., Chernyshov D., Hagemann H. Porous and dense magnesium borohydride frameworks: Synthesis, stability, and reversible absorption of guest species. *Angew. Chem. Int. Ed.* **2011**, 50(47): 11162-11166.

[27] Frontzek M. D., Whitfield R., Andrews K.M., et al. WAND^2 - A versatile wide angle neutron powder/single crystal diffractometer. *Rev. Sci. Instrum.* **2018**, 89(9): 092801.

[28] Kresse G., Furthmüller J. Efficient Iterative Schemes for Ab Initio Total-Energy Calculations Using a Plane-Wave Basis Set. *Phys. Rev. B Condens.* **1996**, 54 (16), 11169-11186.

[29] Blöchl P. E. Projector Augmented-Wave Method. *Phys. Rev. B.* **1994**, 50 (24): 17953-17979.

[30] Joubert D. From Ultrasoft Pseudopotentials to the Projector Augmented-Wave Method. *Phys. Rev. B Condens.* **1999**, 59 (3): 1758-1775.

[31] Perdew J. P., Burke K., Ernzerhof M. Generalized Gradient Approximation Made Simple. *Phys. Rev. Lett.* **1996**, 77 (18): 3865-3868.

[32] Grimme S. Semiempirical GGA-type density functional constructed with a long-range dispersion correction. *J. Comput. Chem.* **2006,** 27(15): 1787-1799.

[33] Pack J. D., Monkhorst H. J. "special Points for Brillouin-Zone Integrations"- a Reply. *Phys. Rev. B.* **1977**, 16 (4): 1748-1749.

[34] Jain A., Ong, S. P., Hautier, G., Chen, W., Richards, W. D., Dacek, S., Cholia, S., Gunter, D., Skinner, D., Ceder, G. et al. Commentary: The Materials Project: A Materials Genome Approach to Accelerating Materials Innovation. *APL Mater.* **2013**, 011002.

[35] Favre-Nicolin V., Černý R. FOX, 'free objects for crystallography': A modular approach to ab initio structure determination from powder diffraction. *J. Appl. Crystallogr.* **2002**, 35(6): 734-743.

[36] Rodríguez-Carvajal J. Recent advances in magnetic structure determination by neutron powder diffraction. *Phys. B Phys. Condens. Matter.* **1993**, 192(1-2): 55-69.

Chapter 6. Adsorption of Light Hydrocarbons in a small-pore Hydridic Framework

Gleb Varyasov[1], Nikolay Tumanov[1], Voraksmy Ban[1], Xiao Li[1], Gail N. Iles[2,3], Dirk Wallacher[2], Matthew R. Hudson[4], Craig M. Brown[4], Bo Richter[5], Torben Jensen[5], Dmitry Chernyshov[6], Scott W. Jorgensen[7], Yaroslav Filinchuk[1,]*

[1]Institute of Condensed Matter and Nanosciences, Université catholique de Louvain, place L. Pasteur 1, B-1348 Louvain-la-Neuve, Belgium

[2]Department of Crystallography, Helmholtz-Zentrum Berlin; 14109 Berlin, Germany.

[3]School of Science, RMIT University; Melbourne, VIC 3000, Australia.

[4]Center for Neutron Research, National Institute of Standards and Technology; Gaithersburg, MD 20899, USA.

[5]Department of Chemistry and Interdisciplinary Nanoscience Center, Aarhus University, Langelandsgade 140, 8000 Aarhus C, Denmark.

[6]Swiss-Norwegian Beamlines at the European Synchrotron Radiation Facility, 71 avenue des Martyrs, Grenoble, 38000, France

[7]Chemical and Environmental Sciences Lab General Motors R&D Center; 30500 Mount Rd, Warren, MI 48090, USA

Abstract

The gamma-phase of magnesium borohydride, γ-$Mg(BH_4)_2$, has a structure of nano-porous 3D framework with one-dimensional pores accessible to gas molecules. Adsorption of light C1-C4 alkanes in γ-$Mg(BH_4)_2$ was studied here by means of diffraction and volumetric techniques. Combination of neutron powder diffraction (NPD) and synchrotron radiation X-ray diffraction (SR-XRD) allowed to understand in detail host-guest interactions in gas-loaded framework and to determine adsorption isobars, isotherms and the isosteric heats of adsorption. γ-$Mg(BH_4)_2$ adsorbs exclusively smaller methane and ethane and shows high gravimetric adsorption capacities and heats of adsorption.

6.1. Introduction

Meeting increase in energy demand in a sustainable manner is one of the most urgent societal challenges. The 2ºC scenario[1] to avoid critical changes on the planet would require optimization of energy efficiency and diversification of energy sources applied nowadays. Methane, a primary component of natural gas (NG), is widely seen as a primary energy carrier on the way towards carbon dioxide emissions reduction[2]. Methane is a cleaner alternative to crude oil and is an abundant energy source. It could be found in natural reservoirs or could be produced from industrial, landfill, or agricultural waste, so-called “biomethane”. Main advantage of biomethane is that its production could have negative carbon footprint, therefore it is expected to at least partially substitute fossil by 2050[2],[3].

Gaseous methane has low energy density of 0.04 MJ/L (vs 38.6 MJ/L for diesel), which hinders its application as a transportation fuel. Use of compressed methane (CNG) in cylinders at high pressures[4] would possess limitations due to hazards in case of cylinder damage. Utilization of liquefied methane (LNG) will require a number of complex and expensive terminals for liquefaction, which will not be realistic in near future.

Another alternative to listed techniques is storage in porous materials[5]–[17]. Methane adsorbed in a proper porous media under 35 bar near ambient temperature, might provide the same energy density as CNG at 250 bars used in current practice[18]. This opportunity attracted significant attention by research communities and different classes of porous materials were investigated for methane and/or light hydrocarbon storage purposes: zeolites[19]–[21], zeolitic imidazolate frameworks (ZIFs)[22]–[26], carbon-based materials[27],[28], porous organic polymers[29], and metal-organic frameworks (MOFs)[6],[7],[13],[14],[16],[30]–[44].

Gamma-phase of magnesium borohydride, γ-$Mg(BH_4)_2$, is the first hydride with functional porosity[45]. Its framework does not contain open metal sites for gas molecule coordination, but its pores are made of hydridic hydrogen atoms, unlike for other known porous solids. The 1D channels can accommodate small guests, which depending on their size reveal more or less cooperative interaction with the framework[46],[47]. In general, the framework remains rigid; however, rotational motion of the BH_4 groups may be correlated with the diffusion of guests along the channel[48]. The latter study by our group points to interesting relations between the size of the guest molecules (varying in Ar-Kr-Xe series) and the kinetics and mechanisms of gas diffusion, showing potential for Kr/Xe separation by γ-$Mg(BH_4)_2$.

In the present work, we studied adsorption of light hydrocarbons (from methane to butane) in the γ-$Mg(BH_4)_2$ framework by means of neutron powder diffraction (NPD) and synchrotron radiation X-ray diffraction (SR-XRD), as well as by volumetric techniques. Only smaller molecules, methane and ethane, are adsorbed into the pores. Refinement of the guest molecule occupancies from the SR-XRD data allowed to plot adsorption isotherms and isobars and characterize thermodynamics of gas sorption as well as guest-host interactions. The study shows that the isosteric heat of adsorption of methane in γ-$Mg(BH_4)_2$ is among the highest reported in the literature.

6.2. Experimental Part

Reagents and chemicals.

γ-$Mg(BD_4)_2$ and its double isotopic substitution γ-$Mg(^{11}BD_4)_2$ were synthesized according to the previously described procedures[45]. Dimethyl sulfide complex of borane ($BH_3 \cdot DMS$) and di-*n*-butylmagnesium (1M in heptane, 10 ml, 10 mmol) were used from Sigma-

Aldrich, $^{11}BD_3 \cdot DMS$ was purchased from KatChem, and used without further purification. High purity CH_4, C_2H_6, CD_4, C_2D_6, C_3H_8, C_4H_8 were purchased from Aldrich.

Neutron diffraction.

Neutron powder patterns for empty framework (γ-$Mg(^{11}BD_4)_2$) and CD_4-filled ($Mg(^{11}BD_4)_2 \cdot 0.63CD_4$) samples were measured at the NIST Center for Neutron Research (Gaithersburg, MD, USA). 1.3 g of $Mg(^{11}BD_4)_2$ was sealed in a vanadium container of length 50 mm and diameter 10.8 mm inside a dry He-filled glovebox. A closed-cycle He refrigerator was used for temperature control. Neutron powder diffraction data were collected using the BT-1 32 detector neutron powder diffractometer. A Ge(311) monochromator with a 75° take-off angle, $\lambda = 2.0787(2)$ Å, and in-pile collimation of 60 minutes of arc were used. Data were collected over the range of 1.3-166.3° 2θ with a step size of 0.05°. The instrument is described in the NCNR WWW site (http://www.ncnr.nist.gov/). First, powder pattern of empty framework was measured at 10 K, then the sample was heated above CD_4 boiling point and loaded with CD_4. Excess of CD_4 was quickly removed by applying vacuum to avoid further CD_4 condensation. After complete loading sample was cooled to 10 K, and powder diffraction data was collected. All atomic coordinates and atomic displacement factors for Mg, B and D were refined independently.

Neutron powder patterns for C_2D_6-filled ($Mg(^{11}BD_4)_2 \cdot 0.66\ C_2D_6$) and C_2H_6-filled ($Mg(^{11}BD_4)_2 \cdot 0.66\ C_2H_6$) samples were measured at the BER-II reactor at Helmholtz Zentrum Berlin (Germany). 0.8 g of $Mg(^{11}BD_4)_2$ was sealed in an aluminum container (Bragg peaks from aluminum were excluded later from the powder pattern) of length 50 mm and diameter 8 mm inside a dry N_2-filled glovebox. Orange cryostat and closed-cycle He refrigerator were used for temperature control. Neutron powder diffraction data were collected using the Fine Resolution Powder Diffractometer E9 (FIREPOD). The Ge(511) monochromator with 111.7(1)° take-off angle, $\lambda = 1.79860(1)$ Å and oscillating radial collimator for background reduction were used. Data were collected over the range of 0-141° *2θ* with a step size of 0.075°. The powder diffraction data for C_2H_6-filled sample was collected at 200 K, the C_2D_6-filled sample was measured at 200 K and 20 K. Position and orientation of gas molecules were found by direct-space methods using FOX program[49] and crystal structure models were refined using FullProf software[50].

Adsorption of CH_4 and C_2H_6 in the porous γ-Mg(BH_4)$_2$ investigated by synchrotron radiation X-ray powder diffraction (SR-XPD).

CH_4 and C_2H_6 loading into the porous structure were studied both at room temperature and varied pressures (producing an isotherm) as well as at fixed pressures and varied temperatures (producing isobars). SR-XPD patterns were collected *in-situ* on γ-Mg(BH_4)$_2$ samples loaded with gasses. A dosing system[51],[52] was used to apply gas pressures on the sample from 0.5 to 65 bar. The sample was enclosed in a 0.5 mm glass capillary under Ar, tightly connected to the dosing system and then outgassed at room temperature to 10^{-3} mbar. For CH_4, the isobars were measured at 10 and 65 bar and the isotherm from 65 bar to vacuum, all upon desorption. For C_2H_6, the isobars were measured at 0.5 and 4 bar upon desorption (temperature increase) and the isotherm from vacuum to 37 bar upon adsorption. No hysteresis was observed upon adsorption/desorption. The temperature was varied in a wide range from gas liquefaction to the full gas desorption in the pores. The heating rate was 2 K/min for the experiments with CH_4 and 5 K/min with C_2H_6. Oxford Cryostream 700+ was used in both cases. XPD data were collected every 2 minutes using MAR345 detector in the experiments with CH_4 and every 30 seconds using PILATUS 2M detector for the experiments with C_2H_6.

Synchrotron radiation powder X-ray diffraction (SR-PXD) data were collected at the Swiss-Norwegian beamline BM1A at the European Synchrotron Radiation Facility (ESRF) (Grenoble, France). The selected wavelength was in the range 0.74 to 0.82 Å and was calibrated, along with the sample-to-detector distances and image plate tilt angles, using a standard LaB_6 sample. The two-dimensional diffraction images were azimuthally integrated using the ESRF Fit2D program[53]. Position and orientation of gas molecules were found by direct-space methods using FOX program[49] and crystal structure models were refined using FullProf software[50].

Adsorption of C_3H_8 and n-C_4H_{10} in the porous γ-$Mg(BH_4)_2$.

The sample of γ-$Mg(BH_4)_2$ was enclosed in a 0.5 mm glass capillary under Ar, tightly connected to the dosing system and then outgassed at room temperature to 10^{-3} mbar. A dosing system[51],[52] was used to apply gas pressures on the sample from from vacuum to the pressure of gas liquefaction. SR-XPD patterns collected in-situ corresponded to empty γ-$Mg(BH_4)_2$ for the entire range of applied pressures, indicating that propane and n-butane are not entering the pores of the framework.

Determination of isosteric heats of adsorption.

The Clausius–Clapeyron equation was used to estimate the absorption enthalpy from the isobars:

$$ln\frac{P_1}{P_2} = \frac{\Delta H}{R}\left(\frac{1}{T_2} - \frac{1}{T_1}\right) \qquad (1)$$

In order to be able to use this expression, the P_1-T_1 and P_2-T_2 conditions from two different isobars must correspond to exactly the same amount of the adsorbed gas. Therefore, we interpolated the experimental composition-temperature diagrams to a fixed grid of compositions at all pressures. For that, the dependence of the adsorbed quantity of gas versus temperature was fitted by the Logistic function of growth:

$$y = \frac{A_1 - A_2}{1 + \left(\frac{x}{x_0}\right)^P} + A_2 \qquad (2)$$

Study of physisorption of methane and ethane by volumetric methods.

The volumetric studies were carried out with IMI-HTP analyzer from Hiden Isochema (UK), which ensures an accurate pressure control and thermal stability. 2.55 mmol of $Mg(BH_4)_2$ sample was loaded and first the adsorption of nitrogen at 190 K up to 41 bar was carried. This was done in order to calibrate the proportion of the amorphous and crystalline phases, as only the latter is contributing to the adsorption. Earlier diffraction study showed that the limiting capacity at saturation with nitrogen is γ-$Mg(BH_4)_2 \cdot 2/3N_2$[45]. Nitrogen adsorption isotherm and the fit with the Langmuir equation are shown in Figure S1, the analysis shows that the fraction of the crystalline phase is 89%. Subsequently, adsorption and desorption isotherms of methane and ethane were performed at room temperature without changing the sample. Full reversibility and no hysteresis were observed. The determined fraction of the crystalline γ-$Mg(BH_4)_2$ is taken into consideration in order to compare directly the data of the volumetric and *in-situ* diffraction techniques, the latter specifically characterizing the crystalline phase only.

6.3. Results and discussion

Hydrogen (H) is the weakest scatterer of X-rays among all elements, thus a precise localization of H-atoms is challenging even for good quality samples. On the other hand, deuterium (D) is a strong scatterer of neutrons, thereby the exact structural positions of deuterium can be determined by means of NPD. Therefore, NPD on deuterated samples was used first for the precise determination of the structure of the host framework, both in empty form and fully loaded with fuel gases. Once the structural details (like orientation and disorder of a guest) were accurately identified by NPD, complementary refinements were done by *in situ* SR-XPD. The latter allowed also to study structural evolution as a function of pressure and temperature, revealing both microscopic picture of interaction and the material’s properties, such as adsorption isobars and isotherms, as well as the thermodynamic parameters characterizing the solid-gas interaction.

Structural analysis of the empty γ-$Mg(^{11}BD_4)_2$ framework by NPD.

The structure of the γ-$Mg(BH_4)_2$ was reported in earlier works[45],[54] and here we present complimentary data on the structure of γ-$Mg(^{11}BD_4)_2$ determined using NPD at low temperature (10 K). Final Rietveld refinement plot is shown in Figure S2 and the summary on structural parameters is given in Table S1. The structure contains 24 formula units $Mg(^{11}BD_4)_2$ per unit cell and 16 accessible voids (pockets), organised into 1D channels. The structural model of γ-$Mg(^{11}BD_4)_2$ obtained in the present work is in good agreement with previously reported γ-$Mg(BH_4)_2$ (see Table S2 and Figure S3) and the difference between the unit cell volumes at 10 K and 298 K is negligible.

Structural analysis of the fully CD_4-loaded γ-$Mg(^{11}BD_4)_2$ by NPD and SR-XPD characterization of methane loading in γ-$Mg(BH_4)_2$.

Adsorption of deuterated methane, CD_4, into γ-$Mg(BD_4)_2$ at 10 K indicated that full capacity is reached at composition $Mg(^{11}BD_4)_2 \cdot 0.63CD_4$. The formula is close to maximum theoretical gas uptake of 0.66 guest molecules per Mg atom, meaning that 15 out of 16 pores per unit cell are effectively occupied. Final Rietveld refinement plot is shown in Figure S4 and structural parameters are summarized in Table S3. The image of gas-filled pore is shown in Figure 1. For the refinement of the γ-$Mg(^{11}BD_4)_2 \cdot 0.63CD_4$ structure model, soft constrains for C-D distances and D-C-D angles in the CD_4 molecule were applied. The CD_4 molecule aligns along the crystallographic 3-fold symmetry axis, but it is orientationally disordered around the perpendicular crystallographic 2-fold axis, since the point group symmetry of the centre of the void is 32 (see Figure S5). No contacts below the sum of Van der Waals (VdW) radii are observed (see Table S4).

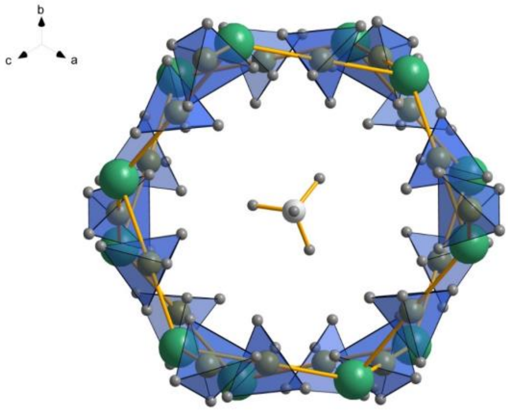

Figure 1. Structure of the methane-loaded void seen along the 1D channel in γ-$Mg(BD_4)_2{\cdot}0.63CD_4$. One of the two orientation of the guest molecule (disordered around the 2-fold symmetry axis running perpendicular to the channel) is shown for clarity. For simplicity Mg−D bonds are omitted and Mg…B contacts are highlighted to show the Mg…BH_4 connectivity.

During the SR-XPD experiments, the position of the CH_4 molecule was determined from the data collected at 188 K and 65 bar (full loading) using global optimization in direct space implemented in FOX[49]. The structure of the γ-$Mg(BH_4)_2$ framework was fixed, and the position, orientation and the occupancy of a methane molecule was refined. A good fit was achieved with one independent CH_4 molecule centred on the 3-fold axis. The resulting model was refined by Rietveld method in Fullprof[50], varying profile and cell parameters, position (the orientation was fixed), the occupancy of the CH_4 molecule and the atomic displacements for the host structure and the guest molecule. The refined composition of the structure is γ-$Mg(BH_4)_2{\cdot}0.608(8)CH_4$, close to the limiting composition γ-$Mg(BH_4)_2{\cdot}0.66CH_4$ for the fully occupied void. The background was described by linear interpolation between selected points. The final discrepancy factors are: R_B = 10.1%, R_F = 9.0 %, R_p = 15.7%, and R_{wp} = 12.0%. The refinement profile is shown in Figure S6. Crystal data and atomic coordinates are listed in Table S5.

Low-temperature SR-XPD structure of γ-$Mg(BH_4)_2{\cdot}0.61CH_4$ agrees very well with NPD data. As mentioned above, the methane molecule in γ-$Mg(BH_4)_2 \cdot 0.61CH_4$ is disordered around the 2 axis, while the carbon atoms remain on a 3-fold axis. At lowest temperatures the carbon atom is disordered by ca. 0.2 Å around the center of the pore (1/8 1/8 1/8 position with point group symmetry 32), the displacement from the center is gradually increasing with temperature to 1.2 Å (see Figure S7). At ambient temperature, the CH_4 molecule is found closer to the apertures made of the borohydride groups, thus revealing shorter C−H···H−B contacts.

Structural analysis of the fully ethane-loaded γ-$Mg(^{11}BD_4)_2$ by NPD and SR-XPD characterization of ethane loading in γ-$Mg(BH_4)_2$.

NPD study of ethane loaded γ-$Mg(^{11}BD_4)_2$ was done both by using natural isotopic ethane C_2H_6 and deuterated C_2D_6. The powder diffraction data for C_2H_6-filled sample was collected at 200 K, the C_2D_6-filled sample was measured at 200 K and at 20 K. In all cases, compositions obtained from diffraction were very close the limiting γ-$Mg(^{11}BD_4)_2 \cdot 0.66C_2H_6$ and γ-$Mg(^{11}BD_4)_2 \cdot 0.66C_2D_6$, the refined occupancies of C_2D_6 and C_2H_6 molecules correspond to the full occupation of the void within one standard uncertainty. The structures were refined applying constraints on C-C distances and H-C-C angles in the C_2H_6 molecule. Final Rietveld refinement plots are shown in Figures S8-S10, structural parameters are summarized in Tables S6-S8.

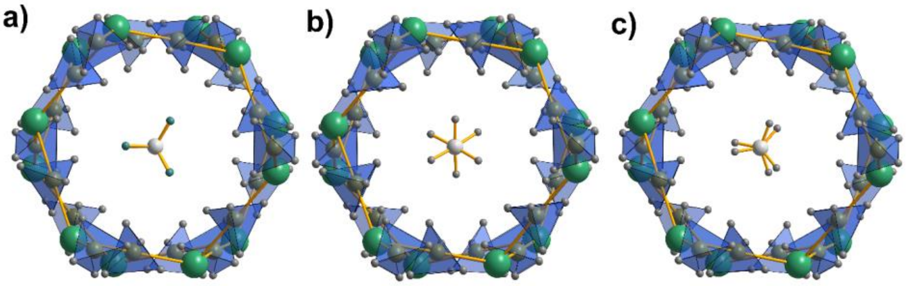

Figure 2. Structure of ethane-loaded void seen along the 1D channel in **a)** γ-$Mg(^{11}BD_4)_2 \cdot 0.66C_2H_6$ at 200 K, **b)** γ-$Mg(^{11}BD_4)_2 \cdot 0.66C_2D_6$ at 20 K, and **c)** γ-$Mg(^{11}BD_4)_2 \cdot 0.66C_2D_6$ at 200 K. staggered conformation of ethane is observed at 20 K and eclipsed at 200 K. For simplicity Mg−D bonds are omitted and Mg…B contacts are highlighted to show the Mg…BH_4 connectivity.

The images of gas-filled pores are shown in Figure 2. In contrast to $Mg(^{11}BD_4)_2 \cdot 0.63CD_4$, no disorder is observed for C_2D_6 and C_2H_6, since the symmetry of ethane in all conformations is consistent with the crystallographic point group symmetry of the centre of the void.

In the structure of $Mg(^{11}BD_4)_2 \cdot 0.66C_2D_6$, determined at 20 K, ethane molecule adopts staggered conformation with torsion angle D3−C1−C1'−D3' of 63.3°. Somewhat surprisingly, the structures derived from NPD data at 200 K for both C_2H_6 and C_2D_6 are showing ethane to adopt a conformation close to the eclipsed one, having the values of the corresponding torsion angle of 1.7° and 20.3°, respectively. This may suggest different strength of guest-host interactions at 20 and 200 K, despite no D···D contacts below the sum of VdW radii are observed (see Table S9).

The position of the C_2H_6 molecule was independently determined from SR-XPD data collected at 200 K and 4 bar (at full loading) using global optimization in direct space implemented in FOX[49]. A good fit was achieved with one independent carbon atom at 100% occupancy centred on the 3-fold axis. The short distance with the symmetry-related neighbor C atoms mapped by the 2-fold symmetry axis gives rise to the covalent C-C bond. The resulting model was completed by one hydrogen atom in the general position and refined by FullProf[50]. Profile and cell parameters were refined along with the position of the carbon atom on the 3-fold axis and the position of hydrogen atom without any constraints. The occupancy of the C_2H_6 molecule and the atomic displacements for the host structure and the guest molecule were refined as well. The background was described by linear interpolation between selected points. The final discrepancy factors are: $R_B = 6.2\%$, $R_F = 6.2\ \%$, $R_p = 15.6\%$, and $R_{wp} = 10.6\%$. The refinement profile is shown in Figure S11. Crystal data and atomic coordinates are listed in Table S10. The refined composition from SR-XPD measured at 200 K and 4 bar is $\gamma\text{-}Mg(BH_4)_2 \cdot 0.603(2)C_2H_6$. To our confidence, the ethane conformation obtained from variable temperature SR-XRD data reproduces the behavior found from NPD – ethane adopts staggered conformation at low temperature and less energetically favorable eclipsed one at higher temperatures.

Adsorption isotherms, isobars and thermodynamics from in situ SR-XRD.

Isobars and isotherms of CH_4 and C_2H_6 adsorption by γ-$Mg(BH_4)_2$ were determined directly from SR-XPD. Sequential Rietveld refinement based on the structural models described above was done against *in situ* data collected at variable pressure and temperature conditions, see the experimental part.

Since the sample of γ-$Mg(BH_4)_2$ contains the porous crystalline[45] and dense amorphous phases[55], the bulk techniques (such as volumetric) provide data on the total gas uptake without an opportunity to evaluate a contribution of each phase. In contrast, the diffraction characterizes the crystalline phase only. To allows for direct comparison between these techniques, an amorphous fraction of $Mg(BH_4)_2$ was determined volumetrically using N_2 adsorption against the known saturation capacity for the crystalline phase, see the experimental part.

Crystallographic isotherms at room temperature are shown in Figure 3 left, along with the corresponding isotherms measured volumetrically (Figure 3 right). One can see an excellent agreement between the two methods, keeping in mind the correction for the amorphous fraction was applied to the volumetric isotherms. Langmuir equation was fitted to the volumetric data, yielding $a_{methane} = 0.661(9)$ per $Mg(BH_4)_2$ and $a_{ethane} = 0.689(15)$ per $Mg(BH_4)_2$. Within the experimental error, these values are identical to the limiting capacity of 2/3 guest molecule per $Mg(BH_4)_2$ (equivalent to one molecule per void). This matches very well our expectations and the crystallographic results, validating the methodology addressing the amorphous phase fraction.

Two adsorption isobars were characterized by diffraction for each gas, with pressure ranges spanning almost an order of magnitude, see Figures 4 and 5. It is a big advantage and convenience of *in situ*

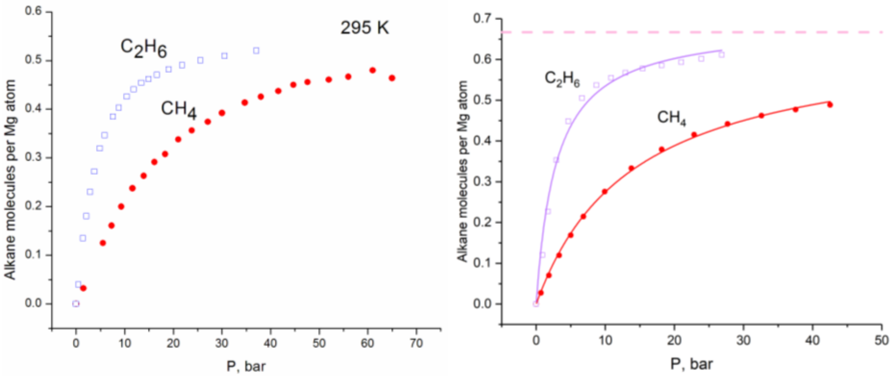

Figure 3. CH_4 and C_2H_6 adsorption isotherms obtained from sequential Rietveld refinement against *in situ* SR-XPD data at 295 K (shown on the left). CH_4 and C_2H_6 adsorption isotherms obtained by volumetric method (shown on the right). The volumetric data were corrected for the amorphous phase fraction and fitted to the Langmuir equation (see text), shown as lines. The horizontal dash line shows the theoretical saturation capacity at 2/3.

crystallography to access adsorption isobars, since the variable temperature diffraction is easier to do automatically than to vary pressure. On the other hand, isobars are usually not accessible by volumetric methods, since a reliable calibration of a volumetric system is not feasible at variable temperatures. This is the reason why we do not present here volumetric isobars.

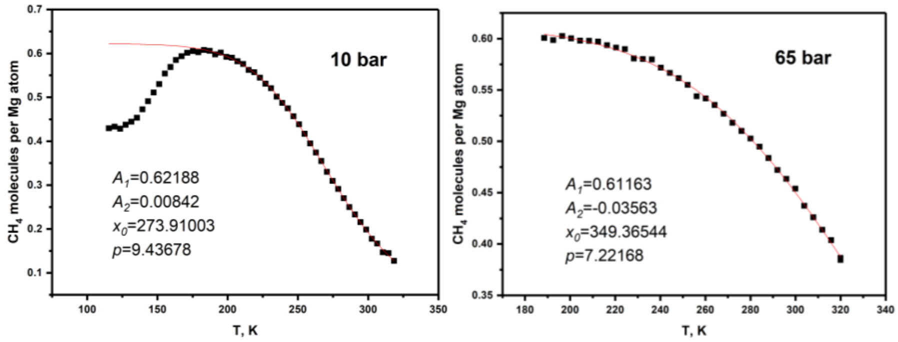

Figure 4. Isobar of CH_4 desorption from γ-$Mg(BH_4)_2$ extracted from *in situ* SR-XPD data collected at 10 bar (left) and 65 bar (right). The experimental data is fitted by logistic function. The decline in the adsorbed capacity below 180 K at 10 bar is likely related to the gas liquefaction; data below 150 K were omitted in the analytical approximation.

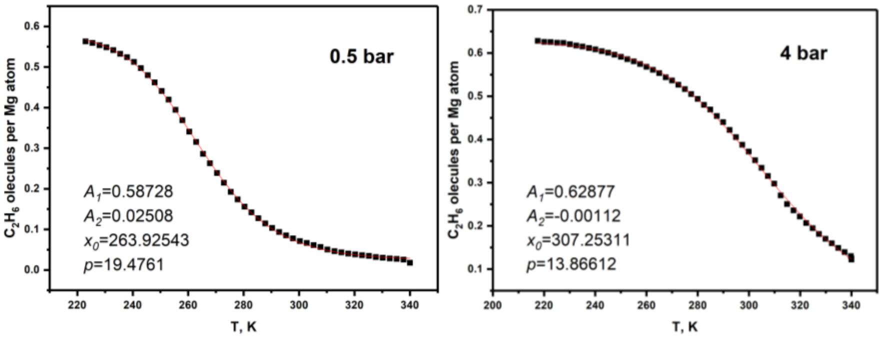

Figure 5. Isobar of C_2H_6 desorption from γ-Mg(BH$_4$)$_2$ extracted from *in situ* SR-XPD data collected at 0.5 bar (left) and 4 bar (right), and fitted by the logistic function.

The Logistic function, described by the expression (2), was used to fit the isobars with high accuracy. The obtained equations, see Figures 4 and 5, allowed us to calculate P-T conditions for a constant-step grid of loadings, which were fed into the Clausius-Clapeyron equation. This yields a smooth (analytically interpolated) dependence of the isosteric heat of adsorption as a function of loading, plotted as back squares for the two gases in Figure 6. Data are shown in the compositional range characterized both in lower- and higher-pressure isobars. For both gases the isosteric heats of adsorption are nearly constant with loading, meaning there is little repulsion between the guest molecules (directly or mediated by the framework).

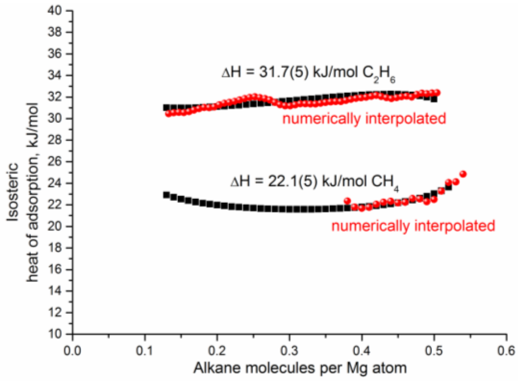

Figure 6. Isosteric heat of adsorption of CH_4 and C_2H_6 in γ-Mg(BH$_4$)$_2$ as a function of loading. Analytical and numerical interpolation methods, applied to isobars in order to apply the Clausius-Clapeyron equation for equal loadings, give essentially the same results.

A numerical interpolation of isobars to a constant-step grid of loadings determines the heats of adsorption shown as red circles in Figure 6. The result is essentially the same but noisier, thus giving advantage to the analytical interpolation. The average values, $Q_{st}(CH_4)$ = 22.1(5) kJ/mol and $Q_{st}(C_2H_6)$ = 31.7(5) kJ/mol, appear to be among the highest values reported so far for porous materials, see Table 1.

Table 1. Comparison of obtained isosteric heats of adsorption to the literature data.

Methane			*Ethane*		
Adsorbent	Q_{st}	*Reference*	*Adsorbent*	Q_{st}	*Reference*
γ-$Mg(BH_4)_2$	22.1	This work	γ-$Mg(BH_4)_2$	31.7	This work
MAF-49	25	[39]	ETS-10	35	[56]
Silicalite-1	18.1-28	[57],[58]	Silicalite-1	29-45	[57]–[60]
polydi-chloroxylene	20.8	[61]	MCM-41	20-25	[62],[63]
PCN-9	23.3	[64]	Na-Y	26.4	[60]
MIL53	17	[65]	US-Ex	21.3	[60]
IRMOF-6	12.1	[66]	ZSM-5	37.5	[60]
activated carbon	16-20.6	[67]–[70]	ZTC	20-25	[71]
Co(bdp)	17	[34]	MSC-30	21.5	[71]
DAY	15	[72]	zeolite 5A	10-30	[73]
MOF-5	12.2	[74]			
ZIF8	12	[74]			
ETS-10	21	[56]			

The selectivity of gas adsorption in the CH_4-C_2H_6 mixtures with different gas ratios was estimated using pyIAST software on the basis of the isotherms retrieved from the crystallographic data[75], see Figure 7. The isotherms were fitted using the Langmuir model. Due to higher enthalpy, C_2H_6 is preferably adsorbed in the γ-Mg$(BH_4)_2$. The simulated gas uptake curves indicate that for the chosen range of CH_4/C_2H_6 mixtures (9/1-1/9 mol.) γ-Mg$(BH_4)_2$ is not suitable for selective separation of ethane and methane. However, no adsorption of C_3H_8 and *n*-C_4H_{10} (at least at the time scale of mites at room temperature, see the experimental part) suggests a feasible separation of hydrocarbons with a carbon chain length of more than two. This is possible due to the void size that does not allow for big molecules inside.

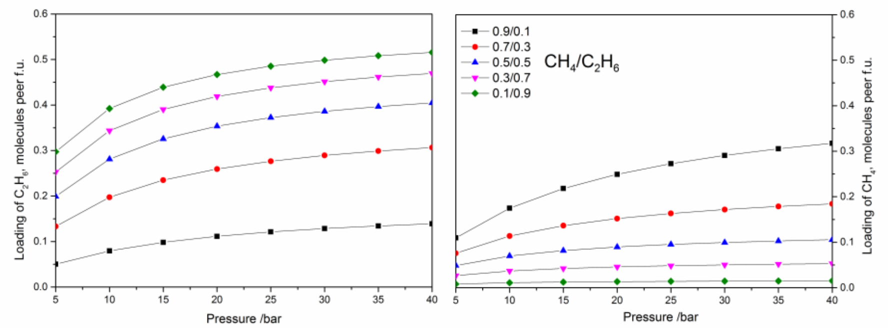

Figure 7. Pressure dependence of C_2H_6 (left) and CH_4 (right) uptakes by γ-Mg$(BH_4)_2$ from gas mixtures with different CH_4/C_2H_6 molar ratios, estimated using pyIAST.

Host-guest interactions and their implications.

Comprehensive crystallographic study reveals different manifestations of atomic interactions. For example, Rietveld refinement shows that the unit cell expands with gas loading at room temperature: the volume increases linearly at a rate of 2.2 Å^3 per adsorbed CH_4 molecule, and at about 12 Å^3 per adsorbed C_2H_6 molecule. This indicates that the smaller methane molecule is matching easier the available pore volume, while the larger ethane requires some framework changes in order to accommodate it. Indeed, methane occupies only one of the two symmetry-related positions around the centre of the pore (see Figure S7b), while ethane takes completely the available space (as it is nearly twice as large as methane), leading to stronger interactions with the host framework (Figure 2). At the same time both NPD and SR-XRD indicate the absence of close C−H···H−B contacts for CH_4 and C_2H_6 located in the pores of the framework. Indeed, the guest molecules are stabilized in pores only by weak VdW interactions; for more detailed illustration of intermolecular contacts for ethane and the related Hirschfield plots see Figure S12. Interestingly, this interaction changes with temperature: first, as temperature increases methane is continuously moving from the centre of the void to its aperture; second, at higher temperatures ethane adopts less energetically favorable conformation. These changes could be attributed to a polarization of hydrocarbon molecules in the framework, reinforcing host-guest interactions at higher temperatures. This phenomenon is known for zeolite-type materials[76]–[78].

Speaking of a polarization of hydrocarbons, it is interesting to consider another extremity: ammonia borane (NH_3BH_3 or AB), isoelectronic to C_2H_6, but bearing significant changes on its hydrogen atoms. Moreover, AB is solid at ambient conditions, owing to strong dihydrogen $NH^{\delta+}$… $H^{\delta-}B$ bonds[79],[80]. All our attempts to infiltrate AB into the pores of the γ-$Mg(BH_4)_2$ framework by using solutions (this work), ball milling or high hydrostatic pressures (ref.[81]) failed, yielding a $Mg(BH_4)_2{\cdot}2AB$ complex at most reactive conditions. The difference compared to an easy incorporation of ethane may be explained either by repulsive interactions of AB with the pore surface, making the absorption thermodynamically unfavorable, or by kinetic difficulties for the diffusion of the polar AB molecule through apertures of the 1D channels.

Crystallography helps to find an answer by looking closer on the aperture and the size of the guests passing through it. The accurate NPD structure of the empty γ-$Mg(^{11}BD_4)_2$ shows that the void in γ-$Mg(BH_4)_2$ is an ellipsoid with narrow aperture defined by the shortest distance between hydrogen atoms of 5.6 Å (the distance between the centre of the aperture at ¼ ¼ ¼ to the nearest D-atoms is 2.819(4) Å). The entire porous channel can be described by a chain of ellipsoidal voids (pockets) oriented along the (111) direction of the cubic cell, connected by narrower apertures. Assuming the VdW radii of hydrogen to be 1.2 Å[82], the guest molecule should have kinetic diameter of less than 3.2 Å in order to move freely along the channel, which is the case for hydrogen molecule with a kinetic diameter of 2.89 Å. Larger molecules (like Kr and Xe) can go through the aperture likely due to a rotational motion of the BH_4 groups correlated with the diffusion of guests[48].

The kinetic diameters of light alkanes are 3.7, 4.0, 4.3, and 4.7 Å for CH_4, C_2H_6, C_3H_8, and n-C_4H_{10}, respectively[83]. Since these values are larger than the size of the aperture opening of 3.2 Å, it can be suggested that the hydrocarbon molecules turn the borohydride groups in order to enter into the voids. Since the pores in the framework are non-interconnected 1D channels, the penetration through the apertures should be rate-determining for adsorption. This is very well in line with a mechanistic picture based on Ar/Kr/Xe adsorption kinetics in γ-$Mg(BH_4)_2$[48] and with known fast reorientational motion of BH_4 in $Mg(BH_4)_2$[84]. In the present work, we observed that only CH_4 and C_2H_6 are adsorbed, whereas higher C_3H_8 and n-C_4H_{10} do not enter the pores even at high pressures. Our analysis shows that this might be not because of a mismatch of the molecule and pore sizes, but rather stem from the very slow kinetics of diffusion through the pore aperture. This point requires more detailed study, with possible applications for gas separation.

6.4. Conclusions

Adsorption of small alkanes in a porous hydride, γ-$Mg(BH_4)_2$, was investigated by an advanced combination of diffraction techniques.

NPD measurements of empty and gas-loaded γ-Mg(^{11}BD$_4$)$_2$ allowed for the precise localization of guests, whereas the SR-XRD study at different temperatures and gas pressures allowed to characterize the structural evolution and determine isosteric heats of adsorption for methane and ethane. γ-Mg(BH$_4$)$_2$ exhibits high gravimetric capacity and one of the highest heats of adsorption reported in the literature, Q_{st}(CH$_4$) = 22.1(5) kJ/mol and Q_{st}(C$_2$H$_6$) = 31.7(5) kJ/mol. The unique nature of the framework made of hydridic BH$_4^-$ anions can possibly explain both the high heats of CH$_4$ and C$_2$H$_6$ adsorption and the diffusion of guests through relatively narrow apertures. Only CH$_4$ and C$_2$H$_6$ are adsorbed by γ-Mg(BH$_4$)$_2$, but not C$_3$H$_8$ and *n*-C$_4$H$_{10}$. Our analysis shows this may be not because of a mismatch of the molecule and pore sizes, but may stem from the very slow kinetics of diffusion through the pore aperture.

6.5. References

[1] Ceres. *A framework for 2 degrees scenario analysis: A guide for oil and gas companies and investors for navigating the energy transition*. **2016**.

[2] Trinomics. *The role of Trans-European gas infrastructure in the light of the 2050 decarbonisation targets*. **2018**.

[3] *A Clean Planet for all. A European long-term strategic vision for a prosperous, modern, competitive and climate neutral economy.* European Commission. **2018**.

[4] Stockmeyer R. google patents. 1985.

[5] Stadie N. P., Murialdo M., Ahn C. C., Fultz B. Unusual entropy of adsorbed methane on Zeolite-templated carbon. *J. Phys. Chem. C.* **2015**, 119(47): 26409-26421.

[6] Thornton A. W., Nairn K. M., Hill J. M., Hill A. J., Hill M. R. Metal- organic frameworks impregnated with magnesium-decorated fullerenes for methane and hydrogen storage. *J. Am. Chem. Soc.* **2009**, 131(30): 10662-10669.

[7] Jiang J., Furukawa H., Zhang Y. B., Yaghi O. M. High methane storage working capacity in metal-organic frameworks with acrylate links. *J. Am. Chem. Soc.* **2016**, 138(32): 10244-10251.

[8] Martin R. L., Simon C. M., Smit B., Haranczyk M. In silico design of porous polymer networks: high-throughput screening for methane storage materials. *J. Am. Chem. Soc.* **2014**, 136(13): 5006-5022.

[9] Gándara F., Furukawa H., Lee S., Yaghi O. M. High methane storage capacity in aluminum metal-organic frameworks. *J. Am. Chem. Soc.* **2014**, 136(14): 5271-5274.

[10] Verploegh R. J., Nair S., Sholl D. S. Temperature and loading-dependent diffusion of light hydrocarbons in ZIF-8 as predicted through fully flexible molecular simulations. *J. Am. Chem. Soc.* **2015**, 137(50): 15760-15771.

[11] Yang W., Greenaway A., Lin X., et al. Exceptional thermal stability in a supramolecular organic framework: porosity and gas storage. *J. Am. Chem. Soc.* **2010**, 132(41): 14457-14469.

[12] Höft N., Horbach J. Condensation of methane in the metal-organic framework IRMOF-1: Evidence for two critical points. *J. Am. Chem. Soc.* **2015**, 137(32): 10199-10204.

[13] Spanopoulos I., Tsangarakis C., Klontzas E., et al. Reticular synthesis of HKUST-like tbo-MOFs with enhanced CH_4 storage. J. Am. Chem. Soc. 2016, 138(5):1568-1574.

[14] Hulvey Z., Vlaisavljevich B., Mason J. A., et al. Critical factors driving the high volumetric uptake of methane in $Cu_3(btc)_2$. *J. Am. Chem. Soc.* **2015**, 137(33): 10816-10825.

[15] Chen C. X., Wei Z. W., Jiang J. J., et al. Dynamic spacer installation for multirole metal-organic frameworks: a new direction toward multifunctional MOFs achieving ultrahigh methane storage working capacity. *J. Am. Chem. Soc.* **2017**, 139(17): 6034-6037.

[16] Li B., Wen H. M., Wang H., et al. A porous metal-organic framework with dynamic pyrimidine groups exhibiting record high methane storage working capacity. *J. Am. Chem. Soc.* **2014**, 136(17): 6207-6210.

[17] Rozyyev V., Thirion D., Ullah R., et al. High-capacity methane storage in flexible alkane-linked porous aromatic network polymers. *Nat. Energy*. **2019**, 4(7): 604-611.

[18] Burchell T., Rogers M. SAE International. *SAE Transaction*. 2000, 109.

[19] Makal T.A., Li J. R., Lu W., Zhou H. C. Methane storage in advanced porous materials. *Chem. Soc. Rev.* **2012**, 41(23): 7761-7779.

[20] Kim J., Maiti A., Lin L. C., Stolaroff J. K., Smit B., Aines R. D. New materials for methane capture from dilute and medium-concentration sources. *Nat. Commun.* **2013**, 4(1): 1-7.

[21] Pophale R., Cheeseman P. A., Deem M. W. A database of new zeolite-like materials. *Phys. Chem. Chem. Phys.* **2011**, 13(27): 12407-12412.

[22] Yaghi O. M., O’Keeffe M., Ockwig N. W., Chae H. K., Eddaoudi M., Kim J. Reticular synthesis and the design of new materials. *Nature*. **2003**, 423(6941): 705-714.

[23] Férey G. Hybrid porous solids: past, present, future. *Chem. Soc. Rev.* **2008**, 37(1): 191-214.

[24] D’Alessandro D. M., Smit B., Long J. R. Carbon dioxide capture: prospects for new materials. *Angew. Chem. Int. Ed.* **2010**, 49(35): 6058-6082.

[25] Banerjee R., Phan A., Wang B., et al. High-throughput synthesis of zeolitic imidazolate frameworks and application to CO_2 capture. *Science*. **2008**, 319(5865): 939-943.

[26] Wang B., Côté A. P., Furukawa H., O’Keeffe M., Yaghi O. M. Colossal cages

in zeolitic imidazolate frameworks as selective carbon dioxide reservoirs. *Nature.* **2008**, 453(7192): 207-211.

[27] Adisa O. O., Cox B. J., Hill J. M. Methane storage in molecular nanostructures. *Nanoscale.* **2012**, 4(11): 3295-3307.

[28] Lu X., Jin D., Wei S., et al. Competitive adsorption of a binary CO_2-CH_4 mixture in nanoporous carbons: effects of edge-functionalization. *Nanoscale.* **2015**, 7(3): 1002-1012.

[29] Dawson R., Cooper A. I., Adams D. J. Nanoporous organic polymer networks. *Prog. Polym. Sci.* **2012**, 37(4): 530-563.

[30] He Y., Zhou W., Qian G., Chen B. Methane storage in metal-organic frameworks. *Chem. Soc. Rev.* **2014**, 43(16): 5657-5678.

[31] Peng Y., Krungleviciute V., Eryazici I., Hupp J. T., Farha O. K., Yildirim T. Methane storage in metal-organic frameworks: current records, surprise findings, and challenges. *J. Am. Chem. Soc.* **2013**, 135(32): 11887-11894.

[32] Eddaoudi M., Kim J., Rosi N., et al. Systematic design of pore size and functionality in isoreticular MOFs and their application in methane storage. *Science.* **2002**, 295(5554): 469-472.

[33] Li B., Wen H. M., Wang H., et al. Porous metal-organic frameworks with Lewis basic nitrogen sites for high-capacity methane storage. *Energy & Environ. Sci.* **2015**, 8(8): 2504-2511.

[34] Mason J. A., Oktawiec J., Taylor M. K., et al. Methane storage in flexible metal-organic frameworks with intrinsic thermal management. *Nature.* **2015**, 527(7578): 357-361.

[35] Burrows A. D., Cassar K., Friend R. M., Mahon M. F., Rigby S. P., Warren J. E. Solvent hydrolysis and templating effects in the synthesis of metal-organic frameworks. *CrystEngComm.* **2005**, 7(89): 548-550.

[36] Akhbari K., Morsali A. Modulating methane storage in anionic nano-porous MOF materials via post-synthetic cation exchange process. *Dalt. Trans.* **2013**, 42(14): 4786-4789.

[37] Mason J. A., Veenstra M., Long J. R. Evaluating metal-organic frameworks for natural gas storage. *Chem. Sci.* **2014**, 5(1): 32-51.

[38] Furukawa H., Ko N., Go Y. B., et al. Ultrahigh porosity in metal-organic frameworks. *Science.* **2010**, 329(5990): 424-428.

[39] Liao P. Q., Zhang W. X., Zhang J. P., Chen X. M. Efficient purification of ethene by an ethane-trapping metal-organic framework. *Nat. Commun.* **2015**,

6(1): 1-9.

[40] Rosi N. L., Kim J., Eddaoudi M., Chen B., O'Keeffe M., Yaghi O. M. Rod packings and metal-organic frameworks constructed from rod-shaped secondary building units. *J. Am. Chem. Soc.* **2005**, 127(5): 1504-1518.

[41] Wu H., Zhou W., Yildirim T. High-capacity methane storage in metal-organic frameworks M_2(dhtp): The important role of open metal sites. *J. Am. Chem. Soc.* **2009**, 131(13): 4995-5000.

[42] Brandt A. R., Heath G. A., Kort E. A., et al. Methane leaks from North American natural gas systems. *Science*. **2014**, 343(6172): 733-735.

[43] Shekhah O., Belmabkhout Y., Chen Z., et al. Made-to-order metal-organic frameworks for trace carbon dioxide removal and air capture. *Nat. Comm.* **2014**, 5(1): 1-7.

[44] Alezi D., Belmabkhout Y., Suyetin M., et al. MOF crystal chemistry paving the way to gas storage needs: Aluminum-based soc-MOF for CH_4, O_2, and CO_2 storage. *J. Am. Chem. Soc.* **2015**, 137(41): 13308-13318.

[45] Filinchuk Y., Richter B., Jensen T. R., Dmitriev V., Chernyshov D., Hagemann H. Porous and dense magnesium borohydride frameworks: Synthesis, stability, and reversible absorption of guest species. *Angew. Chem.* **2011**, 123(47): 11358-11362.

[46] Dovgaliuk I., Dyadkin V., Donckt M. Vander, Filinchuk Y., Chernyshov D. Non-isothermal kinetics of Kr adsorption by nanoporous γ-$Mg(BH_4)_2$ from in situ synchrotron powder diffraction. *ACS Appl. Mater. & interfaces.* **2020**, 12(6): 7710-7716.

[47] Dovgaliuk I., Nouar F., Serre C., Filinchuk Y., Chernyshov D. Cooperative adsorption by porous frameworks: diffraction experiment and phenomenological theory. *Chem. Eur. J.* **2017**, 23(70): 17714-17720.

[48] Dovgaliuk I., Senkovska I., Li X., Dyadkin V., Filinchuk Y., Chernyshov D. Kinetic barriers and microscopic mechanisms of noble gas adsorption by nanoporous γ-$Mg(BH_4)_2$ obtained by means of sub-second X-ray diffraction. *Angew. Chem. Int. Ed.* **2021**, 60(10): 5250-5256.

[49] Favre-Nicolin V., Černý R. FOX, 'free objects for crystallography': a modular approach to ab initio structure determination from powder diffraction. *J. Appl. Crystallogr.* 2002, 35(6): 734-743.

[50] Rodriguez-Carvajal J. Recent advances in magnetic structure determination by neutron powder diffraction. *Phys. B Condens. Matter.* **1993**, 192(1-2): 55-69.

[51] Llewellyn P. L., Horcajada P., Maurin G., et al. Complex adsorption of short linear alkanes in the flexible metal-organic-framework MIL-53 (Fe). *J. Am. Chem. Soc.* **2009**, 131(36): 13002-13008.

[52] Jensen T. R., Nielsen T. K., Filinchuk Y., et al. Versatile in situ powder X-ray diffraction cells for solid-gas investigations. *J. Appl. Crystallogr.* **2010**, 43(6): 1456-1463.

[53] Hammersley A. P., Svensson S. O., Hanfland M., Fitch A. N., Hausermann D. Two-dimensional detector software: from real detector to idealised image or two-theta scan. *Int. J. High Press. Res.* **1996**, 14(4-6): 235-248.

[54] David W. I., Callear S. K., Jones M. O., et al. The structure, thermal properties and phase transformations of the cubic polymorph of magnesium tetrahydroborate. *Phys. Chem. Chem. Phys.* **2012**, 14(33): 11800-11807.

[55] Ban V., Soloninin A. V., Skripov A. V., Hadermann J., Abakumov A., Filinchuk Y. Pressure-collapsed amorphous Mg $(BH_4)_2$: An ultradense complex hydride showing a reversible transition to the porous framework. *J. Phys. Chem. C.* **2014**, 118(40): 23402-23408.

[56] Al-Baghli N. A., Loughlin K. F. Adsorption of methane, ethane, and ethylene on titanosilicate ETS-10 zeolite. *J. Chem. & Eng. Data.* **2005**, 50(3): 843-848.

[57] Zhu W., Kapteijn F., Moulijn J. A. Adsorption of light alkanes on silicalite-1: Reconciliation of experimental data and molecular simulations. *Phys. Chem. Chem. Phys.* **2000**, 2(9): 1989-1995.

[58] Vlugt T. J., Krishna R., Smit B. Molecular simulations of adsorption isotherms for linear and branched alkanes and their mixtures in silicalite. *J. Phys. Chem. B.* **1999**, 103(7): 1102-1118.

[59] Choudhary V. R., Mayadevi S. Adsorption of methane, ethane, ethylene, and carbon dioxide on silicalite-l. *Zeolites.* **1996**, 17(5-6): 501-507.

[60] Stach H., Lohse U., Thamm H., Schirmer W. Adsorption equilibria of hydrocarbons on highly dealuminated zeolites. *Zeolites.* **1986**, 6(2): 74-90.

[61] Wood C. D., Tan B., Trewin A., et al. Microporous organic polymers for methane storage. *Adv. Mater.* **2008**, 20(10): 1916-1921.

[62] He, Seaton N. A. Heats of adsorption and adsorption heterogeneity for methane, ethane, and carbon dioxide in MCM-41. *Langmuir.* **2006**, 22(3): 1150-1155.

[63] Yun J. H., Düren T., Keil F. J., Seaton N. A. Adsorption of methane, ethane, and their binary mixtures on MCM-41: Experimental evaluation of methods for the prediction of adsorption equilibrium. *Langmuir.* **2002**, 18(7): 2693-

2701.

[64] Ma S., Zhou H. C. A metal-organic framework with entatic metal centers exhibiting high gas adsorption affinity. *J. Am. Chem. Soc.* **2006**, 128(36): 11734-11735.

[65] Bourrelly S., Llewellyn P. L., Serre C., Millange F., Loiseau T., Férey G. Different adsorption behaviors of methane and carbon dioxide in the isotypic nanoporous metal terephthalates MIL-53 and MIL-47. *J. Am. Chem. Soc.* **2005**, 127(39): 13519-13521.

[66] Düren T., Sarkisov L., Yaghi O. M., Snurr R. Q. Design of new materials for methane storage. *Langmuir.* **2004**, 20(7): 2683-2689.

[67] Bhatia S. K., Myers A. L. Optimum conditions for adsorptive storage. *Langmuir.* **2006**, 22(4): 1688-1700.

[68] Stadie N. P., Murialdo M., Ahn C. C., Fultz B. Anomalous isosteric enthalpy of adsorption of methane on zeolite-templated carbon. *J. Am. Chem. Soc.* **2013**, 135(3): 990-993.

[69] Himeno S., Komatsu T., Fujita S. High-pressure adsorption equilibria of methane and carbon dioxide on several activated carbons. *J. Chem. Eng. Data.* **2005**, 50(2): 369-376.

[70] Choi B. U., Choi D. K., Lee Y. W., Lee B. K., Kim S. H. Adsorption equilibria of methane, ethane, ethylene, nitrogen, and hydrogen onto activated carbon. *J. Chem. Eng. Data.* **2003**, 48(3): 603-607.

[71] Murialdo M., Stadie N. P., Ahn C. C., Fultz B. Observation and investigation of increasing isosteric heat of adsorption of ethane on zeolite-templated carbon. *J. Phys. Chem. C.* **2015**, 119(2): 944-950.

[72] Lee J. W., Kang H. C., Shim W. G., Kim C., Moon H. Methane adsorption on multi-walled carbon nanotube at (303.15, 313.15, and 323.15) K. *J. Chem. Eng. Data.* **2006**, 51(3): 963-967.

[73] Mofarahi M., Salehi S. M. Pure and binary adsorption isotherms of ethylene and ethane on zeolite 5A. *Adsorption.* **2013**, 19(1): 101-110.

[74] Zhou W., Wu H., Hartman M. R., Yildirim T. Hydrogen and methane adsorption in metal-organic frameworks: A high-pressure volumetric study. *J. Phys. Chem. C.* **2007**, 111(44): 16131-16137.

[75] Simon C. M., Smit B., Haranczyk M. pyIAST: Ideal adsorbed solution theory (IAST) python package. *Comput. Phys. Commun.* **2016**, 200: 364-380.

[76] Khodakov A. Y., Kustov L. M., Kazansky V. B., Williams C. Infrared

spectroscopic study of the interaction of cations in zeolites with simple molecular probes. Part 3.-Adsorption and polarization of methane and ethane on cationic forms of high-silica zeolites. *J. Chem. Soc. Faraday Trans.* **1993**, 89(9): 1393-1395.

[77] Kazansky V. B. State and properties of ion-exchanged cations in zeolites: 2. IR spectra and chemical activation of adsorbed methane. *Kinet. Catal.* **2014**, 55(6): 737-747.

[78] Kazansky V. B., Pidko E. A. Intensities of IR stretching bands as a criterion of polarization and initial chemical activation of adsorbed molecules in acid catalysis. ethane adsorption and dehydrogenation by zinc ions in ZnZSM-5 zeolite. *J. Phys. Chem. B.* **2005**, 109(6): 2103-2108.

[79] Mitoraj M. P. Bonding in ammonia borane: An analysis based on the natural orbitals for chemical valence and the extended transition state method (ETS-NOCV). *J. Phys. Chem. A.* **2011**, 115(51): 14708-14716.

[80] Armstrong D. R., Perkins P. G. Electronic structure of dimeric aminoborane, $(NH_2BH_2)_2$. *J. Chem. Soc. A.* **1970**: 2748-2750.

[81] Jepsen L. H., Ban V., Møller K. T., et al. Synthesis, crystal Structure, thermal decomposition, and ^{11}B MAS NMR characterization of $Mg(BH_4)_2(NH_3BH_3)_2$. *J. Phys. Chem. C.* **2014**, 118(23): 12141-12153.

[82] Bondi A. van der Waals volumes and radii. *J. Phys. Chem.* **1964**, 68(3): 441-451.

[83] Sircar S., Myers A. L. *Gas Separation by Zeolites. In Handbook of Zeolite Science and Technology*. CRC Press, **2003**.

[84] Soloninin A. V., Babanova O.A., Skripov A. V., et al. NMR Study of reorientational motion in alkaline-earth borohydrides: β and γ Phases of $Mg(BH_4)_2$ and α and β Phases of $Ca(BH_4)_2$. *J. Phys. Chem. C.* **2012**, 116(7):4913-4920.

Chapter 7. Kinetic Barriers and Microscopic Mechanisms of Noble Gas Adsorption by Nanoporous γ-$Mg(BH_4)_2$ Obtained by Means of Sub-Second X-Ray Diffraction

Iurii Dovgaliuk[12],* *Irena Senkovska*[3], *Xiao Li*[4], *Vadim Dyadkin*[1],
Yaroslav Filinchuk[4],* *Dmitry Chernyshov*[1]*

[1]Swiss-Norwegian Beamlines at the European Synchrotron Radiation Facility, 38000 Grenoble (France).

[2]Institut des Matériaux Poreux de Paris, Ecole Normale Supérieure, ESPCI Paris, CNRS, PSL Université, 75005 Paris (France).

[3]Inorganic Chemistry I, Technische Universität Dresden Bergstrasse 66, 01069 Dresden (Germany).

[4]Institute of Condensed Matter and Nanosciences, Université Catholique de Louvain, Place L. Pasteur, 1348 Louvain-la-Neuve (Belgium).

This chapter has been published in Angew. Chem. Int. Ed. 2021, 60, 5250–5256. doi.org/10.1002/anie.202015019

Abstract

Gas adsorption by porous frameworks sometimes results in structure "breathing", "pores opening/closing", "negative gas adsorption", and other phenomena. Time dependent diffraction can address both kinetics of the guest uptake and structural response of the host framework. Using sub-second in situ powder X-ray diffraction, three intracrystalline diffusion scenarios have been evaluated from the isothermal kinetics of Ar, Kr, and Xe adsorption by nanoporous g-$Mg(BH_4)_2$*. These scenarios are dictated by two possible simultaneous transport mechanisms: diffusion through the intra- (i) and interchannel apertures (ii) of* γ-$Mg(BH_4)_2$ *crystal structure. The contribution of (i) and (ii) changes depending on the kinetic diameter of the noble gas molecule and temperature regime. The lowest single activation barrier for the smallest Ar suggests equal diffusion of the atoms trough both pathways. Contrary, for the medium-sized Kr we resolve the contributions of two parallel transport mechanisms, which tentatively can be attributed to the smaller barrier of the migration paths via the channel like pores and the higher barrier for the diffusion via narrow aperture between these channels. The largest Xe atoms diffuse only along 1D channels and show the highest single activation barrier.*

7.1. Introduction

Crystalline porous materials such as metal-organic frameworks, covalent organic frameworks, and zeolites are one of the most blossoming fields in chemistry and material science[1–3] due to their regular porosity and great potential for selective adsorption, separation and storage of guest molecules of interest.[4] In the last decades more and more attention has been paid to flexibility of the crystalline porous materials, seriously affecting guest adsorption/desorption and a mechanical response of the material to perturbation of external conditions. It is also a key feature in several fascinating adsorption-driven phenomena, such as “breathing”[5–7], “gate opening/closing”[8, 9], (photo)switching[10, 11] and negative gas adsorption (NGA)[11]. Notably, structural flexibility of the host is often provoked by adsorption and thus the kinetics of the guest uptake and of the framework transformation are coupled. So, the monitoring of dynamics in such materials play a key role for the materials science and for further materials development. To enable such investigations, a wide range of advanced *in situ* characterization methods were explored in recent years, including diffraction, scattering, vibrational and NMR spectroscopies[12, 13]. Thanks to the crystallinity, the *in situ* X-ray, electron, and neutron diffraction methods became indispensable techniques for understanding the mechanisms of gas adsorption or separation in porous crystalline materials, and present a new possibility to crystallographically evaluate the population of individual adsorption sites, to study the cooperativity and to visualize the isotherms of individual pores in materials with hieratical porosity[12, 14, 15].

A common scheme for the structural characterization of a dynamic process, such as adsorption and desorption, assumes crystal structure determination at few different static states representing different stages of adsorption process[16], frequently augmented by macroscopic evaluation of thermodynamics and kinetics as well as by theoretical calculations[17]. However, the time resolved tracking of guest molecules inside the porous framework upon adsorption has not been reported before. This work addresses a possibility to implement a sub-second X-ray powder diffraction for determination of kinetic barriers and visualization of the possible microscopic gas adsorption mechanisms simultaneously, from a single experiment. This approach has a potential to resolve site-specific kinetics of guest uptake, that is not accessible to microscopic methods.

As an object for the time-dependent study, we selected a microporous γ-$Mg(BH_4)_2$, a representative of metal borohydrides which attract much attention as multifunctional materials[18]. This framework has tubular-like pores with ca. 7 Å in size, that is between one and two kinetic diameters of Kr and Xe atoms (3.6-7.2 Å for Kr and 3.95-7.9 Å for Xe), showing a significant non-isothermal kinetics upon Kr adsorption[19][20], therefore interesting for potential separation of these gases[21–23]. In particular, the selective capture of Xe and Kr from the radioactive products generated from nuclear fission is highly needed[24-26].

7.2. Experimental details

Experimental details can be seen in Appendix IV.

7.3. Results and discussion

The light elements of γ-$Mg(BH_4)_2$ host structure enhance the X-ray contrast for the guest atoms such as Ar, Kr or Xe significantly, because of sufficient difference between low scattering (form) factors of Mg (Z=12), B (Z=4) and H (Z=1) and comparable or higher scattering (form) factors of noble gas molecules (e.g., for Kr at $2\theta=0^{\circ}$, it equals to the atomic number Z=36). For this reason the noble gas atoms can be easily localized in the structure close to the center of the pore, while the light B and H atoms contribute little to the total scattering. The additional fluorescence signal of Kr atoms can be observed as an increase of all background points, which originates from the Kr K-edge X-ray absorption (14.3256 keV or 0.8655 Å)[27], achievable in our experimental conditions with higher energy (15 900 keV or 0.77936 Å), see Figure 1. Such combination of the host and guest responsiveness makes this compound ideal candidate for *in situ* investigations by X-rays.

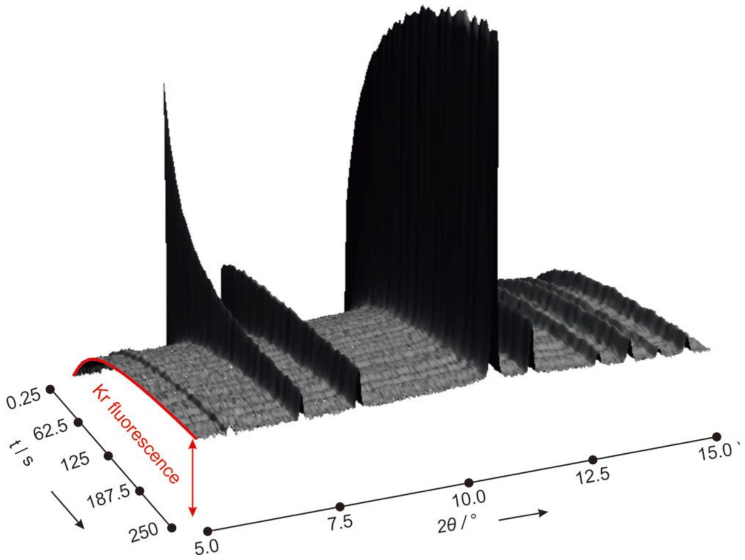

Figure 1. Time-dependent powder diffraction from g-Mg(BH$_4$)$_2$ loaded with Kr gas (p(Kr)=0.5 bar, T=170 K, λ=0.77936 Å). The significant change of the intensities of Bragg peaks and of the fluorescent background correlate with the amount of the adsorbed gas.

The Kr adsorption experiments were performed at 170, 180, 190 and 200 K, in which the sample was exposed to 0.5 bar Kr and four diffraction patterns were collected per second for 2500 seconds. The in situ data show significant changes in the peak intensities in the XRD patterns of γ-Mg(BH$_4$)$_2$ with the Kr adsorption time (see Figure 1 for 170 K). The variation of the background is related to the increase of

Kr fluorescence due its progressive adsorption by the framework[18], which we used as an independent measure of Kr adsorption kinetics.

Sequential Rietveld refinement to the multitude of diffraction patterns confirms the two-phase model, used in our previous variable-temperature experiment[20], see Figures S1 and S2, and Table S1. Kr atoms in the phase (**2**), having smaller unit cell parameters, are closer to the center of the pore cavities, as compared to the dominant phase (**1**). However, a small amount of the secondary phase (**2**) present in the mixture, a strong peaks' overlap for the two phases, and the limitation of the X-ray powder diffraction to locate hydrogen atoms do not allow to capture structural differences associated with the smaller unit cell volume for the phase (**2**). We think that the two phases differ by the orientation of the $[BH_4]^-$ groups, a detail that is hardly seen in an X-ray experiment. The two phases have therefore been treated as isostructural with only slight difference in unit cell dimensions and location of Kr atoms.

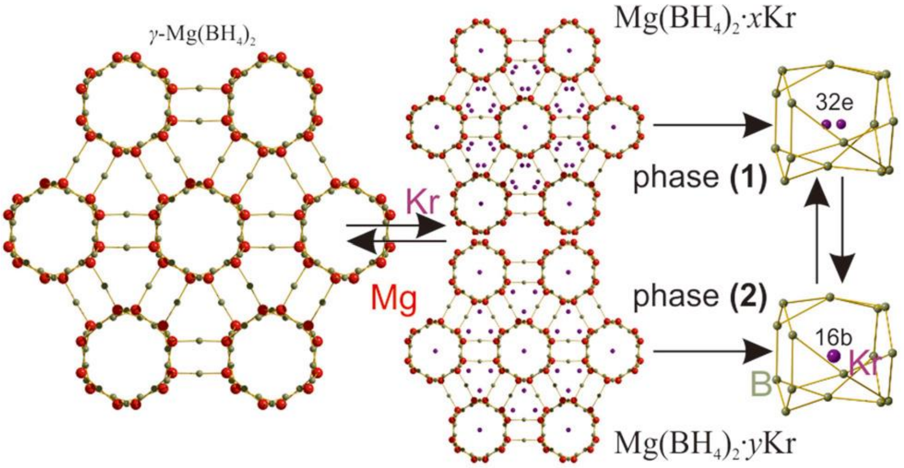

Figure 2. Fragments of the crystal structures representing the phases (1) and (2) of γ-$Mg(BH_4)_2$ loaded with Kr. The minor phase (2) has smaller cell parameter and is modelled by occupation of the middle of the pore (coordinates 1/8, 1/8, 1/8) by Kr atoms. The pores are organized into channels running perpendicular to the plane of the Figure.

In the phase (**1**) $Mg(BH_4)_2 \cdot x$Kr, the guest atoms are located in the

1D channels running along the body diagonal of the cubic unit cell, at the crystallographic position 32e (x, x, x). Secondary $Mg(BH_4)_2{\cdot}y$Kr phase (2) can be represented as a special case of phase (**1**), where the Kr atoms adopt the crystallographic position 16b with (1/8, 1/8, 1/8) coordinates right in the middle of the pore, see Figure 2.

The total Kr uptake for kinetic analysis was extracted using the Kr occupancies in each phase and their refined weight fractions. In the first approximation, Kr adsorption on γ-$Mg(BH_4)_2$ can be considered as an addition reaction, where $Mg(BH_4)_2{\cdot}q_e$Kr adduct is forming (q_e is the total amount of Kr adsorbed at equilibrium for a given temperature and pressure). In an attempt to describe the transformation from empty γ-$Mg(BH_4)_2$ to $Mg(BH_4)_2{\cdot}q_e$Kr, the time-dependent occupancy of Kr (q_t) was derived from the Johnson-Mehl-Avrami-Kolmogorov (JMAK) relation[28, 29], widely used to describe kinetics of different chemical reactions[30]:

$$q_t = q_{min} + (q_e - q_{min})[1 - \exp\left(-(kt)^n\right)] \tag{1}$$

The Equation (1) is a fractional order kinetic model, where q_{min} is amount of preoccupied Kr positions before data collection, q_e is an equilibrium value that sets the maximum for a given thermodynamic conditions, k is Avrami kinetic constant, n is an order of reaction (expected to be $0.5 \leq n \leq 1$ for a diffusion controlled case)[30], t is the time elapsed from the beginning of the process. This relation is widely used to describe adsorption kinetics of various gases/vapors on activated carbons and is known as Linear driving force (LDF) model, if n=1[31]. The LDF model is consistent with a single rate constant (k), relaxation time, and barrier for diffusion into a periodic porous structure[32].

However, the least square fit of the data collected between 170 and 200 K with Equation (1) has shown the need of one additional term to model pore depopulation likely due to radiation damage, at least for the data collected at 200 K. Therefore, the Equation (1) was modified as follows:

$$q_t = q_{min} + (q_e - q_{min})[A(1 - \exp(-(k_1 t)^n)) - (1 - A)\exp(k_2 t)] \tag{2}$$

Here A stands for the non-degraded part of the sample, and the decay constant k_2 maps the rate of sample degradation. Interestingly, the good fit to the data affected by the radiation damage indicates that the exponential terms in equation (2) describe equally well the Avrami kinetics and the kinetics of the radiation damage.

The corresponding Sharp-Hancock plots form the Equation (1) and the obtained Arrhenius plot of the rate constant from equations (1) and (2) versus 1/T result in unexpected behavior. They show partially anti-Arrhenius slope suggesting higher adsorption rates at lower temperatures (190–170 K), while the rate at 200 K is an outlier of the general trend (Figures S3 and S4). The anti-Arrhenius behavior is quite rare and usually can be observed during significant structural transitions in the kinetic process of guest uptake[33-35], while the outlier point indicate a possible need of a different model for the kinetic process. One of the possible kinetic models, enabling to coherently describe the data is the one assuming two barriers[32]:

$$q_t = q_{min} + (q_e - q_{min})[A(1 - \exp(-k_1 t)) + (1 - A)(1 - \exp(-k_2 t))] \tag{3}$$

Similarly to the Equation (2), the double exponent Equation (3) can be modified for the sample degradation at higher temperatures, via inclusion of additional parameters: A_1 (part of the adsorbed Kr limited by a rate constant k_1), A_2 (part of the adsorbed Kr limited by a rate constant k_2) and k_3 maps the rate of the sample degradation:

$$\begin{aligned} q_t = q_{min} + (q_e - q_{min})[A_1(1 - \exp(-k_1 t)) \\ +A_2(1 - \exp(-k_2 t)) - (1 - A_1 - A_2)(\exp(k_3 t))] \end{aligned} \tag{4}$$

Indeed, the resulting Equation (4) successfully describes the experimental data for all investigated temperatures and the fitted q_e confirms the Kr content obtained from isobaric experiments, see Figure 3. On the other hand, Equation (3) works equally well for the data below

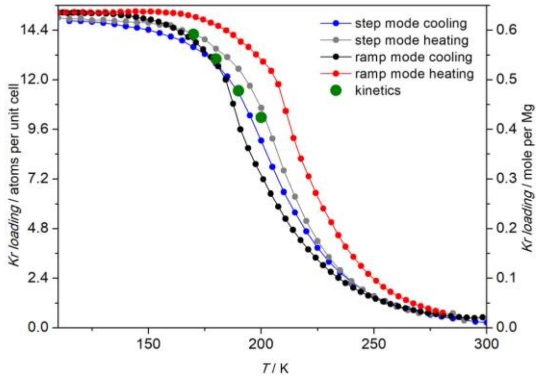

Figure 3. Comparison of calculated Kr content from the isobaric variable-temperature experiments[20] and kinetic data obtained using Equation (4). The fitted values of q_e fall in the middle of the kinetic hysteresis loops, and thus give even better estimate of the equilibrium Kr content than the quasi-equilibrium variable-temperature experiments.

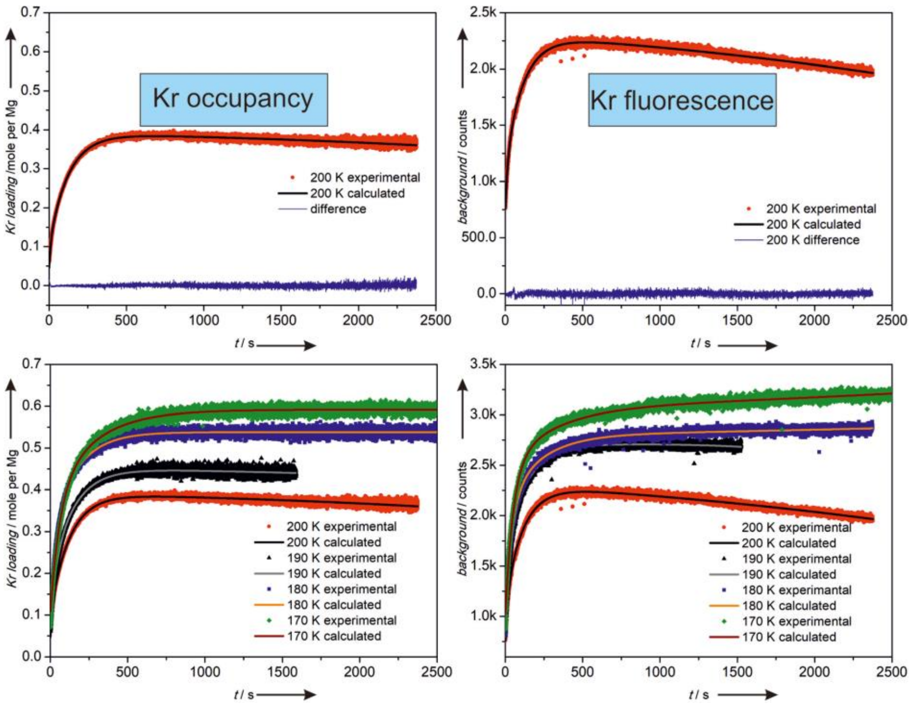

Figure 4. The experimental, calculated, and difference kinetic curves for Kr adsorption at 200 K (top) as well as comparison of the experimental kinetics and fits obtained using Equations (3) and (4) (bottom). Left: Kr occupancies obtained using Rietveld method (each point is an independent refinement of the Kr occupancies in phases (**1**) and (**2**)); Right: measured Kr fluorescence background and corresponding fit obtained using Equations (3) and (4).

200 K due to the smaller effect of the radiation damage. The Equation (4) applied to the Kr fluorescence background shows rates that are very similar to those fitted from Kr occupancies, see Figure 4 and Figure S5. Kr fluorescence is an independent probe to the adsorption kinetics, free of the Rietveld refinement of thousands of powder diffraction patterns and of the related assumptions. However, it is giving access only to the kinetics of the adsorption without the underlying microscopic (structural) picture, and is limited to guests showing strong fluorescent signal, such as Kr. These independent measures suggest that Kr uptake is taking place in the crystalline part of the sample only.

Kr adsorption isotherms were also measured volumetrically at 170, 180, 190 and 200 K up to 1 bar (Figure S6). The adsorption rate analysis was performed at 0.5 bar equilibrium Kr pressure using LDF approximation. The obtained mass transfer coefficients follow the same trend as from the in situ X-ray data (Table S1), proving the reliability of the proposed approach.

The Kr adsorption isotherms were fitted using Langmuir model (Figures S7 and S8) and the derived equilibrium constants were used to extract the thermodynamic parameters from the van’t Hoff plot (Figure S9). The resulting values of ΔH of 18.4(7) kJ/mol of adsorbed Kr and ΔS of 140(4) J/(mol·K) are close to the initial estimates of ΔH=21-24 kJ/mol and ΔS=103-113 J/(mol·K) made from non-isothermal diffraction data[18].

In contrast to the equations (1) and (2), Arrhenius plots derived from the rate constants fitted by equations (3) and (4) demonstrate the ordinary behavior, see Figure 5a. Linear fits to the Arrhenius plots yield kinetic barriers that are nearly equal for kinetic models (3) and (4). According to the Equation (4) applied to Kr occupancies, the radiation damage at 200 K affects about 0.05 part of the sample with the rate k_3 approximately 20 and 230 times lower than k_1 and k_2, respectively, see Tables S2-S4. The parametrization of Equation (4) below 200 K gives similar result for 190 K and much lower values for 180 K and 170 K indicating a suppression of the radiation damage at low temperatures.

We therefore neglected the radiation damage contribution and used double exponent Equation (3) for the data collected below 200 K.

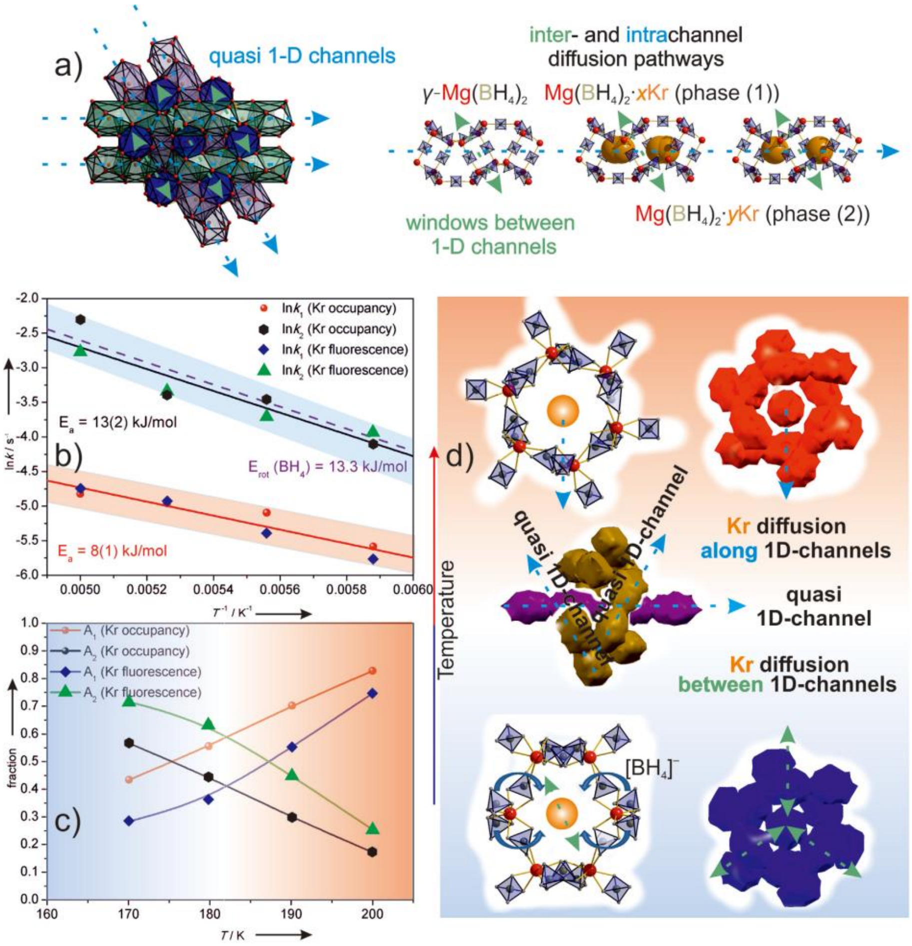

Figure 5. a) The representation of quasi 1D channels with the corresponding pore cavities of empty γ-$Mg(BH_4)_2$ and their filling by Kr molecules. The formed $Mg(BH_4)_2$·(*x, y*)Kr are presented along the [-1 1 1] crystallographic direction. b) The Arrhenius plots of kinetic rates calculated from the Equations (3) and (4) and partial contributions (c) of each exponential component both for the calculated Kr occupancies using Rietveld refinement of powder patterns and the fluorescence background. The corresponding temperature-dependent mechanisms (b and d) of the limiting Kr kinetic rates are shown as a smooth transformation from red to blue: via diffusion along the 1D channels with large pore apertures above 175-188 K (red) and diffusion between these 1D channels, promoted by the rotation of $[BH_4]^-$ groups located in the small apertures below 175-188 K (blue).

The Arrhenius plots obtained from Kr occupancies and fluorescence background yield the first kinetic barrier of 8(1) and the second one of 13(2) kJ/mol. Analysis of the temperature evolution of the pre-exponential factors suggests a dominant contribution of the smaller kinetic barrier above 175-188 K, see Figure 5b and Figure S10. Such a behavior indicates two parallel adsorption mechanisms with different contributions, which change within investigated temperature intervals.

Based on structural consideration, we propose two simultaneous Kr diffusion mechanisms in γ-$Mg(BH_4)_2$ that agree with this observation. The lower barrier represents Kr diffusion along the quasi 1D channels of the nanoporous γ-$Mg(BH_4)_2$, similarly to previously determined gas diffusion along 1D channels in microporous structures (e.g. Xe diffusion in TCF-1 with 7.1 kJ/mol activation energy)[36], while the higher diffusion barrier is more common for the guest-promoting rotary motions in tight channels of some crystal structures[37-39]. In particular, the origin of the higher kinetic barrier of Kr adsorption in γ-$Mg(BH_4)_2$ can be related to the rotational motions of the $[BH_4]^-$ groups in the structure. Notably, previously reported activation energy for $[BH_4]^-$ reorientations around 2-fold (C_2) axis in β-$Mg(BH_4)_2$ polymorph has a very similar value of 13.3 kJ/mol[40]. $[BH_4]^-$ rotations near the 2-fold axis may therefore be considered as a predominant structural mechanism associated with the higher barrier of Kr diffusion. The barriers for $[BH_4]^-$ orientational jumps in γ-$Mg(BH_4)_2$ are significantly higher and include at least two motions[41, 42].

Taking into account these considerations together with the crystal structure of γ-$Mg(BH_4)_2$, we propose two concerted mechanisms for Kr adsorption: the first is caused by Kr diffusion along 1D channels running in *c* direction and it dominates at high temperatures (>175 K), while at low temperatures (<175 K) the second mechanism, namely the diffusion through the windows between channels, governs the kinetics, see Figure 5d. The first kinetic mechanism involves a larger (≈5.8 Å) aperture of the channels, which does not affect the diffusion of Kr (kinetic diameter of 3.6 Å) to such extent as a smaller interchannel aperture with ≈5.0 Å in size. According to contact surface analysis made with Mercury using 0.7 Å grid spacing[43], the smaller aperture is suitable for a diffusion of the guest molecules with a kinetic diameter smaller than 3.4 Å. Thus, rotational motions of $[BH_4]^-$ around 2-fold (C_2) axis of Mg-BH_4-Mg bonds with an activation barrier of 13 kJ/mol can support the diffusion of Kr molecules (kinetic diameter 3.6 Å) via a pedal-wheel mechanism, see Figure 5d.

The characterization of the size and shape of γ-$Mg(BH_4)_2$ by scanning electron microscopy (SEM) reveals the presence of two types of $Mg(BH_4)_2$ particles (see Figure S11). One type of these particles belongs to the porous γ-$Mg(BH_4)_2$ and another one apparently is the amorphous polymorph of $Mg(BH_4)_2$, suggested by the Refs. [41, 44] and our volumetric data. This makes impossible to get the correlations between particle size of γ-$Mg(BH_4)_2$ and Kr uptake time and requires additional studies for the conditions of its shape/size and yield control. In order to link microscopic diffusion mechanisms with the crystal structure of γ-$Mg(BH_4)_2$ and the size of the guest molecules, we additionally performed the kinetic analysis for the smaller Ar (kinetic diameter σ=3.4 Å) and the larger Xe (σ=3.95 Å) atoms, see Figure 6. Contrary to the Kr, they both follow a single barrier resistance with expectedly lower activation energy for Ar (5.4(3) kJ/mol) and the higher one for Xe atoms (9.5(6) kJ/mol), see Figures 6, S12 and Table S5. This suggests that Ar atoms diffuse easily along 1D channels as well as between them within the investigated temperature range. On the other hand, larger Kr atoms (3.8 Å) have higher activation barrier along 1D channels (8(1) kJ/mol) as well as through the interchannel aperture, where its size is matching the penetration limit. The diffusion along the latter is likely hindered by the dynamic rotation of the $[BH_4]^-$ groups between Mg atoms, resulting in higher activation barrier (13(2) kJ/mol). The largest Xe atoms (σ=3.95 Å) apparently do not diffuse through the interchannel apertures at all due to large size. In such case, the obtained intrachannel activation barriers increase in accordance with their larger kinetic diameters in a series Ar < Kr < Xe, being common upon adsorption by other porous materials, see Figure S13[45, 46].

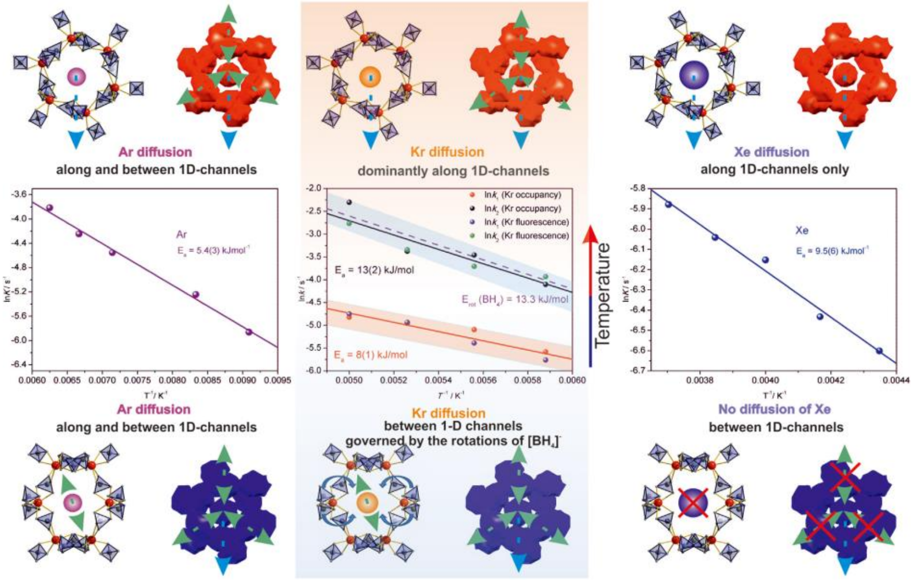

Figure 6. The Arrhenius plots of Ar, Kr and Xe adsorption kinetics and the schemes of corresponding microscopic diffusion mechanisms. Ar and Xe follow a single exponent adsorption behavior, while Kr has a double exponent parallel kinetics, denoted as the first and the second kinetic barriers. The smooth transition from the domination of interchannel to the intrachannel activation barrier upon Kr adsorption by γ-$Mg(BH_4)_2$ is presented by gradient change of color from blue to red (temperature). Color code: Ar-purple, B-olive, H-grey, Kr-orange, Mg-red, Xe-violet

7.4. Conclusions

The understanding of adsorption mechanisms and their corresponding energetic characteristics is of high importance for predictions of the adsorption selectivity. Particularly, the evaluation of structure- and guest-defined activation barriers in dynamic materials may explain such phenomena as selectivity of adsorption-induced phase transitions[47]. The latter enables to use the same porous framework for separation of various guests, depending on the temperature regime. In our case the potential separation of Kr over Xe by γ-$Mg(BH_4)_2$ will be limited by the rotational motions of $[BH_4]^-$ groups below 175-188 K and by the guest diffusivity along 1D channels above this temperature range. The similar kinetic characterization of the Xe adsorption in γ-$Mg(BH_4)_2$ should demonstrate the preferable high temperature (>188 K) range for Xe over Kr kinetic selectivity, providing that its hindered interchannel diffusivity is confirmed experimentally. In line with the previously presented capability to resolve individual site-specific guest uptake characteristics, like thermodynamics[14] and/or adsorption isotherms [14, 19, 20], this work also shows a promising potential of sub-second X-ray powder diffraction to monitor kinetics of guest adsorption for multi-adsorption site frameworks, as this information is completely inaccessible by classical bulk (volumetric, gravimetric, calorimetric) methods. Despite the fact, that sequential Rietveld analysis of thousands of diffraction patterns remains challenging, in the near future it can be combined with other computational methods, like Principal Component Analysis (PCA)[48], which will open much room for its implementation in numerous kinetic studies.

7.5. Reference

[1] G. Férey, *Chem. Soc. Rev.* **2008**, 37, 191-214.

[2] M. Eddaoudi, D. B. Moler, H. Li, B. Chen, T. M. Reineke, M. O’Keeffe, O. M. Yaghi, *Acc. Chem. Res.* **2001**, 34, 319-330.

[3] H. Furukawa, K. E. Cordova, M. O_Keeffe, O. M. Yaghi, *Science.* **2013**, 341, 1230444.

[4] K. Adil, Y. Belmabkhout, R. S. Pillai, A. Cadiau, P. M. Bhatt, A. H. Assen, G. Maurin, M. Eddaoudi, *Chem. Soc. Rev.* **2017**, 46, 3402-3430.

[5] C. Serre, C. Mellot-Draznieks, S. Surblé, N. Audebrand, Y. Filinchuk, G. Férey, *Science.* **2007**, 315, 1828-1832.

[6] C. Serre, F. Millange, C. Thouvenot, M. Noguès, G. Marsolier, D. Louër, G. Férey, *J. Am. Chem. Soc.* **2002**, 124, 13519-13526.

[7] R. Kitaura, K. Seki, G. Akiyama, S. Kitagawa, Angew. *Chem. Int. Ed.* **2003**, 42, 428-431; *Angew. Chem.* **2003**, 115, 444-447.

[8] D. Fairen-Jimenez, S. A. Moggach, M. T. Wharmby, P. A. Wright, S. Parsons, T. Düren, *J. Am. Chem. Soc.* **2011**, 133, 8900-8902.

[9] J. W. Brown, B. L. Henderson, M. D. Kiesz, A. C. Whalley, W. Morris, S. Grunder, H. Deng, H. Furukawa, J. I. Zink, J. F. Stoddart, et al., *Chem. Sci.* **2013**, 4, 2858-2864.

[10] S. Castellanos, F. Kapteijn, J. Gascon, *CrystEngComm.* **2016**, 18, 4006-4012.

[11] S. Krause, V. Bon, I. Senkovska, U. Stoeck, D. Wallacher, D. M. Tcbbens, S. Zander, R. S. Pillai, G. Maurin, F. X. Coudert, et al., *Nature* **2016**, 532, 348-352.

[12] S. Krause, J. D. Evans, V. Bon, I. Senkovska, P. Iacomi, F. Kolbe, S. Ehrling, E. Troschke, J. Getzschmann, D. M. Tcbbens, et al., *Nat. Commun.* **2019**, 10, 3632.

[13] D. B. Ravnsboek, L. H. Sorensen, Y. Filinchuk, F. Besenbacher, T. R. Jensen, *Angew. Chem. Int. Ed.* **2012**, 51, 3582-3586; *Angew. Chem.* **2012**, 124, 3642-3646.

[14] I. Dovgaliuk, F. Nouar, C. Serre, Y. Filinchuk, D. Chernyshov, *Chem. Eur. J.* **2017**, 23, 17714-17720.

[15] H. S. Cho, J. Yang, X. Gong, Y. B. Zhang, K. Momma, B. M. Weckhuysen, H. Deng, J. K. Kang, O. M. Yaghi, O. Terasaki, *Nat. Chem.* **2019**, 11, 562-570.

[16] J. P. Zhang, P. Q. Liao, H. L. Zhou, R. B. Lin, X. M. *Chen, Chem. Soc. Rev.* **2014**, 43, 5789-5814.

[17] L. Sarkisov, R. L. Martin, M. Haranczyk, B. Smit, *J. Am. Chem. Soc.* **2014**, 136, 2228-2231.

[18] M. Paskevicius, L. H. Jepsen, P. Schouwink, R. Černý, D. B. Ravnsbak, Y. Filinchuk, M. Dornheim, F. Besenbacher, T. R. Jensen, *Chem. Soc. Rev.* **2017**, 46, 1565-1634.

[19] Y. Filinchuk, B. Richter, T. R. Jensen, V. Dmitriev, D. Chernyshov, H. Hagemann, *Angew. Chem. Int. Ed.* **2011**, 50, 11162-11166; *Angew. Chem.* **2011**, 123, 11358-11362.

[20] I. Dovgaliuk, V. Dyadkin, M. Vander Donckt, Y. Filinchuk, D. Chernyshov, *ACS Appl. Mater. Interfaces.* **2020**, 12, 7710-7716.

[21] J. J. Perry, S. L. Teich-Mcgoldrick, S. T. Meek, J. A. Greathouse, M. Haranczyk, M. D. Allendorf, *J. Phys. Chem. C.* **2014**, 118, 11685-11698.

[22] B. J. Sikora, C. E. Wilmer, M. L. Greenfield, R. Q. Snurr, *Chem. Sci.* **2012**, 3, 2217-2223.

[23] M. Witman, S. Ling, S. Jawahery, P. G. Boyd, M. Haranczyk, B. Slater, B. Smit, *J. Am. Chem. Soc.* **2017**, 139, 5547-5557.

[24] F. Kerry, *Industrial Gas Handbook: Gas Separation and Purification*, CRC, Boca Raton, **2006**.

[25] J. Liu, P. K. Thallapally, D. Strachan, *Langmuir.* **2012**, 28, 11584-11589.

[26] L. Chen, P. S. Reiss, S. Y. Chong, D. Holden, K. E. Jelfs, T. Hasell, M. A. Little, A. Kewley, M. E. Briggs, A. Stephenson, et al., *Nat. Mater.* **2014**, 13, 954-960.

[27] J. A. Bearden, A. F. Burr, *Rev. Mod. Phys.* **1967**, 39, 125-142.

[28] A. N. Kolmogorov, *Bull. Acad. Sci. USSR Math. Ser.* **1937**, 1, 355-359.

[29] M. Avrami, *J. Chem. Phys.* **1939**, 7, 1103-1112.

[30] R. Serna-Guerrero, A. Sayari, *Chem. Eng. J.* **2010**, 161, 182-190.

[31] E. Glueckauf, *Trans. Faraday Soc.* **1955**, 51, 1540-1551.

[32] A. J. Fletcher, E. J. Cussen,D. Bradshaw,M. J. Rosseinsky, K. M. Thomas, *J. Am. Chem. Soc.* **2004**, 126, 9750-9759.

[33] A. Kondo, N. Kojima, H. Kajiro, H. Noguchi, Y. Hattori, F. Okino, K. Maeda, T. Ohba, K. Kaneko, H. Kanoh, *J. Phys. Chem. C.* **2012**, 116, 4157-4162.

[34] M. R. Caira, T. le Roex, L. R. Nassimbeni, E. Weber, *Cryst. Growth Des.* **2006**, 6, 127-131.

[35] L. J. Barbour, M. R. Caira, L. R. Nassimbeni, J. Chem. Soc. *Perkin Trans. 2* **1993**, 2321-2322.

[36] I. Bassanetti, S. Bracco, A. Comotti, M. Negroni, C. Bezuidenhout, S. Canossa, P. P. Mazzeo, L. Marchió, P. Sozzani, *J. Mater. Chem. A* **2018**, 6, 14231-14239.

[37] A. Comotti, S. Bracco, P. Sozzani, *Acc. Chem. Res.* **2016**, 49, 1701-1710.

[38] A. Comotti, S. Bracco, A. Yamamoto, M. Beretta, T. Hirukawa, N. Tohnai, M. Miyata, P. Sozzani, *J. Am. Chem. Soc.* **2014**, 136, 618-621.

[39] A. Comotti, S. Bracco, P. Valsesia, M. Beretta, P. Sozzani, *Angew. Chem. Int. Ed.* **2010**, 49, 1760-1764; Angew. Chem. 2010, 122, 1804-1808.

[40] A. V. Soloninin, O. A. Babanova, A. V. Skripov, H. Hagemann, B. Richter, T. R. Jensen, *Y. Filinchuk, J. Phys. Chem. C* **2012**, 116, 4913-4920.

[41] V. Ban, A. V. Soloninin, A. V. Skripov, J. Hadermann, A. Abakumov, Y. Filinchuk, *J. Phys. Chem. C* **2014**, 118, 23402-23408.

[42] M. Eagles, B. Sun, B. Richter, T. R. Jensen, Y. Filinchuk, M. S. Conradi, *J. Phys. Chem. C* **2012**, 116, 13033-13037.

[43] C. F. Macrae, I. J. Bruno, J. A. Chisholm, P. R. Edgington, P. McCabe, E. Pidcock, L. Rodriguez-Monge, R. Taylor, J. Van De Streek, P. A. Wood, J. *Appl. Crystallogr.* **2008**, 41, 466-470.

[44] N. P. Stadie, E. Callini, P. Mauron, A. Borgschulte, A. Züttel, *J. Visualized Exp.* **2015**, 95, 7–9.

[45] *Handbook of Zeolite Science and Technology* (Eds.: S. M. Auerbach, K. A. Carrado, P. K. Dutta, Marcel Dekker, New York, **2003**.

[46] Y. Liu, J. Liu, J. Hu, *BMC Chem. Eng.* **2019**, 1–7.

[47] C. A. Fernandez, J. Liu, P. K. Thallapally, M. Strachan, *J. Am. Chem. Soc.* **2012**, 134, 9046-9049.

[48] D. Chernyshov, I. Dovgaliuk, V. Dyadkin, W. van Beek, *Crystals.* **2020**, 10, 581.

Chapter 8. Conclusions of the Results and Perspectives

In this project, we developed a new methodology that is based on diffraction methods to characterize adsorption, both from the point of view of structural study, but also aiming to access the macroscopic properties. The position and orientation of guest molecules are first obtained by global optimization in direct space, followed by a sequential Rietveld refinement of this model along the adsorption isotherms and/or isobars. We extract information about atomic occupancies, which are correlated with the amount of guest determined from the same diffraction experiment, thus giving access to equilibrium pressure-temperature-composition diagrams. Therefore, both micro- and macroscopic pictures of interaction are coming from the same diffraction experiments. We equally used volumetric methods to validate the results and to compare this methodology with classical (bulk) methods. Interestingly, the diffraction-based methods are specific to a given crystalline phase, while bulk methods cannot take into account an amorphous fraction or other crystalline impurities. Another great advantage of the gas adsorption crystallography is the access to adsorption isobars, which are hardly obtainable by volumetric methods, as the non-isothermal calibration is overwhelmingly complicated. Adsorption isobars are more informative, as they cover wider range of chemical potential and thus are better suited to visualize directly anomalies in guest-host interaction.

Porous magnesium borohydride, γ-$Mg(BH_4)_2$, is chosen as adsorbent in this project, as it shows a high-symmetry rigid framework containing 1D channels made of pockets separated by apertures close to the size of small molecules, potentially allowing to sense the differences between them. Also, this compound is about a single known hydridic porous material, with partly negatively charged hydrogen atoms making the surface of the pores, thus giving a chance to discover some unusual adsorption behavior. We synthesized γ-$Mg(BH_4)_2$ in a nearly pure form (quantifying the always-present amorphous fraction), including its double isotopic derivative, γ-$Mg(^{11}BD_4)_2$. We used synchrotron X-ray and neutron powder diffraction to study *in situ* its adsorption properties with regard to different gasses: He, Ne, Ar, Kr, Xe, as well as H_2 (in a form of deuterium), N_2, and small fuel gasses such as methane and ethane. These studies were done in collaborations, the results are grouped as chapters in this thesis, each aiming to be published as a research article.

We show that both adsorption thermodynamics and kinetics can be accessed by diffraction, the former requires to scan different P-T conditions close to equilibrium, while the latter requires to measure diffraction data upon gas adsorption process with a good time resolution. We describe and discuss the optimal methodologies for these two applications. The isotherms and isobars derived from diffraction data were fitted with analytical expressions, allowing to determine adsorption enthalpy, entropy, Gibbs energy etc. Different formalisms were used to describe the interactions, for example providing isosteric heats of adsorption as a function of loading (examples of Ar, CH_4 and C_2H_6), or average values (CH_4 and C_2H_6), or describing interactions with an empirical coefficient. The latter is linked to the description of interactions using Ising-like gas model (example of Ar), but direct DFT simulations based on structural information can also be used to evaluate the heats of adsorption or even build P-T phase diagrams (examples of He, Ne and Ar). On the other hand, diffraction study of adsorption kinetics requires to work with “big data”. Tens of thousands of powder diffraction patterns have to be collected with sub-second time resolution, fitted sequentially by Rietveld method and then analyzed in terms of Arrhenius theory. This work can be hardly done with Lab sources and without automation of experimental protocols and data reduction, typically done at large facilities. Our user experience at synchrotron and neutron facilities is inspired by high scientific culture and work efficiency, as well as by continuous advancements on the forefront research.

One of the outcomes of this study is the understanding of the size effects on the localization of guests inside the pores, governed largely by attractive guest-host and repulsive guest-guest interactions. Unusual guest reorganizations are observed upon loading of light noble gasses (He, Ne and Ar) and of hydrogen. Up to five H_2 molecules can enter the same pore pocket, while for larger guests at most one molecule can enter the pocket. This explains remarkable differences in surface areas of γ-$Mg(BH_4)_2$ measured with H_2 and N_2. Both particular size and shape of the pores, but also the nature of the hydridic hydrogen making the pore can be at the origin of these differences.

γ-$Mg(BH_4)_2$ exhibits high gravimetric capacity and one of the highest heats of adsorption for CH_4 and C_2H_6. Interestingly, larger C_3H_8 and *n*-C_4H_{10} are not adsorbed into the pores. Our analysis shows that this may be not due to a mismatch of the molecular and pore sizes, but rather stem from the very slow kinetics of diffusion through the pore aperture. We hypothesize that hydridic BH_4^- anions can turn and help the diffusion of CH_4 and C_2H_6 through relatively narrow apertures. But this point requires more detailed studies focused on adsorption kinetics.

Indeed, our new diffraction-based methodology to study kinetics

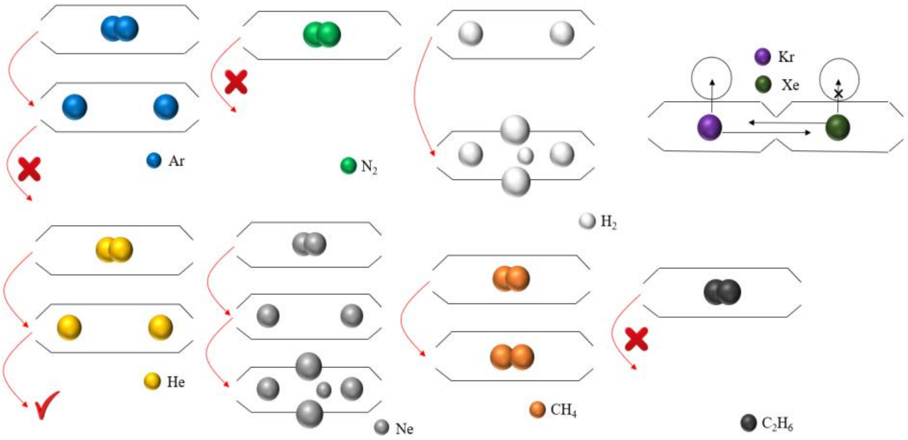

Figure 1. Summary of gas adsorption phenomena in γ-$Mg(BH_4)_2$. Different gasses show different scenarios of localization in the pores, the latter shown as a back frame with open apertures. The red arrows represent the adsorption steps. The black arrows in the top right represent the diffusion pathways for Kr and Xe.

reveals the activation energies related to gas adsorption, giving understanding of the diffusion mechanisms. Slow diffusion is observed for heavier noble gasses, especially for Kr and Xe having kinetic diameters similar to the aperture opening. Mechanisms of gas diffusion are tentatively attributed to the activation barriers found directly from diffraction experiments.

The Figure 1 summarizes the adsorption phenomena in γ-$Mg(BH_4)_2$ for all the gasses investigated in this thesis.

As a perspective, we identify the need to extend the class of porous hydridic materials to other members, beyond γ-$Mg(BH_4)_2$. We made some efforts in this direction, but the results are not presented in this thesis. One idea is to modify the BH_4^- group, still leaving some hydridic hydrogens in place; the other is to combine the borohydrides with different ligands, known to support porosity, such as imidazolates. Characterization of gas adsorption of such new members is required in order to understand which unusual properties found in this work (such as exceptionally high H_2 capacity, high heats of adsorption of hydrocarbons etc.) are due to hydridic nature of the pores and which are due to the size and shape factors.

Another perspective is related to a wider use of the new methodologies to study adsorption of porous materials. There are other interesting crystalline compounds worth a close examination, despite we are limited to small-pore systems, where the guests are well localized and thus accessible to diffraction. We also see a great potential to a wider use of diffraction to study equilibrium diagrams and thermodynamics of gas adsorption. The isobars/isotherms that we obtained are surprisingly reliable, can be fitted with analytical expressions, are highly complementary to bulk measurements and can be coupled with the structural information readily available from the same experiment.

Diffraction-based methodology to study kinetics of gas adsorption also looks very promising, despite it involves measurements and analysis of an immense amount of data. It should certainly be applied to other porous systems, while for the main material of this thesis, γ-$Mg(BH_4)_2$, we identified the breakthrough coming from kinetic studies, defining our immediate future work: a very high selectivity of Kr/Xe separation found at certain P-T conditions is being explored in detail. This may give a way to applications, but may also answer one of our most fundamental questions: is the borohydride group in the aperture turning to allow larger molecules to pass inside the pores? This may define the future of the porous hydrides.

Appendix I: Supporting information of Chapter 3

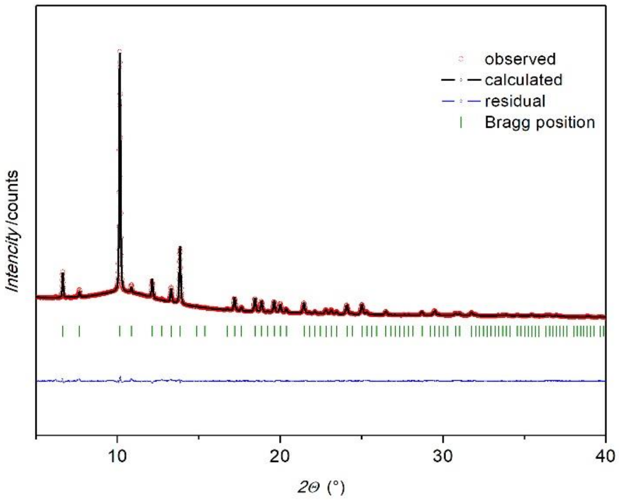

Figure S1. Rietveld refinement (λ = 0.74580Å) of Ar atoms in γ-Mg(BH$_4$)$_2$ (p (Ar) = 1 bar, T = 90 K; a = 15.7824(2) Å; R_{Bragg} = 4.35 %; R_F = 7.82 %).

Table S1. Fractional atomic coordinates and isotropic displacement parameters (Å^2) for Mg(BH$_4$)$_2$·xAr refined from synchrotron powder diffraction a p = 1 bar, T = 90 K.

Atom	Wyck. position	Atomic coordinates			Atomic displacement parameters	Occupancy
		x	*y*	*z*	*Uiso/Ueq*	
Mg1	24d	0.25000	0.12500	0.50000	0.0348 (5)	1
B1	48g	0.30981	0.05981	0.37500	0.0346 (13)	1
H1	96h	0.28571	0.02071	0.43730	0.0599 (12)	1
H2	96h	0.29741	0.13551	0.38560	0.0599 (12)	1
Ar1	32e	0.06150	0.06150	0.06150	0.0984 (15)	0.346 (3)
Ar2	32e	0.10224	0.10224	0.10224	0.0984 (15)	0.308 (3)

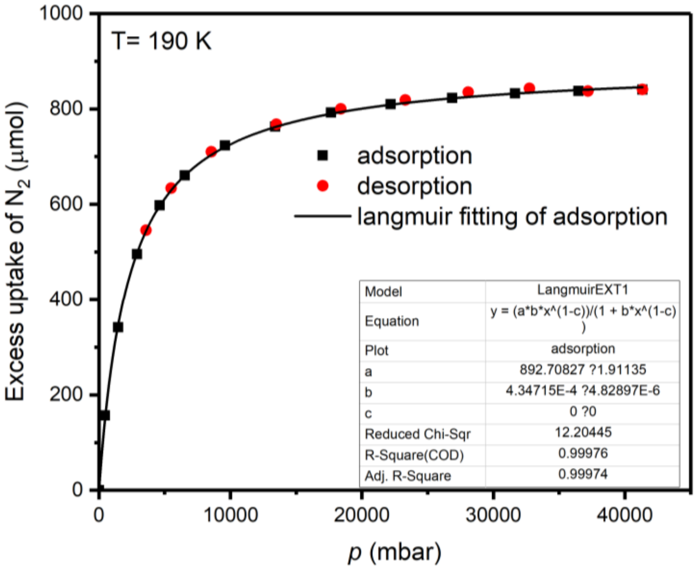

Model	LangmuirEXT1
Equation	y = (a*b*x^(1-c))/(1 + b*x^(1-c))
Plot	adsorption
a	892.70827 ?1.91135
b	4.34715E-4 ?4.82897E-6
c	0 ?0
Reduced Chi-Sqr	12.20445
R-Square(COD)	0.99976
Adj. R-Square	0.99974

Figure S2. N_2 adsorption isotherm and fitting determined by volumetric method.

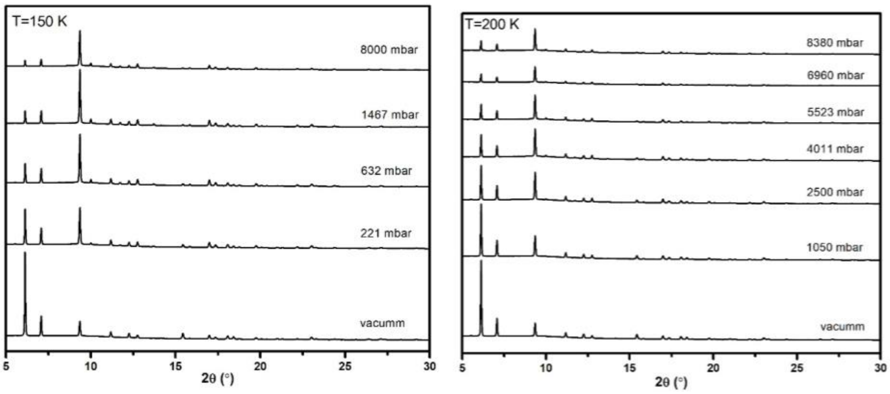

Figure S3. The evolution of powder X-ray diffraction isotherm patterns (λ = 0.68660 Å) of γ - $Mg(BH_4)_2$ with Ar.

Table S2. Table of data points of occupancy versus temperature of Ar isobars

***p*(Ar) = 1 bar**				***p*(Ar) = 10.5 bar**			
***T* (K)**	**Ar(1)**	**Ar(2)**	**Total**	***T* (K)**	**Ar(1)**	**Ar(2)**	**Total**
90.09	12.10	8.46	20.56	132.43	4.93	12.47	17.40
90.30	12.15	8.42	20.57	133.33	5.00	12.43	17.42
90.48	12.01	8.50	20.51	137.47	4.51	12.66	17.17
90.67	11.93	8.55	20.48	141.25	4.11	12.87	16.98
90.84	11.82	8.62	20.44	144.83	3.76	13.04	16.80
91.03	11.68	8.68	20.37	148.41	3.47	13.14	16.62
91.24	11.57	8.74	20.32	151.97	3.24	13.23	16.47
91.45	11.47	8.81	20.29	155.49	3.03	13.28	16.31
91.62	11.33	8.87	20.20	158.94	2.85	13.29	16.14
91.81	11.24	8.92	20.17	162.43	2.70	13.29	15.99
92.02	11.09	9.02	20.11	165.94	2.59	13.24	15.83
92.21	10.97	9.06	20.03	169.44	2.48	13.19	15.67
92.37	10.88	9.13	20.01	172.86	2.37	13.09	15.46
92.56	10.75	9.19	19.94	176.37	2.30	12.95	15.24
92.75	10.64	9.25	19.90	179.87	2.23	12.81	15.04
92.94	10.51	9.32	19.83	183.35	2.15	12.66	14.82
93.18	10.35	9.40	19.76	186.84	2.11	12.43	14.53
93.40	10.22	9.49	19.71	190.28	2.04	12.18	14.23
93.64	10.06	9.58	19.64	193.80	1.98	11.94	13.92
93.92	9.91	9.66	19.56	197.28	1.93	11.64	13.57
94.18	9.75	9.76	19.51	200.79	1.87	11.34	13.21
94.41	9.64	9.82	19.45	204.19	1.83	10.98	12.81
94.65	9.48	9.90	19.38	207.72	1.77	10.62	12.38
94.88	9.36	9.98	19.33	211.22	1.72	10.24	11.96
95.13	9.23	10.05	19.28	214.71	1.66	9.85	11.51

95.35	9.09	10.11	19.20	218.21	1.61	9.42	11.04
95.56	8.98	10.19	19.16	221.60	1.56	9.01	10.57
95.79	8.88	10.23	19.11	225.14	1.50	8.58	10.08
96.02	8.76	10.30	19.06	228.60	1.45	8.17	9.62
96.19	8.68	10.34	19.01	232.12	1.41	7.74	9.14
96.42	8.56	10.39	18.95	235.63	1.35	7.33	8.68
96.61	8.47	10.45	18.93	239.13	1.28	6.93	8.21
96.78	8.40	10.50	18.90	242.53	1.23	6.55	7.78
96.98	8.31	10.55	18.86	246.05	1.18	6.17	7.35
97.14	8.23	10.60	18.83	249.55	1.15	5.79	6.94
97.29	8.17	10.63	18.80	253.04	1.07	5.46	6.53
97.45	8.11	10.67	18.77	256.56	1.05	5.12	6.17
97.58	8.03	10.70	18.74	259.98	1.00	4.81	5.80
97.74	7.98	10.72	18.70	263.49	0.96	4.51	5.47
97.84	7.93	10.76	18.69	266.95	0.94	4.23	5.16
98.01	7.83	10.81	18.64	270.47	0.88	3.97	4.85
98.18	7.74	10.86	18.60	273.89	0.84	3.73	4.56
98.36	7.65	10.91	18.56	277.38	0.80	3.50	4.30
98.59	7.56	10.96	18.51	280.89	0.77	3.27	4.05
98.83	7.42	11.03	18.45	284.41	0.73	3.07	3.80
99.08	7.28	11.12	18.40	287.81	0.71	2.88	3.60
99.39	7.11	11.21	18.32	291.26	0.66	2.72	3.39
99.73	6.95	11.29	18.24	294.80	0.64	2.56	3.20
100.15	6.76	11.41	18.16	298.29	0.62	2.41	3.03
100.55	6.54	11.53	18.07	301.81	0.62	2.25	2.87
101.01	6.30	11.66	17.96	305.24	0.58	2.14	2.72
101.55	6.06	11.79	17.86	308.69	0.54	2.01	2.55
102.20	5.79	11.95	17.73	312.20	0.53	1.90	2.43

102.86	5.52	12.09	17.61	315.74	0.52	1.78	2.30
103.60	5.24	12.24	17.48	319.11	0.49	1.66	2.15
104.43	4.96	12.40	17.36	322.64	0.48	1.59	2.08
105.35	4.68	12.55	17.22	326.11	0.46	1.50	1.96
106.41	4.38	12.71	17.10	329.64	0.46	1.41	1.87
107.53	4.10	12.86	16.96	333.07	0.43	1.35	1.78
108.78	3.83	13.00	16.83	336.56	0.42	1.28	1.70
110.15	3.56	13.14	16.70	339.99	0.39	1.22	1.61
111.65	3.31	13.25	16.57	343.48	0.40	1.14	1.55
113.30	3.10	13.35	16.45	346.92	0.38	1.09	1.47
115.11	2.88	13.45	16.33	350.42	0.38	1.03	1.41
117.16	2.70	13.49	16.19	350.47	0.37	1.00	1.37
119.50	2.55	13.49	16.04	350.30	0.35	0.99	1.34
122.25	2.40	13.49	15.89	350.19	0.35	0.98	1.33
125.23	2.27	13.44	15.72	350.16	0.35	0.99	1.34
128.56	2.17	13.33	15.50				
132.00	2.08	13.19	15.27				
135.47	1.99	12.97	14.96				
138.87	1.92	12.70	14.62				
142.36	1.85	12.36	14.21				
145.83	1.79	11.95	13.74				
149.33	1.70	11.50	13.20				
152.74	1.62	10.96	12.58				
156.20	1.56	10.37	11.92				
159.74	1.47	9.70	11.17				
163.23	1.38	9.02	10.40				
166.69	1.29	8.31	9.61				
170.13	1.22	7.61	8.83				

173.62	1.12	6.93	8.05
177.11	1.05	6.26	7.31
180.55	0.96	5.63	6.59
183.95	0.89	5.05	5.93
187.44	0.82	4.51	5.33
190.79	0.74	4.04	4.78
194.08	0.68	3.59	4.27
196.94	0.63	3.14	3.77
200.64	0.58	2.82	3.39
205.02	0.51	2.48	2.99
208.50	0.47	2.22	2.69
211.99	0.45	1.97	2.42
215.37	0.40	1.78	2.18
218.89	0.39	1.58	1.98
222.41	0.39	1.41	1.80
225.81	0.35	1.28	1.62
229.28	0.36	1.15	1.51
232.77	0.34	1.03	1.38
236.28	0.31	0.95	1.26
239.77	0.32	0.86	1.18
243.25	0.31	0.79	1.10
246.68	0.29	0.71	1.01
250.18	0.30	0.65	0.95
253.68	0.29	0.59	0.88
257.22	0.27	0.54	0.81
260.66	0.27	0.49	0.76
264.10	0.26	0.43	0.69
267.60	0.27	0.41	0.68

271.07	0.29	0.36	0.65
274.62	0.25	0.34	0.59
278.03	0.27	0.29	0.56
281.49	0.25	0.27	0.53
285.03	0.24	0.26	0.49
288.49	0.15	0.19	0.34
292.04	0.13	0.18	0.31
295.37	0.23	0.20	0.43

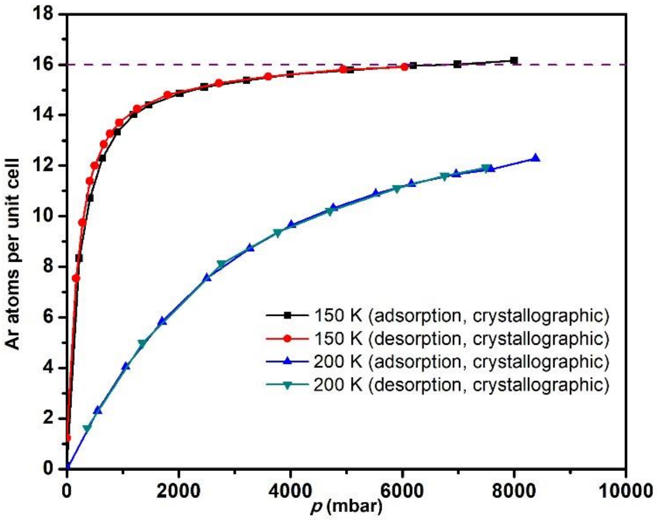

Figure S4. The reversibility of adsorption isotherms from powder X-ray diffraction experiment.

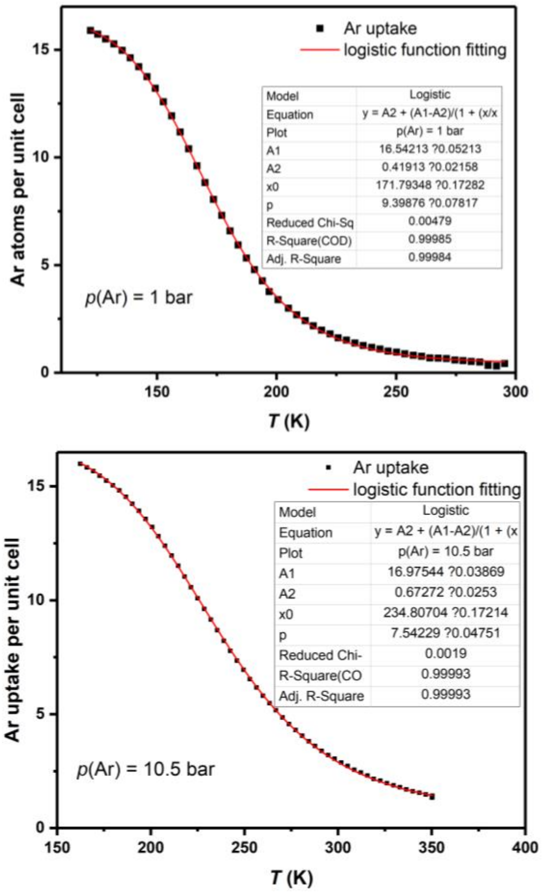

Model	Logistic
Equation	y = A2 + (A1-A2)/(1 + (x/x
Plot	p(Ar) = 1 bar
A1	16.54213 ?0.05213
A2	0.41913 ?0.02158
x0	171.79348 ?0.17282
p	9.39876 ?0.07817
Reduced Chi-Sq	0.00479
R-Square(COD)	0.99985
Adj. R-Square	0.99984

Model	Logistic
Equation	y = A2 + (A1-A2)/(1 + (x
Plot	p(Ar) = 10.5 bar
A1	16.97544 ?0.03869
A2	0.67272 ?0.0253
x0	234.80704 ?0.17214
p	7.54229 ?0.04751
Reduced Chi-	0.0019
R-Square(CO	0.99993
Adj. R-Square	0.99993

Figure S5. Logistic function to fit the Ar adsorption isobars diagram.

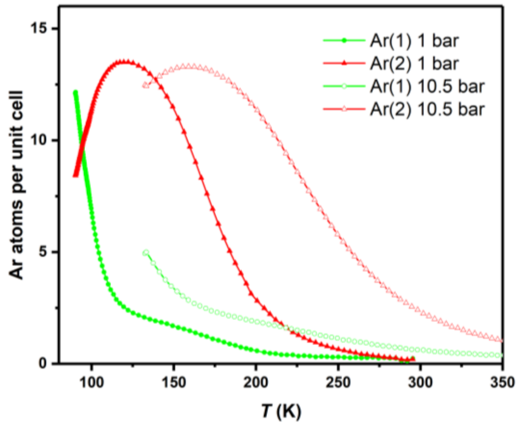

Figure S6. Partial Ar uptake of 1 bar and 10.5 bar isobars.

Appendix II: Supporting information of Chapter 4

Materials and Methods

Hydrogen isotherm measurements An automated Sievert's type apparatus (PCTPro-2000) was used with a so-called micro-doser (MD) from HyEnergy. The original setup was upgraded by a heating and cooling device to regulate the sample temperature. The adsorption and desorption isotherms (0-20 bar) were measured at various temperature (77 K to 298 K) in a sample cell volume of ≈1.3 mL using ultra high purity hydrogen gas (99.999 %). $Mg(BH_4)_2$ (163 mg and 125 mg for γ and α phase, respectively) were evacuated under ultra-high vacuum at 335 K for over-night prior to the measurements in order to remove any adsorbed gas from the surface. The isosteric heat of adsorption is calculated from the absolute adsorbed hydrogen according to a variant of the Clausius-Clapeyron equation (details of calculation are shown in the Chapter 4, supporting information).

Cryogenic H_2 Brunauer-Emmet-Teller (BET) measurement The hydrogen adsorption isotherms of $Mg(BH_4)_2$ at 19.5 K were measured with laboratory-designed volumetric adsorption equipment with a temperature controlled cryostat and is described in detail elsewhere[28]. Around 20 mg of γ- and α-$Mg(BH_4)_2$ was activated under ultra-high vacuum at 335 K overnight, prior to each measurement. For the laboratory-designed cryostat, the temperature control was calibrated by measuring the liquefaction pressure for hydrogen and nitrogen in the empty sample chamber at various temperatures.

Neutron powder diffraction at NIST NPD patterns were measured on the high resolution powder diffractometer BT1 at the NIST Center for Neutron Research (NCNR). The wavelength used was, λ = 2.074 Å. The sample was loaded into a vanadium can placed inside a closed-cycle refrigerator. First, the system was evacuated over night to empty the pores. Deuterium loading into the porous structure was performed in a two-step procedure. A known amount of gas was put into the system, which was slowly cooled to the liquefaction, and then the excess deuterium was pumped off upon heating slightly above the boiling point. The empty γ-Mg($^{11}BD_4$)$_2$ was characterized, as well as a fully D_2-loaded framework, both measurement were at 10 K.

Neutron powder diffraction at HZB NPD patterns were taken on the high-resolution powder diffractometer E9 at the BER-II research reactor at the Helmholtz-Zentrum Berlin. The wavelength used was, $\lambda = 1.7982$ Å. The γ-Mg($^{11}BD_4$)$_2$ sample was loaded into a vanadium can placed inside a liquid-helium 'Orange' cryostat. The system was evacuated and loaded with various amounts of deuterium gas at 25 K using DEGAS gas loading systems. Four NPD patterns were collected at equilibrium pressures of 0.21 mbar, 0.45 mbar, 27 mbar and 205 mbar at 25 K. The deuterium gas was evacuated by application of a vacuum at 100 K (which was confirmed by a subsequent measurement of the empty porous phase) after which 3 bar of N_2 gas was applied at 100 K. The diffraction patterns were collected under these conditions.

Analysis of diffraction data The identification of guest molecules was done by optimization in global space, using FOX software[29], followed by a complete Rietveld refinement in Fullprof[30][31].

In situ inelastic neutron scattering experiments INS spectra were measured at the vibrational spectroscopy beamline VISION at SNS, ORNL (Spallation Neutron Source, Oak Ridge National Laboratory). A cryocooler cycle system which was used to control the temperature of the sample in a range of 5 K - 100 K. Para-hydrogen (pH_2) was prepared by liquefying ultrahigh purity normal hydrogen over Oxisorb (CrO nanoparticles deposited over silica) at 17 K and bleeding the vapor off this system at 22 K. The samples were loaded in aluminum containers that were connected to a gas dosing system in the beamline. The samples were dosed in situ in the cryostat at 35K and cooled down to base temperature, 5 K for measurements. We dosed different amounts of almost pure pH_2 and normal hydrogen, (nH_2). Normal hydrogen is the equilibrium mixture at room temperature consisting of 25% pH_2 and 75% ortho-hydrogen (oH_2).

Chapter S1. Neutron diffraction study of the empty $Mg(^{11}BD_4)_2$ framework, N_2-loaded γ-$Mg(^{11}BD_4)_2\cdot0.66N_2$ and D_2-loaded $Mg(^{11}BD_4)_2$ framework up to the composition γ-$Mg(^{11}BD_4)_2\cdot1.33D_2$.

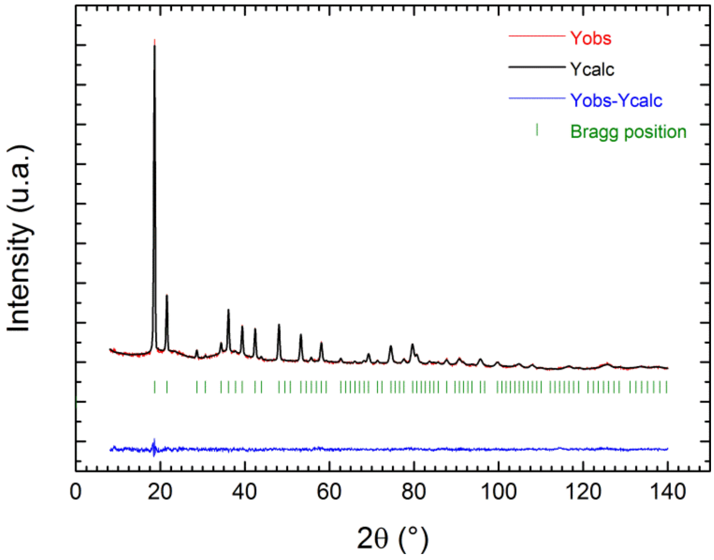

Figure S1. Rietveld refinement profile for the fresh empty-pore γ-$Mg(^{11}BD_4)_2$ sample, using NPD data (NIST) collected at 10 K, λ = 2.079 Å.

Table S1. Structural data for empty γ-$Mg(^{11}BD_4)_2$ sample from NPD experiment (NIST) at 10 K, λ = 2.079 Å. Values in parentheses indicate one standard deviation.

Atom	Wyckoff site	*x*	*y*	*z*	Occupancy	B (Å²)
‘Empty’ γ-$Mg(^{11}BD_4)_2$, space group *Ia*-3*d*, Z = 24, *a* = 15.7401(11) Å, V = 3899.7(5) Å^3, R_p = 23.7%, R_{wp} = 15.7%, χ^2 = 0.866, R_F = 6.07%.						
Mg	24*d*	1/4	1/8	1/2	1	1.7(2)
^{11}B	48*g*	0.3130(3)	*x*-1/4	3/8	1	1.66(9)
D1	96*h*	0.2888(3)	0.0202(3)	0.4363(4)	1	3.53(6)
D2	96*h*	0.3001(3)	0.1391(3)	0.3814(2)	1	3.53(6)

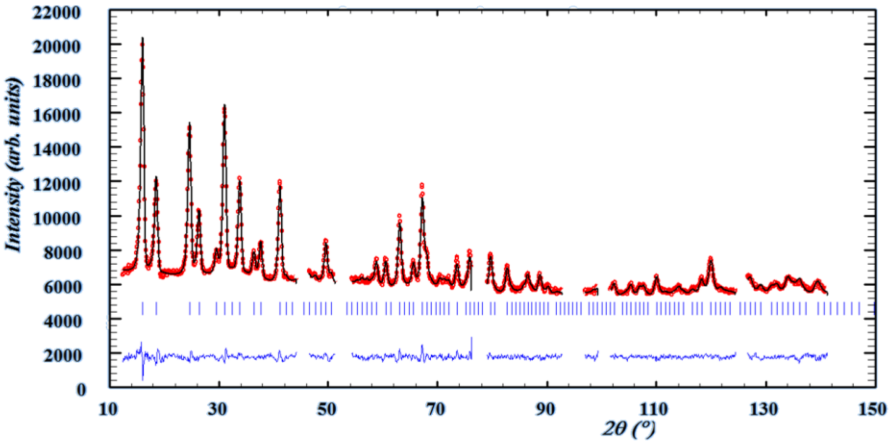

Figure S2. Rietveld refinement profile for the nitrogen-loaded γ-Mg($^{11}BD_4$)$_2$ sample at 100 K and 3 bar (HZB). The angular ranges containing contributions from the Al can were excluded from the refinement. λ = 1.7982 Å.

Table S2. Structural data for the N_2-loaded γ-Mg($^{11}BD_4$)$_2$ sample from NPD experiment (HZB) at 100 K and 3 bar of gas pressure, λ = 1.7986 Å.

Atom	Wyckoff site	*x*	*y*	*z*	Occupancy	B (Å²)
N_2-loaded γ-Mg($^{11}BD_4$)$_2$, space group *Ia*-3*d*, Z = 24, *a* = 15.7498(4) Å, *V* = 3906.85(2) Å^3, R_p = 10.2%, R_{wp} = 9.25%, χ^2 = 2.17, R_F = 2.32%.						
Mg	24*d*	1/4	1/8	1/2	1	1.1(1)
^{11}B	48*g*	0.3130(2)	*x*-1/4	3/8	1	1.42(9)
D1	96*h*	0.2910(3)	0.0197(2)	0.4352(3)	1	3.21(7)
D2	96*h*	0.3015(2)	0.1402(2)	0.3817(2)	1	3.21(7)
N1	96*h*	0.6349(9)	0.6714(18)	0.6650(19)	0.1805(12)*	4.7(7)
N2	96*h*	0.628(2)	0.628(2)	0.6193(18)	0.1805(12)*	4.7(7)

* This value for the N-atoms' occupancy corresponds to 0.722(5) N_2 molecules per Mg atom. This value is correlated with the refined ADPs, and is reasonably close to the limiting composition of 0.667 N_2 molecules per Mg atom.

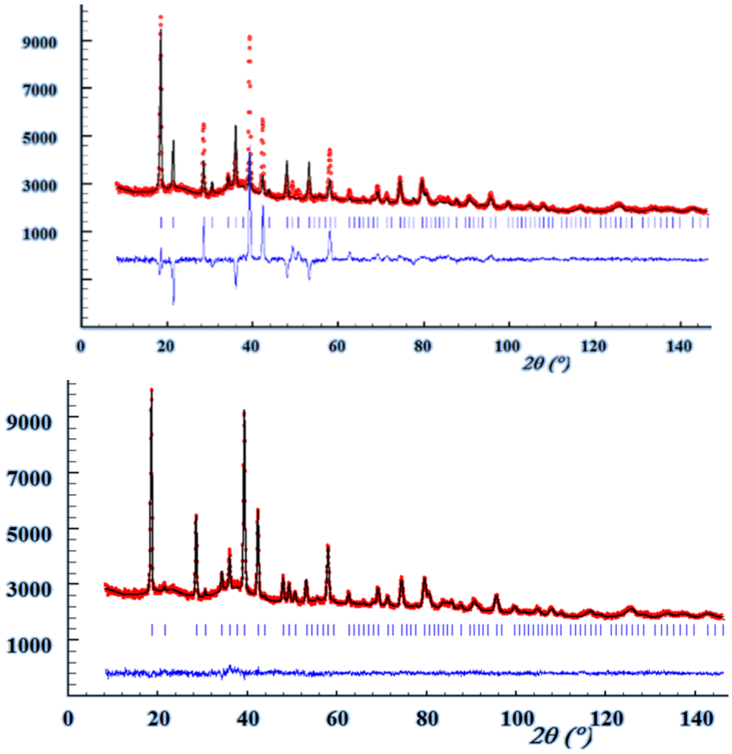

Figure S3. Rietveld refinement profile for NPD NIST data collected at 10 K on the D_2-loaded γ-Mg($^{11}BD_4$)$_2$ sample using: **up,** the structural model for nitrogen localization based on XPD data assuming the limiting composition γ-Mg($^{11}BD_4$)$_2$·0.66D_2[6], and **bottom,** the revised model that allows for the double hydrogen capacity, γ-Mg($^{11}BD_4$)$_2$·1.33D_2. $\lambda = 2.079$ Å.

Table S3. Structural data for D_2-loaded γ-Mg($^{11}BD_4$)$_2$ sample from NPD experiment (NIST) at 10 K. λ = 2.079 Å.

Atom	Wyckoff site	*x*	*y*	*z*	Occupancy	B (Å²)
D_2-loaded γ-Mg($^{11}BD_4$)$_2$, space group *Ia*-3*d*, Z = 24, *a* = 15.7424(3) Å, *V* = 3901.3(1) Å^3, R_p = 21.0%, R_{wp} = 15.4%, χ^2 = 0.889, R_F = 4.83%.						
Mg	24*d*	1/4	1/8	1/2	1	0.8(1)
^{11}B	48*g*	0.3115(3)	*x*-1/4	3/8	1	0.1(1)
D1	96*h*	0.2886(3)	0.0195(3)	0.4349(4)	1	2.90(7)
D2	96*h*	0.3008(3)	0.1375(3)	0.3800(2)	1	2.90(7)
D11	32*e*	0.6843(2)	*x*	*x*	2.156(18)*	11.1(3)

* This value for the D_2 superatom occupancy corresponds to 1.078(9) occupancy of the individual atoms. This value is slightly over 1 due to a correlation in the ADP (refined B = 11.2(3) Å^2), which falls within the expected range for the "superatom" model. When the B-factor is fixed to 8, the occupancy of the "superatom" refines exactly to 1. This corresponds to 1.33 D_2 per Mg atom.

Table S4. Structural data for the D_2-loaded γ-Mg($^{11}BD_4$)$_2$ from NPD experiment (HZB) at 25 K and 0.21 mbar, 0.43 mbar, 27 mbar equilibrium pressures, refined with one superatom (centroid) D_2 site. λ = 1.7982 Å.

Atom	Wyckoff Site	*x*	*y*	*z*	Occupancy	B (Å²)
γ-Mg($^{11}BD_4$)$_2$ at 25 K and 0.21 mbar D_2, space group *Ia*-3*d*, Z = 24, *a* = 15.7678(4) Å *V* = 3920.2(2) Å^3, R_p = 9.5%, R_{wp} = 8.26%, χ^2 = 2.21, R_F = 2.10%.						
Mg	24*d*	1/4	1/8	1/2	1	0.9(1)
^{11}B	48*g*	0.31256(19)	*x*-1/4	3/8	1	0.78(7)
D1	96*h*	0.2903(2)	0.0204(2)	0.4354(3)	1	2.55(5)
D2	96*h*	0.3014(2)	0.1399(2)	0.38137(18)	1	2.55(5)

D11	32*e*	0.6597(5)	*x*	*x*	0.526(8)*	11.2

γ-Mg(^{11}BD$_4$)$_2$ at 25 K and 0.43 mbar D$_2$, space group *Ia*-3*d*, Z = 24, *a* = 15.7687(4) Å, *V* = 3920.9(2) Å^3, R$_p$ = 10.5%, R$_{wp}$ = 9.31%, χ^2 = 2.75, R$_F$ = 2.89%.

Mg	24*d*	1/4	1/8	1/2	1	1.3(1)
^{11}B	48*g*	0.31091(19)	*x*-1/4	3/8	1	0.65(7)
D1	96*h*	0.2890(2)	0.0188(2)	0.4358(3)	1	2.73(5)
D2	96*h*	0.3004(2)	0.1383(2)	0.3815(2)	1	2.73(5)
D11	32*e*	0.6791(2)	*x*	*x*	1.576(7)*	11.2

γ-Mg(^{11}BD$_4$)$_2$ at 25K and 27 mbar D$_2$, space group *Ia*-3*d*, Z = 24, *a* = 15. 7741(4) Å, *V* = 3925.0(2) Å^3, R$_p$ = 10.9%, R$_{wp}$ = 9.71%, χ^2 = 2.99, R$_F$ = 2.33%.

Mg	24*d*	1/4	1/8	1/2	1	1.0(1)
^{11}B	48*g*	0.3116(2)	*x*-1/4	3/8	1	0.42(7)
D1	96*h*	0.2891(2)	0.0184(2)	0.4355(3)	1	2.59(6)
D2	96*h*	0.3007(3)	0.1383(2)	0.3804(2)	1	2.59(6)
D11	32*e*	0.6849(2)	*x*	*x*	2.29(1)*	11.2

* The value of the superatom occupancy corresponds to double occupancy of the individual D-atoms. The full site occupation (2 for the superatom) corresponds to 1.33 D$_2$ per Mg atom.

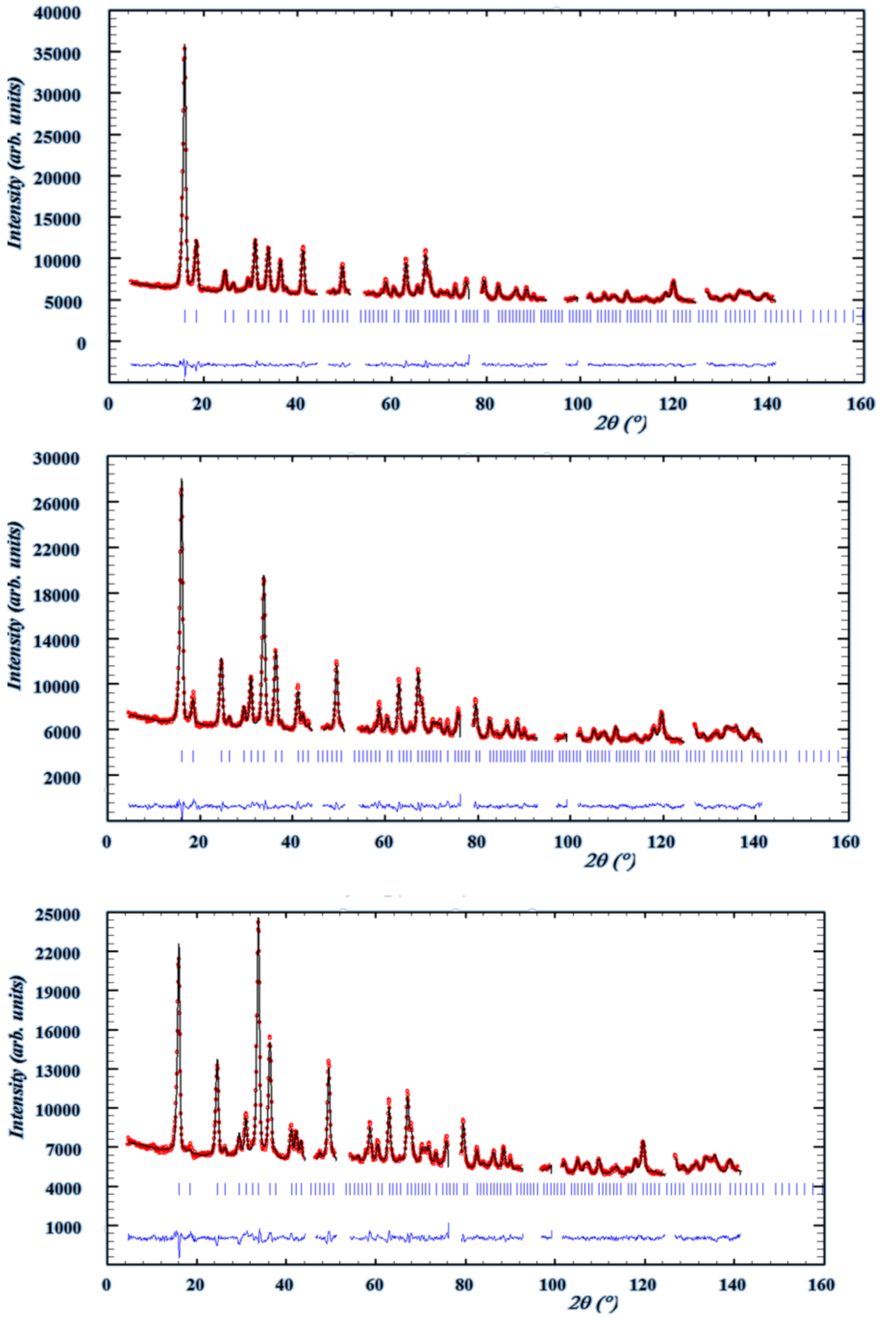

Figure S4. Rietveld refinement profiles for the deuterium-loaded γ-Mg($^{11}BD_4$)$_2$ sample at 25 K and 0.21 mbar (top), 0.43 mbar (middle), 27 mbar (bottom) equilibrium pressures (HZB), refined with one superatom D_2 site. The angular ranges containing contributions from the Al can were excluded from the refinement. λ = 1.7982 Å.

Chapter S2. Re-evaluation of the synchrotron radiation X-ray powder diffraction (SR-XPD) data collected under hydrogen pressures.

The new H_2 localization obtained from the NPD experiments allowed us to re-evaluate the *in situ* SR-XPD data collected on γ–$Mg(BH_4)_2$ under different H_2 pressures and temperatures[6]. Although such data were fitted well using a nitrogen localization model (see Figure S5a), the quality of the Rietveld refinement was improved considerably using the new NPD model and the same SR-XPD data (see Fig S5b): χ^2 decreased to less than half the original value, from 1310 to 610. Importantly, the new geometric model corrects the original estimate of the maximum experimental hydrogen content from γ–$Mg(BH_4)_2\cdot0.80H_2$[6] to γ–$Mg(BH_4)_2\cdot1.32H_2$. The obtained value is very close to the NPD values and to the value expected at full occupancy of the H_2 site (1.33 H_2 per Mg). Structural parameters for the revised SR-XPD experiment at 80 K on 105 bar of H_2 are listed in Table S5.

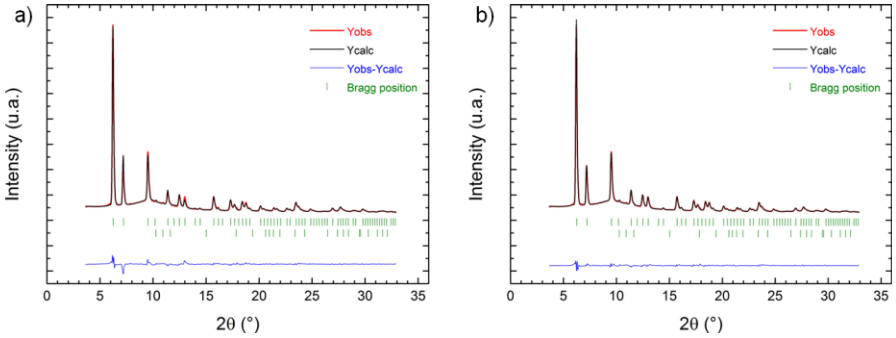

Figure S5. Rietveld refinement profile for the SR-XPD data collected on γ-$Mg(BH_4)_2$ at 80 K and 105 bar of H_2 using a) the X-ray model for nitrogen localization used previously in Ref.[6], b) the revised NPD model, giving the resulting composition γ–$Mg(BH_4)_2\cdot1.32H_2$. The lower line of Bragg reflection tick marks refer to ice forming on the outer side of the cold glass capillary. $\lambda = 0.700930$ Å.

Table S5. Structural parameters for γ-$Mg(BH_4)_2$ loaded at 80 K with 105 bar of H_2, using SR-XPD data and the revised model of hydrogen localization. Nearly double occupancy of H_2 "superatom" indicates the full occupation of the site and thus the composition γ−$Mg(BH_4)_2 \cdot 1.32H_2$. λ = 0.700930 Å.

Atom	Wyckoff site	*x*	*y*	*z*	Occupancy	B (Å²)
Space group *Ia*-3*d*, Z = 24, *a* = 15.7771(6) Å, *V* = 3927.1(3) Å³ R_p = 8.3%, R_{wp} = 8.8%, χ^2 = 610, R_F = 2.2%.						
Mg	24*d*	1/4	1/8	1/2	1	0.9(1)
B	48*g*	0.30981	*x*-1/4	3/8	1	0.9(1)
H1	96*h*	0.28571	0.02071	0.43730	1	2.9(1)
H2	96*h*	0.29741	0.13551	0.13551	1	2.9(1)
H11	32*e*	0.6843	*x*	*x*	1.98(4)*	16.9(1)

* This value for the H_2 superatom occupancy practically corresponds to full occupancy of the site by H_2 molecules, the latter corresponds to 1.33 H_2 per Mg atom.

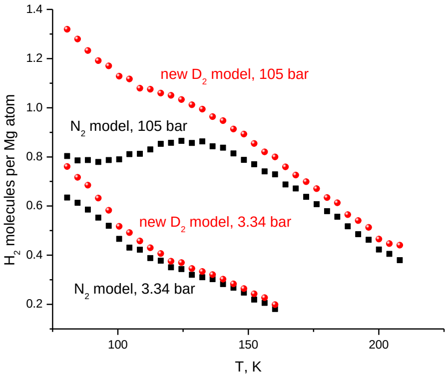

Figure S6. Hydrogen adsorption isobars for γ-$Mg(BH_4)_2$ extracted from *in situ* powder diffraction data using the previous structural model based on localisation of nitrogen (N_2- model) (black squares) and the new NPD model (red circles). Note that there is no drop in adsorbed amount of H_2 at lower temperature when using the new model.

Using the new model and previously reported *in situ* SR-XPD data at 3.34 bar and 105 bar, the H_2 site occupancies were refined as a function of temperature. Figure S6 shows the amount of H_2 adsorbed per Mg atom, both for the old (black squares) and the new (red circles) models. The major differences are observed for the temperatures below 150 K, where an unexplained drop in capacity is eliminated for the new model.

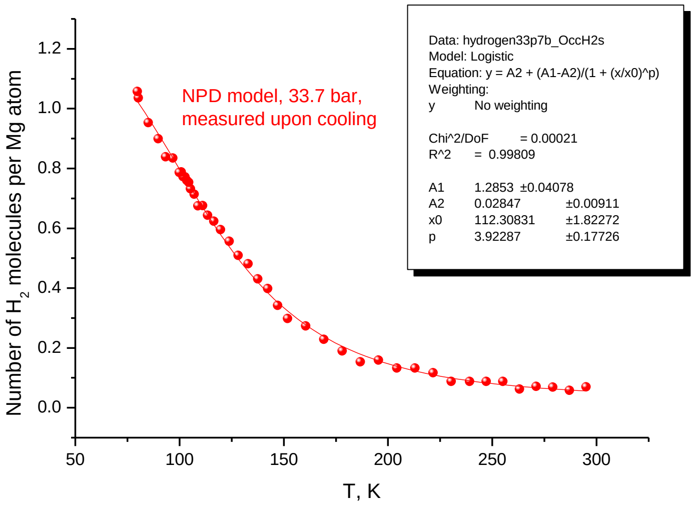

Figure S7. Amount of adsorbed hydrogen in γ-$Mg(BH_4)_2$ extracted from *in situ* SR-XPD data collected at constant pressure of 33.7 bar and temperature varied from 80 K to 300 K. The fit of the logistic function to the experimental isobar yields the H_2 capacity per Mg atom at 1.29(4), which suggest an almost fully occupied site (1.33).

We employed the revised model to characterize hydrogen adsorption at 33.7 bar over a wide range of temperatures, from liquid nitrogen to ambient, using previously unpublished SR-XPD data. The fit of the logistic function to the data is shown in Figure S7, although only a part of the S-curve was measured. The H_2 capacity per Mg atom on saturation refines to, A1 = 1.29(4), which suggest an almost fully occupied site (1.33). Very similar values are obtained at higher pressure, A1 = 1.30(2) at $p(H_2)$ = 105 bar, and even for the low pressure of $p(H_2)$ = 3.34 bar, A1 = 1.4(2). It is highly satisfactory that the saturation limit can be extrapolated so well using the adsorption data covering only the lower half of the loading curve at 3.34 bar. Although the uncertainties become higher at lower pressures, the fit of the logistic function to the data allows estimation of the limiting adsorption capacity. The A2 parameter reflects the capacity on complete desorption, which is indeed zero within three standard uncertainties. The temperature at which half of the maximum hydrogen adsorption capacity is adsorbed, $x_0 = 112 \pm 2$ K.

Chapter S3. Neutron diffraction study of the D_2-loaded $Mg(^{11}BD_4)_2$ framework, up to the composition γ-$Mg(^{11}BD_4)_2 \cdot 2.33D_2$.

Table S6. Structural data for the D_2-loaded γ-$Mg(^{11}BD_4)_2$ from NPD experiment (HZB) at 25 K and 27 mbar and 203 mbar equilibrium pressures, refined with two superatom D_2 sites. λ = 1.7982 Å.

Atom	Wyckoff Site	*x*	*y*	*z*	Occupancy	B (Å²)
γ-$Mg(^{11}BD_4)_2$ at 25 K and 27 mbar D_2, space group *Ia*-3*d*, Z = 24, *a* = 15.7738(3) Å, *V* = 3924.7(1) Å³, R_p = 9.81%, R_{wp} = 8.57%, χ^2 = 2.39, R_F = 2.12%.						
Mg	24*d*	1/4	1/8	1/2	1	1.1(1)
^{11}B	48*g*	0.31105(19)	*x*-1/4	3/8	1	0.70(7)
D1	96*h*	0.2888(2)	0.0185(2)	0.4357(3)	1	2.94(6)
D2	96*h*	0.2998(3)	0.1386(2)	0.3811(2)	1	2.94(6)
D11	32*e*	0.68489(18)	*x*	*x*	2.183(14)*	10.6(2)
D22	48*g*	0.5310(19)	0.7190(19)	5/8	0.141(7)*	10.6(2)
γ-$Mg(^{11}BD_4)_2$ at 25 K and 203 mbar D_2, space group *Ia*-3*d*, Z = 24, *a* = 15.8039(7) Å, *V* = 3947.3(3) Å³, R_p = 18.7%, R_{wp} = 17.1%, χ^2 = 6.72, R_F = 6.05%.						
Mg	24*d*	1/4	1/8	1/2	1	1.4(2)
^{11}B	48*g*	0.3132(3)	*x*-1/4	3/8	1	0.93(9)
D1	96*h*	0.2903(4)	0.0212(4)	0.4333(5)	1	3.10(8)
D2	96*h*	0.2996(4)	0.1388(4)	0.3812(3)	1	3.10(8)
D11	32*e*	0.6947(4)	*x*	*x*	2.05(3)*	16.5(6)
D22	48*g*	0.5434(6)	0.7066(6)	5/8	0.971(13)*	16.5(6)

* The value of the superatom occupancy corresponds to double occupancy of the individual D-atoms. The refined occupancies of the two superatom sites correspond to 1.47 D_2 per Mg atom (assuming the full occupancy for D11) at 27 mbar equilibrium pressure and to 2.33 D_2 per Mg atom (assuming the full occupancy of D11 and half occupancy for D22) at 203 mbar equilibrium pressure.

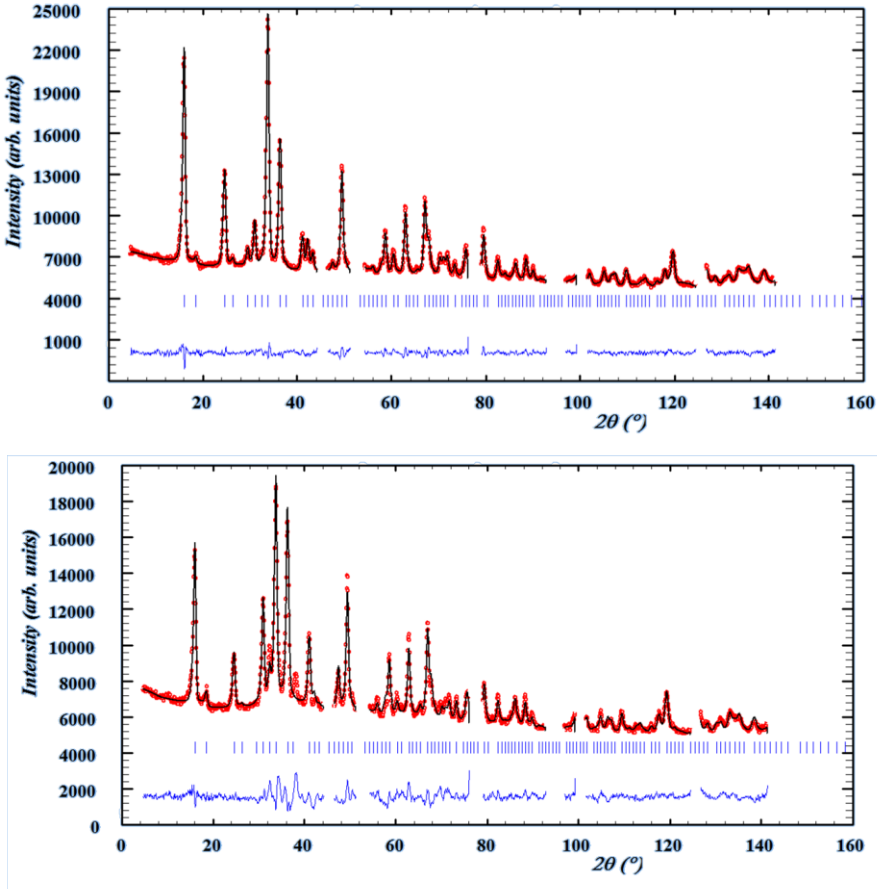

Figure S8. Rietveld refinement profiles for the deuterium-loaded γ-Mg($^{11}BD_4$)$_2$ sample at 25 K and 27 mbar (top) and 203 mbar (bottom) equilibrium pressures (HZB), refined with two superatom D_2 site. The angular ranges containing contributions from the Al can were excluded from the refinement. λ = 1.7982 Å.

Chapter S4. Volumetric measurements.

Quantification of the crystalline fraction of γ-Mg(BH_4)$_2$ using volumetric measurements of nitrogen adsorption isotherm. Upon long-term storage of γ-Mg(BH_4)$_2$ the crystallinity of the sample degrades and the sample slowly transforms into an amorphous phase, manifested by a decreasing diffracted intensity, diffraction peak broadening and appearance of a wavy background. The amorphization also strongly affects the gas adsorption properties for the bulk γ-Mg(BH_4)$_2$ sample. Since a significant fraction of the amorphous phase is always present in each sample, the consistent NPD and X-ray data on N_2 adsorption (2/3 N_2 per Mg on saturation) allowed us to quantify the amount of the amorphous phase by volumetric measurements. We attribute the amount of the adsorbed nitrogen, as determined from a volumetric isotherm, to the adsorption in the crystalline phase only. Direct comparisons of N_2 and H_2 isotherm of bulk γ-$Mg(BH_4)_2$ synthesized on the same sample batch are shown in Figure 4. Note that the difference between Figure 4a (short-term) and 4b (long-term) is only aging time upon storage. The volumetric N_2 uptake at saturation can be converted to the number of N_2 per crystalline/porous Mg in γ-$Mg(BH_4)_2$, resulting in the estimation of amorphous fraction in bulk γ-$Mg(BH_4)_2$ from the NPD and X-ray data (2/3 N_2 per Mg on saturation). Remarkably, the volumetric H_2 uptake corrected for the amorphous phase consistently exhibits γ-$Mg(BH_4)_2 \cdot 2.04$~$2.06\ H_2$, very close to the limiting composition obtained from the crystallographic data (γ–$Mg(BH_4)_2 \cdot 2.33H_2$).

Crystal structure of α- and γ–Mg(BH₄)₂ and their hydrogen storage capacities. The highly symmetric cubic crystal structure of γ–$Mg(BH_4)_2$ (space group *Id*-3*a*), which possesses a 3D net of interpenetrated channels with many corners is shown in Figure S9a. The narrowest part of the channels, 5.8 Å in diameter, is defined by the space between the hydrogen atoms of BH_4 groups that comprise the walls of the channel. γ–$Mg(BH_4)_2$ contains 33 % empty space in the structure, suggesting pronounced gas adsorption potential for this material. Another less porous hexagonal polymorph of magnesium borohydride, α–$Mg(BH_4)_2$ (space group $P6_122$), is also investigated in this study and its structure is illustrated in Figure S9b. This polymorph contains unoccupied voids accounting for 6.4 % volume in the structure, the volume of each void approximately compares to the size of a water molecule[32].

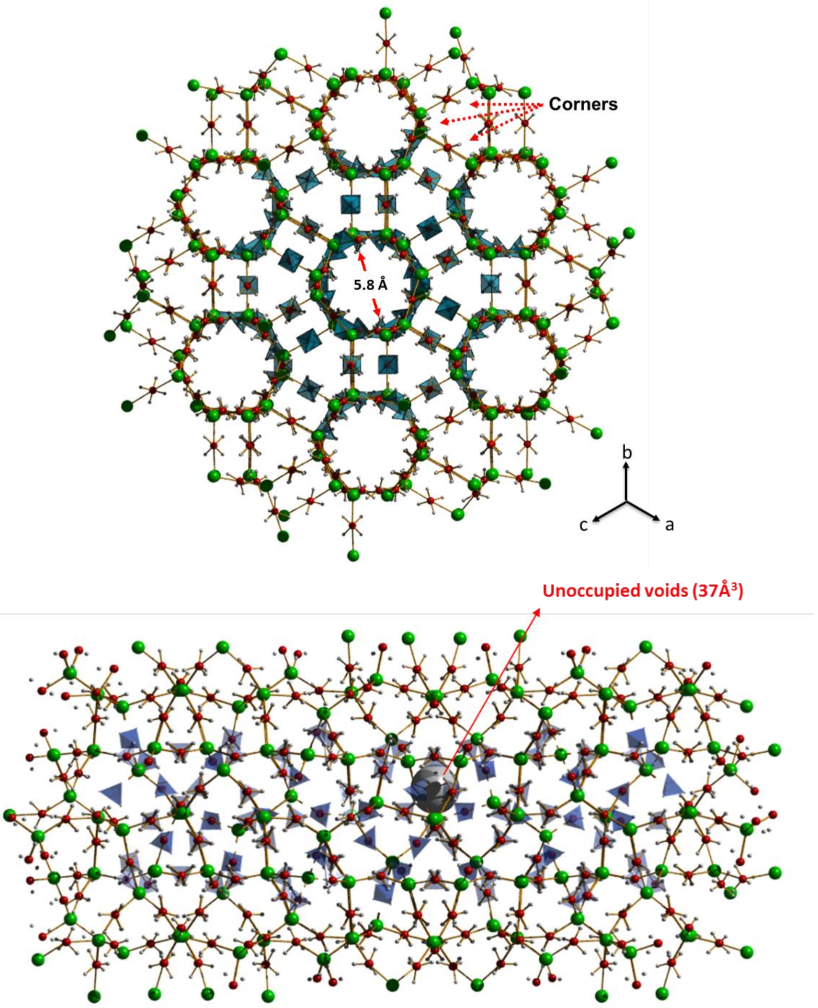

Figure S9. The structure of a) γ-$Mg(BH_4)_2$ and b) α-$Mg(BH_4)_2$, containing respectively empty channels (an aperture of 5.8 Å, the empty volume accounts for ~33% of space in the structure) and unoccupied voids (37 $Å^3$ each void, accounting for 6.4 % of space in the structure). Symbols: Mg (green), B (red) and H (gray). BH_4 group inside unit cell are shown as dark blue tetrahedral.

Excess hydrogen isotherm adsorption curves of the α– and γ–$Mg(BH_4)_2$ measured at 77 K and 298 K are shown in Figure S10. The data measured for γ–$Mg(BH_4)_2$ at 77 K exhibits the characteristic IUPAC type-I curve shape, which is typical for microporous materials. The maximum measured excess hydrogen uptake of γ–$Mg(BH_4)_2$ is 3.4 mass fraction (wt.%) and 0.12 mass fraction (wt.%) H_2 at 77 K and room temperature (RT), $p(H_2)$ = 20 bar, respectively. This is in agreement with the high porosity observed by crystallographic investigations, which reveal a 3D net of interpenetrated channels having a wide mean pore diameter (see Table S7).

In contrast, the excess hydrogen uptake of the polymorph α–$Mg(BH_4)_2$ is significantly lower over the entire pressure range at either temperature. α–$Mg(BH_4)_2$ only absorbs 0.26 mass fraction (wt.%) H_2 at 77 K, $p(H_2)$ = 20 bar, which compares to 0.07 H_2 molecule per Mg atom, or 0.35 H_2 per void in the structure. According to previous crystallographic investigations (*32*), the unoccupied voids (37 Å^3) might be large enough to accommodate a small molecule, such as H_2O (kinetic diameter ~ 2.6 Å). However, this theoretical value was obtained using a probe 'atom' of 1.0 Å radius and may be a suitable predictor of the hydrogen adsorption isotherm since the typical range of intermolecular H···H interaction in α–$Mg(BH_4)_2$ is around 2.7 Å to 2.9 Å. Therefore, the void windows are smaller or may be similar in size to the kinetic diameter of a hydrogen molecule, i.e., 2.8 Å to 2.9 Å. Thus, the small pore size in α–$Mg(BH_4)_2$ may pose a strong kinetic barrier, leading to diffusion limited hydrogen uptake and release in this material. It is notable though, that the well-studied α–$Mg(BH_4)_2$ demonstrates hydrogen adsorption in the small pores, making it the second nano-porous hydride after γ–$Mg(BH_4)_2$.

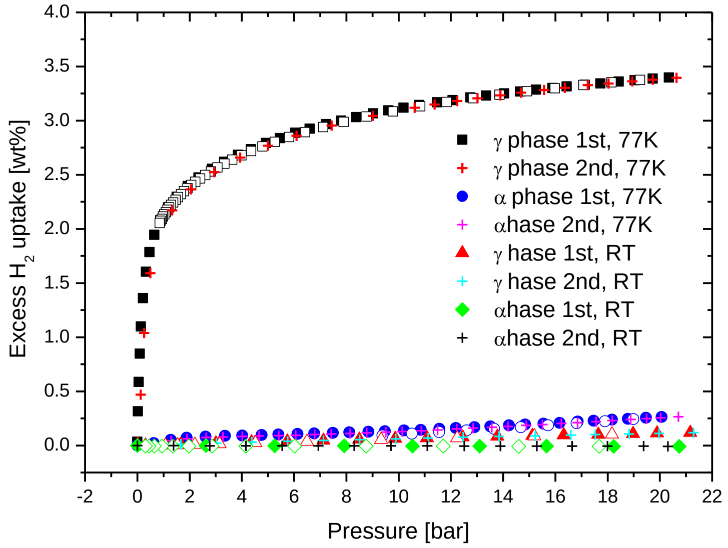

Figure S10. Reversibility of hydrogen uptake and release for α and γ–$Mg(BH_4)_2$ samples; squares, circle, triangles and diamond stand for 77 K - γ–$Mg(BH_4)_2$, 77 K - α–$Mg(BH_4)_2$, RT - γ–$Mg(BH_4)_2$ and room temperature (RT) - α–$Mg(BH_4)_2$, respectively. Cross stands for second measurement of all samples. Closed symbols show the adsorption isotherm and open symbols show the desorption isotherm. Samples were evacuated in vacuum at room temperature for overnight prior to each measurement.

Table S7. Structural characteristics of α- and γ–$Mg(BH_4)_2$ porosity.

	N_2 BET [a] (m^2/g)	**H_2 BET [b] (m^2/g)**	**H_2 Uptake [c] (wt.%)**	**ρ [d] (g/cm^3)**	**Pore window [e] (Å)**	**Pore Diameter (Å)**
γ – $Mg(BH_4)_2$	**610**	**1787**	**4.2**	**0.55**	**5.8**	**7.0** [f]
α – $Mg(BH_4)_2$	**-**	**-**	**-**	**0.78**	**2.8**	**4.1** [g]

[a] **N_2 BET**: nitrogen BET specific surface area at 77 K ($P/P_0 = 3\times10^{-5}$~0.02), [b] **H_2 BET**: hydrogen BET specific surface area at 20 K ($P/P_0 = 5\times10^{-4}$~0.02) using a cross-sectional area of the hydrogen molecule based on the liquid density, [c] **H_2 uptake**: Saturated hydrogen uptake at

19.5 K and 0.7 bar, [d] **ρ**: Skeletal density, [e] **Pore window**: Narrowest channel as pore window considering the van der Waals radius of atoms in the framework, [f] **Pore diameter**: calculated by BJH Adsorption dV/dD pore volume distribution, [g] **Pore diameter**: calculated from crystallographic data.

Calculation of excess adsorption. To remove an influence of the temperature gradient between cooled sample cell and gas reservoir with pressure transducer (298 K) during isotherm measurement at between 77 K and 127 K, non-adsorbing samples (sea sand) possessing the same volume was measured under identical conditions. By subtracting these two measurements, the influence of the temperature gradients as well as systematic errors cancels out. Thus, the excess amount of hydrogen $n_{excess}(p,T)$ adsorbed can be calculated by:

$$n_{excess}(p,T) = n_{experiment}(p,T) - n_{sea\ sand}(p,T)$$

The adsorbed amount is reported in wt.% which is defined as mass of hydrogen m_{ads} per mass of the system, which consists of the sample mass m_S and the adsorbed hydrogen.

$$\text{Hydrogen uptake (wt\%)} = \frac{m_{ads}}{m_s + m_{ads}}$$

Calculation of absolute adsorption out of excess adsorption. The excess uptake should be corrected in order to exactly represent the amount of hydrogen adsorbed on the surface, and that is the so-called absolute uptake. For estimating the absolute amount adsorbed, the volume of the adsorbed layer (V_{ads}) needs to be known. The density of the adsorbed layer is close to the density of the liquid ρ_{lq} and therefore the volume of the adsorbed layer is approximately

$$\boldsymbol{V_{ads} = \frac{n_{excess} \cdot M_{H2}}{\rho_{lq}}}$$

where M_{H2} is the molar mass of hydrogen.

If there was no adsorption, in the volume of the adsorbed layer the amount (n_{gas}) of gas would be present due to the external pressure. This can be calculated from the ideal gas equation

$$\boldsymbol{n_{gas} = \frac{P \cdot V_{ads}}{Z \cdot R \cdot T_{Cold}}}$$

with R the gas constant, Z the correction factor for non-ideal gas

Z = (1.000547- $(6.07{\bullet}10^{-7})$T+(0.000912-$(1.0653{\bullet}10^{-6})$T)•P+((7.373407-0.0901T)•10^{-7})•P^2) at temperature T(K) and pressure P(atom).

The absolute amount adsorbed nabs is therefore:

$$\boldsymbol{n_{abs} = n_{gas} + n_{excess} = n_{excess} \cdot \left(1 + \frac{P \cdot M_{H2}}{Z \cdot \rho_{lq} \cdot R \cdot T_{Cold}}\right)}$$

Evaluation of the isosteric heat of adsorption.

The isosteric heat of adsorption is typically calculated from hydrogen isotherm measurements, e.g., at liquid nitrogen (77 K) and liquid Ar (87 K) temperature. This simple calculation, however, results in a high uncertainty due to the small temperature range. Therefore, hydrogen adsorption isotherms for γ–Mg$(BH_4)_2$ was measured over a wider temperature range within 77 to 297 K, allowing the determination of the heat of adsorption for a wide range of surface coverage in order to minimize the uncertainty.

Figure S11 shows the temperature variation of the excess hydrogen adsorption curves, which provides the strength of the binding potential for hydrogen in γ–Mg$(BH_4)_2$. The steep initial increase of H_2 adsorption indicates a strong interaction between hydrogen and the scaffold, and therefore saturation is reached at low pressure. The isosteric heat of adsorption is calculated from the absolute adsorption isotherms and the

Clausius-Clapeyron equation at different temperature (77 K to 117 K). In Figure 5, the isosteric heat of adsorption is shown. Analysis of the hydrogen adsorption enthalpy gives a maximum value of 6.1 kJ/mol at near zero surface coverage, decreasing to 4.5 kJ/mol with increasing H_2 loading.

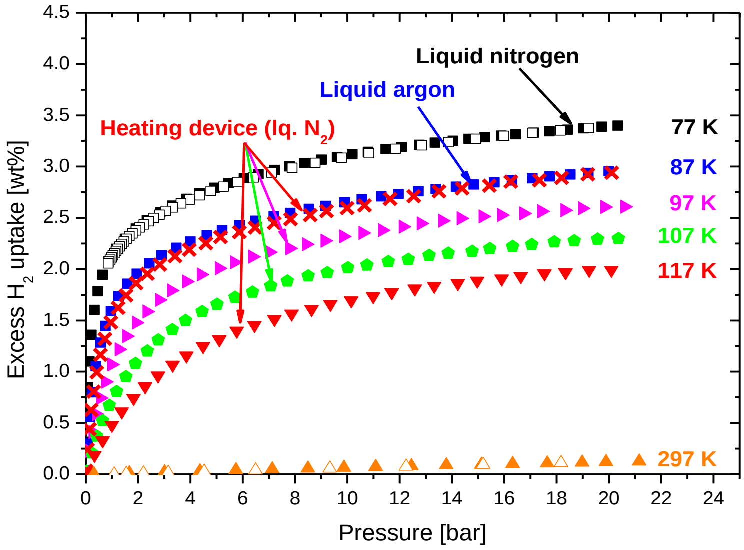

Figure S11. Excess hydrogen uptake in γ–$Mg(BH_4)_2$ at temperatures between 77 K and room temperature. Filled symbols for adsorption, open symbols for desorption.

The isosteric heat of adsorption is calculated from the measured absolute isotherms according to

$$\Delta H = R \cdot \left(\frac{\partial \ln (P)}{\partial \frac{1}{T}} \right)_{\theta}$$

where θ is the surface coverage, R is the gas constant, *P* the pressure and *T* the temperature. Therefore ln(*P*) is plotted versus the reciprocal temperature 1/*T* for different surface coverage θ. This is shown in Figure S12 for γ–$Mg(BH_4)_2$. The slope of the linear fit to this data for each surface coverage θ is proportional to the isosteric heat of adsorption.

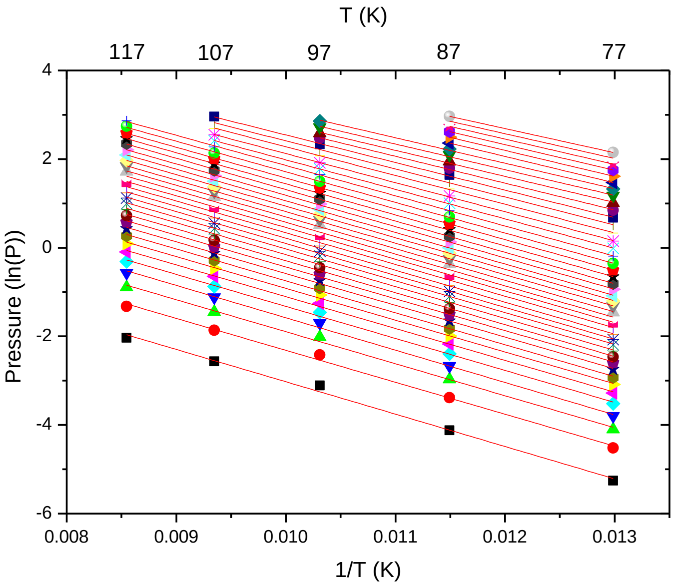

Figure S12. The plot of ln(*P*) versus 1/*T* for γ–$Mg(BH_4)_2$–H_2 system.

Hydrogen sorption isochoric measurement; Temperature dependent pressure change.

In order to understand in detail the hydrogen kinetic effect from the pore window of α- and γ–$Mg(BH_4)_2$, it is important to investigate the influence of temperature in the hydrogen storage system. Therefore, the activated material in the sample holder is loaded with 802 mm Hg hydrogen at room temperature and the connection valve is closed so that the volume available for the gas remains constant. Then, the sample holder is cooled to approximately 11 K where hydrogen should be liquid or solid. The pressure is monitored while the sample is heated to different intermediate temperatures; each temperature is kept constant for approximately 2 min at which point the pressure is recorded.

For the empty sample holder, the pressure is almost 0 mmHg at around 11 K as the hydrogen in the sample holder is liquefied. Slightly above 15 K the phase transition from liquid to gas is observed by a sudden increase of the pressure in the sample holder. Then, the slope becomes smaller with increasing temperature as the hydrogen remains in the gaseous phase and the pressure increases only due to thermal expansion, as Figure S13 shown.

With γ–$Mg(BH_4)_2$ in the sample holder, the pressure develops differently. The pressure remains constant (~ 0 mm Hg) up to approximately 30 K. Afterwards, the pressure increases linearly until approximately 140 K. Thereafter the pressure matches that of the empty sample holder. This different pressure behavior is mainly caused by hydrogen adsorption on the material. At higher temperature, hydrogen starts to desorb, resulting in increasing pressure in the sample holder.

In contrastive, for α-$Mg(BH_4)_2$ the pressure develops almost same as was observed using an empty sample holder. This means that the pores inside α-$Mg(BH_4)_2$ are not accessible for hydrogen and the small pore window is effectively closed even at high temperature.

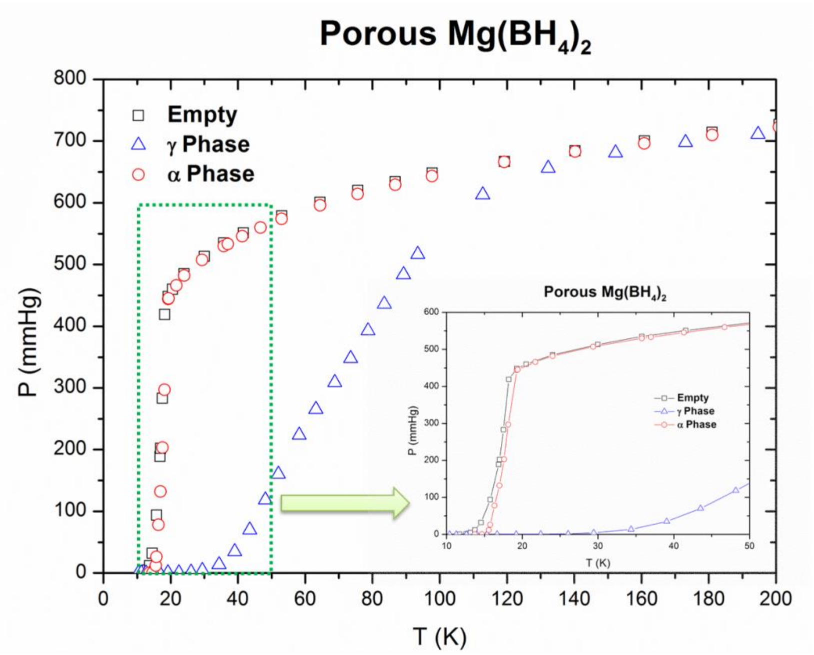

Figure S13. Pressure change in the sample holder with temperature variation (square: the empty sample holder, circle: containing α-$Mg(BH_4)_2$, triangle: containing γ–$Mg(BH_4)_2$.

Chapter S5. Inelastic Neutron Scattering - *In situ* study of H_2-loaded $Mg(^{11}BD_4)_2$ framework.

5.1 Quantum rotation of H_2

The quantum rigid rotor and the particle in a box are two of the most important applications of the Schrödinger equation. In the case of a diatomic molecule, the translational energy levels can be calculated using a simple model of a particle within a three-dimensional box, and rotational energy levels are given by $E_J = J(J+1)B_{rot}$, where B_{rot} is the rotational constant (7.35 meV for solid hydrogen) and $J = 0, 1, 2, \cdots$ is the rotational quantum number (Figure S14)[15].

The hydrogen molecule is composed of two indistinguishable fermions that produce two different nuclear spin isomers and must preserve the overall wave function anti-symmetry. H_2 molecules with antiparallel nuclear spins can only exist with even rotational states ($J = 0, 2, \cdots, \mathrm{even}$) parahydrogen ($pH_2$) While molecules with parallel nuclear spins must have odd rotational states ($J = 1, 3, \cdots, \mathrm{odd}$), orthohydrogen ($oH_2$) Due to the zero-point energy, molecular hydrogen's behavior is dictated by quantum molecular dynamics, which is influenced by interaction potentials that may vary in a spatial dimension. Confined quantum particles entrapped in cage-like potentials provide an opportunity to probe the coupled translational-rotational states under model-like conditions[21].

INS spectra obtained from highly confined hydrogen using normal hydrogen (nH_2) represent a convolution of oH_2 and pH_2 excitations, which complicates subsequent interpretation. Even at boiling temperature (~20 K), a mixture of oH_2 and pH_2 persists for long times due to the inefficiency of angular momentum exchange in the absence of a catalyst. Owing to the different cross-sections of oH_2 and pH_2 is possible to differentiate the vibrational from the rotational features of hydrogen. We thus followed the method of Ulivi et al[20]. We performed two independent measurements using different ortho-para concentrations (one formed from nH_2, and another using nearly pure pH_2) to extract the pure component spectra by a linear combination (Figure S16) and make unambiguous assignments.

The spectral intensity is given by:

$$S_{Total}(Q,\omega) \sim S_{Self_{CoM}}(Q,\omega) \otimes \sum_{JJ'} \delta\left(\omega - \omega_{JJ'}\right) \cdot v(J,J',Q)$$

where ω is the energy tranfer, Q is the momentum tranfer, $S_{Self_{CoM}}(Q,\omega)$ is the dynamical structure factor for the motion of the center of mass (also called Density of States DoS), the $\otimes$ symbol denotes a convolution product. The Dirac δ functions are centered at the energies of the rotational transitions, $\omega_{JJ'}$ of the H_2 molecule. The intensity factor $v(J,J',Q)$ is function of the momentum transfer Q and depends on the rotational transition $J \rightarrow J'$ of the molecule.

INS is not subject to selection rules. Therefore all transitions are allowed. At low temperatures, only the lowest rotational levels are populated, $J = 0,1$. The intensity factors are calculated using the rigid rotor approximation[33]. The transitions contributing to the overall intensity are, for oH_2, the rotational elastic $J_{1\rightarrow1}$ and the inelastic $J_{1\rightarrow2}$, while for pH_2 only the $J_{0\rightarrow1}$has an appreciable contribution, the $J_{0\rightarrow0}$ is weighted by the coherent cross section of hydrogen and can be neglected. In practice, this means that for nH_2, the intensity below 12 meV corresponds to the rattling transitions of the oH_2 molecules (Figure S16 left). In the case of highly enriched pH_2, there is no appreciable intensity below 13 meV. The intensity above the rotational features (red and blue peaks in Figure S16) is the convolution of the rotational transitions with the vibrational tranistions.

In the case of nH_2 all transitions have intensity, Table S8 shows the observed transitions in the spectrum (SI) and the experimental positions of the peaks (the resolution of VISION is $\Delta\omega/\omega = 2\%$. It can be seen that all observed transitions are compatible with a value of $B_{rot} = 7.22$ meV.

The presence of higher order rotational features in the spectra is highly unusual, it is a consequence of the trapping of the hydrogen molecule inside the cavity and a strong reduction of the Debye-Waler factor due to such confinement.

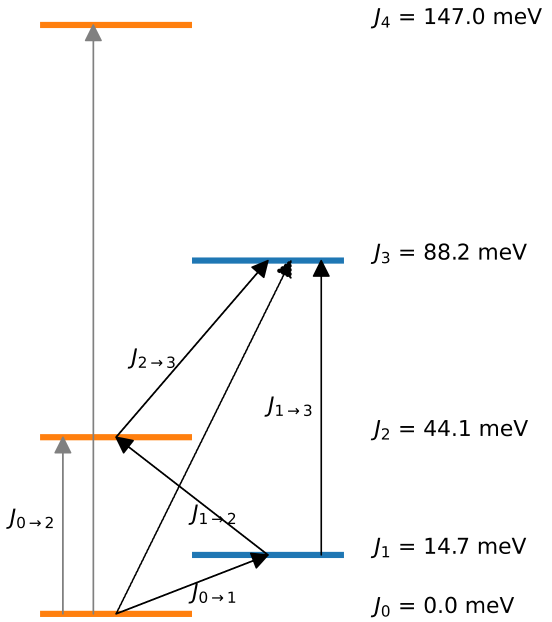

Figure S14. Scheme of rotational energy transitions of H_2. The transitions in black are observable transitions while the red arrow indicate a non-observable transition.

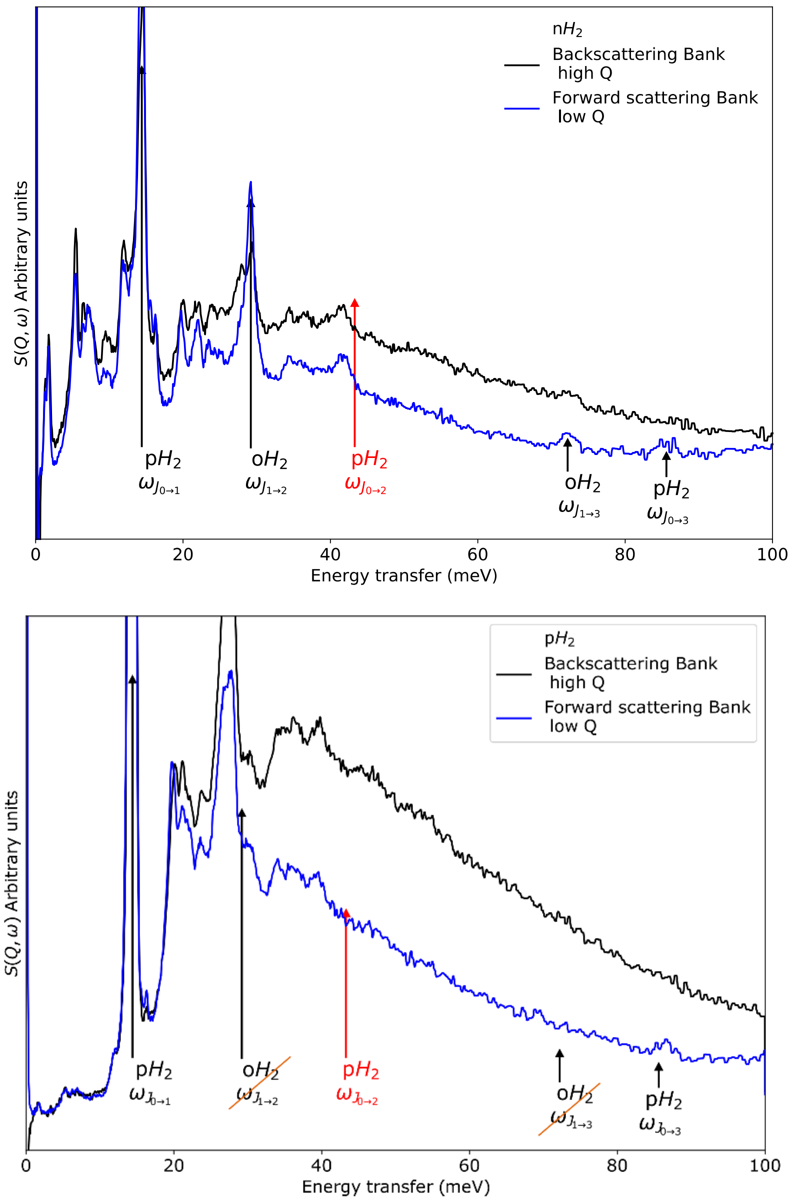

Figure S15. INS spectra of nH_2 **(upper)** and pH_2 **(bottom)** in $Mg(BD_4)_2$ for back and forward scattering. The arrows indicate the rotational transitions from para and ortho hydrogen. For nH_2, we observe the high-energy transitions $J_{1\to3}$ and $J_{0\to3}$ that are not seen in most cases due to the high momentum transfer in VISION. For pH_2, the transitions $J_{1\to3}$ and $J_{1\to2}$ are not observable because they start from the ortho state J_1. The transition $J_{0\to2}$ is not observed as it has a negligible cross section[18] (see Table S8).

Table S8. Rotational energy transitions corresponding to the B_{rot} = 7.22 meV. Experimental data see Figure 3 in the main text of the article. Uncertainties are 1 standard deviation.

$\boldsymbol{B_{rot}} \mathbf{= 7.22\ meV}$	$\boldsymbol{\omega_{rot}}$	**Exp**		$\boldsymbol{\omega_{rot}}$	**Exp**		$\boldsymbol{\omega_{rot}}$	**Exp**
$\boldsymbol{J_{0\to1}}$	14.4	14.4 $\pm$ 0.2	$\boldsymbol{J_{0\to2}}$	43.3	-----	$\boldsymbol{J_{0\to3}}$	86.6	85.6 $\pm$ 1.7
$\boldsymbol{J_{1\to2}}$	28.9	29.2 $\pm$ 0.4	$\boldsymbol{J_{1\to3}}$	72.2	72.3 $\pm$ 0.7	$\boldsymbol{J_{1\to4}}$	130.0	-----

5.2 INS roto-vibrational analysis

5.2.1 Para and normal hydrogen in $Mg(BD_4)_2$

Figure S16 (left) shows the INS spectra of $Mg(BD_4)_2$ with a load of 2.8 mmol of nH_2 (black trace), nH_2 is around the statistical mixture at room temperature (75% oH_2 and 25% pH_2). The area shown in gray is the signal of orthohydrogen and it is proportional to the vibrational transitions σ_{vib} of the hydrogen molecule. The vibrational transitions are given by low-energy phonons that correspond to the density of states (DoS) of the hydrogen molecule. The oH_2 spectrum (gray shaded area) show five well-defined phonon transitions located at 1.8 meV (a), 5.5 meV (b), 6.4 meV (c), 7.2 meV (d) and 11.9 meV (e). The peaks that are shown in red and blue are the peaks of parahydrogen rotational transitions $\sigma_{rot_{J(0\to1)}}\ with\ a.cross - section\ of\ {\sim}2 \times 80\ \mathrm{barn}$. The intensity observed in the data above 15 meV are the overtones of vibrational phonon modes (DoS) of the oH_2 given by its combination with the rotational transitions $\sigma_{rot+vib}{\sim}\sigma_{rot_{J(0\to1)}} \otimes \sigma_{vib}$.

Figure S16 (right) shows two rotational peaks that correspond to the transition ($J_{0\to1}$) located at 13.9 meV ((f) perturbed - red) and 14.6 meV ((g) unperturbed - blue). We used a Gaussian fitting for both rotor peaks. The analysis determines the area of each peak in arbitrary units, for the unperturbed (39.56) and the perturbed (14.26). The ratio of the areas that correspond to the population is 2.77 for the maximum load, Table S9 has all the relevant information for the peak fitting at maximum coverage.

The spectral intensity for molecular hydrogen for a roto-vibrational transition is given by $\sigma_{rot+vib} \sim \sigma_{rot} \otimes \sigma_{vib}$. For the case of pH_2, the cross-section of the transition $J_{0\to0}$ is very small ($\sigma_{rot_{J(0\to0)}} \sim 0$ barn)[18]. Hence, the vibrational model of the pH_2 are not well-visible below the rotational transition. In contrast, for oH_2, the cross-sectional area of the vibrational modes is given by $\sigma_{vib} \sim 2 \times 80$ barn. This difference in cross-sectional area readily visible when comparing the spectra of nH_2 and pH_2 (see Figure S16 left – grey area).

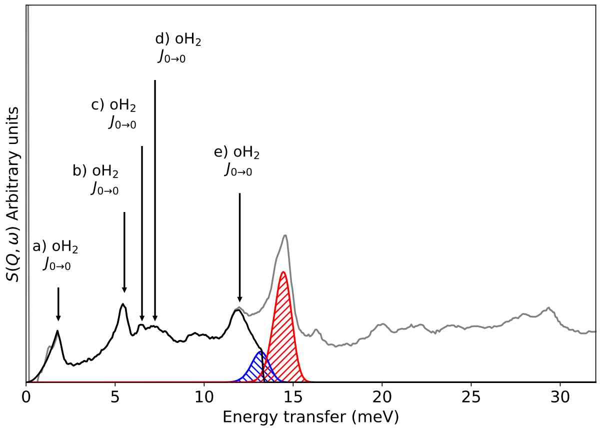

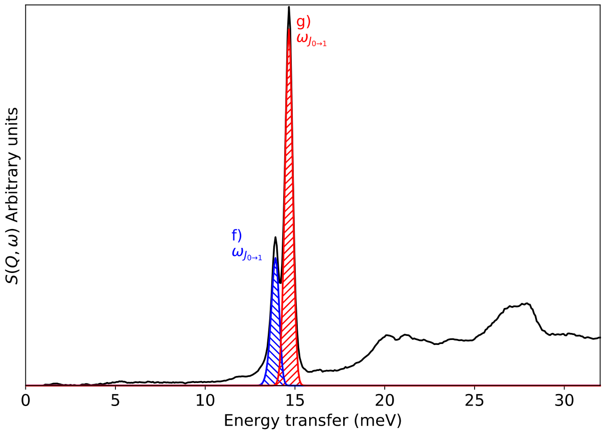

Figure S16. INS spectra of hydrogen in $Mg(BD_4)_2$. **Left**, spectrum of 16.8 mmol/g of nH_2 ($Mg(BD_4)_2 \cdot 1.04H_2$), **right**, the spectrum of 23.5 mmol/g of pH_2 ($Mg(BD_4)_2 \cdot 1.46H_2$). The peaks in red represent the rotational transition of $J_{0\to1}$, centered around 14.6 meV, while the blue peak is a $J_{0\to1}$ centered around 13.9 meV. The greyed area in the left panel is the extracted vibrational density of states of the hydrogen molecule.

Table S9. Gaussian analysis parameters of the rotor transitions ($J_{0\to1}$).

	Peak	**Center [meV]**	**Area [a.u.]**	**FWHM**	***σ***	***γ***
nH_2* *(16.8 mmol/g)	*perturbed* (f)	13.20	4.05	1.18	0.654	-1.33
	unperturbed (g)	14.45	14.56	1.14	0.654	-1.33
pH_2* *(23.5 mmol/g)	*perturbed* (f)	13.90	15.20	0.50	0.264	-1.02
	unperturbed (g)	14.65	40.90	0.50	0.264	-1.02

5.2.2 INS as function of pH_2 loading and temperature

Figure S17 show the INS spectra as function of pH_2 loading collected at 5 K. At the lowest loading (5.88 mmol/g), the spectra show an overall higher resolution allowing us to clearly observe peaks at 1.6 meV, 16.3 meV and 22.0 meV that overlap or are overwhelmed at higher loadings. At lower concentrations, the vibrational transitions are better defined. A peak at 27.8 meV is well defined and doesn't overlap other peaks. The overall intensity of the spectra increases with increasing pH_2 loading and with all the features remaining similar at similar energies for all dosing points. Table S10 show the results of the Gaussian analysis of the rotational peaks at 13.9 and 14.6 meV.

Figure S18 show the INS spectra of the highest loading of pH_2 (23.5 mmol/g) ($Mg(BD_4)_2 \cdot 1.46H_2$) as function of temperature (5 – 215 K). The peak at 13.9 meV and 27.8 meV disappear simultaneously when the temperature reaches 95 K. The peak at 14.7 meV is clearly visible up to 155 K and some intensity remain even at 185 K.

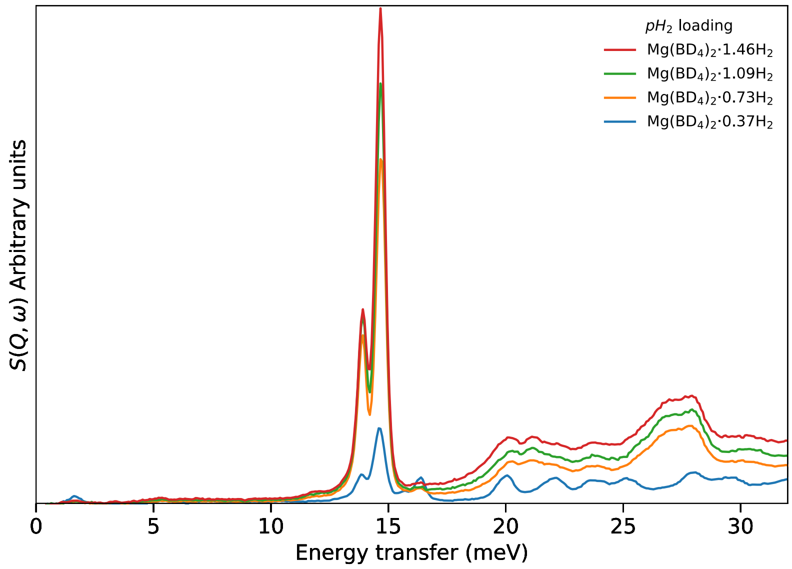

Figure S17. INS spectra of $Mg(BD_4)_2$ for different pH_2 loading collected at 5 K. The spectra show an increasing uptake with loading, and similar features at all energies.

Table S10. Fitting parameters for the rotational features of pH_2 as a function of coverage. Peak 1 is "perturbed rotor" while peak 2 is standard pH_2 $J_{0\rightarrow1}$ rotor transition.

Loading nominal (mmol)	Loading (mmol/g)	H_2 per unit cell	Peak 1 center (meV)	Peak 2 center (meV)	Ratio peak areas	Area Peak1+ Peak2 (normalized)	Area spectra (normalized)
1.0	5.88	0.37	13.82	14.63	2.85	0.180	0.305
2.0	11.8	0.73	13.89	14.69	2.19	0.715	0.656
3.0	17.6	1.09	13.89	14.68	2.34	0.860	0.816
4.0	23.5	1.46	13.90	14.67	2.69	1	1

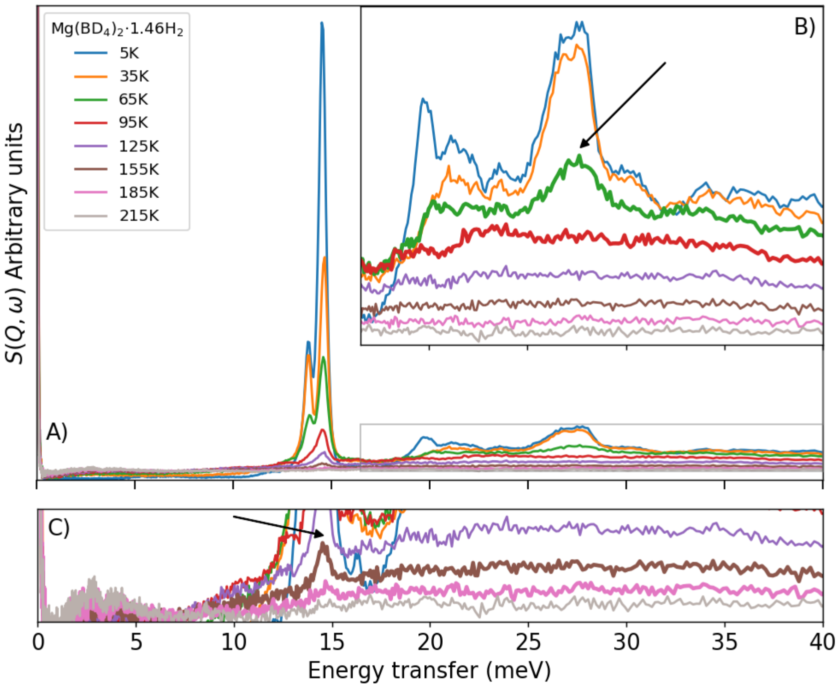

Figure S18. A) INS spectra of 23.5 mmol/g of pH_2 ($Mg(BD_4)_2 \cdot 1.46H_2$) collected at different temperatures. B) Zoom view of the peak around 17meV, the peak at 27.8 meV disappears after 65 K. C) Zoom view for higher temperatures. The peak at 14.7 meV is observable up to 185 K.

5.3. Simultaneous quantum rotational excitation (SQRE)

To fully account for all the intensity distribution of the pH_2 (Figure S19) spectra, we note that there is a peak at 27.8 meV that has an energy that is twice the energy of the "perturbed rotor" peak (blue hatched area). If we have almost pure pH_2, there is no rotational transition that has such energy transfer (see Table S8). In the case of pH_2 under pressure (SI section 5.5) there is a peak that appears at an energy twice that of the rotational line when the pressure increases. This peak is due to a process that involves "one neutron" simultaneously exciting two rotational transitions on two neighboring molecules or a *simultaneous quantum rotational excitation* (SQRE). This should not be confused with multiple scattering. This a single quantum event that constitutes evidence of the strong coupling between these hydrogen molecules due to pressure.

Figure S19 (red and blue area) shows the result of the convolution of the different rotor peaks. These peaks are calculated by convoluting the perturbed rotor (13.9 meV - blue) and unperturbed rotor (14.6 meV - red) with themselves, respectively. These convolutions produce the blue (27.8meV) and red (29.2 meV) modes, respectively. Of these peaks, only the one at 27.8 meV is observed for the experiment using pH_2.

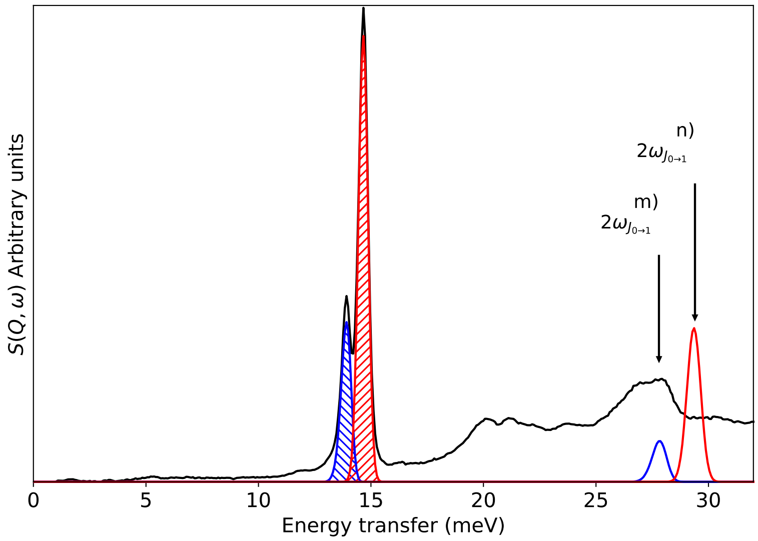

Figure S19. INS spectra of $Mg(BD_4)_2$ with a load of 23.5 mmol/g of pH_2 (black). Two additional peaks are marked in blue and red located at 27.8 and 29.2 meV corresponding to the convolution of each peak with itself.

5.4. Calculation of overtone vibrational modes and SQRE

The higher energy part of the INS spectra (16 < E < 30 meV) above the rotational peak has several peaks that compose the overtones. These overtones are the combination of the vibrational modes (DoS) with the rotational peaks. Figure S20 shows the product of convoluting the oH_2 DoS (purple upper area) with the pH_2 rotational lines (blue + red hatched areas). The resulting overtone curve (dark grey) is composed by the peaks located at (h)16.3 meV, (i)20.1 meV, (j)21.3 meV, (k)23.6 meV, and (l)26.6 meV, which correspond to the overtones of the phonon modes (a,b,c,d,e), respectively. Second order overtones (light grey area) are calculated by convoluting the overtones (dark grey area) with the oH_2 DoS (purple upper area).

The experimental data show another peak located exactly at 27.8 meV, this peak correspond to the SRQE (blue area) of the ‘perturbed’ rotor (see Figure S19). The sum of the first and second order overtones (dark yellow) plus the calculated SQRE (blue area) result in a curve (green) that reproduce the experimental pH_2 INS spectra. The experiment (black) shows no signal located at 29.2 meV that would correspond to the SQRE of the ‘unperturbed’ rotor, that would correspond to the peak shown in red.

Only the SQRE at 27.8 meV is observable while the other at 29.2 meV is not, indicating that the rotor peaks are not coupled. This suggest that there are two independent environments for the hydrogen molecule. The ratio of the areas the rotors $J_{0\rightarrow1}$ is 2.7 (see Table S3), which is a direct measurement of the ratio of hydrogen populating each environment.

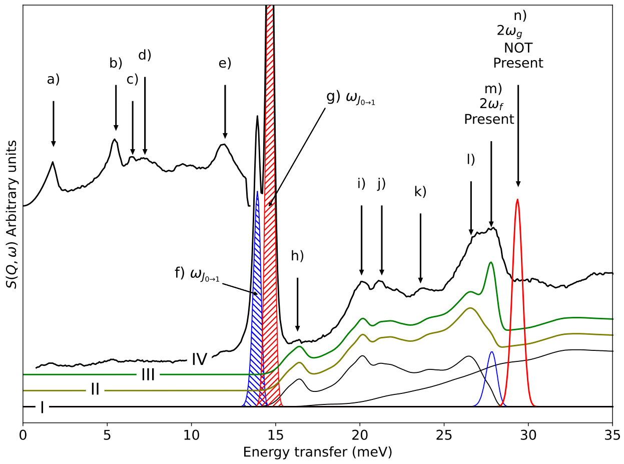

Figure S20. INS spectra of $Mg(BD_4)_2$ with a load of 23.5 mmol/g of pH_2 (black). The vibrational modes DoS [a-e] (grey upper area) are convoluted with the rotor transitions [f,g] to obtain the overtones [h-l] (16-28 meV grey area). The sum of the overtones and the bifold rotor [m] (green line) reproduces the experiment (E > 16 meV). The blue peak m) in necessary to account for the intensity. The peak n) does not exist in the data. This is because peak f) and g) are distinct pH_2 molecules. Note that in the case of pH_2 there are no rotational transitions that can account for peak m).

5.5. Comparison with H_2 at high-pressure

As a means of comparison, we present additional INS experiments of pH_2 and nH_2 at high-pressure. The experiments were measured using VISION spectrometer at the Spallation Neutron Source (SNS) at Oak Ridge National Laboratory (ORNL) in Tennessee, USA. A high-pressure dosing device was used coupled with CuBe high-pressure cell at 5K to reach pressures up to 4000 bar.

Figure S21 show the INS spectra of solid pH_2 at 200 bar and 2500 bar. In both cases, there is a peak near 14.6 meV that corresponds to the rotation $J_{0\rightarrow1}$, and overtones $\omega_{J_{0\rightarrow1}} \otimes \omega_{vib}$ are located between 16 meV and 28 meV. The overtone modes located between 16 meV and 29 meV shift to higher energies with increasing pressure. Interestingly, at the higher pressure a SQRE is observed near 29.0 meV, which corresponds to the convolution of the rotor peak with itself. Because the experiment was performed using pH_2, the rotational transition ($J_{1\rightarrow2}$) that should be located at 29.2 meV is not observed as the J=1 state is not populated because it corresponds to an ortho-spin-state.

Figure S22 a comparison of the experiment using pH_2 in $Mg(BD_4)_2$. The high-pressure experiment was scaled (y-axis) and translated (x-axis) so the rotational peak matches the high-pressure peak a 13.2 meV (red) and the unperturbed peak at 14.6 meV (blue) (see Figure S16 right). Hence, the SQRE (Figure S21) energy is shifted the same as the rotor, showing that the corresponding SQRE of the “perturbed” peak (m) is observable while the SQRE of the “unperturbed” (n) is not visible in the spectra.

Figure S23 shows the INS spectra of solid nH_2 for two high-pressure points (~0 bar and 2400 bar), the spectra show the rotational transition ($J_{0\rightarrow1}$) shifting to lower energies with increasing pressure. The shift to lower energies of the rotor is due to the quadrupole interaction of oH_2. A vibrational mode (rattling) is located at lower energies (5 meV to 13 meV) and moves towards higher energies with increasing pressure. The overtones of the vibrational modes are located between 15 and 29 meV, and shift to higher energies with increasing pressure. Contrary to the pH_2 high-pressure experiment, the peak located at 29.2

meV is the ortho rotation ($J_{1\to2}$) (green-line), and a SQRE $(2\omega_{J_{0\to1}})$ is not well-defined.

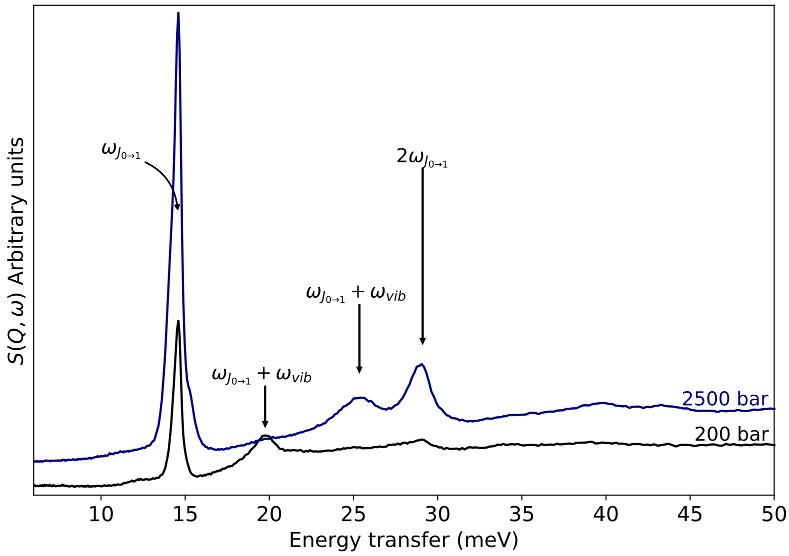

Figure S21. INS spectra of solid pH_2 at 200 (black) and 2500 bar (blue). The peak near 14.6 meV correspond to the rotation $J_{0\to1}$ and its intensity increases with pressure while its energy is reduced. At higher pressure, SQRE is located at 29.0 meV.

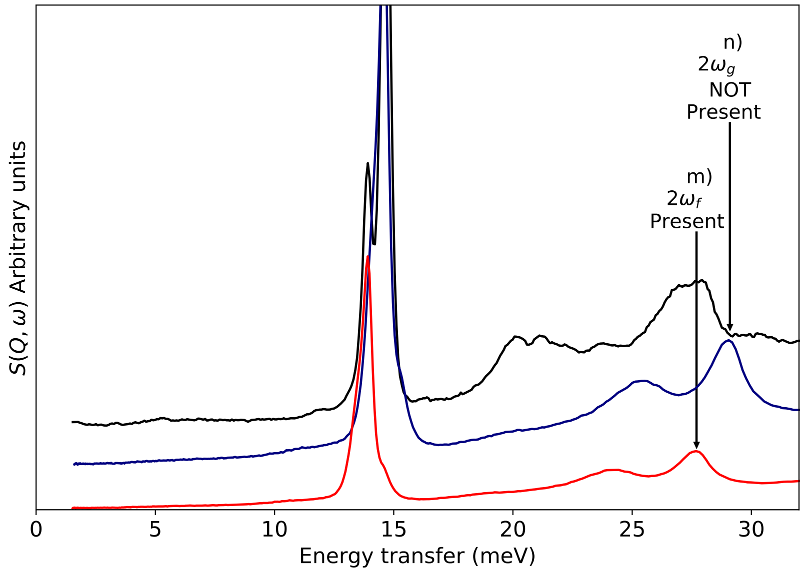

Figure S22. INS spectra $Mg(BD_4)_2$ with a load of 23.5 mmol/g of pH_2 (black). To compared intensities and energies the INS spectrum of pH_2@2500 bar is scaled (x- and y- wise) to correspond to both rotor intensities (13.9 meV (red) and 14.6 meV (blue)).

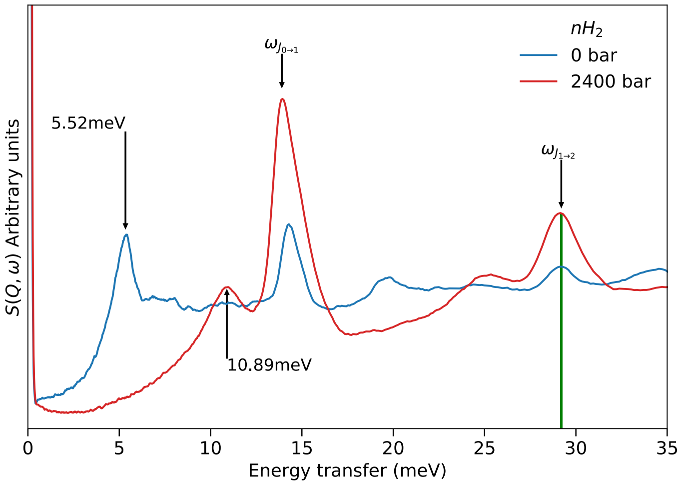

Figure S23. INS spectra of solid nH_2 at high-pressure collected at 5 K. The INS spectra near 0 bar and at 2400 bar show a mode that is located at 5.52 meV and 10.89 meV, respectively. The peaks located near 14.0 meV and at 29.2 meV correspond to rotational transitions $J_{0\rightarrow1}$ and $J_{1\rightarrow2}$, respectively.

5.6 Density of hydrogen confined in Mg(BD$_4$)$_2$

By looking at the effect of pressure on highly enriched pH_2 and nH_2 (see SI section 5.5) on the phonon spectrum of hydrogen; we can calibrate a "representative density" required for the effect of pressure to be observable.

Figure S24 upper left show a linear interpolation of the phonon energies of nH_2 as a function of the pressure (orange line). The phonon energies (blue triangles) were taken from the full experiment of solid nH_2 (0 bar to 4000 bar) (Figure S23).

The different vibrational modes observed in the DoS (Figure S16 left) are shown as green points correspond to a vibration in the three directions. The highest energy is 11.9 meV represents the higher vibration mode that correspond to a high-pressure environment of 2915 bar (Figure S24 green circle).

The density of bulk hydrogen has been previously reported as function of pressure by Silvera et al.[34] (Fig S24 upper right). Assuming a pressure of 2915 bar (red- dotted), the corresponding density is 132 g/L. A value much higher than bulk -liquid (70.9 g/L) and -solid (86.7 g/L) density at 1 bar. This value is 1.51 times higher than the bulk-solid density at 1 bar.

The cross-sectional area of the H_2 molecule as function of pressure (Figure S24 bottom left) was calculated assuming a hexagonal close packing and is given by:

$$\sigma = f \cdot \left({}^{m}\!/_{\rho N_A} \right)$$

where $f = {}^{\sqrt{3}}\!/_{\sqrt[3]{4}} = 1.091$ is the hexagonal closed-packing factor, m is the molar mass, ρ is the volumetric density and N_A is the Avogadro number (Rouquerol, Rouquerol et al. 1999, Lowell, Shields et al. 2004). The corresponding cross-sectional area for 2915 bar is 9.40 Å^2.

The H_2-H_2 intermolecular distance as function of pressure (Figure S24 bottom right) is given by the relation:

$$\sigma = \frac{\sqrt{3}}{2} \cdot r^2$$

where σ is the cross-sectional area of H_2 and r is the intermolecular distance[35]. The corresponding intermolecular distance for a pressure of 2915 bar is 3.29 Å.

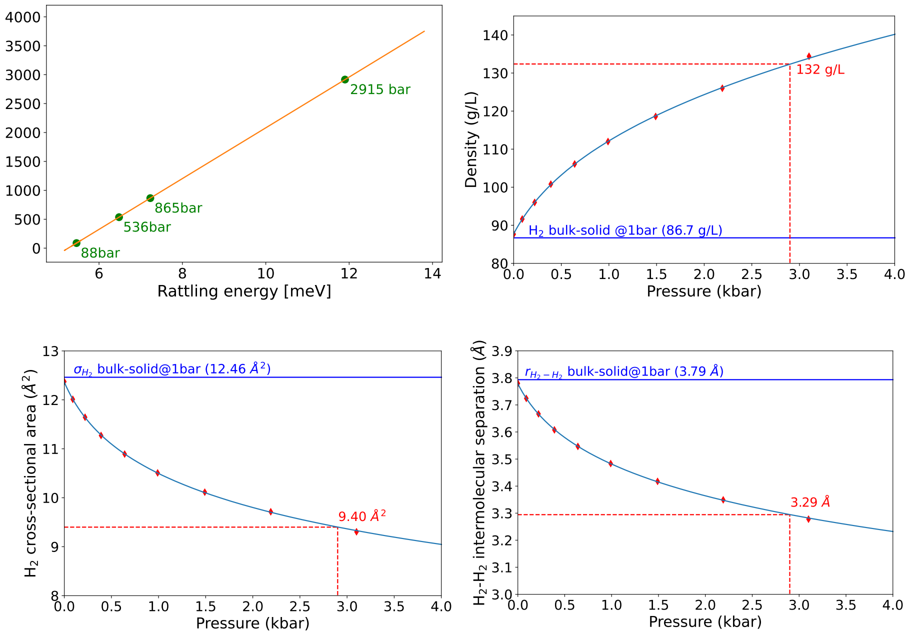

Figure S24. Upper left, linear interpolation of the phonon energies of nH_2 as a function of the pressure. The energies observed in the phonon modes [b-e] in Figure S2 are shown as green points. The phonon mode at 11.9 meV [e] corresponds to a pressure environment of 2915 bar. Upper right, hydrogen density as a function of pressure Bottom left, corresponding cross-sectional area of hydrogen as a function of the pressure. Bottom right, H_2-H_2 intermolecular separation as function of pressure. The corresponding separation for a phonon mode of 11.9 meV (Figure S2 peak [e]) is 3.29 Å.

References

1. U. Eberle, M. Felderhoff, F. Schüth, Chemical and physical solutions for hydrogen storage. *Angew. Chemie - Int. Ed.* **48**, 6608–6630 (2009).

2. M. Hirscher, V. A. Yartys, M. Baricco, J. B. von Colbe, D. Blanchard, R. C. Bowman Jr., D. P. Broom, C. E. Buckley, F. Changn, P. Chen, Y. W. Cho, J.-C. Crivello, F. Cuevas, W. I. F. David, P. E. de Jongh, R. V. Denys, M. Dornheim, M. Felderhoff, Y. Filinchuk, G. E. Froudakis, David M. Grants, E. MacA. Gray, B. C. Hauback, T. He, T. D. Humphries, T. R. Jensen, S. Kim, Y. Kojima, M. Latroche, H.-W. Li, M. V. Lototskyy, J. W. Makepeace, K. T. Møller, L. Naheed, P. Ngene, D. Noréus, M. Nygård, S.-i. Orimo, M. Paskevicius, L. Pasquini, D. B. Ravnsbæk, M. V. Sofianos, T. J. Udovic, T. Vegge, G. S. Walkers, C. J. Webb, C. Weidenthaler, C.

Zlotea, Materials for hydrogen-based energy storage – past, recent progress and future outlook. *J. Alloys and Compd.* **827**, 153548 (2020).

3. M. Hirscher, Hydrogen storage by cryoadsorption in ultrahigh-porosity metal-organic frameworks. *Angew. Chemie - Int. Ed.* **50**, 581-582 (2011).

4. L. J. Murray, M. Dinc, J. R. Long, Hydrogen storage in metal-organic frameworks. *Chem. Soc. Rev.* **38**, 1294-1314 (2009).

5. W. Grochala, P. P. Edwards, Thermal decomposition of the non-interstitial hydrides for the storage and production of hydrogen. *Chem. Rev.* **104**, 1283-1315 (2004).

6. Y. Filinchuk, B. Richter, T. R. Jensen, V. Dmitriev, D. Chernyshov, H. Hagemann, Porous and dense magnesium borohydride frameworks: Synthesis, stability, and reversible absorption of guest species. *Angew. Chemie - Int. Ed.* **50**, 11162-11166 (2011).

7. G. N. Iles, F. Devred, P. F. Henry, G. Reinhart, T. C. Hansen, Neutron diffraction studies for realtime leaching of catalytic Ni. *J. Chem. Phys.* **141**, 034201 (2014).

8. C. M. Brown, Y. Liu, T. Yildirim, V. K. Peterson, C. J. Kepert, Hydrogen adsorption in HKUST-1: a combined inelastic neutron scattering and first-principles study. *Nanotechnology* **20**, 204025 (2009).

9. I. F. Silvera, The solid molecular hydrogens in the condensed phase: Fundamentals and static properties. *Reviews of Modern Physics* **52**, 393-452 (1980).

10. A. Davoodabadi, A. Mahoudi, H. Ghasemi, The potential of hydrogen hydrate as a future hydrogen storage medium. *iScience* **24**, 101907 (2021).

11. H. Liu, I. I. Naumov, R. Hoffmann, N. W. Ashcroft, R. J. Hemley, Potential high-Tc superconducting lanthanum and yttrium hydrides at high pressure. *PNAS* **114**, 6990-6995 (2017).

12. S. S. Batsanov, Van der Waals Rradii of hydrogen in gas-phase and condensed molecules. *Struct. Chem.* **10**, 395-400 (1999).

13. R. M. Hazen, H. K. Mao, L. W. Finger, R. J. Hemley, Single-crystal x-ray diffraction of n-H_2 at high pressure. *Phys. Rev. B* **36**, 3944-3947 (1987).

14. A. J. Ramirez-Cuesta, Y. Q. Cheng, Studying materials and processes with VISION, VirtuES and ICEMAN. Modeling INS data with DFT methods. *Hamon.* **30**, 154-159 (2020).

15. I. F. Silvera, The solid molecular hydrogens in the condensed phase: Fundamentals and static properties. *Rev. Mod. Phys.* **52**, 393-452 (1980).

16. P. C. H. Mitchell, S. F. Parker, A. J. Ramirez-Cuesta, J. Tomkinson, Eds., *Vibrational Spectroscopy with Neutrons With Applications in Chemistry, Biology, Materials Science and Catalysis* (World Scientific Publishing, Singapore, 2005).

17. J. Bahadur, C. I. Contescu, A. J. Ramirez-Cuesta, E. Mamontov, N. C. Gallego, Y. Q. Cheng, L. L. Daemen, Y. B. Melnichenko, Properties of immobile hydrogen confined in microporous carbon. *Carbon* **117**, 383-392 (2017).

18. J. A. Young, J. U. Koppel, Slow neutron scattering by molecular hydrogen and deuterium. *Phys. Rev.* **135**, A603-A611 (1964).

19. J. Z. Larese, T. Arnold, L. Frazier, R. J. Hinde, A. J. Ramirez-Cuesta, Direct observation of H_2 binding to a metal oxide surface. *Phys. Rev. Lett.* **101**, 165302 (2008).

20. L. Ulivi, M. Celli, A. Giannasi, A. J. Ramirez-Cuesta, D. J. Bull, M. Zoppi, Quantum rattling of molecular hydrogen in clathrate hydrate nanocavities. *Phys. Rev. B* **76**, 161401(R) (2007).

21. T. A. Strobel, A. J. Ramirez-Cuesta, L. L. Daemen, V. S. Bhadram, T. A. Jenkins, C. M. Brown, Y. Q. Cheng, Quantum dynamics of H_2 trapped within organic clathrate cages. *Phys. Rev. Lett.* **120**, 120402 (2018).

22. T. Düren, F. Millange, G. Férey, K. S. Walton, R. Q. Snurr, Calculating geometric surface areas as a characterization tool for metal - organic frameworks. *J. Phys. Chem. C.* **111**, 15350-15356 (2007).

23. M. Hirscher, B. Panella, B. Schmitz, Metal-organic frameworks for hydrogen storage. *Microporous Mesoporous Mater.* **129**, 335-339 (2010).

24. C. J. Pickard, R. J. Needs, Structure of phase III of solid hydrogen. *Nat. Phys.* **3**, 473-476. (2007).

25. W. L. Mao, J. Mao, A. F. Goncharov, V. V. Struzhkin, Q. Guo, J. Hu, J. Shu, R. J. Hemley, M. Somayazulu, Y. Zhao, Hydrogen clusters in clathrate hydrate. *Science* **297**, 2247-2249 (2002).

26. C. F. Matta, L. Huang, L. Massa, Characterization of a trihydrogen bond on the basis of the topology of the electron density. *J. Phys. Chem. A* **115**, 12451-12458 (2011).

27. M. Jabłoński, Charge-inverted hydrogen bond vs. other interactions possessing a hydridic hydrogen atom. *Chem. Phys.* **433**, 76-84 (2014).

28. B. Streppel, M. Hirscher, BET specific surface area and pore structure of MOFs determined by hydrogen adsorption at 20 K. *Phys. Chem. Chem. Phys.* **13**, 3220-3222 (2011).

29. V. Favre-Nicolin, R. Černý, FOX, “free objects for crystallography”: A modular approach to ab initio structure determination from powder diffraction. *J. Appl. Crystallogr.* **35**, 734-743 (2002).

30. J. Rodríguez-Carvajal, Recent advances in magnetic structure determination by neutron powder diffraction. *Phys. B Phys. Condens. Matter.* **192**, 55-69 (1993).

31. J. Rodriguez-Carvajal, “FULLPROF: a program for Rietveld refinement and pattern matching analysis” (Satellite Meeting on Powder Diffraction of the XV Congress of the IUCr. Toulouse, France, 1990).

32. Y. Filinchuk, R. Černý, H. Hagemann, Insight into $Mg(BH_4)_2$ with synchrotron X-ray diffraction: Structure revision, crystal chemistry, and anomalous thermal expansion. *Chem. Mater.* **21**, 925–933 (2009).

33. I. Weinrauch, I. Savchenko, D. Denysenko, S. M. Souliou, H. H. Kim, M. Le Tacon, L. L. Daemen, Y. Cheng, A. Mavrandonakis, A. J. Ramirez-Cuesta, D. Volkmer, G. Schutz, M. Hirscher, T. Heine, Capture of heavy hydrogen isotopes in a metal-organic framework with active Cu(I) sites. *Nat. Commun.* **8**, 14496 (2017).

34. I. F. Silvera, V. V. Goldman, The isotropic intermolecular potential for H_2 and O_2 in the solid and gas phases. *J. Chem. Phys.* **69**, 4209-4213 (1978).

35. R. Balderas-Xicohténcatl, “High-density hydrogen monolayer formation and isotope diffusion in porous media”, thesis, University of Stuttgart, Stuttgart, Germany (2019).

Appendix III: Supporting information of Chapter 6

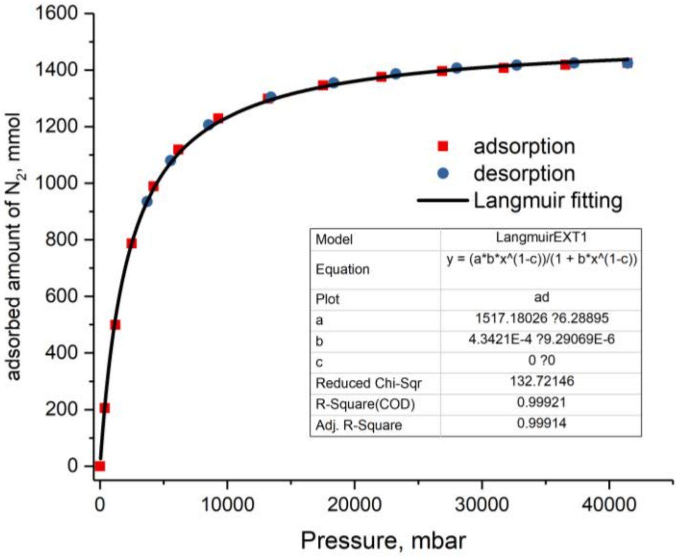

Model	LangmuirEXT1
Equation	y = (a*b*x^(1-c))/(1 + b*x^(1-c))
Plot	ad
a	1517.18026 ?6.28895
b	4.3421E-4 ?9.29069E-6
c	0 ?0
Reduced Chi-Sqr	132.72146
R-Square(COD)	0.99921
Adj. R-Square	0.99914

Figure S1. Nitrogen adsorption and desorption in γ-$Mg(BH_4)_2$ sample at 190 K and up to 41 bar. The proportion of the crystalline γ-$Mg(BH_4)_2$ is estimated to be 89%, using the parameter a = 1517(6) µmol and sample the mass of 136.7 mg. The limiting composition at saturation is known to be γ-$Mg(BH_4)_2 \cdot 2/3N_2$.

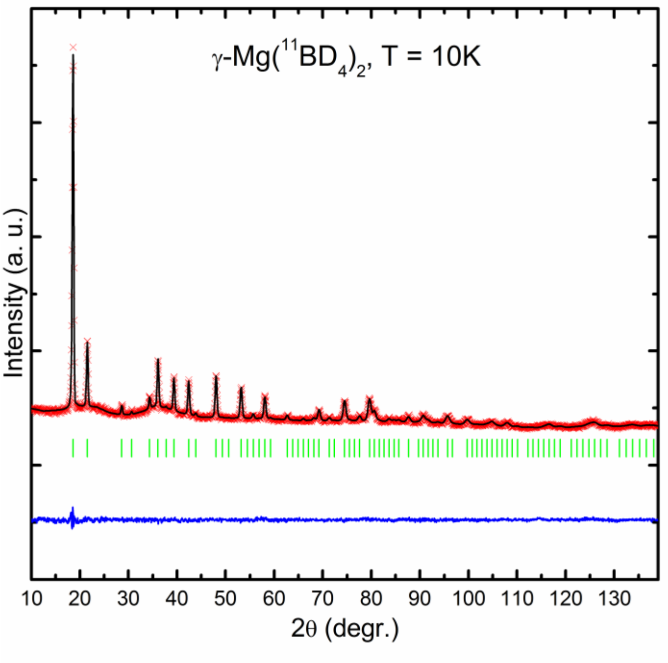

Figure S2. NPD Rietveld refinement ($\lambda = 2.0787(2)$ Å) for empty γ-$Mg(^{11}BD_4)_2$ at 10 K. Experimental and calculated data are shown in red symbols and black line, respectively. Blue line shows the difference curve, while green marks show Bragg positions.

Table S1. Experimental structural parameters for γ-Mg(BD4)2 at 10 K, from NPD. Space group *Ia*-3*d*, *a* = 15.740(1) Å, *V* = 3899.6(8) Å^3.

Atom	Wyckoff site	x	y	z	Occupancy
Mg	24d	1/4	1/8	1/2	1
B	48g	0.3130(3)	0.0630(3)	3/8	1
D1	96h	0.2888(3)	0.0202(3)	0.4363 (4)	1
D2	96h	0.3001(3)	0.1391(3)	0.3814(2)	1

Table S2. Comparison of the structural data for γ-$Mg(BD_4)_2$ derived from NPD data (this work) and for γ-$Mg(BH_4)_2$ from SR-XPD data (ref.[1]).

	NPD data	SR-XPD data
Formula	$Mg(^{11}BD_4)_2$	$Mg(BH_4)_2$
Space group	*Ia*-3*d*	*Ia*-3*d*
a (Å)	15.7401(11)	15.7575(16)
V (Å^3)	3899.6(8)	3912.6(7)
M (g mol^{-1})	62.60	53.99
T (K)	10	298

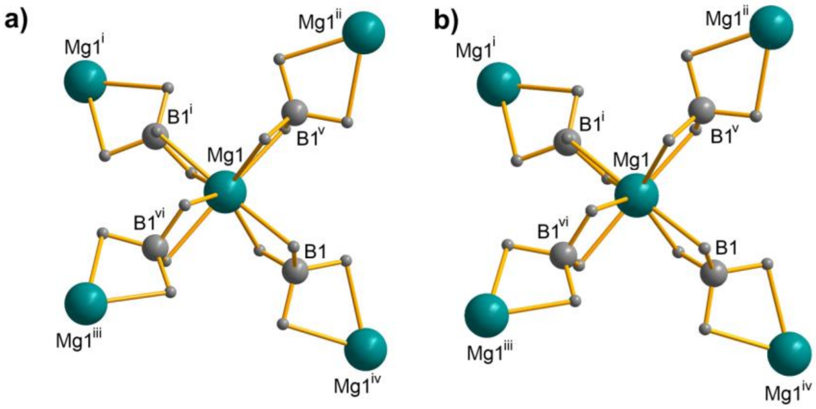

Figure S3. Coordination environment of Mg in γ-$Mg(^{11}BD_4)_2$ (a, this work, from NPD data) and in γ-$Mg(BH_4)_2$ (b, ref.[1], XR-XRD data). Labels on D and H atoms are omitted for clarity. Symmetry operations: (i) −0.25+x, 0.25−y, 0.25+z; (ii) −0.25+x, 0.25+y, 0.75−z; (iii) 0.25+x, 0.75−y, −0.25+z; (iv) 0.25−x, 0.25+y, −0.25+z; (v) 0.75−x, 0.25−y, −0.25+z; (vi) 0.25+x, 0.25−y, 0.75+z. Mg atom has distorted tetrahedral environment and the Mg−D bond lengths are 2.025(5) Å and 2.039(3) Å, for D1 and D2, respectively. Those reported for γ-$Mg(BH_4)_2$ were slightly shorter, 1.958 Å and 1.998 Å. The B···Mg···B' angles have close values of 99.440(3)° and 100.443° (for B1···Mg···B1^{vi}) and 132.220(2)° and 129.603° (for B1···Mg···B1^{i}), in the structures of γ-$Mg(^{11}BD_4)_2$ and γ-$Mg(BH_4)_2$, respectively.

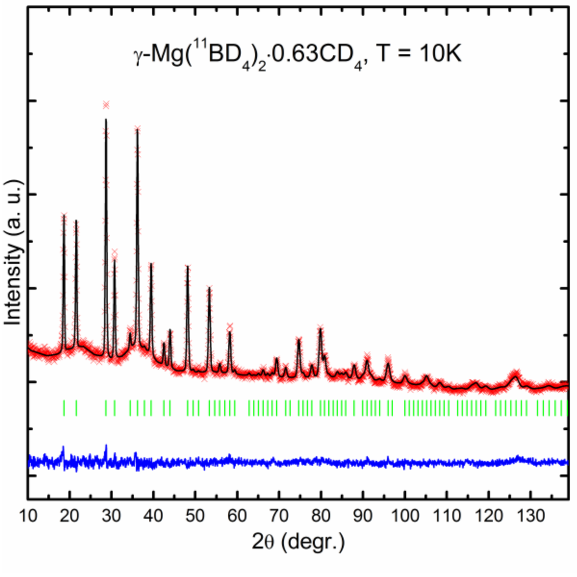

Figure S4. NPD Rietveld refinement (λ = 2.0787(2) Å) for γ-$Mg(^{11}BD_4)_2 \cdot 0.63CD_4$ at 10 K. Experimental and calculated data are shown in red symbols and black line, respectively. Blue line shows the difference curve, while green marks show Bragg positions.

Table S3. Experimental structural parameters for gas-loaded γ-$Mg(BD_4)_2 \cdot 0.63CD_4$ at 10 K, from NPD. Space group *Ia*-3*d*, *a* = 15.7054(3) Å, *V* = 3873.9(2) Å^3.

Atom	Wyckoff site	*x*	*y*	*z*	Occupancy
Mg	24*d*	1/4	1/8	1/2	1
B	48*g*	0.31368(13)	0.06368(13)	3/8	1
D1	96*h*	0.28949(13)	0.02088(13)	0.43630	1
D2	96*h*	0.30084(13)	0.13981(13)	0.38140	1
C1	32*e*	0.1291(3)	0.1291(3)	0.1291(3)	0.475(5)
D3	32*e*	0.0885(3)	0.0885(3)	0.0885(3)	0.475(5)
D4	96*h*	0.1059(6)	0.1940(6)	0.1383(9)	0.475(5)

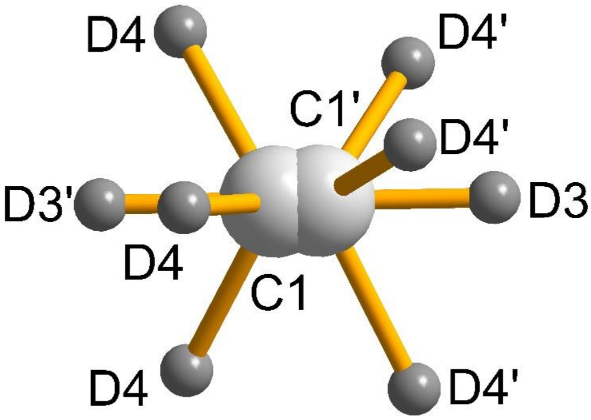

Figure S5. Orientational disorder of CD_4 in γ-$Mg(BD_4)_2 \cdot 0.63CD_4$ at 10 K.

Table S4. Geometry of the shortest D···D contacts between the γ-$Mg(^{11}BD_4)_2$ host and the guest CD_4 molecules.

γ-$Mg(^{11}BD_4)_2 \cdot 0.63CD_4$, 10 K				
Contact	D···D	∠B−D···D	∠C−D···D	Symmetry operation
B1−D1···D4−C1	2.993(10)	139.6(2)	142.6(7)	-
$B1^i$−D2···D4−C1	3.009(11)	139.7(2)	129.3(7)	(i) 3/4−x, 1/4−y, −1/4+z

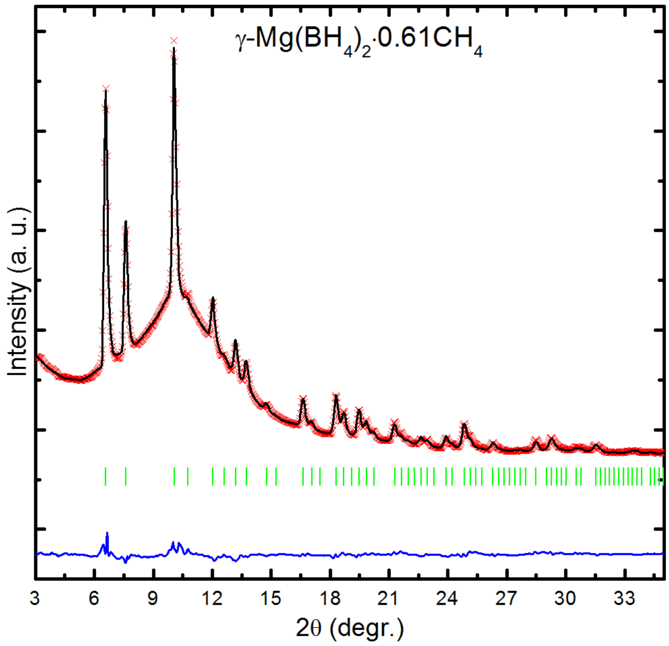

Figure S6. SR-XRD Rietveld refinement profile for γ-Mg(BH$_4$)$_2$·0.61CH$_4$ at 188 K under 65 bar of CH$_4$. The blue marks show Bragg positions (λ = 0.740569 Å).

Table S5. Experimental structural parameters for γ-Mg(BH$_4$)$_2$·0.61CH$_4$ at 188 K under 65 bar of CH$_4$, from SR-XRD. Space group *Ia*-3*d*, *a* = 15.779(3) Å, *V* = 3928(1) Å^3.

Atom	Wyckoff site	*x*	*y*	*z*	Occupancy
Mg	24*d*	1/4	1/8	1/2	1
B	48*g*	0.30981	*x*-1/4	3/8	1
H1	96*h*	0.28571	0.02071	0.43730	1
H2	96*h*	0.29741	0.13551	0.38560	1
C1	32*e*	0.1029(5)	*x*	*x*	0.456(6)
H3	32*e*	0.0628(5)	*x*	*x*	0.456(6)
H4	96*h*	0.0889(5)	0.1697(5)	0.0900(5)	0.456(6)

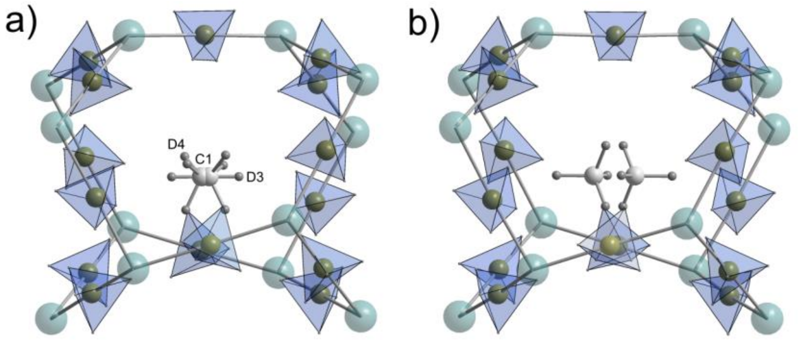

Figure S7. Changing position of the methane molecules as the temperature increases, (a) γ-$Mg(BD_4)_2 \cdot 0.63CD_4$ at 10 K and (b) γ-$Mg(BH_4)_2 \cdot 0.61CH_4$ at 188 K under 65 bar. A gradual change between the two illustrated extremities was observed by *in situ* SR-XRD. The ball-and-stick model complemented with BH_4^- polyhedra is used for clarity.

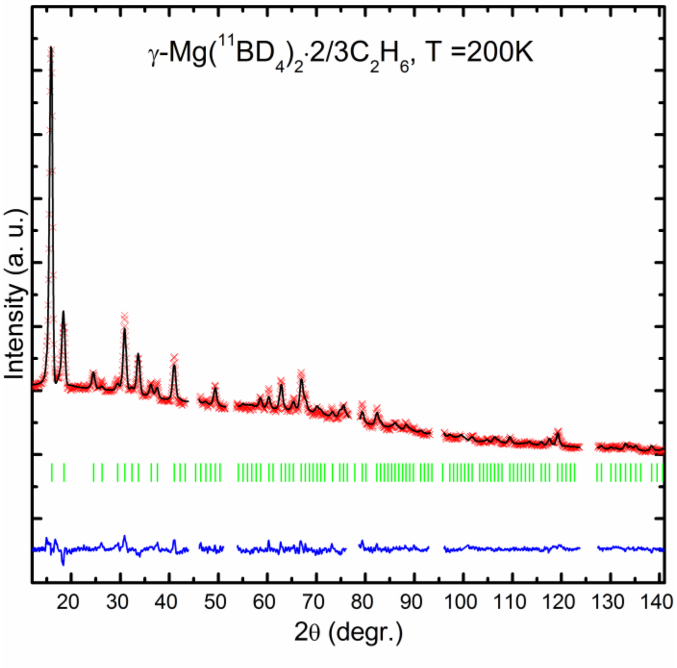

Figure S8. SR-XRD Rietveld refinement (λ = 1.79860(1) Å) for γ-Mg($^{11}BD_4$)$_2$·0.66C_2H_6 at 200 K. Experimental and calculated data are shown in red symbols and black line, respectively. Blue line shows the difference curve, while green marks show Bragg positions. Regions near Bragg reflections from the Al container were excluded.

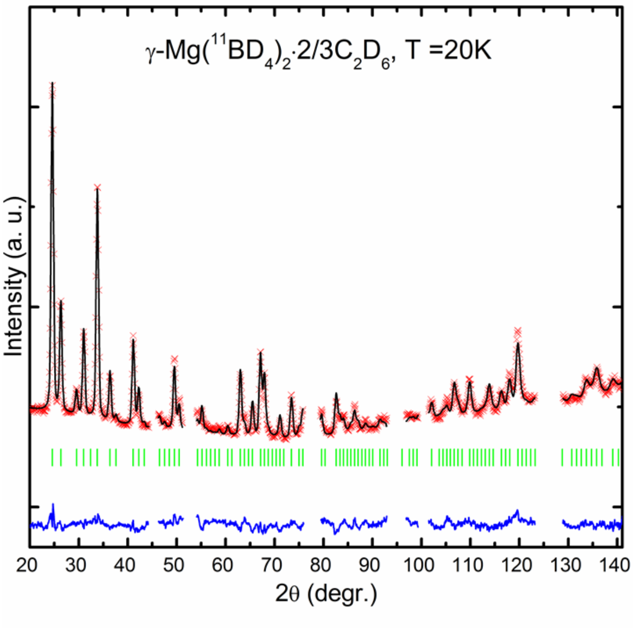

Figure S9. NPD Rietveld refinement (λ = 1.79860(1) Å) for γ-Mg(^{11}BD$_4$)$_2$·2/3C$_2$D$_6$ at 20 K. Experimental and calculated data are shown in red symbols and black line, respectively. Blue line shows the difference curve, while green marks show Bragg positions. Regions near Bragg reflections from the Al container were excluded.

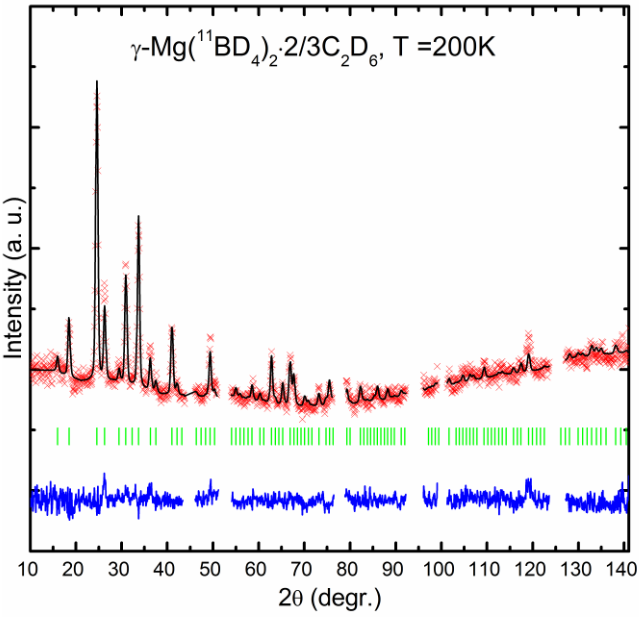

Figure S10. NPD Rietveld refinement (λ = 1.79860(1) Å) for γ-Mg($^{11}BD_4$)$_2$·0.66C_2D_6 at 200 K. Experimental and calculated data are shown in red symbols and black line, respectively. Blue line shows the difference curve, while green marks show Bragg positions. Regions near Bragg reflections from the Al container were excluded.

Table S6. Experimental structural parameters for γ-Mg($^{11}BD_4$)$_2$·0.66C_2H_6 at 200 K from NPD. Space group *Ia*-3*d*, *a* = 15.8079(10) Å, *V* = 3950.2(5) Å^3.

Atom	Wyckoff site	*x*	*y*	*z*	Occupancy
Mg	24d	1/4	1/8	1/2	1
B	48g	0.30981	0.05981	3/8	1
D1	96h	0.28571	0.02071	0.43730	1
D2	96h	0.29741	0.13551	0.38560	1
C1	32e	0.1524(2)	0.1524(2)	0.1524(2)	1
H3	96h	0.165(2)	0.2096(11)	0.1180(12)	1

Table S7. Experimental structural parameters for γ-Mg($^{11}BD_4$)$_2$·0.66C_2D_6 at 20 K from NPD. Space group *Ia*-3*d*, *a* = 15.7704(5) (12) Å, *V* = 3922.2(4) Å^3.

Atom	Wyckoff site	*x*	*y*	*z*	Occupancy
Mg	24d	1/4	1/8	1/2	1
B	48g	0.3137(3)	0.0637(3)	3/8	1
D1	96h	0.2865(4)	0.0197(4)	0.4327(5)	1
D2	96h	0.2979(4)	0.1371(4)	0.3819(3)	1
C1	32e	0.15274(15)	0.15274(15)	0.15274(15)	1
D3	96h	0.0337(3)	0.1082(4)	0.1058(3)	1

Table S8. Experimental structural parameters for γ-Mg($^{11}BD_4$)$_2$·0.66C_2D_6 at 200 K from NPD. Space group *Ia*-3*d*, *a* = 15.8184(12) Å, *V* = 3958.1(9) Å^3.

Atom	Wyckoff site	*x*	*y*	*z*	Occupancy
Mg	24d	1/4	1/8	1/2	1
B	48g	0.30981	0.05981	3/8	1
D1	96h	0.28571	0.02071	0.43730	1
D2	96h	0.29741	0.13551	0.38560	1
C1	32e	0.1533(7)	0.1533(7)	0.1533(7)	1
D3	96h	0.0438(13)	0.1233(13)	0.0959(16)	1

Table S9. Geometry of D···D contacts between γ-$Mg(^{11}BD_4)_2$ host and C_2D_6 guest species.

Contact	D···D(H)	∠B−D···D(H)	∠C−D(H)···D	Symmetry operation
γ-$Mg(^{11}BD_4)_2{\cdot}0.66C_2D_6$, 20 K				
B1−D1···D3−C1	3.035(9)	124.7(4)	121.3(4)	-
B1^{i}−D2···D3−C1	2.534(9)	142.6(5)	148.2(5)	(i) 3/4−x, 1/4−y, −1/4+z
γ-$Mg(^{11}BD_4)_2{\cdot}0.66C_2D_6$, 200 K				
B1−D1···D3−C1	2.883(23)	129.6(4)	139.0(2)	-
B1^{i}−D2···D3−C1	2.847(21)	139.6(4)	126.4(2)	(i) 3/4−x, 1/4−y, −1/4+z

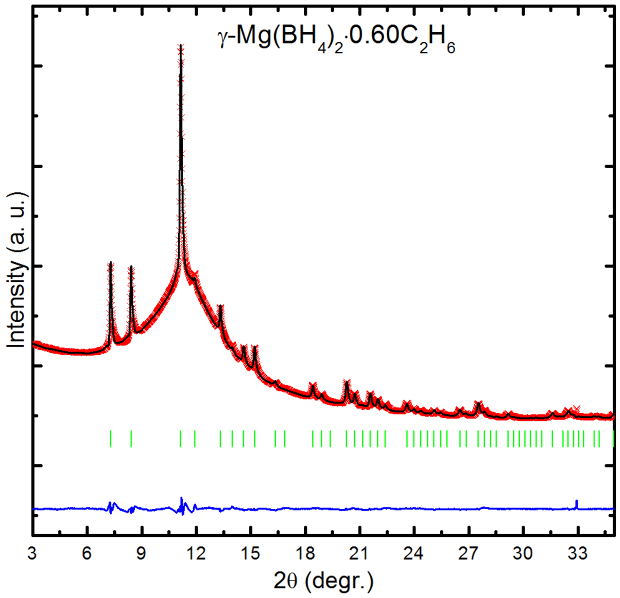

Figure S11. SR-XRD Rietveld refinement for γ-Mg(BH$_4$)$_2$·0.60C$_2$H$_6$ at 200 K under 4 bar of C$_2$H$_6$. The blue marks show Bragg positions (λ = 0.822570 Å).

Table S10. Experimental structural parameters for γ-Mg(BH$_4$)$_2$·0.60C$_2$H$_6$ at 200 K under 4 bar of C$_2$H$_6$, from SR-XRD. Space group *Ia*-3*d*, *a* = 15.8386(2) Å, *V* = 3973.32(7) Å^3.

Atom	Wyckoff site	*x*	*y*	*z*	Occupancy
Mg	24*d*	1/4	1/8	1/2	1
B	48*g*	0.30981	*x*-1/4	3/8	1
H1	96*h*	0.28571	0.02071	0.43730	1
H2	96*h*	0.29741	0.13551	0.38560	1
C1	32*e*	0.1513(3)	*x*	*x*	0.904(3)
H3	96*h*	0.055(2)	0.1260(18)	0.092(3)	0.904(3)

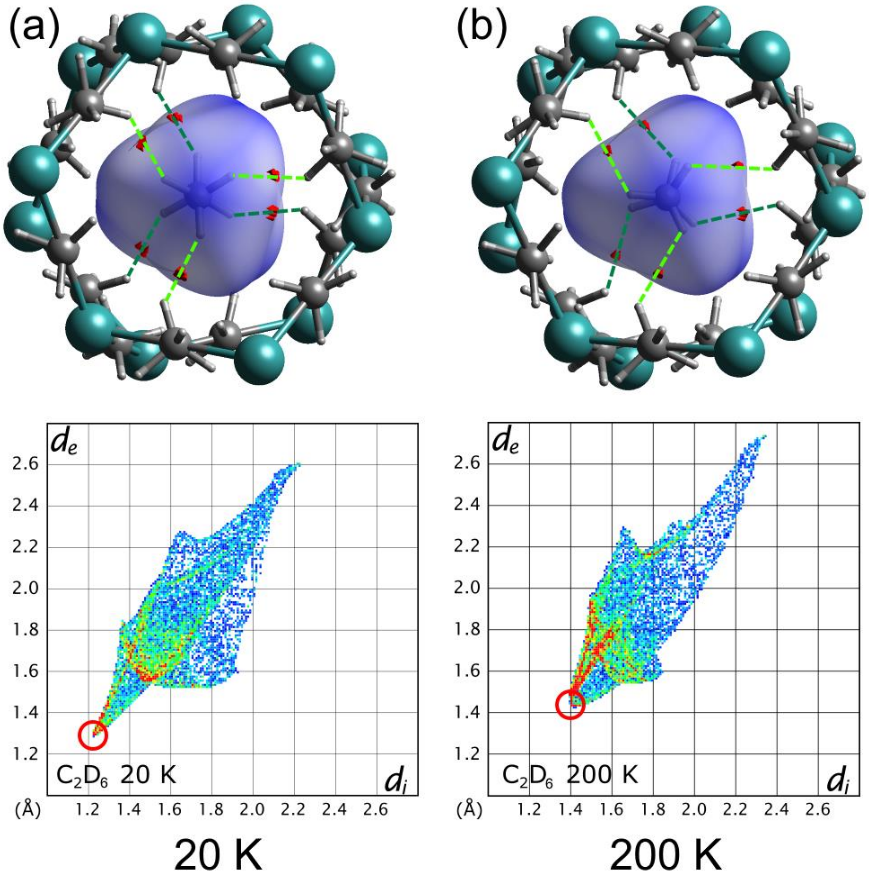

Figure S12. Structures and Hirschfield plots for γ-$Mg(^{11}BD_4)_2 \cdot 0.66C_2D_6$ at 20 K (a) and at 200 K (b). For better analysis of host-guest contacts, the Hirschfield plots were built using CrystalExplorer[2].

References

[1] Filinchuk Y., Richter B., Jensen T. R., Dmitriev V., Chernyshov D., Hagemann H. Porous and dense magnesium borohydride frameworks: synthesis, stability, and reversible absorption of guest species. *Angew. Chem.*. **2011**, 123(47): 11358-11362.

[2] Wolff S. K., Grimwood D. J., McKinnon J. J., Turner M. J., Jayatilaka D., Spackman M. A. Crystal explorer. *University of Western Austr.* **2012**.

Appendix IV: Supporting information of Chapter 7

In situ X-ray diffraction

The sample of γ-$Mg(BH_4)_2$ was prepared according to the synthetic procedure described elsewhere.[1] The grinded powder of γ-$Mg(BH_4)_2$ was loaded into 0.5 mm glass capillary in the argon filled glove box. The filled capillary was connected to the gas-loading manifold, equipped with the electronic manometer (working range of 0 - 100 bar with 0.01% full scale accuracy). Prior to gas loading, the sample was heated to 350 K under vacuum, in order to remove the traces of Ar. After evacuation, gas pressure was set to 0.5 bar.

The selected temperatures were controlled using Oxford Cryostream 700+. The preheated capillary with γ-$Mg(BH_4)_2$ (350 K, p(Ar, Kr, Xe) = 0.5 bar) was removed from the hot nitrogen stream using programmable goniostat,[2] in order to keep the sample at room temperature (minimizing gas adsorption before the beginning of data collection). The nitrogen blower without a sample was cooled for such kinetic datapoints: 110, 120, 140, 150, 160 K for Ar; 200, 190, 180 and 170 K for Kr; 220, 230, 240, 250, 260 K for Xe (with 2 minute waiting time for a temperature stabilization). The sample was fast moved into set capillary position under nitrogen gas stream and approximately 10000 data frames per temperature with 0.2, 0.25 and 0.5 s exposure for Ar, Kr and Xe, respectively, were collected. After data collection the same part of a capillary was heated back to 350 K (6 K/min rate) in order to remove gas molecules from γ-$Mg(BH_4)_2$ for the next temperature point. This procedure was repeated for the next temperature, changing the capillary position by 1 mm in order to have a fresh portion of the sample in the beam (not affected by radiation damage).

The in situ SXRPD data were collected at BM01 (SNBL/ESRF in Grenoble, France) using PILATUS@SNBL diffractometer.[3] The monochromatic beam (λ = 0.6866, 0.77936 and 0.66735 Å for the experiments with Ar, Kr and Xe, respectively) was calibrated on LaB_6 powder with PyFAI.[4] The obtained calibrations were implemented to Bubble for further azimuthal integration of 2D images. The resulting structures of Kr were refined using the models from Ref. [5] in a sequential mode by Rietveld method implemented into Fullprof software.[6]

The sequential crystal structure refinement details Several structural models and their combinations were checked for the refinement of time-dependent powder diffraction patterns, see for example Figure S1. The single phase refinement using $Mg(BH_4)_2 \cdot x$Kr phase (**1**) structural model[5] does not match our time-dependent experimental data, especially at 180 and 170 K. It was found that the peak intensities do not correspond to the single phases and the peaks have slightly asymmetric shape. The asymmetry position change in time from the lower to higher 2theta angles, if compared to the peaks of the main Mg(BH4)2·xKr phase (**1**), which is present within full time scale. That is why the sequential data analysis was divided into 2 parts. The first “starting time” part was considered as a mixture of empty (non-filled) γ-$Mg(BH_4)_2$ and main $Mg(BH_4)_2 \cdot x$Kr phase (**1**), see Figure S1. The refinement of such mixture was performed using the same profile parameters. The limiting point of the “starting time” was chosen, when the unit cell parameters of γ-$Mg(BH_4)_2$ became almost equal to $Mg(BH_4)_2 \cdot x$Kr phase (**1**) and started to decrease. The “ending time” part was modeled as a mixture of main $Mg(BH_4)_2 \cdot x$Kr phase (**1**) and minor $Mg(BH_4)_2 \cdot y$Kr phase (**2**), which has smaller cell parameters, than phase (**1**), see Figure S2.

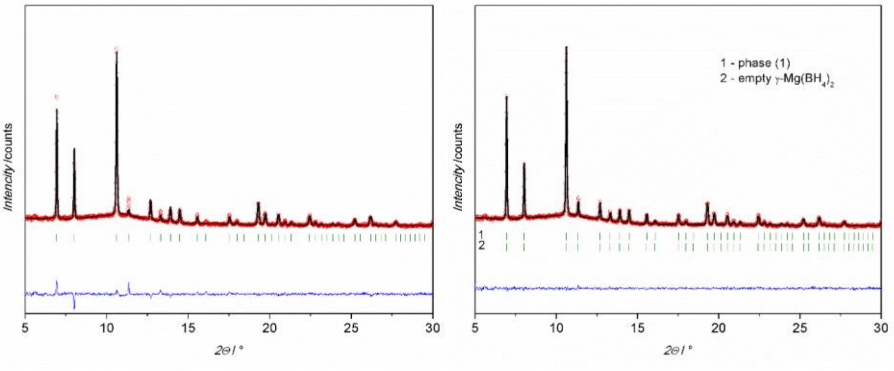

Figure S1. The comparison of powder X-ray diffraction pattern refinements with a single phase (**1**) (left) and as phase mixture, containing phase (**1**) and empty γ-$Mg(BH_4)_2$ (right) (T = 170 K; 25 seconds of the adsorption time). The difference curve (in blue) suggests, that the two-phase model is more preferable.

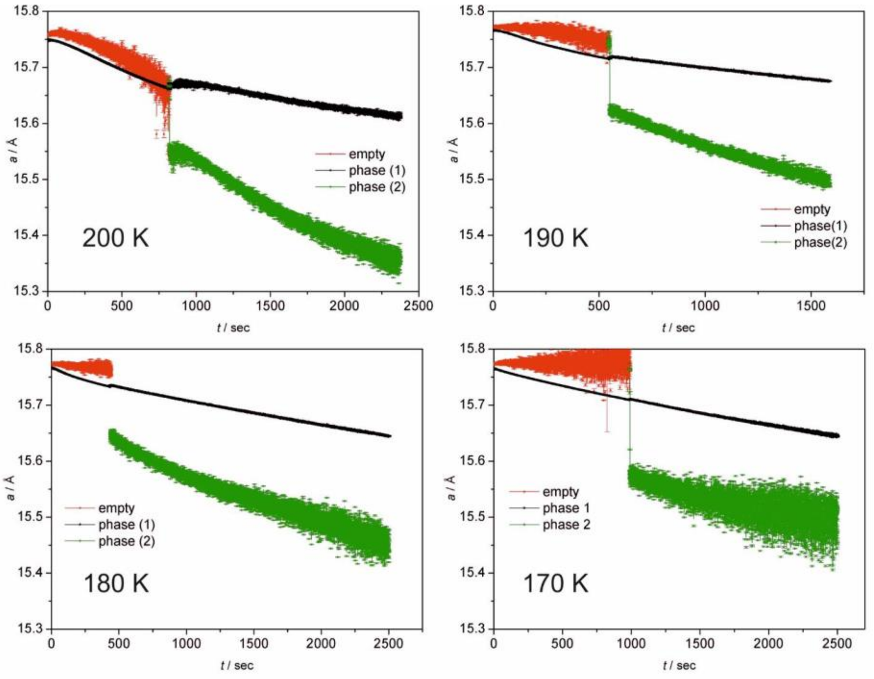

Figure S2. The unit cell parameters of two phase-models define the time limits for powder diffraction refinements.

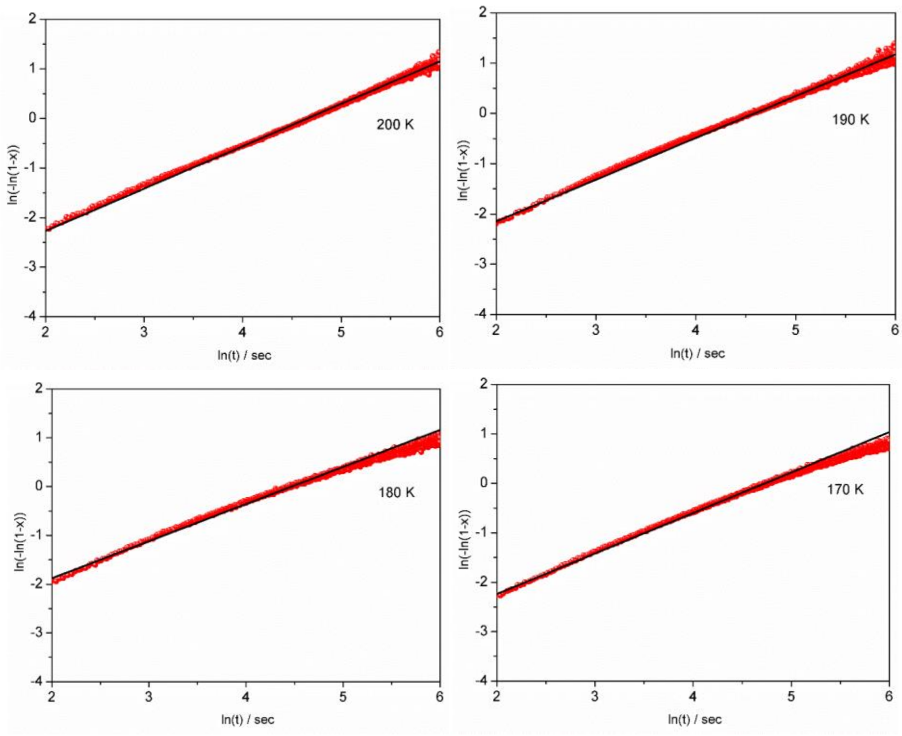

Figure S3. The Sharp – Hancock plots from Johnson-Mehl-Avrami-Kolmogorov (JMAK) relation (1), where *x* is a loading fraction.

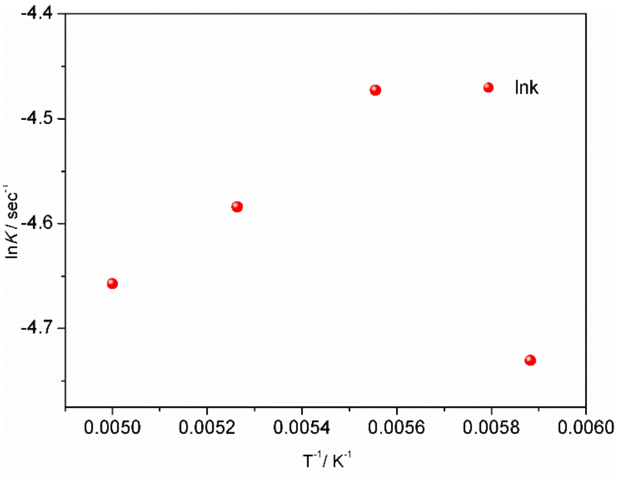

Figure S4. The Arrhenius plot of the rate constants logarithm, obtained from the Sharp – Hancock plots and the Equations (1) and (2).

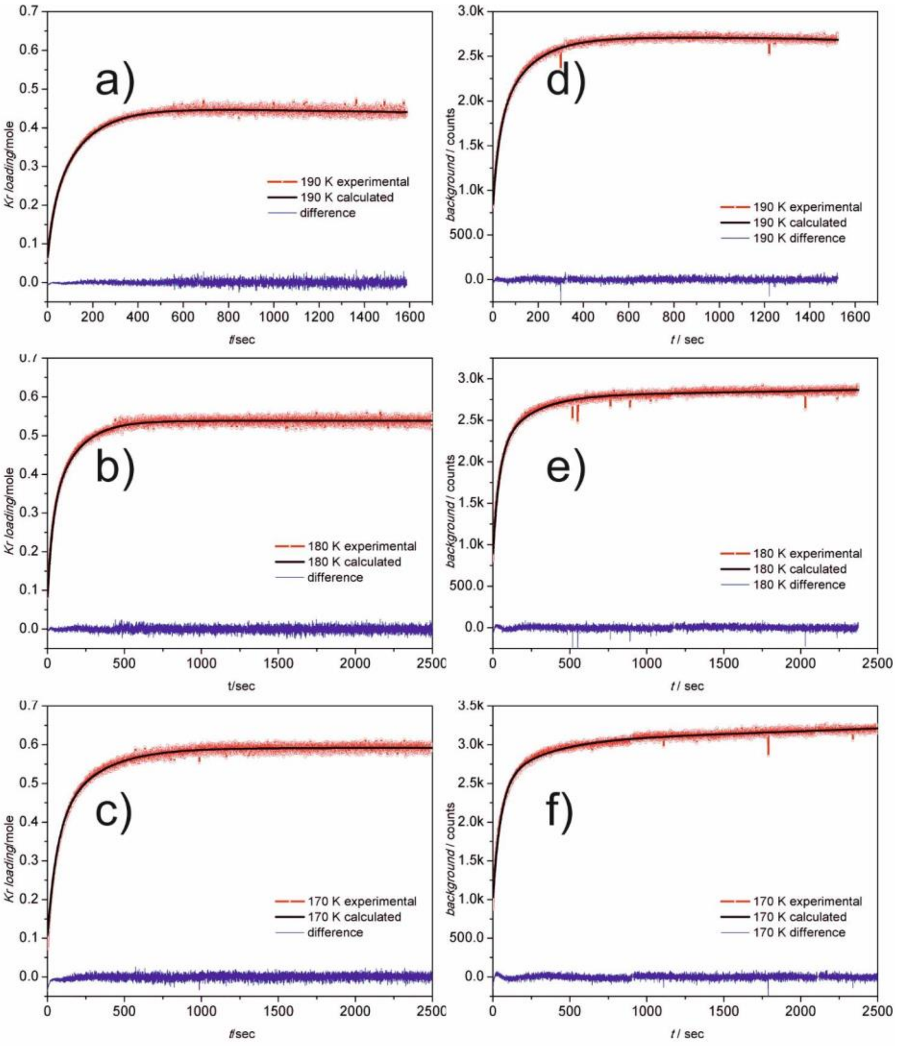

Figure S5. The parametric fits of the kinetic curves of Kr adsorption, using Equation (4): a-c) from the Kr occupancies; d-f) from the fluorescence background.

Volumetric measurements of adsorption isotherms

Krypton (170 – 200 K) and nitrogen (190 K) adsorption isotherms were measured on the same sample (sample mass 50 mg) using a volumetric BELSORP-HP apparatus, connected to a self-designed cell mounted on a closed cycle helium cryostat DE-202AG. It is operated by a temperature controller LS-336 (Lake Shore), and the heat produced by the cryostat is removed from the system by a helium compressor ARS-4HW.

The N_2 data was used to quantify the amount of the crystalline γ-$Mg(BH_4)_2$ in the sample, which amounts to 60%.

The sample was handled in the inert atmosphere in the glovebox filled with Ar. Prior the measurements, the sample was evacuated for 16 h at 343 K. Between the measurements at different temperatures, the sample was heated to 298 K and evacuated for 2 h. Nitrogen adsorption isotherm at 190 K up to 45 bar was collected after the Kr adsorption experiments, on the same sample still in the same cell. Prior to nitrogen adsorption the sample was evacuated at 343 K for 16 h.

The kinetic data collected were analyzed by adsorption rate analysis software BELDyna^{TM}, using LDF approximation:

$$\frac{dq}{dt} = K_s a_p (q^* - q) \tag{S1}$$

Linear equilibrium equation:

$$q^* = H \cdot P \tag{S2}$$

Batch adsorption operating equation:

$$W_{(q-q_{0n})} = v(P_{0n} - P) \tag{S3}$$

H: equilibrium (Henry) constant [cm^3/g]

P: pressure [Pa]

P_0: initial pressure [Pa]

P_e: equilibrium pressure [Pa]

q: adsorbed amount [cm^3/g]

q_0: initial adsorption amount [cm^3/g]

$K_s a_p$: mass transfer coefficient [1/sec] *t*: time [s]

V: gas phase volume [cm^3]

W: adsorbent amount [g]

By solving simultaneous above Equations (S1), (S2) and (S3), the following solution is obtained:

$$\frac{P}{P_{on}} = 1 - \left(\frac{P_{on} - P_{en-1}}{P_{on}}\right)\left(\frac{1}{\alpha+1}\right)\left[1 - exp\left\{-K_s\, a_p\left(\frac{\alpha+1}{\alpha}\right)t\right\}\right] \quad \text{(S4)}$$

$$\frac{P - P_{en}}{P_{on} - P_{en}} = 1 - \left(\frac{P_{on} - P_{en-1}}{P_{on} - P_{en}}\right)\left(\frac{1}{\alpha+1}\right)\left[1 - exp\left\{-K_s\, a_p\left(\frac{\alpha+1}{\alpha}\right)t\right\}\right] \quad \text{(S5)}$$

In the above equations, $\alpha = V/(W \cdot H)$ (separation factor).

Providing that $P = CRT$, the Equation (S5) transforms into:

$$\frac{C - C_{en}}{C_{on} - C_{en}} = 1 - \left(\frac{C_{on} - C_{en-1}}{C_{on} - C_{en}}\right)\left(\frac{1}{\alpha+1}\right)\left[1 - exp\left\{-K_s\, a_p\left(\frac{\alpha+1}{\alpha}\right)t\right\}\right] \text{(S6)}$$

For the adsorption rate analysis program, the Equation (S6) is used.

The data obtained for the points at 50 kPa are summarized in the Table S1.

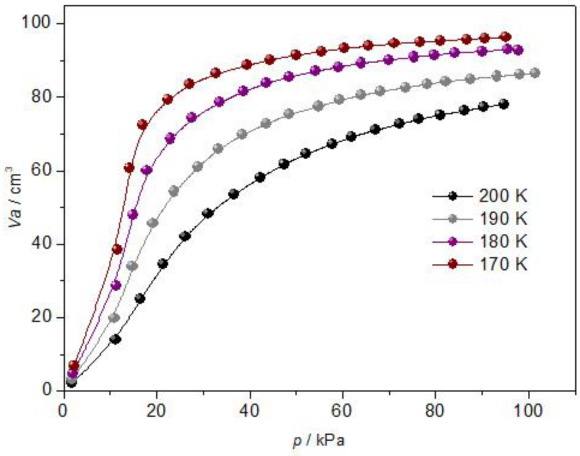

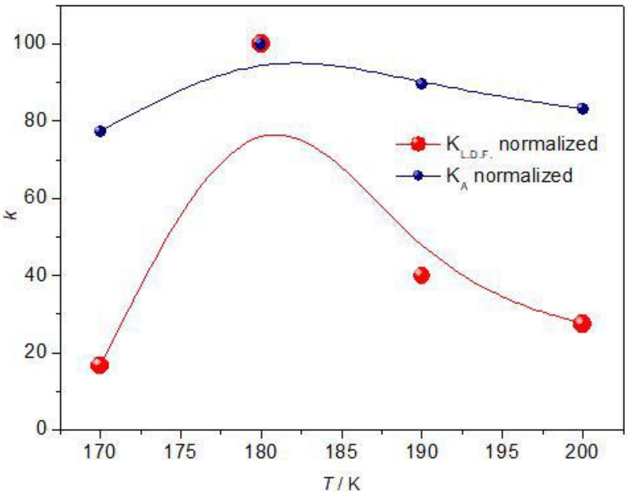

Figure S6. a) The Kr adsorption isotherms (up to 100 kPa) at various temperatures; b) The comparison of the temperature-dependencies of the normalized kinetic rates from Linear Driving Force (L.D.F.) approximation ($K_{L.D.F.}$ from volumetric studies at 50 kPa in red) with a fractional order kinetic model (K_A - Avrami kinetic constant in dark blue), obtained from Sharp – Hancock plots (the details are given in Tab. S1).

Table S1. The comparison of Linear driving force (L.D.F.) approximation (KL.D.F. from volumetric studies) and a fractional order kinetic model (K_A - Avrami kinetic constant from *in situ* X-ray powder diffraction) at *p*(Kr) = 50 kPa.

T, K	K_A, 1/sec	*n*	$K_{L.D.F.}$ $n = 1$
200	0.00949	0.86	0.0269
190	0.01021	0.83	0.0392
180	0.01141	0.76	0.0982
170	0.00882	0.82	0.0163

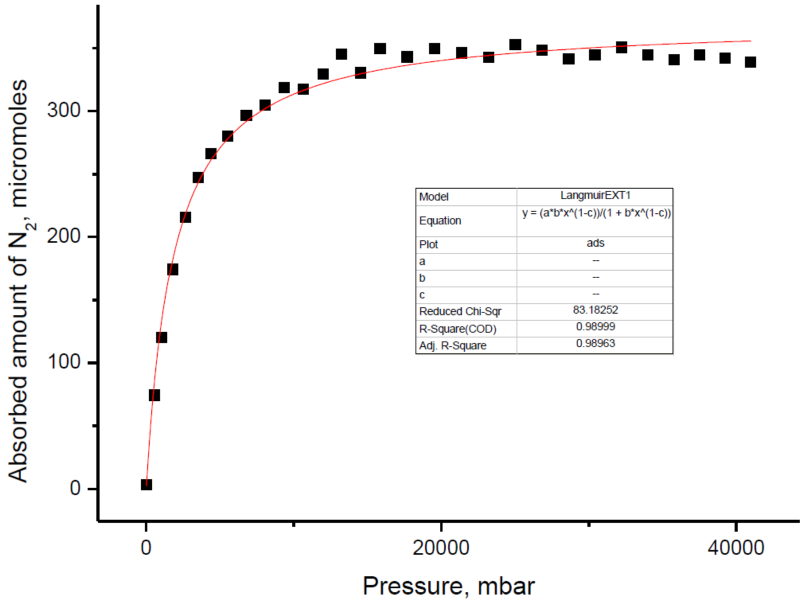

Model	LangmuirEXT1
Equation	y = (a*b*x^(1-c))/(1 + b*x^(1-c))
Plot	ads
a	--
b	--
c	--
Reduced Chi-Sqr	83.18252
R-Square(COD)	0.98999
Adj. R-Square	0.98963

Figure S7. Nitrogen adsorption isotherm at 190 K up to 45 bar, used to quantify the fraction of the crystalline γ-$Mg(BH_4)_2$ in the sample, knowing that the limiting composition in saturation is γ-$Mg(BH_4)_2 \cdot 0.667N_2$. To estimate the capacity in the saturation, the fit of the Langmuir equation to the data was done, yielding a = 371(3) μmol and b = $5.4(3) \cdot 10^{-4}$. Considering that the sample mass of 50 mg, the fraction of the crystalline γ-$Mg(BH_4)_2$ is estimated to be 60%.

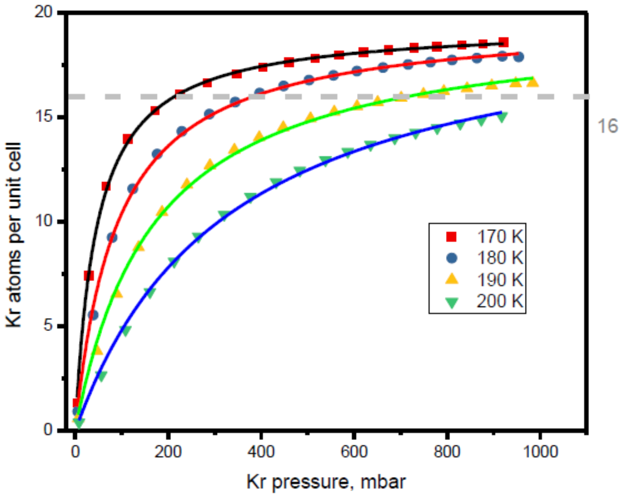

Figure S8. Kr adsorption isotherms, corrected for the fraction of the crystalline γ-

$Mg(BH_4)_2$. The fits made by Langmuir equation overestimate slightly the limiting capacity of 16 Kr per unit cell (0.667 Kr per Mg), due to uncertainties of calibration with N_2. The fitted values at 170 K: a = 19.45(4) Kr/cell and b = $2.17(3)\cdot10^{-2}$; at 180 K: a = 19.75(7) Kr/cell and b = $1.11(2)\cdot10^{-2}$; at 190 K: a = 19.8(1) Kr/cell and b = $5.9(2)\cdot10^{-3}$; at 200 K: a = 20.7(2) Kr/cell and b = $3.03(9)\cdot10^{-3}$.

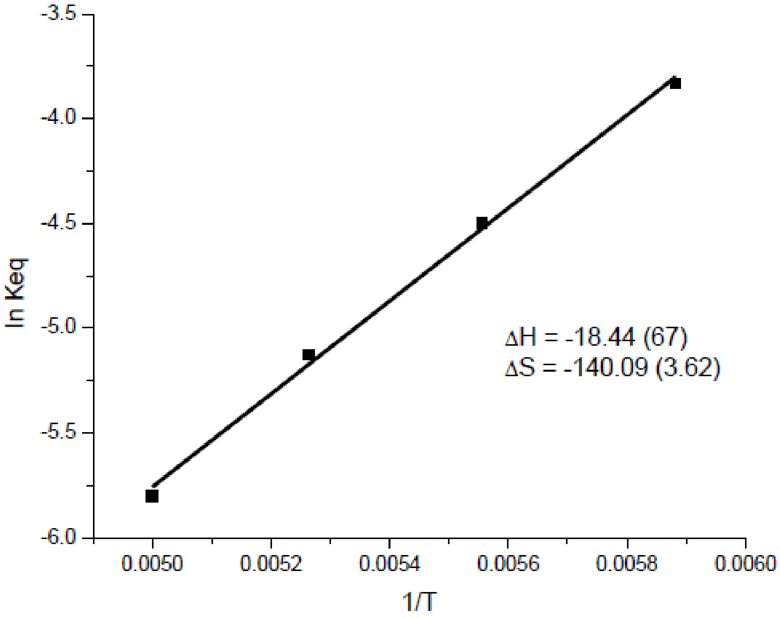

Figure S9. Van' t Hoff plot made with equilibrium constants, K_{eq}, obtained from the Langmuir equations fitted to the Kr adsorption isotherms, see the previous Figure S8. The resulting values: ΔH = -18.4(7) kJ/mol of adsorbed Kr, ΔS = -140(4) J/(mol·K).

Table S2. The details of the refined parameters from the kinetic Equation (4) for Kr occupancies.

T, K	k_1, sec^{-1}	k_2, sec^{-1}	k_3, sec^{-1}	A_1	A_2
200	0.00805(3)	0.100(4)	0.00043(2)	0.789(5)	0.163(3)
190	0.0070(1)	0.034(1)	0.00043(34)	0.68(3)	0.288(9)
180	0.00613(5)	0.0315(6)	0.00244(264)	0.556(5)	0.444(5)
170	0.00376(5)	0.0165(2)	0.00005(129)	0.40(4)	0.60(5)

Table S3. The details of the refined parameters from kinetic Equation (3) for Kr occupancies.

T, K	k_1, sec^{-1}	k_2, sec^{-1}	A_1
190	0.00809(5)	0.047(2)	0.775(6)
180	0.00617(4)	0.0318(6)	0.558(4)
170	0.00359(3)	0.0160(2)	0.419(4)

Table S4. The details of the refined parameters from the kinetic Equation (4) for Kr fluorescence.

T, K	k_1, sec^{-1}	k_2, sec^{-1}	k_3, sec^{-1}	A_1	A_2
200	0.00863(5)	0.063(2)	0.00031(1)	0.622(7)	0.212(3)
190	0.00719(7)	0.0354(6)	0.0028(5)	0.552(6)	0.448(5)
180	0.00456(9)	0.0246(3)	0.0003(1)	0.38(2)	0.67(2)
170	0.0031(1)	0.0196(2)	0.0003(1)	0.31(1)	0.77(3)

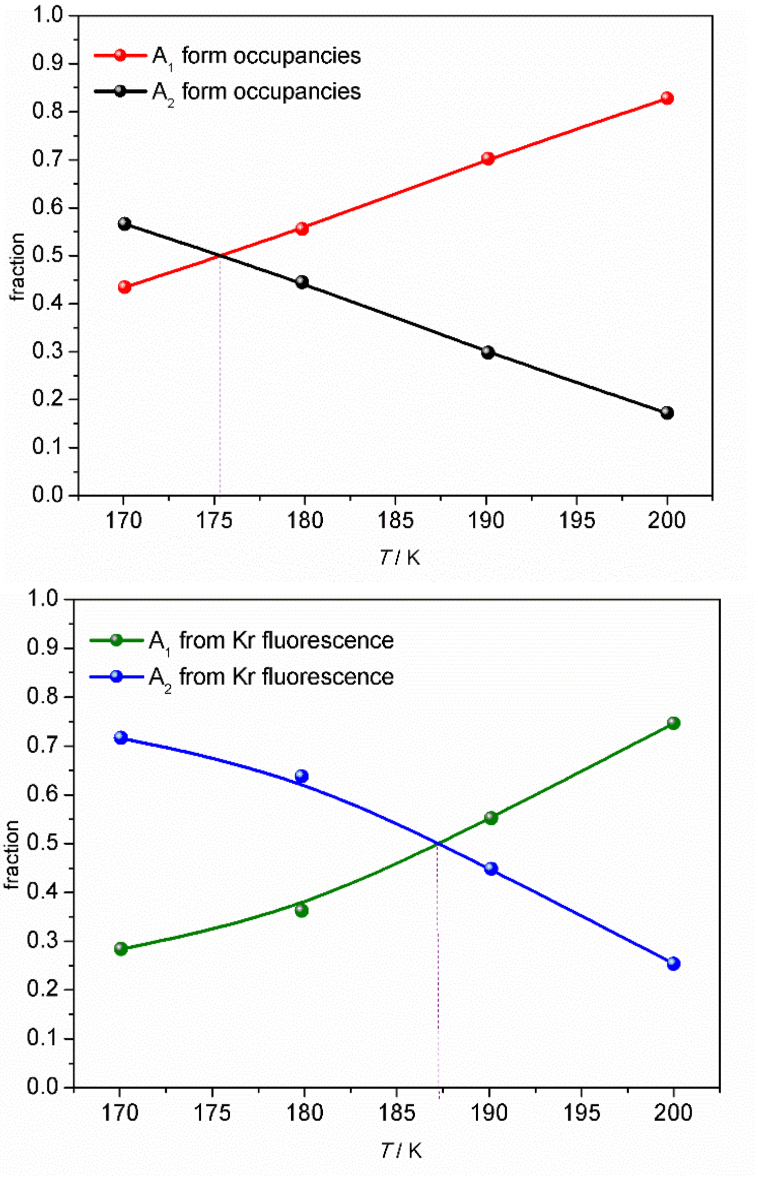

Figure S10. The linear interpolation of the contributions from Kr occupancies (top) and fluorescence (bottom).

Scanning Electron Microscopy (SEM)

For scanning electron microscopy measurement the sample was placed on a silica wafer and dried at 353 K for 60 minutes. Subsequently the sample was sputtered with gold to enhance surface conductivity. The measurement was carried out using a 2 kV acceleration voltage and a working distance of 4.1 mm on a SU8020 from Hitachi device.

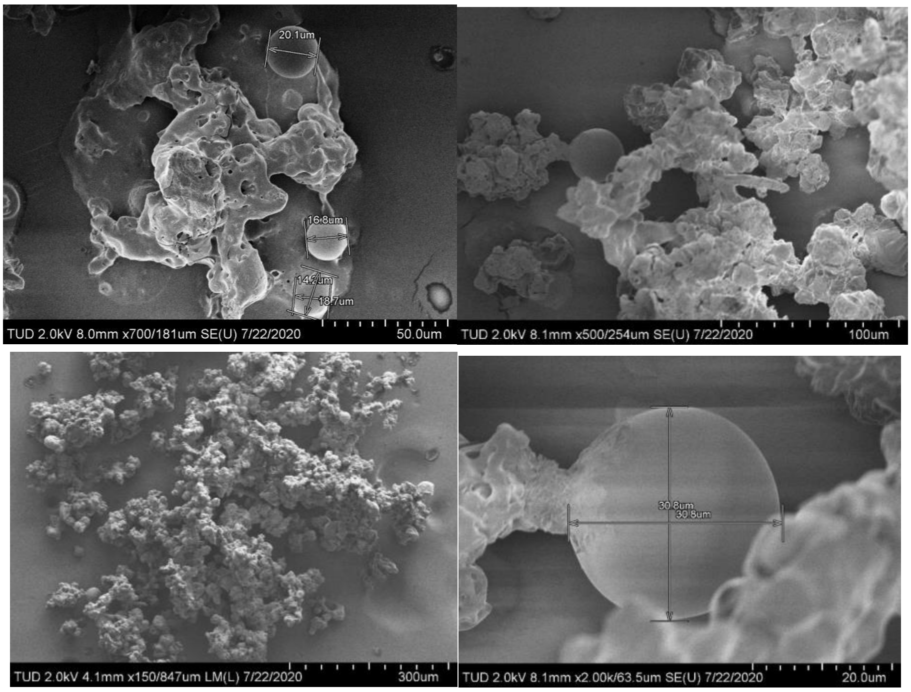

Figure S11. The SEM images suggest the presence of two kinds of $Mg(BH_4)_2$ particles: spherical and of undefined shape. It points on the co-existence of crystalline, porous γ-$Mg(BH_4)_2$ phase (which adsorbs the noble gases) and other amorphous polymorph of $Mg(BH_4)_2$ (which is non porous), in agreement with the volumetric studies.

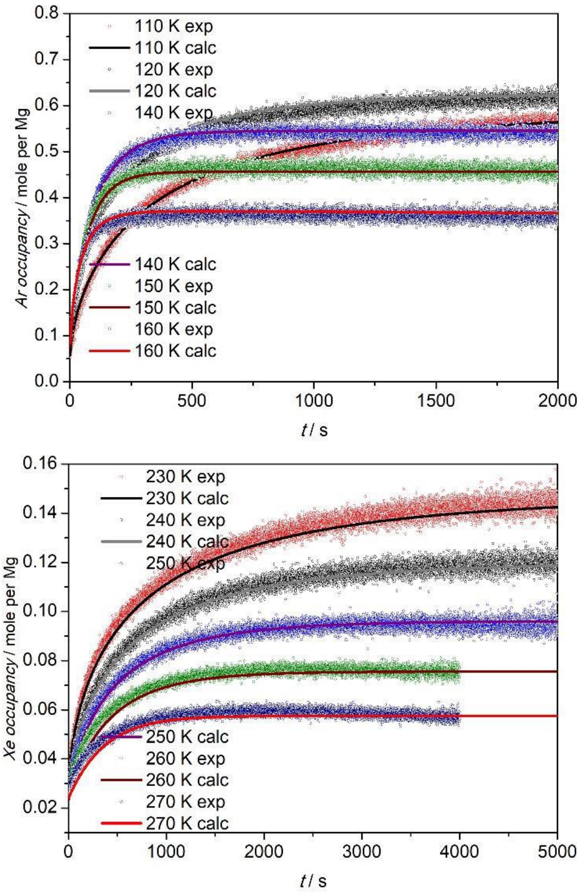

Figure S12. The experimental and calculated adsorption kinetic plots of Ar (up) and Xe (bottom), obtained from the sequential refinement of the variable-time crystal structures of $Mg(BH_4)_2 \cdot q_t(Ng)$.

Table S5. The parameters of kinetic models from Ar and Xe uptake by γ-$Mg(BH_4)_2$.

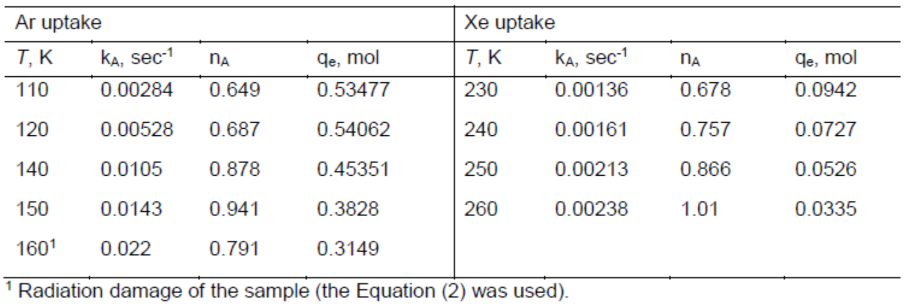

Ar uptake				Xe uptake			
T, K	k_A, sec^{-1}	n_A	q_e, mol	*T*, K	k_A, sec^{-1}	n_A	q_e, mol
110	0.00284	0.649	0.53477	230	0.00136	0.678	0.0942
120	0.00528	0.687	0.54062	240	0.00161	0.757	0.0727
140	0.0105	0.878	0.45351	250	0.00213	0.866	0.0526
150	0.0143	0.941	0.3828	260	0.00238	1.01	0.0335
160[1]	0.022	0.791	0.3149				

[1] Radiation damage of the sample (the Equation (2) was used).

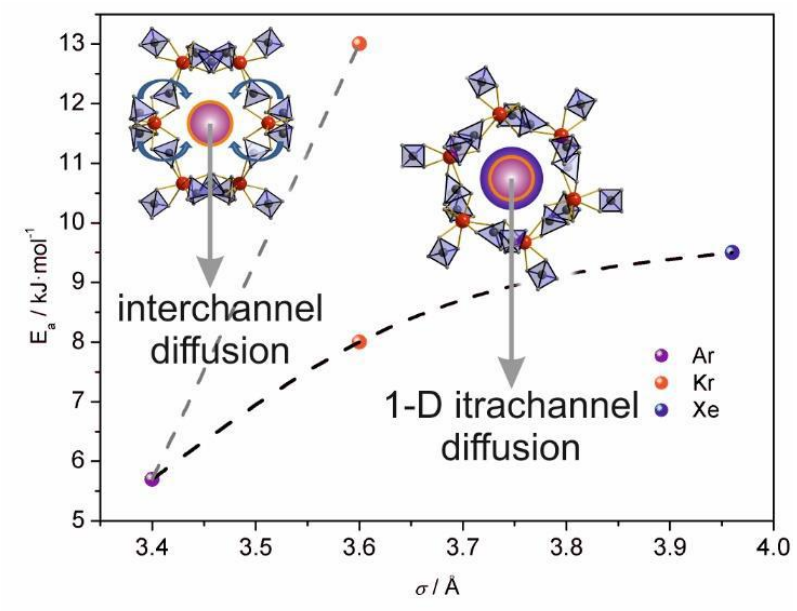

Figure S13. Activation barriers as a function of noble gas kinetic diameter.

References

[1] Y. Filinchuk, B. Richter, T. R. Jensen, V. Dmitriev, D. Chernyshov, H. Hagemann, *Angew. Chem. Int. Ed.* **2011**, 50, 11162-11166.

[2] D. Rojo-Gama, L. Mentel, G. N. Kalantzopoulos, D. K. Pappas, I. Dovgaliuk, U. Olsbye, K. P. Lillerud, P. Beato, L. F. Lundegaard, D. S. Wragg, et al., *J. Phys. Chem. Lett.* **2018**, 9, 1324-1328.

[3] V. Dyadkin, P. Pattison, V. Dmitriev, D. Chernyshov, *J. Synchrotron Radiat.* **2016**, 23, 825-829.

[4] G. Ashiotis, A. Deschildre, Z. Nawaz, J. P. Wright, D. Karkoulis, F. E. Picca, J. Kieffer, *J. Appl. Crystallogr.* **2015**, 48, 510-519.

[5] I. Dovgaliuk, V. Dyadkin, M. Vander Donckt, Y. Filinchuk, D. Chernyshov, *ACS Appl. Mater. Interfaces* **2020**, 12, 7710-7716.

[6] J. Rodríguez-Carvajal, *Phys. B Condens. Matter.* **1993**, 192, 55-69.